



Kent Academic Repository

Webber, J. Beau W. (2000) *The Characterisation of Porous Media*. Doctor of Philosophy (PhD) thesis, Physics.

Downloaded from

<https://kar.kent.ac.uk/13453/> The University of Kent's Academic Repository KAR

The version of record is available from

<http://www.kent.ac.uk/physical-sciences/publications/theses/jbwww.html>

This document version

Author's Accepted Manuscript

DOI for this version

Licence for this version

CC BY (Attribution)

Additional information

Versions of research works

Versions of Record

If this version is the version of record, it is the same as the published version available on the publisher's web site. Cite as the published version.

Author Accepted Manuscripts

If this document is identified as the Author Accepted Manuscript it is the version after peer review but before type setting, copy editing or publisher branding. Cite as Surname, Initial. (Year) 'Title of article'. To be published in *Title of Journal*, Volume and issue numbers [peer-reviewed accepted version]. Available at: DOI or URL (Accessed: date).

Enquiries

If you have questions about this document contact ResearchSupport@kent.ac.uk. Please include the URL of the record in KAR. If you believe that your, or a third party's rights have been compromised through this document please see our [Take Down policy](https://www.kent.ac.uk/guides/kar-the-kent-academic-repository#policies) (available from <https://www.kent.ac.uk/guides/kar-the-kent-academic-repository#policies>).

CHARACTERISING POROUS MEDIA

A THESIS SUBMITTED TO
THE UNIVERSITY OF KENT AT CANTERBURY
IN THE SUBJECT OF PHYSICS
FOR THE DEGREE
OF DOCTOR OF PHILOSOPHY.

By
John Beausire Wyatt Webber
January 2000

Contents

List of Tables	x
List of Figures	xv
Abstract	xvi
Acknowledgements	xvii
1 Introduction.	1
1.1 Porous materials.	1
1.2 Properties of porous materials.	1
1.3 Porosity and pore size measurement techniques on porous media.	2
1.3.1 Gas adsorption.	3
1.3.2 Mercury Intrusion.	5
1.3.3 Thermoporosimetry (DTA/DSC).	5
1.4 Measurements on Porous Materials by NMR.	6
1.4.1 Cryoporometry for measuring pore size distributions.	6
1.4.2 Multidimensionally resolved pore size distributions.	7
1.4.3 Bounded liquid fraction and diameter determination.	7
1.4.4 Fluid transport and diffusion in fine porous material.	8
1.4.5 Direct 1D, 2D, 3D imaging of coarsely structured materials.	8
1.4.6 NMR relaxation in pores.	8
1.5 Measurements on Porous Materials by SANS.	8
1.6 The scope of this Thesis.	9
1.7 Accuracies of quoted results.	10

2	NMR Theory.	11
2.1	Interaction of radiation with matter.	11
2.2	Zeeman energy level splitting in a magnetic field.	11
2.2.1	Protons in a magnetic field.	13
2.3	Magnetisation due to Boltzmann distribution.	13
2.4	The time evolution of nuclear spin systems in a magnetic field.	16
2.5	The Bloch equations.	17
2.6	The NMR Hamiltonian operator.	19
2.7	Dipolar interactions, spin-spin relaxation.	19
2.7.1	The Dipolar Hamiltonian.	20
2.7.2	Spectral densities.	21
2.7.3	Motional narrowing.	22
2.7.4	Spin-spin relaxation in pores.	22
2.8	NMR spin echoes.	23
3	NMR Cryoporometry method.	26
3.1	NMR Cryoporometry equations.	26
4	NMR Cryoporometry experimental apparatus.	29
4.1	Bulk and 1D resolved cryoporometry apparatus.	29
4.2	2D and 3D spatial resolution cryoporometry apparatus.	36
5	NMR cryoporometry temperature control.	41
5.1	Liquid nitrogen droplet cooled probe.	41
5.2	Peltier cooled probe.	43
5.3	Gas flow cooled probe.	45
5.4	Temperature cycle control.	46
6	Sample preparation for cryoporometry.	48
7	NMR Cryoporometry calibration.	50
7.1	Cryoporometer volumetric calibration.	50
7.2	Receiver gain calibration.	51
7.3	Temperature dependence of volumetric sensitivity.	53
7.3.1	Resistivity of copper.	53

7.3.2	Volumetric sensitivity.	53
7.3.3	Density changes.	55
7.3.4	Calibration of volumetric temperature coefficient.	56
7.3.5	NMR relaxation effects on volumetric calibration.	58
7.3.6	Corrections for T2 relaxation.	62
7.4	Calibration of melting point depression of cyclohexane in porous silica.	63
7.4.1	Sample preparation.	63
7.4.2	Cryoporometric measurements.	63
7.4.3	Melting point depression calculation.	64
7.5	Calibration of melting point depression of water in porous silica.	70
7.5.1	Sample preparation.	70
7.5.2	Cryoporometric measurements.	70
7.5.3	Melting point depression calculation.	71
7.5.4	The effect of pore size dependent T2.	71
7.5.5	Calibrated porosity measurement.	73
8	Multidimensionally Resolved Pore Size Distributions.	78
8.1	Spatially resolved cryoporometry.	78
8.2	1D NMR Cryoporometry.	79
8.3	2D Resolved Pore Size Distributions	83
8.4	3D Resolved Pore Size Structure	89
8.5	Conclusion	95
9	Cryoporometry on large pore materials.	96
9.1	Sample preparation.	97
9.2	Measurement runs.	97
9.3	Cryoporometric results.	97
9.4	Calibrations as a function of warming rate.	98
9.5	Cryoporometric resolution.	102
9.6	Conclusion.	105
10	Natural fractal pore size distributions.	106
10.1	Self similarity and Fractal dimension.	106
10.2	Self similarity in measured pore size distributions.	107

11 Densities and solid-solid density correlations.	110
11.1 Introduction.	111
11.2 Model porous systems: constraints and simplifications.	112
11.2.1 Structural length scales observed in porous silica systems.	112
11.2.2 Continuum simplification.	116
11.2.3 Bulk density constraints on simple pore and lattice geometries.	117
11.3 Models of simple porous systems.	118
11.3.1 Single cylindrical tube.	119
11.3.2 Cylindrical voids.	120
11.3.3 Spherical Geometries.	123
11.4 Density measurements: sol-gel and templated silicas.	131
11.4.1 Porous silica density measurements.	131
11.4.2 Grain densities and silica filling factors.	132
11.4.3 Lattice spacings.	134
11.5 Imbibing liquids to determine porous parameters.	135
11.5.1 Silica (voidless) lattice density.	135
11.5.2 Measuring pore and packing void volume.	137
11.5.3 Deducing pore throat diameters.	139
11.6 Summary.	142
12 Neutron scattering theory.	143
12.1 Wave – Particle duality.	143
12.2 Scattering and density distribution relationships.	143
12.3 Scattering from porous media.	148
12.4 The Guinier approximation.	149
12.5 The Porod law.	152
12.6 Combining the Guinier and Porod descriptions.	152
12.7 Obtaining $G(r)$ for these scattering forms.	154
12.8 Babinet’s Theorem.	154
12.9 Chordal analysis.	154
13 Neutron scattering from silica.	156
13.1 Neutron scattering apparatus.	156
13.1.1 Neutron production, thermalisation and monochromatisation.	157

13.1.2	Apparatus for Neutron Scattering Diffraction – D4B.	158
13.1.3	Apparatus for Small Angle Neutron Scattering – D22.	160
13.2	Sample Preparation.	162
13.3	Measurement of Scattering Intensity.	162
14	Neutron Scattering Analysis.	163
14.1	Neutron Scattering from water.	163
14.2	Calibration and normalisation for small angle scattering.	163
14.2.1	DoD22 show and analysis program.	167
15	The calculation of $G(r)$ for model porous structures.	173
15.1	Project aims.	173
15.2	Evaluation of scattering for porous structures.	174
15.2.1	Separation of scattering $I(q)$ into $P(R \cdot q)$, $S(q)$	174
15.2.2	Monte-Carlo integration of density correlation functions $G(r)$	175
15.3	Project simplifications.	175
15.4	First tests.	176
15.5	Obtaining $G(r)$ in a continuous medium.	179
15.6	Monte-Carlo $G(r)$ integration of simple bodies.	181
15.7	Construction of lattices of pores.	181
15.7.1	Simulating Cubical lattices of Spherical pores.	183
15.7.2	Simulating Square lattices of Cylindrical pores.	184
15.7.3	Simulating Hexagonal lattices of Cylindrical pores.	184
15.7.4	Simulating Hexagonal Close Packed lattices of Spherical pores.	185
15.8	Ensembles of lattices with a statistical spread.	186
15.9	Implementation of Monte-Carlo integration of models	187
15.10	Monte-Carlo integration of porous models.	189
15.11	Preliminary consideration of Monte-Carlo $G(r)$ s.	190
16	Analysis of sol-gel silica scattering in q, r domains.	192
16.1	Analysis in q domain, comparison with Monte-Carlo data.	192
16.2	Analysis of silica scattering in the spatial domain.	203
16.2.1	Comparison of $G(r)$ for sol-gel silicas with that for slabs.	204
16.2.2	Conversion to density units.	205

16.2.3	Chordal representation.	206
16.2.4	Comparison with $G(r)$ data from Monte-Carlo calculations.	207
16.2.5	$G(r)$ data, Monte-Carlo $G(r)$ at large radius.	208
17	Neutron scattering calibration of pore diameter.	213
17.1	Scattering void form factors and lattice structure factors.	214
17.2	Characterisation by radius of $d(r)$ maximum.	215
17.3	Radius of $d(r)$ maximum: variation with D/a for various lattices.	216
17.4	Applying measured silica parameters to Monte-Carlo calculations.	220
17.5	Neutron scattering pore diameter variance.	221
17.6	Neutron scattering pore diameter results.	224
17.7	Summary.	226
18	Conclusions.	229
18.1	Developments of NMR Cryoporometry.	229
18.2	Conclusions from density and imbibation experiments.	230
18.3	Developments of SANS analysis of pore scattering.	231
A	Equation of motion for a quantum spin.	232
B	The Dipolar Hamiltonian.	235
C	NMR CRYOPOROMETER.	239
C.1	Over view.	239
C.2	Running the Cryoporometer.	240
C.3	Instrument Front Panel.	240
C.3.1	Left of Display.	240
C.3.2	Right of Display.	243
C.3.3	Centre of Display.	244
D	Determination of cryoporometric resolution.	245
E	T2 corrections for pore volume signal.	251
F	Warming rate for constant resolution.	254
F.1	Constant resolution on a linear scale.	254
F.2	Constant resolution on a logarithmic scale.	255

F.2.1	Defining a warming profile.	256
G	Numerical simulation of bulk melting step.	257
H	Radius of a sphere in a tetragon of spheres.	261
I	Volume of a cap of a sphere.	264
J	Surface area of a cap of a sphere.	265
K	Analytic derivation of $G(r)$ for a uniform solid sphere.	267
K.1	Effect on $g(r)$ of finite sample volume.	267
L	Calculation of $G(r)$ for an infinite slab.	269
M	$I(q)$ to $G(r)$ transformations for standard forms.	276
M.1	q domain to r domain transformation.	276
M.1.1	Guinier : $I(q)$ Gaussian.	276
M.1.2	Ornstein-Zernike : $I(q)$ Lorentzian.	277
M.1.3	Guinier-Porod : $I(q)$ Lorentzian squared.	277
M.1.4	Porod : $I(q)$ inverse quartic q	278
M.1.5	Porous media : $I(q)$ sech.	278
N	Angular intensity fall-off due to a flat detector.	280
O	Attenuation due to angled scattering in a thick sample.	283
P	$I(q)$ to $G(r)$, $G(r)$ to $I(q)$.	286
P.1	$I(q)$ to $G(r)$	286
P.2	$G(r)$ to $I(q)$	287
Q	Appendices for Monte-Carlo integration of $G(r)$.	288
Q.1	Generating random unit vectors in 3D, using von Neuman's method. . .	288
Q.2	Generate a Gaussian distribution, using the Central Limit Theorem. . .	289
Q.3	Generate non-uniform distributions by remapping a uniform distribution.	289
Q.3.1	Generate a distribution $\propto x$ by remapping a uniform distribution.	290
Q.3.2	Generate a Sech distribution by remapping a uniform distribution.	291

R Fourier transform of Sech is Sech.	292
R.1 Demonstration of relationship : $\text{Sech} \leftrightarrow \text{Ft}(\text{Sech})$	292

List of Tables

1	Magnetisation per proton, as a function of frequency and temperature. .	15
2	NMR Hamiltonian terms	19
3	Dipolar Hamiltonian terms	20
4	Gas adsorption diameters for Unilever (A) silica.	63
5	Slope k and surface layer Sl for C_6H_{12} in Silica.	69
6	Nominal diameters for Unilever (A) and (B) silica.	70
7	Calculation of pore volume for eight porous silicas.	75
8	Warming rate measurements.	97
9	Analytic and MC values for silica filling factors on an HCP lattice. . .	128
10	Compression of Behrens silicas on addition of liquid, and deduced grain packing fraction.	132
11	Densities and silica fractions for porous silicas.	133
12	Minimum silica fraction f for given pore geometries.	134
13	Volumes and densities for (voidless) silica lattices.	136
14	Dry and wet packing volumes for seven porous silicas.	137
15	Silica fraction and dry and wet grain packing fractions.	138
16	Pore void diameter D_{void} to lattice spacing a	138
17	Lattice spacing a for various pore geometries.	139
18	Deduced pore throat diameters for seven porous silicas.	141
19	Parameters for seven sol-gel silicas.	212
20	Coefficients to obtain $d_{Max}D/a$ for various lattices.	219
21	Calculation of neutron scattering pore diameters for silicas.	225
22	Measured bulk step ΔT , ΔM , when using cyclohexane.	250
23	Measured bulk step ΔT , ΔM , when using water.	250

List of Figures

1	Pore size in sandstone as measured by two methods.	3
2	Quantised nuclear spin momentum.	12
3	Quantised spin precession cones for protons.	13
4	NMR spin echo.	23
5	Generation of a spin echo.	24
6	NMR spectrometer with Lindacot cooler	29
7	NMR Receiver circuit diagram	30
8	NMR Transmitter circuit diagram	31
9	Cryoporometer instrument rack	32
10	NMR Cryoporometric apparatus	33
11	Cryoporometer LabVIEW frontpanel.	34
12	Cryoporometer LabVIEW top level diagram.	35
13	Diagram of the imaging spectrometer.	37
14	Interface between SMIS PC and Bruker.	38
15	Four quadrant R.F. multiplier diagram and PCB.	39
16	Multiple low pass Butterworth filters for NMR recieved signals.	40
17	Cryoporometry NMR probe.	42
18	Peltier cooled NMR probe.	43
19	Peltier probe performances.	44
20	Gas flow cooling system.	45
21	Temperature cycling sub.vi	47
22	Measured gain curve for receiver.	51
23	Corrected high amplitude gain curve for receiver.	52
24	Low level gain curve for receiver.	52
25	Resistivity of copper vs. T_K	54

26	Amplitude changes due to Boltzmann and ρ_{Cu}	56
27	Boltzmann and coil resistance corrections for C_6H_{12} and H_2O	58
28	Measured T_2 of cyclohexane in the bulk.	59
29	Solid echoes from bulk cyclohexane.	60
30	Melting point depression for cyclohexane in silica (2τ : 4ms).	66
31	Melting point depression for C_6H_{12} in SiO_2 (2τ :4ms,10ms).	67
32	Melting point depression for C_6H_{12} in SiO_2 (2τ :20ms,40ms).	68
33	k vs. τ for cyclohexane in silica.	69
34	Melting point depression for water in silica (2τ : 4ms).	72
35	40Å melting point curves for water.	73
36	Melting point depression for water (2τ : 4ms,10ms,20ms,40ms).	74
37	τ dependence for water in 40Å, 60Å, 100Å silica.	76
38	τ dependence for water in 140Å, 200Å, 500Å silica.	76
39	1D Cryoporometry.	80
40	1D imaging sequence.	81
41	1D Cryoporometry.	82
42	2D Cryoporometry sample with xy porous structure	83
43	2D imaging sequences.	85
44	Selected intensity maps from the temperature run.	86
45	Monotonic intensity maps from the temperature run.	86
46	Liquid Proton Density images vs. Temperature.	86
47	Porosity maps vs. Pore Diameter.	87
48	Localised Pore Size Distributions.	88
49	2D map of Median Pore Size.	89
50	Colour map of Median Pore Size.	90
51	3D imaging sequence.	91
52	3D porous sample resolved into 500Å and 60Å components	93
53	3D porous sample resolved into 500Å and 60Å components	94
54	Cryoporometric measurements on 158Å, 250Å Trisopor.	99
55	Cryoporometric measurements on 480Å, 1000Å Trisopor.	100
56	Cryoporometric measurements on 1930Å Trisopor and 200Å silica.	101
57	Calculated probe pore size resolution	104
58	Pore size distributions for underfired clay.	108

59	Pore size distributions for chalk.	108
60	SEM micrograph of a typical sol-gel grain ($150\mu\text{m}$).	114
61	SEM micrograph of sol-gel structures of diameter $2.2\mu\text{m}$	114
62	Normalised pore volume distributions for sol-gel silicas.	115
63	Neutron scattering from porous silica MCM-41.	116
64	Isolated tube geometry.	119
65	Lattice of tubes – a flawed model.	120
66	Square lattice of cylindrical voids.	121
67	Hexagonal lattice of cylindrical voids.	122
68	Solid silica spheres or spherical voids on a cubic lattice.	124
69	Silica filling factor for spherical voids on a cubic lattice.	126
70	Spherical voids on an HCP lattice.	127
71	Silica filling factor for spherical voids on an HCP lattice.	129
72	Filling factors for spherical voids on cubic, random and HCP lattices.	130
73	Model of throat between two pores in 40\AA Merck SiO_2	140
74	Pore size distributions for MgO nanocrystals in silica.	142
75	Vector diagram for elastic scattering.	144
76	Bragg scattering.	144
77	Schematic of instrument layout at ILL.	156
78	Maxwell distributions $F(\lambda)$ for neutrons.	158
79	View of D4B neutron diffractometer.	159
80	Schematic for D4B neutron diffractometer.	159
81	Schematic of D22 small angle diffractometer.	160
82	View of D22 neutron collimator and attenuators.	161
83	View of D22 multidetector in 20m long vacuum chamber.	161
84	Sech approximation to Placzek fall-off from water scattering.	164
85	Scattering intensity from porous silicas.	166
86	DoD22: Help, Command and Status windows.	168
87	DoD22: Raw: 2D $I(X,Y)$ map, parameter table, $I(Q)$	169
88	DoD22: Water Efficiency Map, $\text{Geom}(\theta_s)$, $\text{Atten}(\theta_s)$	170
89	DoD22: Water normalisation as performed by <i>analyse</i>	171
90	DoD22: Analysed: 2D $I(X,Y)$ map, parameter table, $I(Q)$	172
91	An initial test calculation of $J(r)$ for a sphere.	177

92	An initial test calculation of $\gamma_0(r)$ for a sphere.	177
93	Corrected $G(r)$ when measuring in a finite spherical volume.	178
94	Calculated $\gamma_0(r)$ for a sphere constructed from a continuous medium.	180
95	$\gamma_0(r)$ for some simple bodies, as calculated by Monte-Carlo integration.	182
96	Cryoporometric Gaussian variance for 100Å Merck silica.	188
97	$G(r)$ for spherical voids on an HCP lattice, var = 0.	191
98	$G(r)$ for spherical voids on an HCP lattice, D/a = 1.	191
99	$I(q)$ for C500, C200 SiO ₂ + hydrogen subtracted.	193
100	$I(q)$ for 100Å, C60 SiO ₂ + hydrogen subtracted.	194
101	$I(q)$ for 60Å, 40Å SiO ₂ + hydrogen subtracted.	195
102	C200 silica scattering, Gaussian distribution of spheres.	196
103	C200 silica with Guinier and Guinier-Porod fits.	197
104	C500 silica with Guinier, Guinier-Porod, sech fits.	198
105	C200 silica with Guinier, Guinier-Porod, sech fits.	198
106	$I(q)$ for C500, C200 SiO ₂ + MC.	200
107	$I(q)$ for 100Å, C60 SiO ₂ + MC.	201
108	$I(q)$ for 60Å, 40Å SiO ₂ + MC.	202
109	$I(q)$ for 25Å SiO ₂ + MC.	203
110	$\gamma_0(r)$ for C200 silica, sphere, infinite & finite slabs.	204
111	L(l) for C500 silica by FFT + analytic transformation.	206
112	$G(r)$ for C200 silica vs. Monte-Carlo calculation.	207
113	$G(r)$ for seven sol-gel silicas, + Monte-Carlo.	209
114	$G(r)$ for seven sol-gel silicas, + spheres.	210
115	$G(r)$ for C200 silica at large radius + MC.	211
116	Measured and Monte-Carlo $\gamma_0(r)$, $d(r)$	215
117	Theoretical variation of $d_{Max}(D/a)$	218
118	Monte-Carlo variation of $d_{Max}(D/a)$	220
119	Maximum in $d(r)$, as a function of Gaussian variance.	223
120	Variance calibration for spheres on an HCP lattice.	223
121	Gas adsorption pore diameter vs. neutron scattering.	227
122	NMR cryoporometric pore diameter vs. neutron scattering.	227
123	bulk liquid melting step, for cyclohexane in 1930Å Trisopor.	247
124	Plot of ΔT_b as a function of warming rate	249

125	Warming rate for constant resolution.	255
126	First order simulation of bulk melting step.	258
127	First order simulation of bulk melting step.	259
128	Bulk melting steps: measured and simulated.	260
129	A regular tetragon of spheres	261
130	Base of tetragon	262
131	Side view of tetragon	262
132	Geometry of slice δx , for the integration of the cap of a sphere.	264
133	Geometry of slice δx , for the integration of the cap of a sphere.	265
134	Intersection of a sphere with a plane slab.	270
135	Constant $G(r)$ for a sphere straddling a slab.	271
136	Integration surface for $\rho(R,Z)$ for $G(r)$ for a slab.	272
137	$G(r)$ for an infinite plane slab.	275
138	$I(q)$, $\gamma(r)$ for various standard forms.	279
139	Angled scattering onto a flat detector.	281
140	Angled scattering through a thick sample.	283
141	D22 fall-off in water scattering, $\text{Geom}(\theta_s)$, $\text{Atten}(\theta_s)$	285
142	Distribution $\propto x$ + Uniform Distribution.	290
143	Gaussian and Sech Distributions.	291

Abstract

This thesis describes the characterisation of a range of sol-gel silicas, mainly by the physical techniques of NMR cryoporometry, density and imbibation measurements and Small Angle Neutron Scattering.

The developments made to these techniques as part of this work include

- Construction of the first full cool/warm cycle automated NMR cryoporometer, with continual pore size distribution graphing.
- Calibration of melting point constants with respect to gas-adsorption and neutron scattering.
- Detailed characterisation of the thermal properties of the cryoporometer.
- Development and measurement of the first multi-dimensionally resolved pore size maps by NMR cryoporometry.
- Demonstration that simple density and imbibation measurements can, when combined with models, provide a wealth of information concerning the silicas.
- Development of novel continuous medium Monte-Carlo integration methods to calculate the solid-solid density correlation function for porous media, showing excellent agreement with experimental SANS results.

In particular, with the second point, there has been an attempt to use SANS to provide an absolute calibration scale for pore size, nominally given by gas-adsorption.

Acknowledgements

I would like to thank my supervisor Prof. John H. Strange for his support while I worked on this thesis, for his many useful ideas for worthwhile developments, and for his essential lecture courses. I would like to thank Prof. John C. Dore for the opportunity to perform neutron scattering measurements, and for his many helpful explanations regarding a technique that was new to me.

I would like to thank Prof. Jack G. Powles for his invaluable lecture course, and for many useful discussions. I would also like to thank Dr. Morley R. Halse and Dr. Mike Mallett for their indispensable help and support, and Dr. Louis H. Ryder for assistance on QM. I would like to thank Prof. Bob J. Newport for a most useful book and helpful discussions, and Dr. Gavin Mountjoy for many helpful sessions on the subject of SANS, and to thank them both for computing time on a DEC Alpha workstation at an important phase in understanding the results from modeling porous structures.

I must express my especial thanks to Dr. W. Allan B. Evans for the many times he has assisted me with some mathematical point that was unclear to me – this thesis would not be the same without his help.

For technical assistance I thank Mr. Ken Stevens, Mr. Bernard D. Doolin, Mr. Trevor W. Reece, Mr. Kevin P. Scroggins, Mr. Jay F. Day, and, for circuit boards, Mr. Peter J. Verrall. For mechanical construction, and an unfailing supply of cryogenics and good cheer, I thank Mr. Don F. Riley, Mr. Ian Ross and Mr. Roy Kitch, and, for constructing the NMR probes, Mr. John Howes.

I would like to thank my family and friends for their support while working on this thesis.

Chapter 1

Introduction.

1.1 Porous materials.

Porous materials occur widely and have many important applications. They can, for example, offer a convenient method of imposing fine structure on adsorbed materials. They can be used as substrates to support catalysts and can act as highly selective sieves or cages that only allow access to molecules up to a certain size.

Food is often finely structured. Many biologically active materials are porous, as are many construction and engineering materials. Porous geological materials are of great interest; high porosity rock may contain water, oil or gas; low porosity rock may act as a cap to porous rock, and is of importance for active waste sealing.

1.2 Properties of porous materials.

There are a number of important properties of porous materials :

- Porosity.
- Specific surface area.
- Permeability.
- Breakthrough capillary pressure.
- Diffusion properties of liquids in pores.
- Pore size distribution.
- Radial density function.

In this work we shall mainly be concerned with porosity, pore size distribution and radial density function.

1.3 Porosity and pore size measurement techniques on porous media.

- Crushing – measure the volume of the porous material, crush it to remove the void space, and re-measure the volume.
- Optically – this may involve filling the pores with a material such as black wax or Wood’s metal, sectioning and inspecting with a microscope or scanning electron microscope.
- Imbibation – weighing before and after filling the pores with a liquid.
- Gas Adsorption – measure the change in pressure as a gas is adsorbed by the sample.
- Mercury Intrusion – Measure the volume of mercury forced into the sample as a function of pressure.
- Thermoporosimetry – fill the pores with a liquid, freeze it, then measure the heat evolved as the sample is warmed, until all the liquid is melted.
- NMR Cryoporometry – fill the pores with a liquid, freeze it, then measure the amplitude of the NMR signal from the liquid component as the sample is warmed, until all the liquid is melted.
- Small Angle Neutron Scattering (SANS) – scatter neutrons from the pores, then the smaller the dimensions of the variations in density distribution, the larger the angle through which the neutrons will be scattered.

The two most common methods of measuring pore size are gas (usually nitrogen) adsorption, and mercury intrusion, which are discussed below.

Many of these methods give results that quite frequently differ from one another. This is often because they are in fact measuring different things – some measurements are directly on the pores themselves, others (such as mercury intrusion) are in effect measuring the necks that give access to the pores.

A typical example is shown in figure 1, for a sandstone, of mercury intrusion (circles) compared with micro-photography (triangles) [Dullien, 1979].

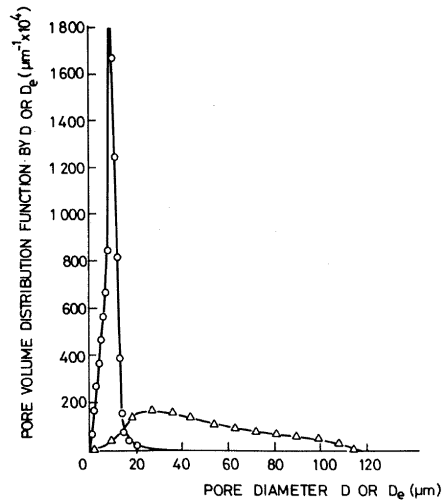


Figure 1: Pore size in sandstone as measured by mercury intrusion (circles) and photomicrography (triangles). Dullien, 1975.

1.3.1 Gas adsorption.

The volume of gas adsorbed by a porous media is measured as the pressure of the gas is increased and then decreased [Allen, 1975].

Gas adsorption isotherms are usually described by an equation of the form [Langmuir, 1918] :

$$\frac{P}{V} = \frac{1}{b \cdot V_m} + \frac{P}{V_m}$$

Where P is the pressure and V is the volume adsorbed per unit mass of adsorbent; V_m is the volume adsorbed at the complete monolayer point, b is a constant.

An extension of this is the BET equation, which treats multilayer adsorption [Brunauer et al., 1938] :

$$\frac{x}{V \cdot (1 - x)} = \frac{1}{c \cdot V_m} + \frac{(c-1) \cdot x}{c \cdot V_m}$$

where $x = \frac{P}{P_0}$, P_0 being the vapour pressure of the bulk liquid, c is a constant.

One may go further and calculate the specific surface area S of the solid :

$$S = \frac{N \cdot \sigma^\circ \cdot V_M}{M_v}$$

σ° is the area occupied by a single adsorbed molecule, N is Avagadro's number, M_v is the gram molecular volume = 22.41 {l}. In this work we use pore diameters determined by gas adsorption to establish a relationship between the melting point depression (as measured by NMR cryoporometry) and the pore diameter in the porous medium.

Gas adsorption commonly uses the BJH method [Barret et al., 1951] based on the Kelvin equation to calculate pore size distributions from the desorption $P(v)$ curve, using a pore model of right cylinders [Thomson, 1871, Gregg and Sing, 1967] :

$$R \cdot T \cdot \ln \frac{P_s}{P_0} = -2\gamma \cdot \frac{V_M}{R_k} \cdot \cos(\phi)$$

where :

R_k = Kelvin radius,

R = gas constant = $8.314 \text{ J} \cdot \text{K}^{-1} \cdot \text{mol}^{-1}$,

T = boiling point of nitrogen = 77.3 K

P_s = pressure of sample,

P_0 = ambient pressure,

γ = adsorbate surface tension at T ,

V_M = molar volume of adsorbate.

ϕ = angle of contact between liquid and walls = 0°

for Nitrogen :

V_M = $34.6 \text{ ml} \cdot \text{mol}^{-1}$

γ = $8.855 \cdot 10^{-3} \text{ N} \cdot \text{m}^{-1}$

This is for cylindrical geometry, and may be written in the form [Gregg and Sing, 1967]

$$\frac{R_k}{2} = -\frac{\gamma \cdot V_M}{R \cdot T \cdot \ln \frac{P_s}{P_0}} \cdot \cos(\phi)$$

which may be re-cast into a more general form for other pore geometries :

$$\frac{v_p}{a_p} = -\frac{\gamma \cdot V_M}{R \cdot T \cdot \ln \frac{P_s}{P_0}} \cdot \cos(\phi)$$

where (per gram of solid) v_p is the pore volume, a_p is the pore surface area.

Thus for non-intersecting spherical pore geometry one obtains

$$\frac{v_p}{a_p} = \frac{R_k}{3}$$

and for the spherical pore geometry with multiple throats that we shall discuss in chapter 11.5.3, with 50% of the pore area intact, one obtains

$$\frac{v_p}{a_p} = \frac{2 \cdot R_k}{3}$$

1.3.2 Mercury Intrusion.

In mercury intrusion the volume of mercury forced into the sample is measured as a function of the applied pressure [Allen, 1975]. Since this capillary pressure is related to the diameter of the neck leading to the pores, rather than the pore diameters themselves, the results are not strictly comparable with gas adsorption.

If dV is the volume of pores having entry diameters between D_e and $D_e + dD_e$, then [Ritter and Drake, 1945] :

$$dV = \alpha(D_e) \cdot dD_e$$

where $\alpha(D_e)$ is a distribution function for pore diameter. We may then write :

$$\alpha(D_e) = \frac{P_c}{D_e} \cdot \frac{d(V_T - V)}{dP_c}$$

where V_T is the total pore volume of the sample and V is the volume of pores with entry diameters smaller than D_e .

Mercury intrusion calibration has not been used in this work, with the exception of providing nominal pore diameters for large pore diameter Trisopor[®] silicas.

1.3.3 Thermoporosimetry (DTA/DSC).

Differential Thermal Analysis or Differential Scanning Calorimetry is a technique that can be used to study the behaviour of liquids in pores, in a similar manner to NMR cryoporometry. When applied to porous materials, the names Thermoporometry, Thermoporosimetry are frequently used [Brun et al., 1977, Jackson and McKenna, 1990, Jallut et al., 1992, Ishikiriyama et al., 1995, Ishikiriyama and Todoki, 1995].

The sample and liquid (1 → 5mg) is placed in a small sealed capsule, and a thermocouple used to monitor the difference in temperature to an empty capsule, as both are smoothly first reduced in temperature and then increased in temperature.

The signal obtained is not directly proportional to the volume of liquid melted, as in the case of NMR cryoporometry, but is a measure of the heat absorbed/emitted by the sample. It is divided by the thermal mass of the sample (i.e. different porous substrates will have different scale factors) and is multiplied by the temperature scanning rate.

Further, in the case of very small pore sizes with deep supercoolings, the amplitude of the transition becomes so small and spread-out that it is often not seen, where NMR

cryoporometry obtains clear transitions of very good signal-to-noise, as one goes from: ‘no melted liquid’ to ‘all liquid in pores melted’ over a wide temperature range.

1.4 Measurements on Porous Materials by NMR.

There are a number of techniques based on Nuclear Magnetic Resonance that can be used to study porous materials, both directly and indirectly :

- Cryoporometry for measuring pore size distributions.
- Multidimensionally resolved cryoporometric pore size distributions.
- Bounded liquid fraction and diameter determination.
- Fluid transport and diffusion in fine porous material.
- Direct 1D, 2D, 3D imaging of coarsely structured materials.
- NMR relaxation in pores.

All of these techniques (with the exception of the measurement of bulk fluid transport) have been used or developed during the course of this work; however detailed discussion will be primarily limited to cryoporometry, with and without spatial discrimination.

1.4.1 Cryoporometry for measuring pore size distributions.

As the main part of this project a novel method of determining median pore size and pore size distributions of porous materials has been developed, both on bulk samples and as a function of spatial position inside a sample with structured porosity.

NMR cryoporometry is based on the technique of freezing a liquid in the pores and measuring the melting temperature by Nuclear Magnetic Resonance. Since the melting point is depressed for crystals of small size, the melting point depression gives a measurement of pore size.

The method is non-destructive, and is suitable for pore diameters in the range of a few nanometers to around $1\mu\text{m}$.

Commercially important porous materials that have been studied as part of this project include the porous glasses, the alumina and aluminosilicates such as clays and zeolites, activated and other porous carbons, concrete, and water and oil bearing shales, sandstones and limestones, and polymer materials such as rubber and artificial skin.

NMR cryoporometry is often the method of choice and is always valuable to complement existing porous measurement techniques such as gas adsorption and mercury porosimetry. It is here shown to have good linear agreement in porous silica glasses with gas adsorption measurements. It is able to provide fully calibrated porosity measurements as a function of incremental pore diameter. One major advantage of NMR cryoporometry over other techniques is in its ability to perform non-destructive spatial imaging.

1.4.2 Multidimensionally resolved pore size distributions.

Part of this project has been the development of the novel technique of measuring pore size distributions with 1, 2 and 3-dimensional spatial resolution, using NMR cryoporometry in conjunction with standard magnetic resonance imaging techniques.

Nuclear Magnetic Resonance is here used both as a convenient technique for measuring the fraction that is liquid, deep inside the porous material, and as a way of spatially encoding the pore size density to produce a pore size distribution map.

In rocks, for example, the pore size in faulted regions is often less than in the bulk rock.

1.4.3 Bounded liquid fraction and diameter determination.

If a sample contains liquid where at least part is confined or bounded, say in closed pores or vesicles, it is often possible to determine the bounded liquid fraction and bounded diameter, using the technique of measuring the diffusion distance as a function of time. This has been done both using pulsed magnetic gradients, and by using the static gradients found in the fringe field of a superconducting magnet.

An ultra stable 30A gradient pulser unit was designed and constructed, and a variable temperature gradient probe designed and constructed.

A software implementation of the full equation describing the signal expected from bounded diffusion in a static gradient was written, for the fringe field measurements.

A 6 pulse constant relaxation time diffusion measuring pulse program was written; this technique is subject to occasional co-incident echo errors – a routine was written to identify these echos, so that they could be eliminated from the measured data.

These techniques work best for vesicle diameters in the range $0.1\mu\text{m}$ to $10\mu\text{m}$.

1.4.4 Fluid transport and diffusion in fine porous material.

The above diffusion techniques can be used to study flow and static self diffusion in porous materials or powder beds, providing information on how readily liquids may pass through the material [Mitzithras et al., 1992, Valiullin et al., 1997].

1.4.5 Direct 1D, 2D, 3D imaging of coarsely structured materials.

In larger granular beds 3D imaging may be used to study liquid distribution and percolation paths. Flow-diffraction may also be studied. [DePanfilis and Packer, 1999].

Imaging has also been used to study phase separation of multicomponent systems, on progressive freezing/melting, a phenomena applicable to many food stuffs, as well as biological samples. Thus one uses a measurement as a function of temperature, as in cryoporometry, but studies structured concentration dependent melting.

Current resolution is typically 0.1mm in 20mm for 3D structures.

1.4.6 NMR relaxation in pores.

A somewhat more indirect technique is to measure the decay times of the Nuclear Magnetic Resonance signals. This can provide approximate information on the diameter of the pores containing the liquid; more importantly it can provide information on the local environment of the liquid, on the internal surface morphology and on the surface wettability [Stapf et al., 1996, Allen et al., 1997, 1998, Booth and Strange, 1998], all with optional spatial resolution.

1.5 Measurements on Porous Materials by SANS.

When neutrons are scattered elastically from density distributions in the porous materials, the prime characteristic is that the bigger the ratio of the wavelength of the neutrons to the characteristic size of the density distributions, the wider the angle of scattering of the neutrons. Thus in principle neutrons (and X-rays) could offer an absolute calibration of pore size, if we can determine the proportionality constant [Ramsay and Booth, 1983, Gardner et al., 1994, Margaca et al., 1997, Ramsay, 1998].

Our pores are densely packed, and we will find that we can not use unchanged the scaling constant for an isolated sphere. We will even find that for a given lattice of pores, as the pores decrease in size in the lattice, the angle of scattering does not always

increase, as stated above. However for a given ratio of pore diameter to lattice spacing, and for a constant variance of pore and lattice spacing there is currently no known reason why neutrons should not be able to provide a relative measure of pore sizes. It is thus surprising that we find that while the calibration we obtain agrees remarkably well with the well established gas adsorption scale for large pores, it differs strongly for small pores. This is currently not understood.

1.6 The scope of this Thesis.

A large part of this work covers the development of the NMR cryoporometry method of measuring pore size distributions, and the implementation, calibration and application of a scanning NMR cryoporometer based on a solid state spectrometer, IEEE instrumentation and LabVIEW software running on a PC. This offers fully programmed cooling and warming of the NMR probe, and online graphical display of the amplitude of signal from the melting liquid, and of the calculated pore size distribution.

The development of this apparatus followed on from earlier work at UKC [Strange et al., 1993, Alnaimi et al., 1994] using apparatus based on a similar spectrometer and a BBC computer [Strange, 1994, Alnaimi, 1994]. This used manual control of cooling, and natural warming of the probe, followed by later off-line analysis of the measured data. Other groups have used standard NMR spectrometers to gather NMR cryoporometric data for later analysis [Hansen et al., 1996].

A major extension of the NMR cryoporometric technique, first developed as part of this work, has been to add spatial resolution. Structured pore size information is presented with 1, 2 and 3 dimensional resolution [Strange and Webber, 1995, Strange et al., 1996, Strange and Webber, 1997a,b].

Density and imbibation experiments were performed on sol-gel silicas, to establish average properties of the silicas.

Small Angle Neutron Scattering and Neutron diffraction experiments were performed on sol-gel silicas, to determine the solid-solid radial distribution functions $G(r)$.

A range of existing methods of analysing such data exist [Guinier, 1939, Porod, 1951, Martin et al., 1986, Hurd et al., 1987, Teubner and Strey, 1987, Schmidt, 1991, Li and Ross, 1994, Ramsay, 1998] These all give different scalings of pore size for a given scattering, with no clear method of differentiating between them.

Thus geometric models of structures of pores were considered, the average properties considered analytically, and a novel continuous media Monte-Carlo integration technique developed to evaluate the solid-solid radial distribution functions for the porous models. The models and their deduced properties were then used to evaluate, compare and combine the NMR pore volumetric information, the density and imbibation results, and the SANS data, giving far more information than any individual technique could in isolation, and resulting in a neutron scattering calibration of pore-size.

1.7 Accuracies of quoted results.

Numerical results quoted on graphs are in the main generated directly by the programs generating the graphs; the final digits are retained for subsequent computations and are usually to be regarded as of dubious significance.

In the text of this work, final subscripted numerals are similarly retained for any later computations, and are to be regarded as of dubious significance.

Weighings quoted to 1mg probably have an uncertainty of around $\pm 1\text{mg}$; weighings quoted to a higher precision were performed on a more stable balance and are probably good to $\pm 0.1\text{mg}$.

The accuracy of measured pore diameters is more problematic; the only reliable decider is closeness of repeated measurements, and in the main for the cryoporometric calibrations porosity measurements were repeated at least twice on each sample, with two different samples being made using each silica and liquid. Frequently a repeatability of median pore diameter of better than 1% is obtained in the middle of the calibration range, though with the direct nitrogen injection Lindacot cooling random temperature fluctuations cause some measurements to vary more (see the scatter in the calibration graphs in chapter 7).

With gas flow cooling the range of pore diameters for which one can expect a 1% repeatability is considerably wider. Figures 54, 55, 56 in chapter 9.3 show graphically the typical repeatability of pore size distribution measurements on large pore silicas when using gas-flow cooling.

The quotable accuracy of the pore diameters is discussed further in chapter 7, where NMR cryoporometry is calibrated against nominal gas adsorption pore diameter, and is in part a function of the definition of pore diameter for arbitrarily shaped pores.

Chapter 2

NMR Theory.

2.1 Interaction of radiation with matter.

When radiation interacts with matter it does so in a quantised manner [Planck, 1929] :

$$\Delta E = h\nu = \frac{h\omega}{2\pi} = \hbar\omega$$

where ΔE is the energy difference, ν is the frequency of the radiation, ω is the angular frequency, h is Planck's constant and

$$\hbar = \frac{h}{2\pi}$$

2.2 Zeeman energy level splitting in a magnetic field.

If a nucleus with a spin I and a magnetic moment μ is placed in a magnetic field, there will be an interaction energy [Abragam, 1961, Harris, 1987, Farrar and Becker, 1971]; this will be quantised, the energy states obeying Fermi-Dirac statistics, such that the magnitude of the nuclear spin angular momentum =

$$P = \hbar (I(I+1))^{1/2}$$

where there are $(2I+1)$ non-degenerate energy levels $m_I = I, I-1, I-2, \dots, -I$.

If we define the magnetogyric ratio for a nucleus

$$\gamma = \frac{\mu}{P}$$

where μ is the magnetic moment of the nucleus, then :

$$\mu = \gamma P = \gamma \hbar (I(I+1))^{1/2}$$

$$\mu_z = \gamma P_z = \gamma \hbar m_I$$

For a classical magnetic moment $\boldsymbol{\mu}$ placed in a magnetic field \mathbf{B} , along the $+z$ direction, there is an interaction energy

$$E = -\boldsymbol{\mu} \cdot \mathbf{B} = -\mu_z B$$

For a nucleus with spin m_I in such a magnetic field we have

$$E = \hbar \omega = -\gamma \hbar m_I B$$

Since the selection rule governing such transitions is $\Delta m_I = \pm 1$, we get :

$$\omega = |\gamma| B$$

For a macroscopic sample, we may view such a process as the classical (Larmor) precession of a magnetic moment $\boldsymbol{\mu}$ in a magnetic field \mathbf{B}_0 , with a precession angular frequency

$$\omega_0 = -\gamma \mathbf{B}_0$$

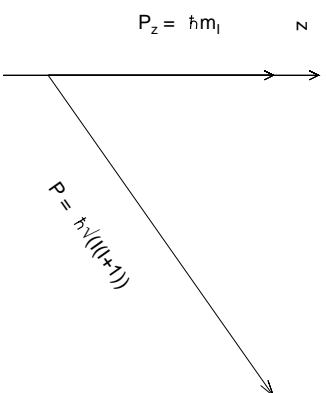


Figure 2:
Quantised nuclear spin momentum.

2.2.1 Protons in a magnetic field.

For protons, with spin $I = 1/2$, there will be 2 energy levels $m_I = \pm\frac{1}{2}$.

$$\begin{aligned} P &= \hbar \left(\frac{1}{2} \cdot \frac{3}{2}\right)^{1/2} = \frac{\sqrt{3}}{2} \cdot \hbar \\ P_z &= \hbar m_I = \pm\frac{1}{2}\hbar \end{aligned}$$

Hence in figure 3 we have for the angle θ that the quantised angular momentum vectors make with the z direction :

$$\theta = \cos^{-1} \frac{P_z}{P} = \cos^{-1} \frac{\pm 1}{\sqrt{3}} = \pm 54^\circ 44' 8.2''$$

Thus the spins precess in two cones that make angles θ with the z direction, at a rate determined

by $\omega = \gamma_p B$, where for protons,

$$\gamma_P = 2.675197 \times 10^8 \text{ rad s}^{-1} \text{ T}^{-1},$$

hence $\gamma_P/2\pi = 42.5771 \text{ MHz T}^{-1}$.

At typical experimental temperatures, thermal excitations cause both cones to have nearly equal populations of spins.

2.3 Net magnetisation from the population imbalance due to Boltzmann distribution.

Given a spin 1/2 system with two energy levels due to Zeeman energy level splitting in a magnetic field, Maxwell-Boltzmann statistics tells us [Reif, 1965, p.345], that taking into account the distinguishability of the particles, the population of state S will be a function of energy level E_s , and absolute temperature T :

$$N_E = \frac{e^{\frac{-E_s}{k_B T}}}{\sum_r e^{\frac{-E_r}{k_B T}}}$$

where the total population =

$$N = \sum_r n_r$$

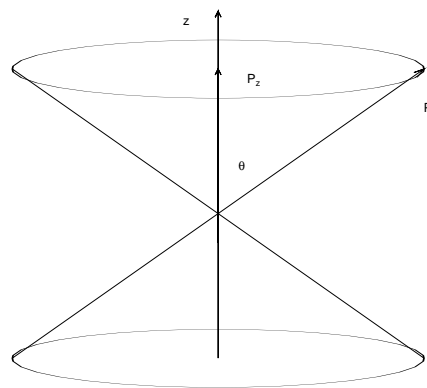


Figure 3: Quantised spin precession cones for protons.

Suppose there are $N\uparrow$ spins in the lower energy state and $N\downarrow$ spins in the upper energy state, such that :

$$N = N\downarrow + N\uparrow$$

If the energy difference between the two states is ΔE , then at equilibrium the population of the lower energy level $N\uparrow$ will be greater than that of the upper $N\downarrow$:

$$N\uparrow = N\downarrow \cdot e^{\frac{\Delta E}{k_B T}}$$

Thus we may write :

$$\begin{aligned} N &= N\downarrow + N\downarrow \cdot e^{\frac{\Delta E}{k_B T}} \\ &= N\downarrow \cdot \left(1 + e^{\frac{\Delta E}{k_B T}} \right) \\ \therefore N\downarrow &= \frac{N}{1 + e^{\frac{\Delta E}{k_B T}}} \\ \therefore N\uparrow &= \frac{N}{1 + e^{\frac{\Delta E}{k_B T}}} \cdot e^{\frac{\Delta E}{k_B T}} \end{aligned}$$

Thus if each spin has a z component of magnetic moment $\mu_z = \gamma P_z = \gamma\hbar/2$ (for spin $1/2$), the net magnetisation \mathbf{M}_0 in a field \mathbf{B}_0 along the $+z$ direction will also be along the $+z$ direction, with a magnitude given by [Harris, 1987, p.10] :

$$\begin{aligned} M_0 &= \mu_z \cdot \Delta N \\ &= \gamma\hbar m_I \Delta N \\ &= \frac{1}{2} \cdot \gamma\hbar \Delta N \\ \therefore M_0 &= (N\uparrow - N\downarrow) \cdot \mu_z \\ &= \left(\frac{N}{1 + e^{\frac{\Delta E}{k_B T}}} \cdot e^{\frac{\Delta E}{k_B T}} - \frac{N}{1 + e^{\frac{\Delta E}{k_B T}}} \right) \cdot \mu_z \\ &= \frac{N \cdot \left(e^{\frac{\Delta E}{k_B T}} - 1 \right)}{e^{\frac{\Delta E}{k_B T}} + 1} \cdot \mu_z \end{aligned}$$

This Padé form is exact, however since for NMR splittings at conventional temperatures $\Delta E \ll k_B T$ (for protons at 600MHz $\Delta E/k_B \approx 0.03K$), we make the approximation $\exp(x) \approx 1 + x$, for small x . We also have $\Delta E = \hbar\omega_0 = \hbar\gamma B_0$ and $\mu_z = \gamma\hbar/2$.

Hence :

$$\begin{aligned}
 M_0 &\approx \frac{N \cdot (1 + \frac{\Delta E}{k_B T} - 1)}{1 + 1 + \frac{\Delta E}{k_B T}} \cdot \mu_z \\
 &\approx \frac{N}{2} \cdot \frac{\Delta E}{k_B T} \cdot \mu_z \\
 &= \frac{N}{2} \cdot \gamma \hbar \frac{1}{2} \cdot \frac{1}{k_B T} \cdot \hbar \omega_0 \\
 &= \frac{N}{2} \cdot \gamma \hbar \frac{1}{2} \cdot \frac{1}{k_B T} \cdot \hbar \gamma B_0 \\
 &= \frac{N}{4} \cdot \gamma^2 \hbar^2 \cdot \frac{B_0}{k_B T}
 \end{aligned}$$

In table 1 we list the exact Padé form result, and the (small) fractional error in the approximation, for a number of different temperatures, and for some NMR frequencies used in this study. We note that for the range of temperatures used ($\sim 100K \rightarrow 300K$), the approximation is of quite sufficient accuracy.

T{K}	Magnetisation $\times 10^{30}$			Error $\times 10^6$		
	20MHz	100MHz	300MHz	20MHz	100MHz	300MHz
1	6.77	33.85	101.56	0.5199	64.9889	1754.6676
3	2.26	11.28	33.85	0.0193	2.4070	64.9889
10	.68	3.39	10.16	0.0005	0.0650	1.7547
30	.23	1.13	3.39	0.0000	0.0024	0.0651
100	.07	.34	1.02	0.0000	0.0001	0.0018
300	.02	.11	.34	0.0000	0.0000	0.0001
1000	.01	.03	.10	0.0000	0.0000	0.0000

Table 1: Magnetisation per proton, as a function of frequency and temperature. The fractional error of the approximate expression is also listed.

Thus the magnetisation measured for a particular NMR experiment will be due to this population difference inverted, giving rise to a Free Induction Decay (or echo) whose amplitude will thus be to a good approximation (all other factors being equal) inversely proportional to temperature.

2.4 The time evolution of nuclear spin systems in a magnetic field.

The total magnetic moment \mathbf{M} of a macroscopic sample is the resultant of the many nuclear moments $\boldsymbol{\mu}$, such that

$$\mathbf{M} = \sum_i \boldsymbol{\mu}_i = \gamma \mathbf{P}$$

where \mathbf{P} is the total spin angular momentum.

A classical magnetic moment \mathbf{M} in a magnetic field \mathbf{B} experiences a torque that changes the angular momentum \mathbf{P} :

$$\frac{d\mathbf{P}(t)}{dt} = -\mathbf{B} \times \mathbf{M}$$

hence

$$\frac{d\mathbf{M}(t)}{dt} = -\gamma \mathbf{B} \times \mathbf{M}$$

Quantum mechanically one has for the Hamiltonian of the interaction energy of an isolated spin \mathbf{I} with a magnetic field \mathbf{B}

$$\mathcal{H} = -\gamma \hbar (\mathbf{B} \cdot \mathbf{I})$$

where $\hbar \mathbf{I}$ is the angular momentum operator.

Then for the equation of motion one has the Liouville – von Neuman eqn. [Abragam, 1961, IIB, (11)] :

$$\frac{\hbar}{i} \frac{d\mathbf{I}}{dt} = [\mathcal{H}, \mathbf{I}] = -\gamma \hbar [\mathbf{B} \cdot \mathbf{I}, \mathbf{I}]$$

For the z component we obtain (appendix A) [Abragam, 1961, IIB, (12)] :

$$\begin{aligned} \frac{\hbar}{i} \frac{dI_z}{dt} &= -\gamma \hbar (B_x [I_x, I_z] + B_y [I_y, I_z]) \\ &= \frac{-\gamma \hbar}{i} (B_x I_y - B_y I_x) \\ &= \frac{-\gamma \hbar}{i} (\mathbf{B} \times \mathbf{I})_z \end{aligned}$$

This has the same form as the above classical expression; thus we conclude that the expectation value of $\langle I_z \rangle$ for a free spin \mathbf{I} behaves as does a classical magnetic moment. Since it is linear, it also describes the average behaviour of many non-interacting spins. Thus for a macroscopic sample composed of non-interacting spins we may use the above classical expression.

2.5 The Bloch equations.

We now wish to consider the evolution of many weakly interacting spins, in a magnetic field B_0 in the z direction, and a weak additional magnetic field B_1 rotating in the xy plane with angular frequency ω . We wish to include the effect of weak interaction between the nuclear spins, and between the nuclear spins and the bulk material ('lattice') [Bloch, 1946].

We have seen that we expect an equilibrium magnetization in the z direction, based on the Boltzmann distribution; if M_z is perturbed away from the equilibrium value $M_z(\infty) = M_0$, we expect it to return to equilibrium at a rate dependent on the transitional probabilities between the Zeeman energy levels. i.e. we expect a first order behaviour of the form :

$$\frac{dM_z(t)}{dt} = \frac{M_z(\infty) - M_z(t)}{T_1}$$

such that there is an exponential recovery to the equilibrium magnetization with a time constant T_1 , known as the *spin-lattice* or *longitudinal relaxation time*. T_1 is thus set by the rate at which the spins can exchange energy with the 'lattice'.

The rotating B_1 field is assumed to be much weaker than B_0 , such that the Boltzmann equilibrium magnetization $M_x(\infty)$, $M_y(\infty)$ in the xy plane is effectively zero. As we shall see, magnetization decay in the transverse plane is not necessarily a simple first order relaxation process, but has additional phase interactions. However, in a liquid, in a highly uniform B_0 field, we may follow Bloch and approximate the behaviour as a first order process of the form :

$$\frac{dM_{x,y}(t)}{dt} = -\frac{M_{x,y}(t)}{T_2}$$

such that there is an exponential decay of the transverse magnetization with a time constant T_2 , known as the *spin-spin* or *transverse relaxation time*. T_2 is then set by the rate at which the spins can exchange energy with each other, to come to a common *spin temperature*.

We may then write :

$$\frac{d\mathbf{M}(t)}{dt} = -\gamma\mathbf{B} \times \mathbf{M} - \frac{M_x(t)\mathbf{i}' + M_y(t)\mathbf{j}'}{T_2} - \frac{(M_z(t) - M_z(\infty))\mathbf{k}'}{T_1}$$

where the \mathbf{i}' , \mathbf{j}' , \mathbf{k}' axes rotate at angular frequency ω .

If we expand the vector product into its components, we get

$$\begin{aligned} \mathbf{B} \times \mathbf{M} &= \begin{vmatrix} B_x & M_x & \mathbf{i}' \\ B_y & M_y & \mathbf{j}' \\ B_z & M_z & \mathbf{k}' \end{vmatrix} \\ &= (B_y M_z - B_z M_y)\mathbf{i}' \\ &+ (B_z M_x - B_x M_z)\mathbf{j}' \\ &+ (B_x M_y - B_y M_x)\mathbf{k}' \end{aligned}$$

but

$$\begin{aligned} B_x &= B_1 \cos(\omega t) \\ B_y &= -B_1 \sin(\omega t) \\ B_z &= B_0 \end{aligned}$$

$$\begin{aligned} \therefore \mathbf{B} \times \mathbf{M} &= (-B_1 M_z \sin(\omega t) - B_0 M_y)\mathbf{i}' \\ &+ (B_0 M_x - B_1 M_z \cos(\omega t))\mathbf{j}' \\ &+ (B_1 M_y \cos(\omega t) + B_1 M_x \sin(\omega t))\mathbf{k}' \end{aligned}$$

$$\begin{aligned} \therefore \frac{d\mathbf{M}(t)}{dt} &= \left(\gamma B_0 M_y + \gamma B_1 M_z \sin(\omega t) - \frac{M_x(t)}{T_2} \right) \mathbf{i}' \\ &+ \left(-\gamma B_0 M_x + \gamma B_1 M_z \cos(\omega t) - \frac{M_y(t)}{T_2} \right) \mathbf{j}' \\ &+ \left(-\gamma B_1 M_x \sin(\omega t) - \gamma B_1 M_y \cos(\omega t) - \frac{M_z(t) - M_z(\infty)}{T_1} \right) \mathbf{k}' \end{aligned}$$

2.6 The NMR Hamiltonian operator.

We have considered isolated spins with a magnetic moment in a magnetic field, and then weakly interacting spins. We now wish to consider interactions in more detail, particularly with reference to their effects on the *spin-spin* relaxation.

There are many possible ways for such spins to interact. It is convenient to describe the energies of interaction in the form of an NMR Hamiltonian operator $\hat{\mathcal{H}}$, separating it into the following distinct terms, whose origin is given in table 2 :

$$\hat{\mathcal{H}} = \hat{\mathcal{H}}_Z + \hat{\mathcal{H}}_{RF} + \hat{\mathcal{H}}_{dd} + \hat{\mathcal{H}}_Q + \hat{\mathcal{H}}_{CS} + \hat{\mathcal{H}}_{SR} + \hat{\mathcal{H}}_J$$

$\hat{\mathcal{H}}_Z$: Zeeman	$\hat{\mathcal{H}}_{CS}$: Chemical Shift
$\hat{\mathcal{H}}_{RF}$: Radio Frequency	$\hat{\mathcal{H}}_{SR}$: Spin-Rotation
$\hat{\mathcal{H}}_{dd}$: dipole-dipole	$\hat{\mathcal{H}}_J$: J or spin coupling
$\hat{\mathcal{H}}_Q$: Quadrupole	

Table 2: NMR Hamiltonian terms and their origin.

We have considered the first two terms; Quadrupole coupling is not present in protons, and quadrupolar nuclei are only present at a very small impurity level in the samples used. The last three terms have only a small interaction energy and the magnets used for this work were not highly homogeneous; thus the range of Larmor frequencies in the sample made the last three terms negligible. Hence the main term still to be considered is the dipole-dipole interaction, being the interaction between the magnetic moments of neighbouring spins.

2.7 Dipolar interactions, spin-spin relaxation.

Magnetic interactions acting on the quantised nuclear spins may result in changes to the amplitude and phase of the detected NMR signal, which comes from the component of the magnetization vector in the xy plane, rotating at the Larmor frequency $\omega_0 = \gamma B_0$. This magnetisation will in general decay with a characteristic time T_2 , due to the magnetic interactions, the resulting signal being known as a Free Induction Decay (FID).

2.7.1 The Dipolar Hamiltonian.

The interaction energy between two quantised dipoles $\boldsymbol{\mu}_1 = \gamma_1 \hbar \mathbf{I}_1$, $\boldsymbol{\mu}_2 = \gamma_2 \hbar \mathbf{I}_2$, with a vector \mathbf{r}_{12} between $\boldsymbol{\mu}_1$ and $\boldsymbol{\mu}_2$ is related to the classical expression, and is given by the dipolar Hamiltonian. Expressed in frequency units, this may be written as [Abragam, 1961, Ch. VIII G], [Harris, 1987, Ch. 4.1] :

$$h^{-1} \hat{\mathcal{H}}_{dd} = \frac{\mu_0}{4\pi} \gamma_1 \gamma_2 \frac{\hbar}{2\pi} r_{12}^{-3} \left(\mathbf{I}_1 \cdot \mathbf{I}_2 - 3 r_{12}^{-2} (\mathbf{I}_1 \cdot \mathbf{r}_{12})(\mathbf{I}_2 \cdot \mathbf{r}_{12}) \right) \quad \{Hz\}$$

It can be shown (see appendix B) that this may be expressed as the sum of a finite series of terms [Harris, 1987, Ch. 4.1], each the product of an operator and a second order spherical harmonic :

$$h^{-1} \hat{\mathcal{H}}_{dd} = \frac{\mu_0}{4\pi} \gamma_1 \gamma_2 \frac{\hbar}{2\pi} r_{12}^{-3} (A + B + C + D + E + F) \quad \{Hz\}$$

Term	Operator	Spherical Harmonic	Interaction
A	$\mathbf{I}_{1z} \mathbf{I}_{2z}$	$J_0: -(3 \cos^2 \theta - 1)$	Classical Dipolar
B	$(\mathbf{I}_{1+} \mathbf{I}_{2-} + \mathbf{I}_{1-} \mathbf{I}_{2+})$	$J_0: \frac{1}{4} (3 \cos^2 \theta - 1)$	Flip Flop
C	$-(\mathbf{I}_{1+} \mathbf{I}_{2z} + \mathbf{I}_{1z} \mathbf{I}_{2+})$	$J_1: \frac{3}{2} \sin \theta \cos \theta e^{-i\phi}$	$\Delta m = \pm 1$
D	$-(\mathbf{I}_{1-} \mathbf{I}_{2z} + \mathbf{I}_{1z} \mathbf{I}_{2-})$	$J_1: \frac{3}{2} \sin \theta \cos \theta e^{+i\phi}$	$\Delta m = \pm 1$
E	$-(\mathbf{I}_{1+} \mathbf{I}_{2+})$	$J_2: \frac{3}{4} \sin^2 \theta e^{-2i\phi}$	$\Delta m = \pm 2$
F	$-(\mathbf{I}_{1-} \mathbf{I}_{2-})$	$J_2: \frac{3}{4} \sin^2 \theta e^{+2i\phi}$	$\Delta m = \pm 2$

Table 3: Dipolar Hamiltonian terms A to F, and their significance.

The A term is the classical interaction of one magnetic dipole on another, such that the precession rate of one spin will be altered by the local magnetic field due to the field of the other's magnetic dipole. Since in general the local fields will be random, then if they are static (as in a rigid solid), the FID will decay in a Gaussian manner. However if they are time-varying in a random manner, the decay will be exponential.

The B term is due to the flipping of two spins, such that if one goes up, the other goes down, with a net $\Delta m = 0$ (i.e. net energy is unchanged, but the phase of the interacting pair is randomised); the decay will then be exponential.

For spins separated by a fixed characteristic distance, this may give rise to an FID that is initially Gaussian, but then dips below the axis (i.e. changes phase); cyclohexane behaves in this manner in the rigid and plastic phases (see figures 28, 29).

The other terms all require a net change in state Δm , which implies that they require a fluctuation with comparable energy (see chapter 2.7.2).

The equilibration of the spin system proceeds at a rate T_2 , which can be at a faster rate than T_1 , since T_1 is limited by the rate at which energy can be exchanged with the lattice, whereas T_2 has terms that involve no net change of energy.

The processes involved in T_1 and T_2 relaxation lead to a loss of phase as a result of the interaction, and this information is not recoverable. There is an additional mechanism that leads to a loss of net coherent magnetisation in the xy plane, resulting in a relaxation at a rate known as T_2^* . This occurs when different magnetic fields are present in the sample, due to local or B_0 magnetic gradients. The different magnetic vectors then precess at differing rates, causing a decay in the net observable magnetization vector.

Thus we have

$$T_2^* \leq T_2 \leq T_1$$

In some cases loss of net transverse magnetisation is permanent, in other cases it may be at least partially restored (see chapter 2.8).

2.7.2 Spectral densities.

T_1 relaxation is caused by magnetic fluctuations (usually caused by thermal fluctuations) at frequencies to which the spins are sensitive, inducing stimulated transitions between energy levels.

The T_1 , $T_{1\rho}$ and T_2 relaxation rates are found from the spectral density functions J of the fluctuations; for like spins we get [Harris, 1987, Ch. 4.3] :

$$\begin{aligned} 1/T_1 &= 4 \cdot C \cdot [J_1(\omega_0) + J_2(2\omega_0)] \\ 1/T_{1\rho} &= C \cdot [J_0(2\omega_1) + 10 \cdot J_1(\omega_0) + J_2(2\omega_0)] \\ 1/T_2 &= C \cdot [J_0(0) + 10 \cdot J_1(\omega_0) + J_2(2\omega_0)] \end{aligned}$$

where

$$C = \frac{3}{8} \gamma^4 \hbar^2 I(I+1) \left(\frac{\mu_0}{4\pi} \right)^2$$

We see that all relaxation rates are affected by fluctuations at the Larmor frequency ω_0 (C,D terms in dipolar Hamiltonian) and at $2 \cdot \omega_0$ (E,F terms). T_2 relaxation is also caused by low frequency fluctuations (A,B terms); this results in the T_2 in rigid solids often being very short, due to the slowly varying fields of the local environment, thus giving a broad spectrum line. The T_2 for ice and for cyclohexane in the brittle phase

is typically around $10\mu\text{s}$ but is longer for cyclohexane in the plastic phase (see figures 28–29).

2.7.3 Motional narrowing.

If the spins are moving so fast that within the period of an NMR precession the spins see the orientational average of the local field, then the line-broadening effect of the local fields is lost, since the above spherical harmonics average to zero, and instead of a short T_2 decay (typical of a solid), T_2 will in the high-temperature limit become equal to T_1 .

Such behaviour is common in mobile liquids, such as the bulk water and cyclohexane used in this project. It is this difference between the behaviour of the T_2 in the solid and the liquid upon which this project in part depends. (see chapter 3).

2.7.4 Spin-spin relaxation in pores.

When a mobile liquid is confined in a pore, the spins will diffuse and interact with the surface. Thus relaxation at the surface will reduce the average relaxation times of the bulk liquid [Brownstein and Tarr, 1977, 1979, d’Orazio et al., 1990], acting in much the same way as would paramagnetic ions in the liquid.

In the fast exchange limit with a fully filled sample we obtain a single T_2 , that is a weighted average of the surface liquid relaxation time T_{2s} and the bulk liquid relaxation time T_{2b} .

Thus one has

$$\frac{1}{T_2} = \frac{V_s}{V} \cdot \frac{1}{T_{2s}} + \frac{V_b}{V} \cdot \frac{1}{T_{2b}}$$

$V = V_s + V_b$, being the volumes of the total, surface and bulk regions.

For well characterised materials such as sol gel silicas, this phenomena is sufficiently well understood for it to be used as a method of determining average pore diameter and pore filling factors, based on the measured relaxation times [Gallegos et al., 1986, Stapf et al., 1996, Allen et al., 1997, 1998]. It is often also applied to other materials such as cement and clays; however for these materials it is not clear that the surface relaxation inducing interactions are sufficiently characterised as yet for it to predict the average pore diameter with any great confidence.

2.8 NMR spin echoes.

The T_2 of a mobile bulk liquid such as cyclohexane is typically about the same as the T_1 , usually in excess of a second. However in the permanent magnet used, the magnetic field homogeneity was such that following a 90° R.F. pulse (tipping the magnetisation from the z into the xy plane) spins in different regions of the sample precess at different rates, resulting in a randomising of the spin vectors, and the loss of the net magnetisation in the xy plane. Thus the signal following the 90° pulse decays, giving a Free Induction Decay (FID) lasting a few milliseconds (T_2^*). It is possible to recover this magnetisation, however, (subject to T_2) using a later 180° R.F. pulse, (see figure 4).

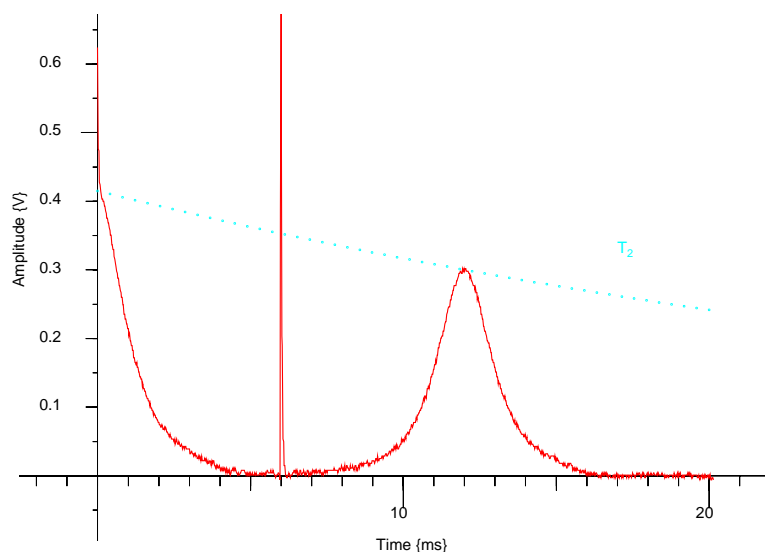


Figure 4:

NMR spin echo, generated by a $90^\circ_{y'} - \tau - 180^\circ_{x'} - \tau - echo$ sequence, where $90^\circ_{y'}$ occurs at $t = 0$ and $180^\circ_{x'}$ at $t = 6\text{ms}$. The echo is centred at $t = 12\text{ms}$.

We will use a coordinate system $x'y'z$, rotating at the Larmor frequency $\omega = \gamma \cdot B_0$ around the z axis.

In figure 5a, the equilibrium magnetisation in a field B_z is along the z direction. Applying a B_1 R.F. field rotating at the same rate as the precession of the magnetisation in the B_0 field, along the y' direction, the net magnetisation is tipped into the x' direction using a 90° pulse, due to the precession around this B_1 field in the rotating frame.

In figure 5b, we see different spins dephasing at different rates, according to the local magnetic field : $\omega(x, y, z) = \gamma \cdot B_0(x, y, z)$, such that after a time τ a particular spin has accumulated a phase difference $\Delta\phi = \tau \cdot \Delta\omega = \tau \cdot \gamma \cdot \Delta B_0$. For sufficiently long τ ,

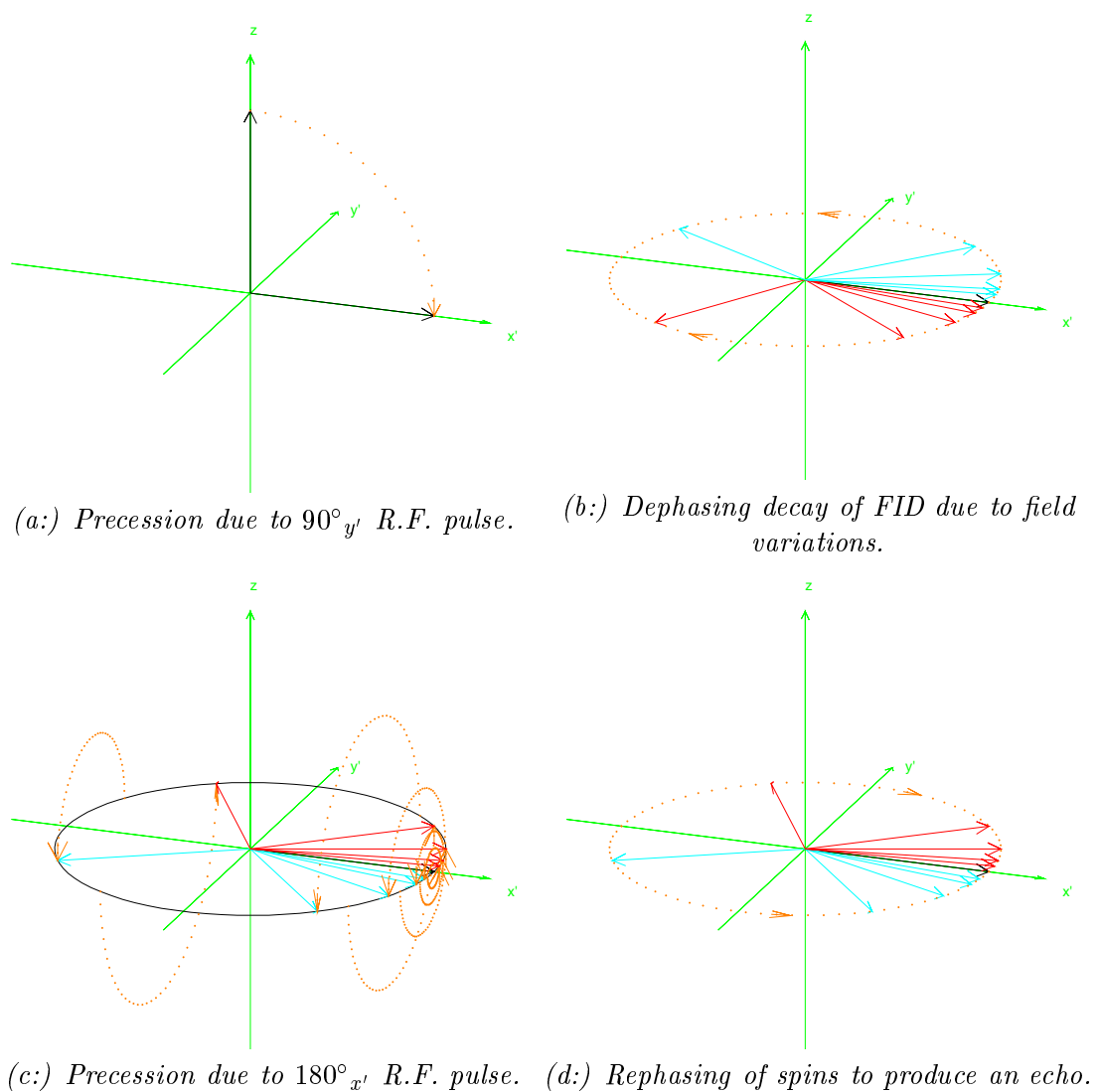


Figure 5:

Generation of a spin echo in an inhomogeneous magnetic field using a $90^\circ_{y'} - \tau - 180^\circ_{x'} - \tau - \text{echo}$ sequence, where the blue vectors are in a higher field than the red ones, and thus precess faster.

the spins will be randomised, there will be no net magnetisation and the FID will have decayed.

In figure 5c, we see that the action of a $180^\circ_{x'}$ pulse is such as to convert a phase gain to a phase lag, and visa versa. Thus those spins that are in a higher field, that had accumulated a phase gain $\Delta\phi$ will now have a phase lag of $\Delta\phi$.

In figure 5d, we see that after a further time τ , if the fields experienced by the spins are constant, these spins will have accumulated a further phase gain $\Delta\phi$ and will now have a net phase of 0. i.e. the spins will have re-focussed to form an echo. They will of course then dephase again as per figure 5b. The amplitude of the echo will be reduced from that of the FID by the action of the *transverse* or *spin-spin* relaxation, T_2 .

An important proviso is that the field experienced by a spin should be constant. However the spins in a liquid are mobile, and in the time τ of an NMR experiment can move to a different field. Then the refocusing will be imperfect, and there will be a further reduction in the amplitude of the echo. How significant this effect is, is a function of the diffusion rate of the liquid, the gradients from the B_0 magnet, and any other gradients, due to effects such as iron in a particular porous medium, or field gradients caused by susceptibility changes in a porous medium.

One way of reducing the effects of signal loss due to diffusion, is to use a Carr-Purcell-Meiboom-Gill (CPMG) sequence, where one follows the 90° pulse with a chain of $180^\circ_{x'}$ pulses at 2τ intervals, with a reduced τ to reduce the time for diffusion between pulses. This works since the diffusional reduction of the signal is proportional to τ^3 .

For most of this work, particularly in porous silica, a simple $90^\circ_{y'} - \tau - 180^\circ_{x'} - \tau - echo$ sequence was used, with the echo amplitude being recorded. However for some work on clays, with strong internal gradients, a CPMG sequence was used, with the n^{th} echo amplitude being recorded.

Chapter 3

NMR Cryoporometry method.

NMR Cryoporometry is a method suitable for measuring pore sizes and pore size distributions in the range of less than 30Å to over 3000Å pore diameter. The technique involves freezing a liquid in the pores and measuring the melting temperature by Nuclear Magnetic Resonance. Since the melting point is depressed for crystals of small size, the melting point depression gives a measurement of pore size.

3.1 NMR Cryoporometry equations.

We may define porosity as the fraction of the sample volume occupied by pore void; an important characterising parameter is the porosity as a function of pore diameter and spatial location, i.e. the pore size distribution within a material.

Recent work by Jackson and McKenna [Jackson and McKenna, 1990] demonstrated that the melting point depression of a variety of liquids confined in silica glasses varied inversely with the mean pore diameter as determined by gas adsorption isotherm measurements.

This behaviour is closely related to the capillary effect; both reflect the change in free energy caused by the curvature of the interfacial surface. This behaviour was originally described by equations developed by J.W. Gibbs, based on theoretical considerations of the equilibrium states of heterogeneous substances [Gibbs, 1875, 1878, 1906 reprinted 1961, 1928].

Initial impetus to this field of research was given by J. Thomson who considered the related theory of the depression of melting-point of ice caused by pressure or other stress [Thomson, 1849, 1862]. Sir W. Thomson (his brother, later Lord Kelvin) derived a related theory for the equilibrium pressure at curved liquid/vapour surfaces, that

describes capillary condensation (the Kelvin equation, see chapter 1.3.1) [Thomson, 1871].

J.J. Thomson later considered the effect of curvature on the equilibrium temperature of a liquid droplet [Thomson, 1888], [Defay et al., 1951, 1966, eqn. 15.83]. When extended to small crystals [Defay et al., 1951, 1966, eqn. 15.92] this is consistent with the Gibbs and Kelvin equations; the contact angle is assumed to be 180° . Expanding and taking the first term gives us the standard form.

Thus the Gibbs-Thomson equation for the melting point depression ΔT_m for a small crystal of diameter x is given by [Jackson and McKenna, 1990] :

$$\Delta T_m = T_m - T_m(x) = \frac{4\sigma_{sl}T_m}{x\Delta H_f\rho_s} \quad (1)$$

where :

$$\begin{aligned} T_m &= \text{normal melting point of bulk liquid} \\ T_m(x) &= \text{melting point of crystals of diameter } x \\ \sigma_{sl} &= \text{surface energy at the liquid-solid interface} \\ \Delta H_f &= \text{bulk enthalpy of fusion (per gram of material)} \\ \rho_s &= \text{density of the solid} \end{aligned}$$

We may rewrite equation 1 as :

$$\Delta T_m = \frac{k}{x} \quad (2)$$

To exploit this effect for pore size measurement [Strange et al., 1993] a porous sample containing a liquid is cooled until all the liquid is frozen, and then gradually warmed while monitoring the amplitude of the NMR proton spin echo from any liquid present. The liquid is usually chosen to be water or cyclohexane, the latter offering the large melting point depression factor k of $1825 \text{ K}\text{\AA}$. i.e. a depression of nearly 20K in 100\AA pores.

NMR is a sensitive technique for distinguishing between solid and liquid, as the coherent transverse nuclear spin magnetisation decays much more rapidly in a solid than in a mobile liquid (chapter 2.7). Measurement of the volume of liquid present is usually most conveniently made using a $90^\circ_x - \tau - 180^\circ_y - \tau - \text{echo}$ sequence (chapter 2.8), where the time interval 2τ is set to be longer than the solid decay time but less than the decay time in the liquid (chapter 7.1). For water and cyclohexane 2τ times of 4ms to 40ms were typically used.

The amplitude V of the echo is related to the volume v of solid that has melted to a liquid at a particular temperature T and thus the volume of the pores that have dimension less than or equal to the corresponding dimension x in equation 2. A further small increase in temperature T produces a small increase in liquid volume Δv proportional to the volume of pores with diameter x to $x + \Delta x$. The pore size distribution function dv/dx can therefore be obtained from the slope of the curve of v vs T using :

$$\frac{dv}{dx} = \frac{k}{x^2} \cdot \frac{dv}{dT} \quad (3)$$

where x is related to the temperature by the equation 2. The value of k used was determined using gas adsorption data, using the nominal pore sizes of a number of sol gel silicas as calibration values (chapters 7.5.3, 7.4.3). Further calibration work was performed using small angle neutron scattering (chapters 11 to 17), in an attempt to establish an absolute calibration scale. Good agreement was established between the two methods for large pores, but a significant divergence was found for small pores.

Thus the calculated pore size distribution gives one in effect the incremental volume of the pores at a particular pore diameter, for unit increment of pore diameter. If one normalises the distribution to unit volume of the dry porous matrix, one obtains the units $\{\text{\AA}^{-1}\}$. If one normalises the distribution to unit mass of the dry porous matrix, one obtains the units $\{1 \cdot \text{\AA}^{-1} \cdot \text{g}^{-1}\}$. Thus if one then integrates these pore size distributions over the measured pore diameter range, one obtains respectively f_v , the volume fraction of the matrix occupied by void space, and p_m , the mass normalised total porosity of the pores $\{1 \cdot \text{g}^{-1}\}$.

There has been considerable work by both NMR and neutron scattering to understand the changes that occur in water/ice and cyclohexane when enclosed in small pores [Steytler et al., 1983a,b, Steytler and Dore, 1985, Dunn et al., 1988, Dore et al., 1989, 1991, Farman et al., 1992, Teixeira et al., 1997, Baker et al., 1997, Allen et al., 1997, Booth and Strange, 1998, Allen et al., 1998, Margaca et al., 1999].

Chapter 4

NMR Cryoporometry experimental apparatus.

4.1 Bulk and 1D resolved cryoporometry apparatus.

For bulk cryoporometry measurements and 1D resolved cryoporometry measurements, I commissioned a wide frequency range solid state NMR spectrometer, based on digital R.F. switching technology, that I had designed and constructed earlier for NMR relaxation measurements, see figures 6, 7, 8. This employed a solid-state NMR pulse programmer I had designed (figure 9) to produce the NMR pulse sequences; a 90° - τ - 180° - τ -Echo sequence was used for the cryoporometric measurements, with the echo amplitude being monitored to determine the liquid fraction.

The magnet used was a 21.5 MHz (protons) MullardTM permanent magnet, with a 35mm gap, into which was inserted a Dewar containing the NMR probe, with cooling primarily by direct injection of liquid nitrogen (Lindacot) [Norris and Strange, 1969], see chapter 5.1.

The sample size was a standard 5mm high resolution NMR sample tube, with a sample



Figure 6: NMR spectrometer – Transmitter in foreground, then matching box, then receiver, with Lindacot cooler connected to the probe.

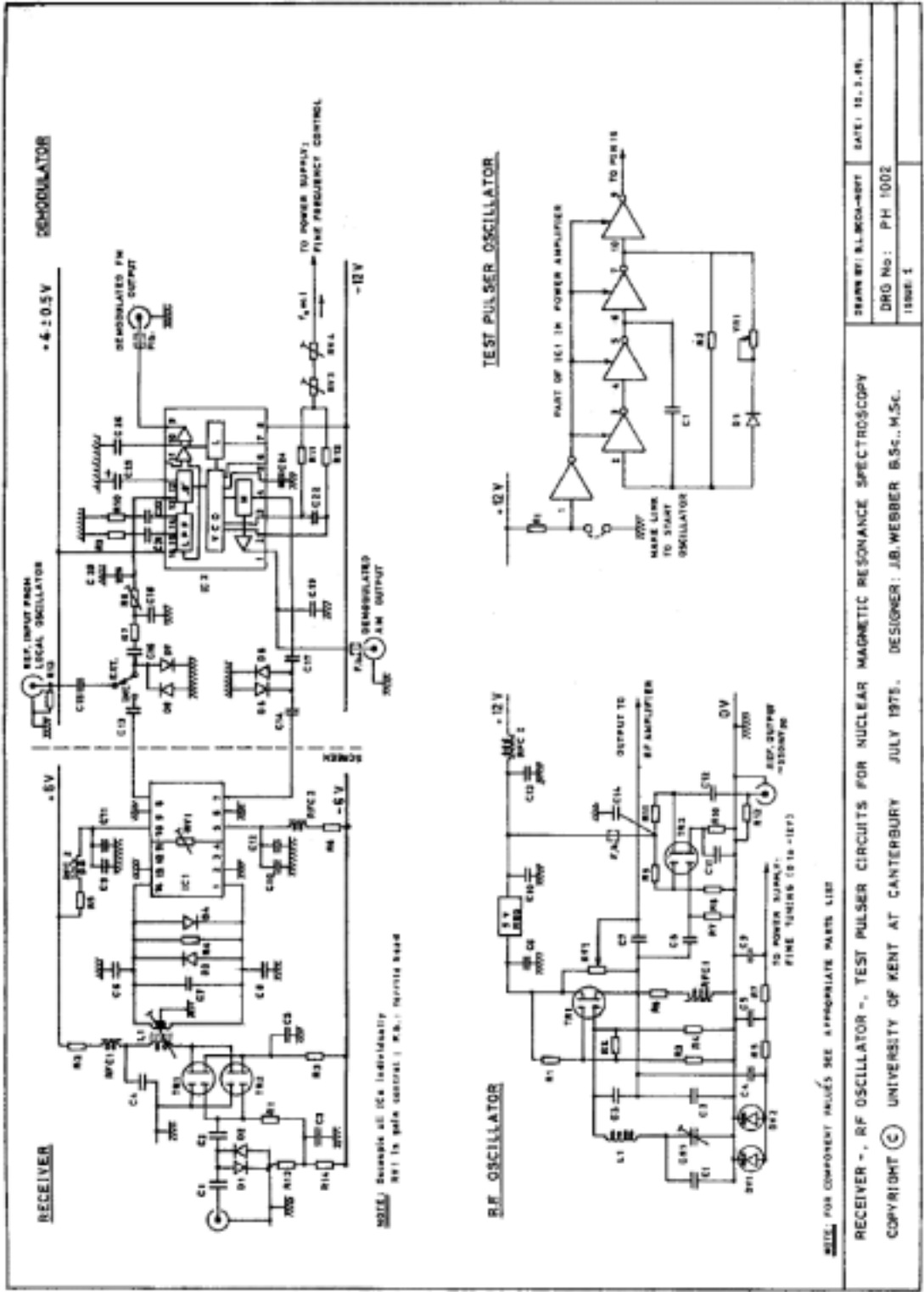


Figure 7: NMR Receiver circuit diagram, for bulk and 1D cryoporometry.

length of 20mm or less. The probes that were constructed for this project, and the methods that were used to cool them, are described in chapter 5.

The experiment was controlled from, and the results calculated using a 486 66MHz personal computer (PC) running a LabVIEW™ 3.01 for Windows™ program that I designed for this project. For this project the PC was interfaced by an IEEE488 bus to a Gould™ 1604 digital oscilloscope and a Hewlett Packard™ 34401A multimeter, and by serial interface to a Control Techniques™ 452+ proportional-integral-derivative temperature controller (see figure 10).

Figure 9 shows the instrument rack that was assembled for the bulk and 1D cryoporometry measurements. From the top there is : temperature controller, NMR pulse programmer, NMR system power supply, LabVIEW control and status display, control keyboard, digital oscilloscope, PC, sample temperature meter.

The LabVIEW program enabled the creation of an interactive 'front panel', giving the user control of the experiment and displaying the results numerically and graphically (see front panel diagram 11).

The block diagram of the top level LabVIEW control and data gathering program is shown in figure 12, the full diagram with all sub-level and test routines filling a lever-arch file.

For a description of the use of the instrument, see appendix C, and for an outline of the temperature control see chapter 5.1 (temperature cycling).

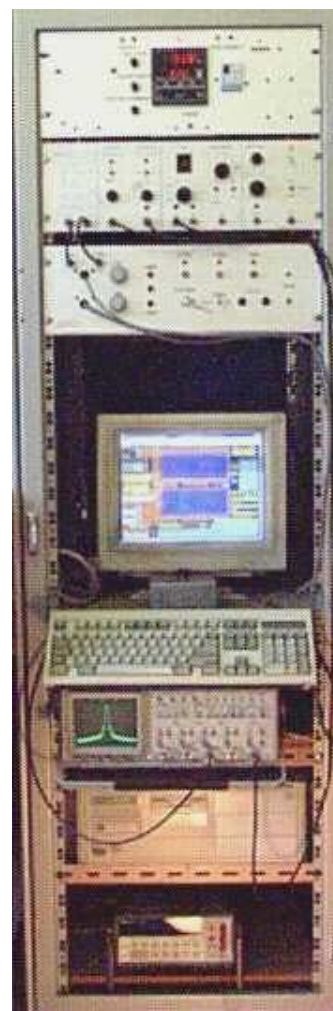


Figure 9: Cryoporometer instrument rack for bulk and 1D measurements.

Cryoporometric Apparatus

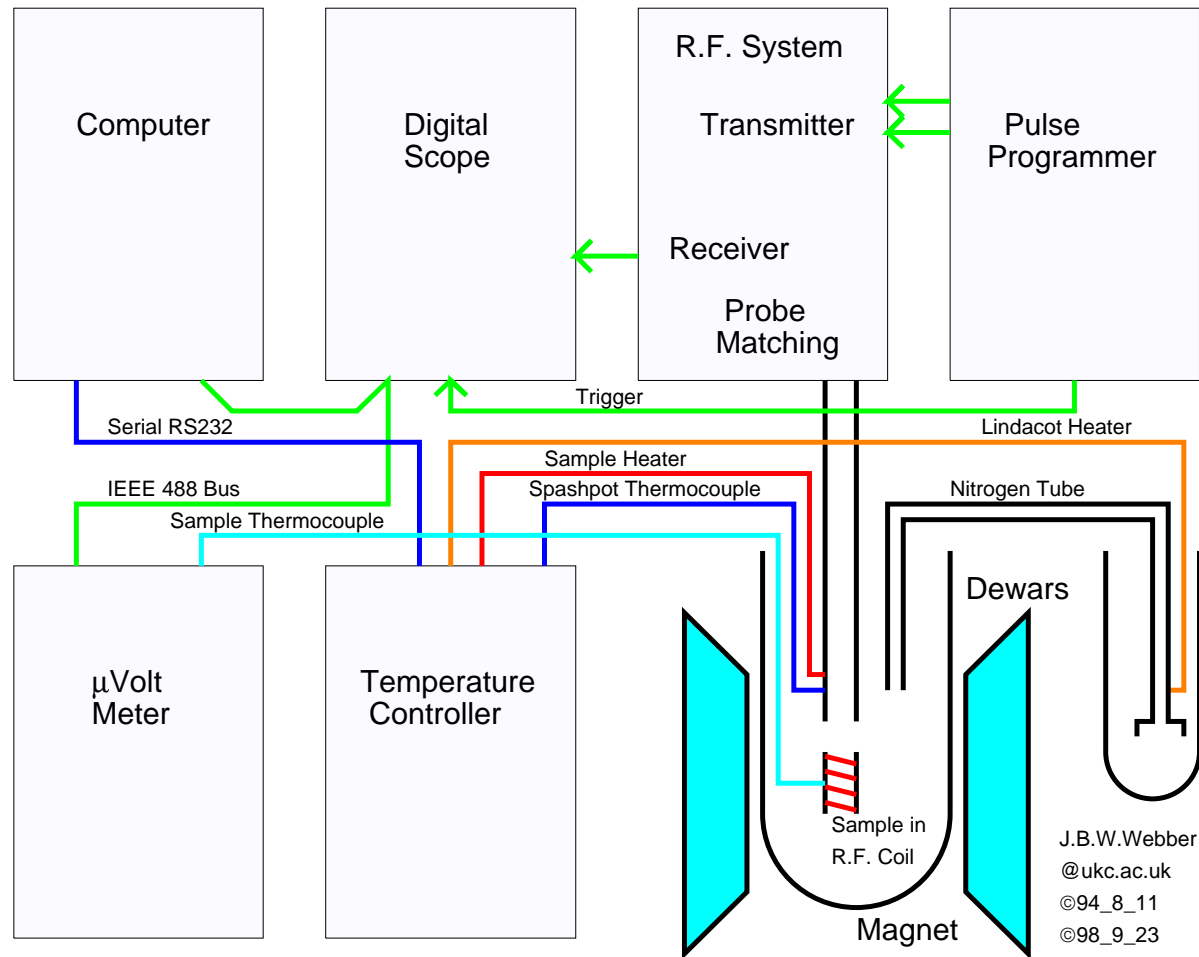
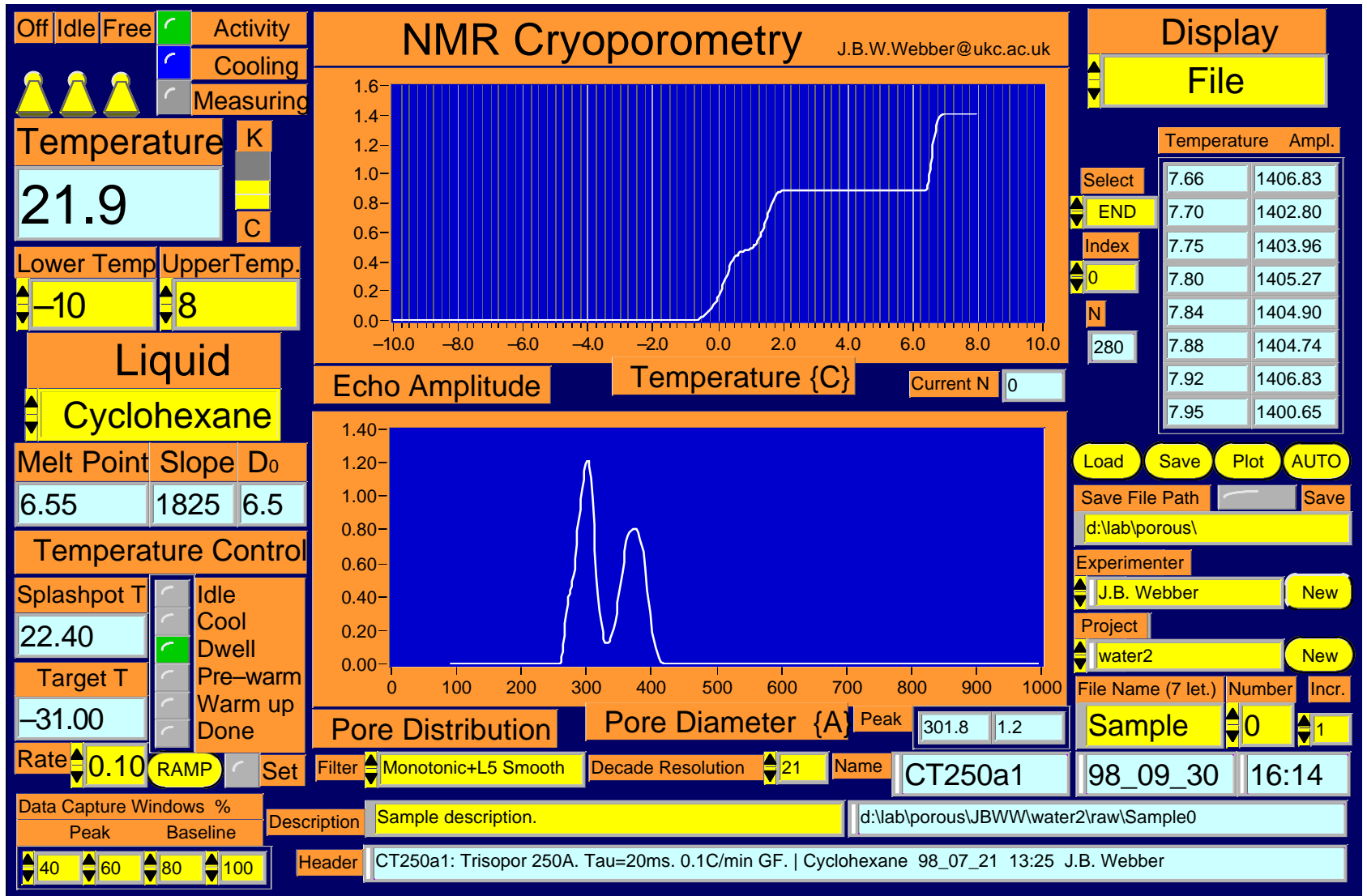


Figure 10: NMR Cryoporometric apparatus, for bulk and 1D cryoporometry.

Figure 11: LabVIEW frontpanel for cryoporometer control and status.



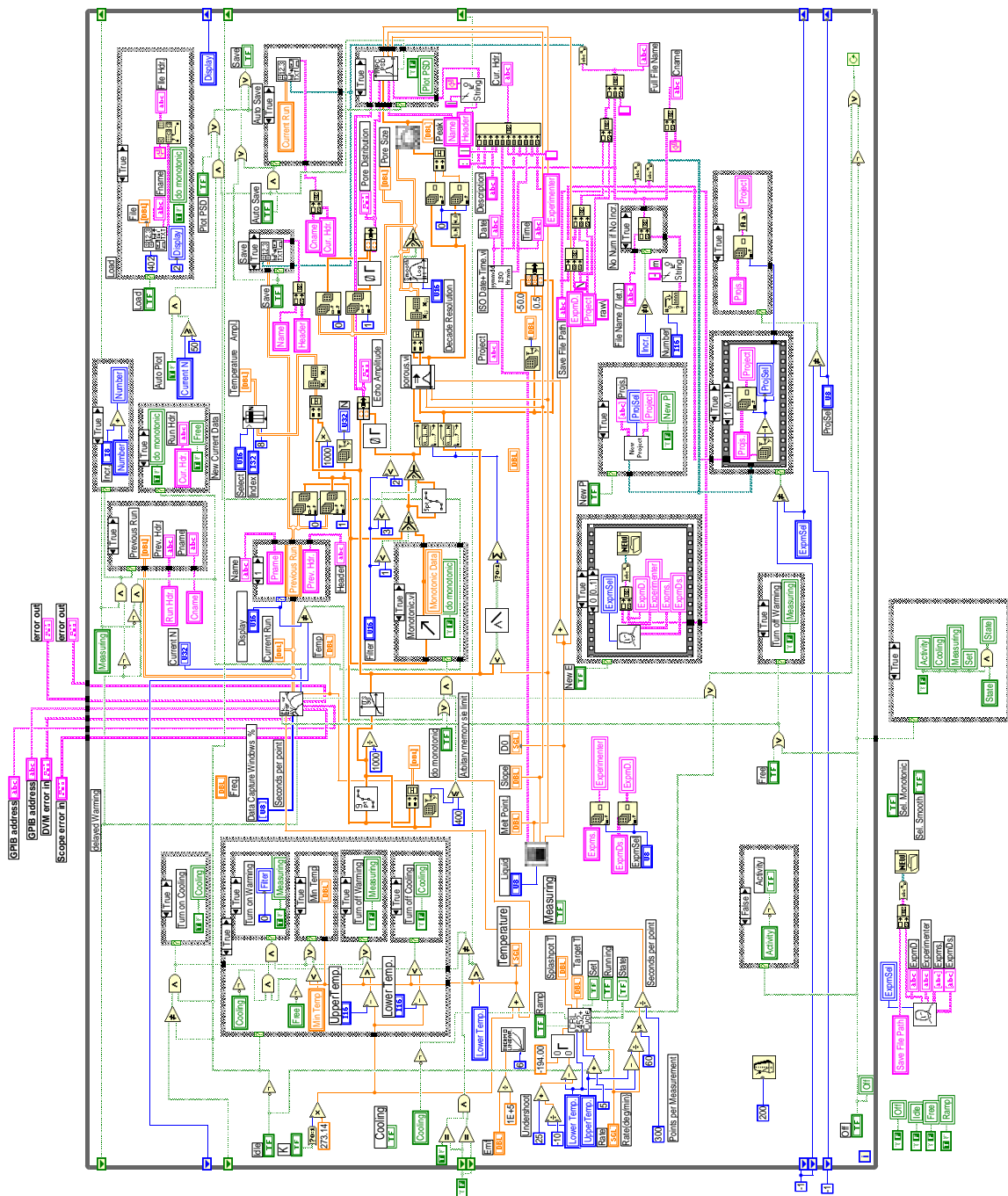


Figure 12: LabVIEW top level block diagram for cryoprotector.

4.2 2D and 3D spatial resolution cryoporometry apparatus.

For the two-dimensional and three-dimensional cryoporometry measurements, the spectrometer used was a modified BrukerTM CXP200 console with a Doty ScientificTM DSI1000A 1kW Class AB R.F. power amplifier and three TechronTM 7700 series gradient amplifiers. Rather than employing the usual Bruker AspectTM computer, I interfaced the Bruker to an industrial grade 486 DX33 personal computer running SMISTM software and with SMIS plug in modules including an AT&TTM DSP32C digital signal processor (figure 13).

I designed and constructed the interface between the Bruker and the PC (figure 14) using a single chip AlteraTM EPM5128 programable gate array, programmed to mimic the action of the Bruker Aspect computer device bus interface (20 bit data + 8+3+2 controls). This was originally designed to be driven from the cartridge port of an Atari STE, and was initially used in this way, but a simple re-wire to the PCB of a second copy allowed it to be driven by 11 bits of a parallel port from the PC [Macnair, 1995]. It provided control of the Bruker frequency synthesizer (20+20 bits), frequency sweep unit (16+20 bits), modulator control (20+4+4 bits), filter control (12 bits) and output device interface (20+20 bits), and these may thus now be directly controlled from the SMIS software, calling Forth routines written by Dr. M.J.D. Mallett to duplicate the actions of the SMIS hardware controlling routines.

Gating and phase selection of the Bruker R.F. was from the software controled pulse sequencer in the SMIS system. For soft pulses for slice selection, I designed and constructed a four quadrant R.F. multiplier (figure 15) based on an Analog DevicesTM AD834 R.F. multiplier chip, AD5539 R.F. amplifier, and NE630N switch. This was introduced before the 20W broadband amplifier, and controlled from an analogue channel of the SMIS sequencer, programmed to generate a $\text{sinc}(t/T_0)$ function of width T_0 . Shown are the 500MHz bandwidth multiplier, an op-amp for differential to single ended conversion, and output gate switch to ensure that the linear output amplifier receives negligible signal when the pulse is off.

I constructed sixth order Butterworth low-pass equal capacitor Salen and Key filters [Aikens and Kerwin, 1972, Huelsman, 1976] (using surface mount resistors and capacitors) with selectable cut-off frequencies of 100kHz, 300kHz and 1MHz (plus unfiltered)

Figure 13: Diagram of the imaging spectrometer, based on a Bruker console and SMIS control computer.

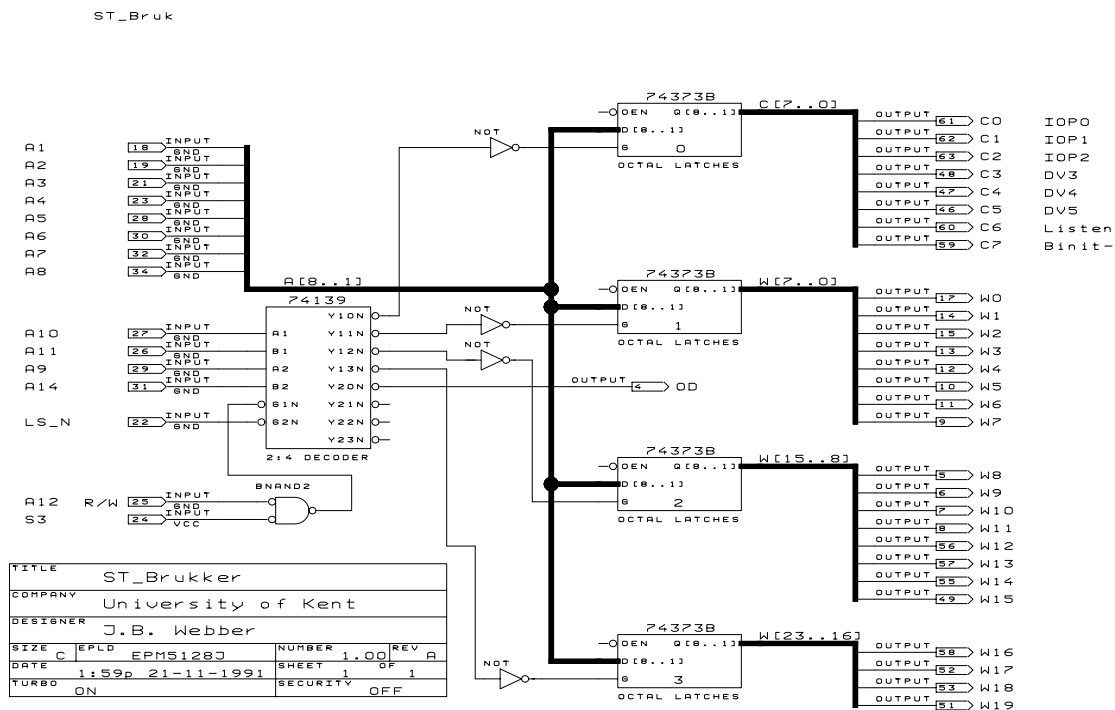


Figure 14: Control interface between SMIS PC parallel interface and Bruker spectrometer, mimicking the Bruker Aspect computer device bus interface, implemented using an Altera programmable logic device EPM5128.

and introduced them in both receiver channels, for use at higher bandwidths than the Bruker receiver filters (figure 16).

The R.F. and gradient coils [Hayes et al., 1985, Strange and Halse, 1996] were designed by Andrew Macnair [Macnair, 1995] and Magnex Ltd. and constructed by Sarah Codd [Codd, 1996] for imaging broadline materials. The R.F. coil was of birdcage construction; the z gradient along the main magnetic field B_0 was generated by a solenoidal Maxwell pair, and the x and y gradients were generated by Golay saddle coils.

The magnet used was a 200mm horizontal bore MagnexTM superconducting magnet, operating at 105MHz for protons. The sample access diameter (room temperature, inside the gradient and R.F. coils) was 25mm. Into this was inserted the narrow neck of a dewar, about 100mm long, with 12.5mm internal diameter clear bore, that then swelled out (allowing hand access) and extended to the edge of the magnet. This then allowed the temperature of the sample to be varied.

50 Ohm Mixer

J.B. Webber 93_05_24

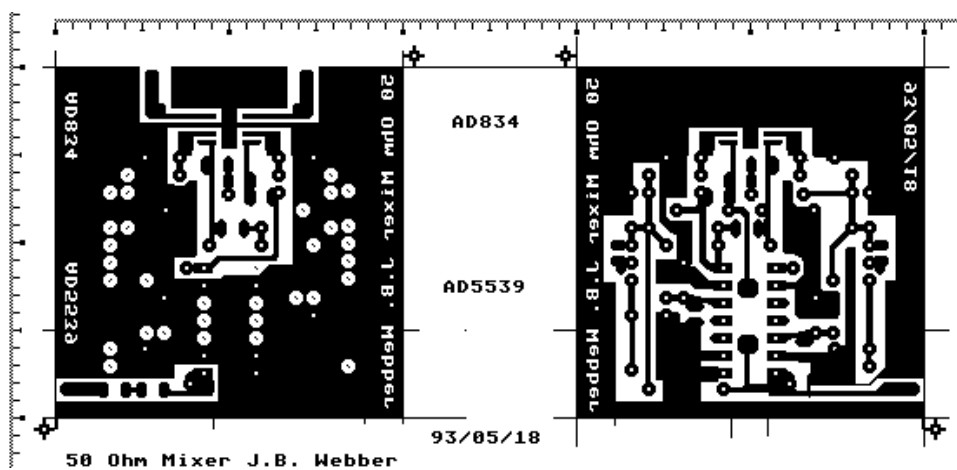


Figure 15: Four quadrant R.F. multiplier diagram and PCB, for amplitude modulation of NMR transmitter pulse, for bandwidth shaping and slice selection.

Figure 16: Dual channel low pass 100kHz, 300kHz, 1MHz (+ bypass) 6th order Butterworth filters for NMR recieved signal U and V channels.

Chapter 5

NMR cryoporometry temperature control.

The main prerequisites for the sample temperature control for cryoporometry were that it be able to cool the probe below -120°C (150K) when using cyclohexane as the indicator liquid, and down to liquid nitrogen (77K) when using liquids such as butane; that it should be able to warm the sample at a controlled rate, with little in the way of temperature excursions; that all the sample be as nearly at the same temperature as possible. It was important for the recorded temperature be as close to the true sample temperature as possible.

5.1 Liquid nitrogen droplet cooled probe.

The cooling technique used for most of these measurements was direct injection of liquid nitrogen into a 'splash-pot' in the probe (Lindacot system) [Norris and Strange, 1969]. This was achieved by pulsing current in a heater coil in an inverted cup in liquid nitrogen in a Dewar, forcing droplets of liquid nitrogen into the probe. The liquid nitrogen droplets were ducted into a 'splashpot' chamber built into the body of the probe, where the droplets evaporate. Thus the full latent heat of evaporation of the nitrogen was available to cool the probe.

The thermal mass of the splashpot then served to smooth the temperature excursions from the evaporating nitrogen droplets. A resistive heater was built into the body of the probe, enabling it to be warmed above room temperature.

The probe (figure 17) consisted of the brass body containing the splashpot and heater, a lower removable copper chamber containing the sample and R.F. coil, and a screened upper plate, allowing mounting of the triaxial LemoTM R.F. connector, thermocouple connectors for the splashpot and the sample (with ferrite R.F. noise filters), and the heater connector. This also acted as a support for the nitrogen droplet inlet tube. The various sections of the probe are linked by thin walled stainless tubing.

To maintain the sample all at a uniform temperature, a copper foil was wound around the sample tube, ensuring that it was non-shorting. This then also served to ensure that the R.F. field produced by the NMR probe coil was axial and uniform within the foil, giving a uniform B_1 field. A heavy copper link provided a thermal path to the splashpot; a copper-constantan thermocouple was soldered to the foil, to monitor the sample temperature. A dewar of melting ice was used as a reference temperature for the other copper-constantan junction, and the E.M.F. monitored by a Hewlett-PackardTM 34401A IEEE multifunction averaging meter.

The temperature was controlled by a Control TechniquesTM 452+ Proportional-Integral-Derivative temperature controller, monitoring the temperature in the splash-pot with a copper-constantan thermocouple, and with a serial interface and dual heat/cool output.

The heat output of the controller was connected to a mains burst-fire thyristor unit; the cool output was connected to a 12v 2A current pulser, with adjustable repeat rate, pulse width, and current (figure 9), that was connected to the Lindacot heater coil (figure 6). The main limitation of this temperature control system, is the pulsed nature the cooling; when used with the Control Techniques temperature controller, the temperature ramp is sometimes less uniform than one would like, particularly when studying large pores giving only a few degrees of melting point depression.

A further limitation is that it requires cryogenics, and the Lindacot Dewar at present requires manual filling before each temperature run, thus reducing the number of runs



Figure 17: Liquid nitrogen cooled cryoporometry NMR probe, used for bulk and 1D measurements.

possible in a day to typically four. It would be possible to add automatic Dewar re-filling, with the addition of sensor inputs, digital control outputs and a cryogen rated valve and pressure safety release, using gas pressure to perform the transfer.

5.2 Peltier cooled probe.

As part of this project an alternative probe was designed and constructed, using three thermoelectric cooling elements built into the body of the probe, with water cooling to remove the waste heat. Due to space limitations in the probe dewar, the size of the elements was limited, and the maximum cooling achieved was only down to 0°C (figure 18); thus this probe was not actually used for cryoporometric measurements.

The probe was constructed from two copper sections, joined by thin walled stainless tubes. The lower section contained the sample coil in a threaded chamber, and a copper finger provided a thermal path to the Peltier elements. The upper chamber provided a thermal path from the Peltier elements to a water cooled chamber, and a support plate for the triaxial LemoTM R.F. connector; for the blue thermocouple connectors for the probe lower body and the sample; for the grey power connector for the Peltier elements and for the blue and black push fit connectors for the cooling water tubes.

The Peltier elements used were R.S. part No. 197-0332; these were rated at $\Delta T = 67^{\circ}\text{C}$ @ 0W heat flux, and 9.2W heat pumping power @ $\Delta T = 0^{\circ}\text{C}$. The elements were used both in the configuration of one in series with two in parallel (which gave a ΔT of about 22°C), and also as just two in parallel (which gave a ΔT of about 20°C), both at about 5A current. Thus one concludes that with the probe in the Dewar, the heat flux is about $13\text{W} = 54 \text{ Cal}\cdot\text{s}^{-1}$ at 0°C . That it is this high is partly due to the very narrow vacuum gap enforced by the magnet pole spacing, and partly due to conduction through the elements themselves and the probe R.F. and thermocouple stainless tubes. Thus the ΔT was insufficient for



Figure 18:
Peltier cooled NMR probe.

Thermal characteristics of Peltier cooled probes.

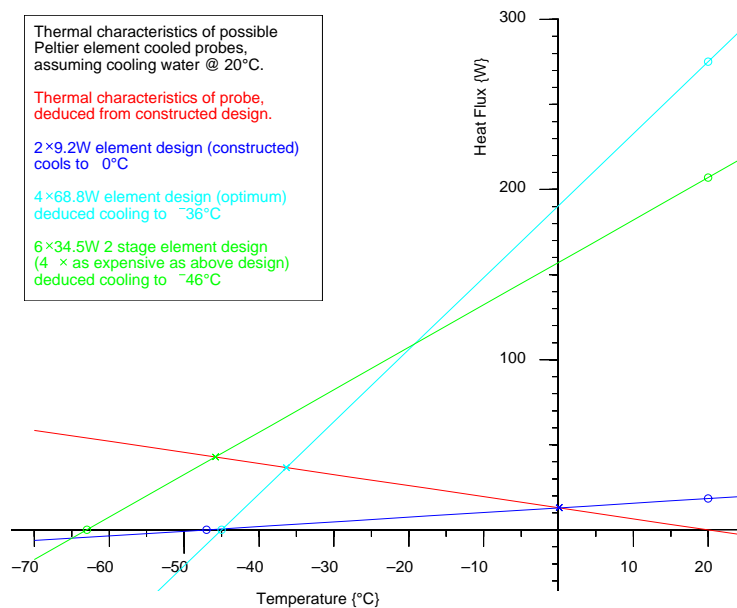


Figure 19: Plotting the thermal performances of Peltier elements, and the performance of the constructed Peltier cooled probe allows us to deduce the performance of alternative designs.

actual use.

A design that might be more successful would be to have an extended Dewar, that swells out above the magnet pole-faces, allowing larger Peltier elements with substantially greater heat pumping power. If elements of R.S. part No. 238-3010 were used, rated at $\Delta T = 65\text{C}^\circ$ @ 0W heat flux, and 68.8W heat pumping power @ $\Delta T = 0\text{C}^\circ$, then if four were used in parallel, a $\Delta T = 56\text{C}^\circ$ should be achievable, giving a lower operating temperature of about -36C° , with a heat flux of about $37\text{W} = 153 \text{ Cal}\cdot\text{s}^{-1}$ (see figure 19).

If six two stage elements each with $\Delta T = 83\text{C}^\circ$ @ 0W heat flux, and 34.5W heat pumping power @ $\Delta T = 0\text{C}^\circ$ (R.S. part No. 197-0398) were used, the lower temperature only drops by 10C° , for a factor four increase in cost.

The major advantage of a Peltier cooled probe is that it requires no cryogen; as a result all 24 hours of the day are available for temperature runs, and just not the working day to which the existing cryogen cooled probes are limited.

5.3 Gas flow cooled probe.

A third design was evaluated, based on standard gas flow techniques.

A commercial gas flow Dewar insert (Bruker) with flexible Dewar piping was used to construct a gas flow system. A neck extension was designed for a standard 25 litre Nitrogen dewar to enable a gas tight connection. Nitrogen gas was then boiled off using a resistive heater connected to a 60V 5A power supply (Roband VAREX 60-5) (usually used in the range 3A to 4 A), and passed through a



Figure 20: Gas flow cooling system, shown with 3D imaging system in the stray field configuration.

200W process air heater tube (R.S. part No. 200-2480). All non Dewar tubing was lagged with 6.5cm dia. foam pipe lagging, and the process heater was additionally first lagged with a few layers of ceramic paper for safety reasons; an earth safety connection was soldered to the body of the heater.

The gas flow system was originally constructed for use with the 3D imaging NMR system (see Apparatus, Chapter 4.2) (figure 20), but was adapted for use with the cryoporometer by ducting the cold gas into the probe's normal liquid N₂ inlet tube to the splashpot. The process heater was connected to the burst-fire mains controller of the temperature controller.

Using 2A to the evaporative heater, it was not possible to maintain a temperature of 0°C at the sample; with 3A about -15°C was achievable, and with 4A about -70°C was reachable. However, with maximum output from the temperature controller to the air flow process heater, it was only then able to warm to about -15°C.

Thus for the samples being studied (i.e. water in large diameter pores) it was necessary to cool the sample to -25°C (to ensure that all the water was frozen) and then measure over the range -10°C to +5°C. A slightly modified cryoporometric sequence was programmed, to enable this (*Pore Measurement GFlow*). However it was found necessary to use 4A to the evaporator during the cooling, and 3A during the warming and measuring. It was also particularly important to switch off both heaters at the end of the run, as damage would occur if all the liquid evaporated or the gas flow stopped for any

reason.

Clearly for regular use it would be preferable to add further electronic sensing and switching, to ensure automated operation and protection.

The liquid nitrogen consumption was found to be considerably higher than when using direct injection of liquid nitrogen droplets using the Lindacot system. The Lindacot system used a 25 litre dewar of liquid nitrogen in a week, corresponding to about 20 runs over a typical temperature range of -50°C to 10°C , at a rate of $0.5^{\circ}\text{C}\cdot\text{min}^{-1}$; with the gas flow system it was necessary to re-fill the dewar every day, corresponding to 2 runs, with a minimum temperature of -25°C , and measuring over -10°C to $+5^{\circ}\text{C}$ at a rate of $0.05^{\circ}\text{C}\cdot\text{min}^{-1}$.

Nonetheless, for these initial trials, the gas flow system provided a valid method of obtaining a smoother and slower warming than could be provided by the Lindacot nitrogen droplet system, and was thus particularly useful for studying large pore diameter samples (see measurements on Trisopor[®] porous glass, chapter 9.3).

The acquisition of a 50 litre N_2 Dewar allowed the construction of a second more efficient gas cooled unit, where dried air of regulated pressure was passed by a solenoid valve on a time-switch to two ports on the Dewar, each with their own valves – the first enabled rapid cool-down, the second was via an adjustable needle-valve, set for the amount of cooling required. Vented cold gas was used as before, via the process heater. The fail-safe action of the program was modified. It would still be advantageous to construct a low thermal loss take-off point.

5.4 Temperature cycle control.

The cryoporometric temperature cycle for these probes was controlled by a LabVIEW[™] program *Temperature Cycle case* (figure 21) with a number of states, the first one of which is **Idle**. The upper and lower temperatures over which a measurement is to be performed are set by the user on the main cryoporometric LabVIEW front panel (figure 11), which also displays the states. The main program then calculates the lowest temperature to which the splash-pot must be taken, allowing for supercooling of the sample, and (temperature dependent) offsets between the splash-pot and the sample temperature.

When the temperature cycle is enabled, the state changes to **Cool**, when a steadily

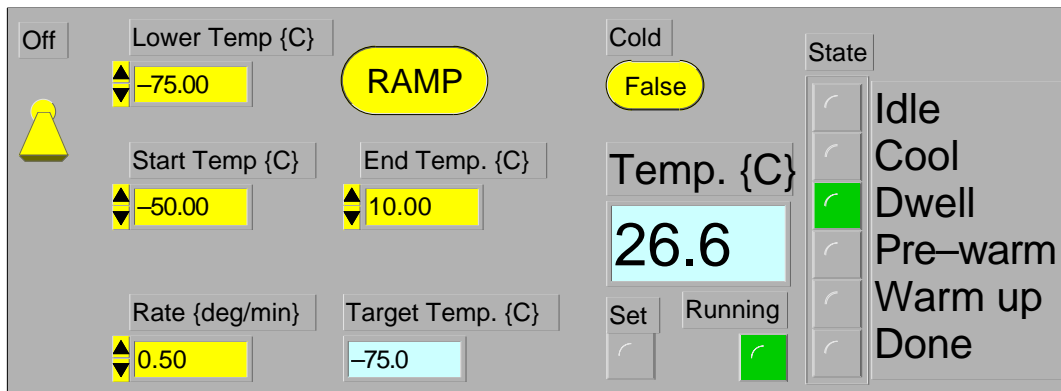


Figure 21: Temperature cycling LabVIEW sub.vi showing temperature cycle states and start and end measuring temperatures.

ramping down ($5\text{ C}^{\circ}\cdot\text{min}^{-1}$) target temperature is sent to the Control Techniques temperature controller via the serial interface. When the target temperature reaches the calculated lower temperature, the state changes to **Dwell**. It remains in this state for at least 15 minutes, to ensure proper cooling of the probe, and until the sample temperature reaches the start set temperature.

The state then changes to **Pre-warm**, and the target temperature ramps up ($2\text{ C}^{\circ}\cdot\text{min}^{-1}$) until it reaches the start set temperature. The state then changes to **Warm up**, and the ramp rate changes to the rate set by the user (default $0.5\text{ C}^{\circ}\cdot\text{min}^{-1}$). Measurements are taken, and averaged so as to generate finally about 300 data points spread uniformly over the measurement temperature range. At each measurement the melting point curve is displayed, and the pore size distribution is calculated and displayed.

Measurements are then performed until the upper set temperature is reached, when the state switches to **Done**, and the temperature ramping is stopped. The data is then saved (if AUTO is enabled), and it is plotted to a networked laser printer; the monotonic function is then applied to the data. Previous 'Current Data' is copied to 'Previous Data', together with a record of it's name and comment line.

It should be noted that as the temperature controller offers no way of actually turning the cooling off, the Idle and Done states are dynamic ones, where the target temperature is continually adjusted to be the same as the current measured temperature.

An alternative version of the temperature control software allows for measurements to be made on a slowly ramped cooling part of the cycle, as well as on the warming part, for investigating temperature hysteresis effects.

Chapter 6

Sample preparation for cryoporometry.

When preparing a series of samples for cryoporometry, first empty 5mm diameter thin walled high-resolution NMR sample tubes were cut to about 7cm length, and sealed at one end. They were dried in an oven, and then were weighed together with a numbered cap. About 12mm to 15mm of the porous sample was added, and the samples re-weighed. The porous samples were then dried overnight, usually at 120°C, in a metallic numbered holder, and re-weighed. Comparisons of weights before and after drying acted as confirmation that samples had not been interchanged.

Weighing tests on porous silicas showed that an hour was sufficient for most of the adsorbed moisture to be lost at 120°C, and that after a few hours at 120°C there was little further weight loss until the temperature was raised to 250°C. It was assumed that this latter loss of weight was due to surface OH groups being driven off, and was probably associated with silica surface modification. Thus for normal preparation the drying was limited to overnight at 120°C.

Using a syringe, just sufficient indicator liquid (usually water or cyclohexane) was added to the porous material to cause the grains to stick together from surface tension. The aim was to achieve about 110% filling – i.e. to have the pores fully filled, and an extra 10% liquid in the inter-granular space. Gas expressed from the pores frequently caused void space to form in the tubes, and the porous material had to be tapped down. It was particularly important not to overfill to excess those samples using water as an indicator liquid, as otherwise they would shatter when cooled. Any samples that were

later found on measurement to be not over 100% filled were then rejected.

The water used was either distilled water, or de-ionised, filtered, water, with a final reverse osmosis treatment stage, which had a conductivity of about one tenth that of the distilled water. The cyclohexane was anhydrous grade, in sure-seal bottles. The cyclohexane was added to the porous material under a dry nitrogen atmosphere, in a glove box. Early tests had shown that contamination with water could result in a small proportion of pre-melting of the cyclohexane.

The samples were then re-weighed, and the mass of porous material and indicator liquid calculated.

The samples were then flame sealed – they were attached via a silicone tube to a vacuum line with a liquid nitrogen filled cold trap (to prevent oil backstreaming) and a rotary vacuum pump. The tubes were immersed in liquid nitrogen to the depth of the sample. As soon as the nitrogen stopped boiling vigorously, the tap to the vacuum was opened. (It was important not to let the sample reach liquid nitrogen temperature while air was in it, as air could then be condensed, which would later expand and shatter the sample tube.) Cooling the sample prevented the indicator liquid from evaporating. The neck of the sample tube was then heated using a natural gas/ oxygen torch, until it collapsed, and then further heated until it could be separated; the tip was then heated to white heat, to ensure a good seal. The samples were labelled when cool.

It should be noted that no freeze-pump-thaw cycle was used to remove dissolved paramagnetic oxygen, as a shorter T_1 was useful for faster signal averaging.

Chapter 7

NMR Cryoporometry calibration.

NMR Cryoporometry is a secondary method of measuring pore sizes, in that the cryoporometric melting point depression constant for the liquid being used must be first calibrated using known pore sizes. It does however have the major advantages of a directly calibratable measurement of pore volume, of non-destructive pore size measurement, and of spatial resolution of pore size. As we shall see, it shows good pore size linearity with gas adsorption measurements.

7.1 Cryoporometer volumetric calibration.

There are a number of points that must be taken into consideration when wishing to obtain an accurate measurement of the pore volume as a function of pore size, when using an NMR cryoporometer, as one is measuring an NMR signal as a function of temperature.

The NMR signal intensity due to a fixed volume of liquid may change for a number of reasons:

- the Boltzmann factor will change with temperature; (chapter 2.3);
- the quality factor Q of the receiver coil will change with temperature and tuning;
- the density of the liquid will change with temperature;
- the T_1 and T_2 of the liquid will change with temperature;
- the T_2 of the liquid will be a function of the local pore surface area;
- the T_2^* of the liquid will be a function of any local magnetic field gradients due to magnetic particles in pore walls, or due to susceptibility gradients in pores;

- there may be a diffusion weighed loss of magnetization from such gradients in pores, as well as the B_0 magnet gradients;
- the receiver gain may be a function of time or signal amplitude.

Finally it should be noted that simple cryoporometry theory assumes that as well as the signal amplitude from the liquid being (after calibration) proportional to the mass of melted liquid, the signal from the solid is (at the time of measurement) negligible. These effects must be taken into account in the instrument calibration.

7.2 Receiver gain calibration.

The receiver had been shewn to have good stability with time; however all receivers have a maximum voltage output they can deliver before gain reduction sets in, and amplitude detecting receivers have a minimum signal they can reliably detect.

The receiver design used had employed a dual multiplier phase locked loop design to give a true amplitude output, and had been shewn to have good linearity at low signals ($1\mu\text{V}$ i/p, 10mv o/p) when it was constructed. It had also been shewn to have good linearity in excess of 1V output, and the gain was set so that for normal porous samples the maximum output was less than 1V .

Nonetheless it was felt desirable to calibrate this particular receiver.

A Farnell PSG1000 synthesizer was connected to the receiver input, via a nine switch 100dB Hatfield 687A attenuator ($1,2,2,5,10,20,20,20,20$ dB). The receiver output was taken to the HP digital volt meter and the Gould oscilloscope otherwise used for cryoporometry. The precision of the attenuator was far less than that of the receiver/DVM, but as it was possible to generate the same attenuation by more than one combination it was in principle possible to obtain a self-consistent set of corrected attenuations. This had indeed been successfully done when the receiver was designed, a smooth gain curve being obtained. This time, however, it was found that the attenuator switches had aged,

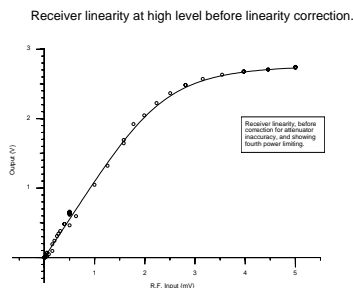


Figure 22: Measured gain curve for receiver, showing receiver gain compression and calibration attenuator inaccuracy.

and the gain curve obtained was far from smooth.

However we may reasonably assign the average smooth departure from a straight line to the gain compression that we are trying to measure, and random variations to instability in the attenuator.

In figure 22 we graph the raw results; we see that the receiver output follows a typical limiting curve – i.e. one that can be expressed as in inverse relationship of the form :

$$Y = \frac{1}{\frac{1}{Limit} + \frac{1}{X}}$$

We actually find that for this data the best fit (solid line in figure 22) is actually for a fourth power limiting curve, of the form :

$$Measured = \left(\frac{1}{\frac{1}{Limit^4} + \frac{1}{(Gain \times RFAmplitude)^4}} \right)^{\frac{1}{4}}$$

Hence we may write :

$$RFAmplitude = \frac{1}{Gain} \cdot \left(\frac{1}{\frac{1}{Measured^4} - \frac{1}{Limit^4}} \right)^{\frac{1}{4}}$$

$$\therefore Corrected = \left(\frac{1}{\frac{1}{Measured^4} - \frac{1}{Limit^4}} \right)^{\frac{1}{4}}$$

In figure 23 we plot the large amplitude corrected output (with attempts at corrections for attenuator inaccuracy); Gain was 1188.2₅, and Limit was 2.79₀V. Since the readings were logged on the digital oscilloscope as well as the DVM, a gain calibration was calculated for that, of 1.01₁, which must be applied first. A function *nmrrxcor* was written to apply the 4th order inverse correction.

We note that since receiver noise is also compressed, then expanded, we do not expect worse noise at large amplitude, until digitisation noise is significant. An arbitrary hard limit of 5.5V was imposed.

In figure 24 we plot the small amplitude corrected output. Thus we now have an output that is linearly proportional to the input from less than (0.5μV, 0.5mV) to (5mV, 5V),

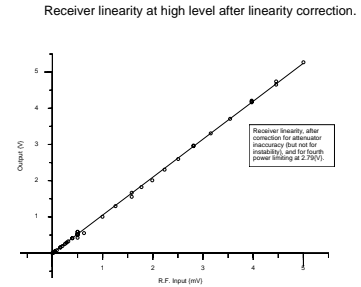


Figure 23: Corrected high amplitude gain curve for receiver, using 4th power limit.

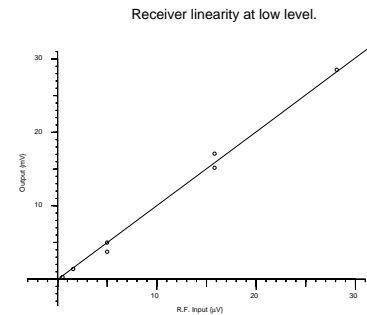


Figure 24: Low level gain curve for receiver.

a linear dynamic range of 10^4 .

This is far superior to conventional diode amplitude detection. Having amplitude detection allows the use of a permanent magnet with no temperature stabilisation, since there is no phase sensitivity.

7.3 Temperature dependence of volumetric sensitivity.

We have considered the effect of the variation in sample magnetisation due to the Boltzmann effect, in chapter 2.3. We need to consider other effects which may cause the signal to change in amplitude as a function of temperature, for a fixed volume of liquid sample.

7.3.1 Resistivity of copper.

The resistivity of metals such as copper is known to vary with the 5th power of absolute temperature at low temperatures, but to be approximately proportional to temperature at higher temperatures.

If we plot the resistivity $\rho(T_K)$ of copper as a function of absolute temperature T_K in the range 100K \rightarrow 1000K [Kaye and Laby, 1966], we see (figure 25) that it is well fitted by a quadratic $\rho(T_K) = -0.2823 + 0.006405 \cdot T_K + 7.817 \cdot 10^{-7} \cdot T_K^2$ over this range, but that a straight line $\rho(T_K) = -0.3271 + 0.006866 \cdot T_K$ is adequate over the range 100K \rightarrow 500K.

7.3.2 Volumetric sensitivity.

The amplitude A of the detected NMR signal for a given mass of sample is in part determined by the quality factor Q of the probe tuned circuit.

For a series resistance R in an LCR tuned circuit we have for the Q at resonance :

$$Q = \frac{\omega_0 \cdot L}{R}$$

The frequency ω_0 is the NMR frequency, and is effectively fixed, and the inductance L is determined by physical geometry of the coil. The size of the coil will change through thermal expansion, and the most important effect of this will be to change the condition of being at resonance; however this NMR system is designed to be used for

Resistivity of copper for 100K to 1000K

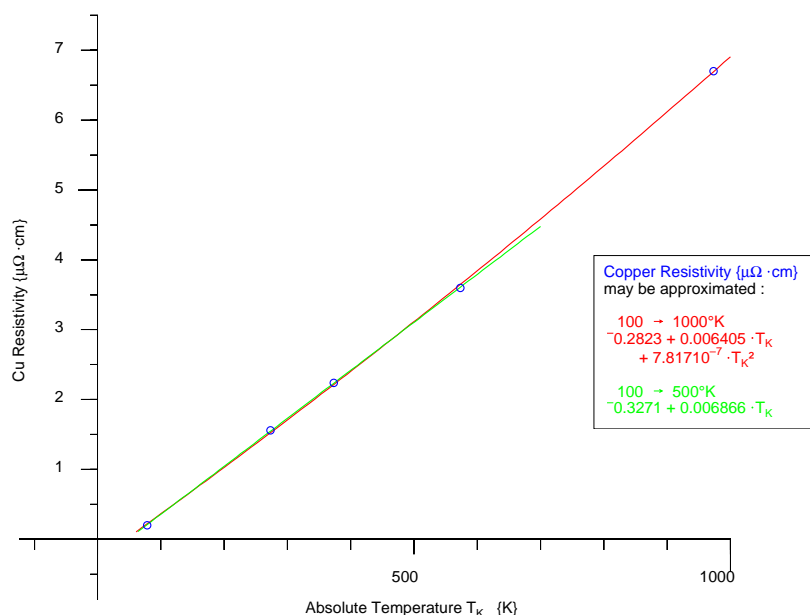


Figure 25: An approximation for the resistivity $\rho(T_K)$ of copper from 100K to 1000K .

measuring relaxation in solids as well as liquids, and hence has a probe bandwidth of in excess of 1MHz, with final receiver bandwidth being determined by a filter. Thus as the coefficient of thermal expansion of copper [Kaye and Laby, 1966] is only $16.7 \cdot 10^{-6}$, there is little de-tuning effect with frequency.

The effective series resistance of R will be composed of the resistance $R_{Cu}(T_K) = \frac{R_{Cu}(0^\circ C)}{\rho(0^\circ C)} \cdot (\alpha + \beta \cdot T_K)$ of the copper coil, and other resistances that will in effect have zero thermal temperature coefficient (not being dependent on probe temperature), due to such effects as the electrical resistance of the parts of the resonant circuit outside the probe, the radiation resistance of the R.F. coil, the resistive loading effect of the receiver coupling, and the fixed resistor in parallel with the tuned circuit added to increase the probe bandwidth.

Thus we may write for the total resistance :

$$R_T(T_K) = R_Z + \frac{R_{Cu}(0^\circ C)}{\rho(0^\circ C)} \cdot (\alpha + \beta \cdot T_K)$$

Thus we conclude that over the temperature range 100K \rightarrow 500K we may write for variation in Q due to probe temperature changes :

$$\begin{aligned} \frac{Q(T_K)}{Q(0^\circ C)} &= \frac{R_Z + R_{Cu}(0^\circ C)}{R_Z + R_{Cu}(0^\circ C) \cdot \frac{\alpha + \beta \cdot T_K}{\alpha + \beta \cdot T_K(0^\circ C)}} \\ &= \frac{\frac{R_Z}{R_{Cu}(0^\circ C)} + 1}{\frac{R_Z}{R_{Cu}(0^\circ C)} + \frac{\alpha + \beta \cdot T_K}{\alpha + \beta \cdot T_K(0^\circ C)}} \\ &= \frac{\frac{R_Z}{R_{Cu}(0^\circ C)} + 1}{\frac{R_Z}{R_{Cu}(0^\circ C)} + -0.21127 + 0.0044348 \cdot T_K} \end{aligned}$$

At this stage the ratio $\frac{R_Z}{R_{Cu}(0^\circ C)}$ is unknown, however we may initially assume R_Z to be zero, and thus obtain the maximum possible effect due to coil resistance changes.

Thus if we plot, relative to the values at 0°C, the change in signal intensity A due to probe Q changes =

$$\frac{Q(T_K)}{Q(0^\circ C)} = \frac{\alpha + \beta \cdot 273.13}{\alpha + \beta \cdot T \Delta K}$$

and the change in signal intensity due to the change in the Boltzmann factor =

$$\frac{B(T_K)}{B(0^\circ C)} = \frac{273.13}{T_K}$$

then we obtain figure 26.

Hence we see that the change due to the probe coil resistance dominates at low temperatures, but the two effects are very similar near room temperature.

7.3.3 Density changes.

It is important to remember that the NMR signal is proportional to the number of resonant nuclei in the sample, i.e. to the mass of the sample of constant composition, while for porometric information we usually require the pore volume.

Clearly, as the measurements are taking place below the bulk melting point of the liquids, no density information is available other than by extrapolating the values from above the bulk melting point.

One possible way of obtaining measured density information for the liquid in the pores, above and below the bulk melting point, is to use small angle neutron scattering, as the initial slope (for r below the first structural peak) of $d(r)$ depends directly on the density $\rho_0(r)$ [Newport et al., 1988], where :

$$d(r) = 4\pi r \cdot (\rho(r) - \rho_0(r))$$

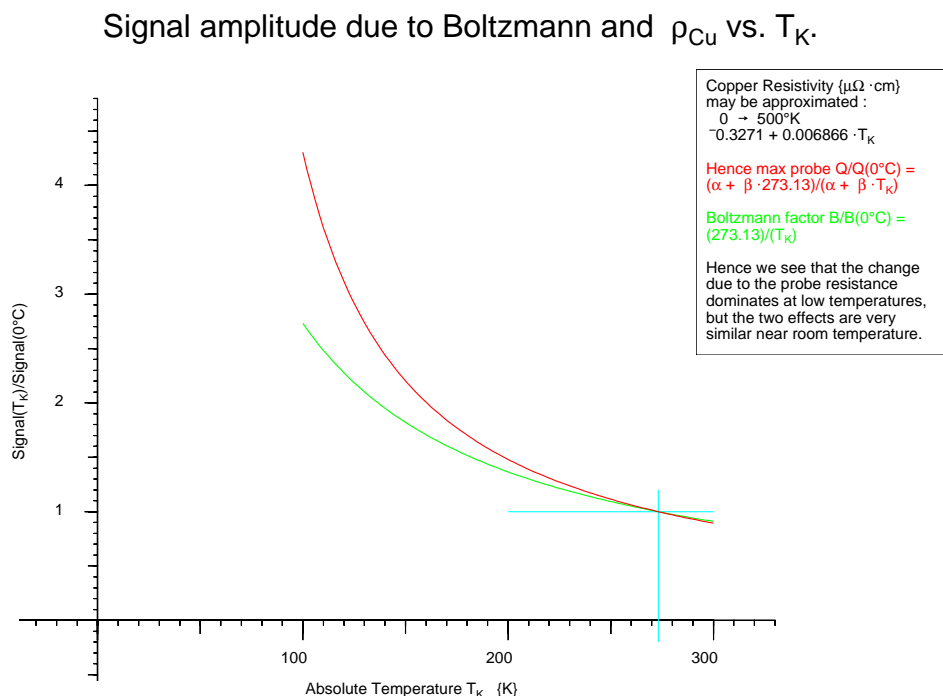


Figure 26: Amplitude changes, as a function of T_K , due to the Boltzmann effect (green line) and the resistivity of the copper sample coil (red line).

An alternative method (that has been shown, as part of this work, to be of good sensitivity) is to use neutron scattering to measure the first structural peak, due to nearest neighbour separations. Fitting this gives sufficient accuracy to follow density variations as a function of temperature.

However one problem with measuring the first structural peak only, is that this measures inter-atomic changes; we wish to know the inter-molecular changes, which may not vary in the same way with temperature. Thus ideally it is preferable to measure peaks at larger radii.

7.3.4 Calibration of volumetric temperature coefficient.

A bulk sample of low freezing point liquid, such as isopentane, has been used to assist with the calibration of system sensitivity as a function of temperature [Strange et al., 1993].

In this work a sample of n-pentane (M.P. -129.72°C) doped with the free-radical 'TEMPO' (2,2,6,6-Tetramethyl-1-piperidinyloxy, Sigma T7263) has been used with success to compensate for Boltzmann and Q change effects when using the gas flow cooling system

(chapter 5.3).

The free-radical was added to reduce the T_1 relaxation time of the pentane from some seconds, to a value that remained at a fraction of a second over the full temperature range, thus ensuring that, at the repetition time of about four seconds, there was negligible variation in the measured signal amplitude due to T_1 relaxation changes.

When using the gas flow cooling system the signal amplitude was then found to vary with temperature in a manner that was consistent with that expected from chapter 7.3.2 and to be very stable with time.

The best-fit value for the ratio $R = \frac{R_Z}{R_{Cu}(0^\circ C)}$ over the temperature range $-50^\circ C$ to $25^\circ C$ was found to be 1.26; the residual plot for the corrected pentane signal showed a slight fall off by $-100^\circ C$, the curve being well fitted by the cubic polynomial in temperature $T\{^\circ C\}$: $1.000_8 + -2.022_8 \times 10^{-4} \times T + -2.64_1 \times 10^{-6} \times T^2 + 7.0_9 \times 10^{-8} \times T^3$

Hence we have obtained a value for our one unknown in chapter 7.3.2, such that

$$\frac{Q(T_K)}{Q(0^\circ C)} = \frac{R+1}{R + \frac{\alpha + \beta \cdot T_K}{\alpha + \beta \cdot T_K(0^\circ C)}} \approx \frac{510}{214 + T_K} \approx \frac{273.13}{115 + 0.536 \cdot T_K}$$

Thus we may apply corrections for Boltzmann and for Q changes due to sample coil resistance changes with temperature, using these coefficients, with the routine *nmrbqcor*. When doing so for the results in chapter 9, we find that the plateau from the signal above the bulk melting point (from all the melted liquid) is, after the above correction, consistently flat (within reasonable experimental error), see figure 27.

This then allowed for reliable calibration of the system volumetric sensitivity, for each run, by measuring the signal amplitude of this plateau (extrapolating to the measured bulk melting point in case of any residual slope) and using the measured mass of total liquid in the sample (see appendix D).

However when performing repeated runs with the Lindacot cooling system [Norris and Strange, 1969] (chapter 5.1) the temperature dependence of the NMR probe sensitivity was found to slowly increase over a number of runs. This was attributed to a build up of water in the probe, due to fine ice crystals being carried over with the liquid nitrogen droplets. It was then necessary to remove the sample and heat the probe to $120^\circ C$, and allow it to dry overnight. With the gas flow system, the ice remains in the 25l dewar, and the evaporated nitrogen gas is very dry; this then serves to dry the NMR probe.

Thus with the Lindacot system the procedure adopted was first to apply the Boltzmann

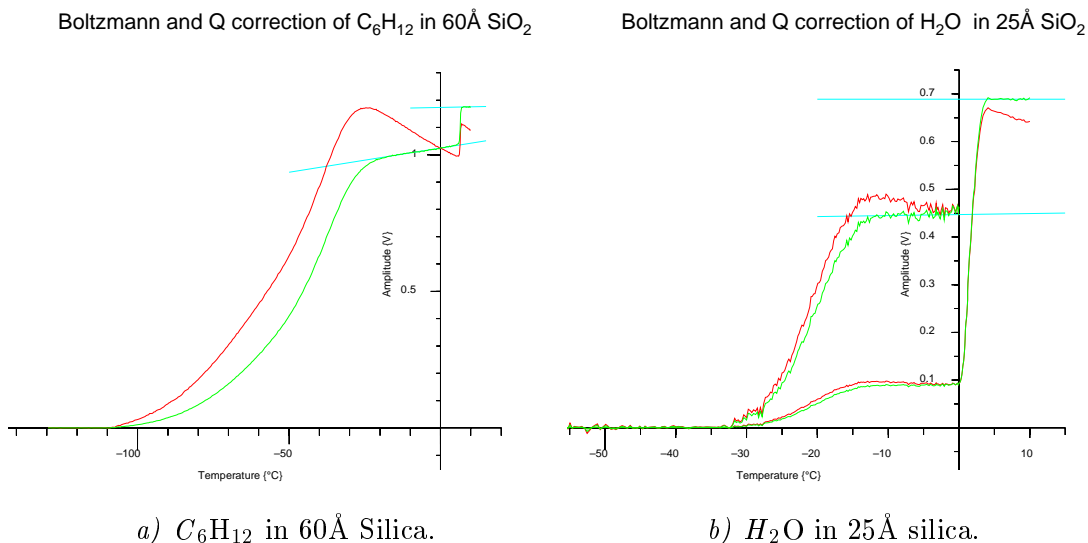


Figure 27: Signal intensity from a) cyclohexane in 60\AA Unilever silica, b) water in 25\AA Sigma silica, before (red) and after (green) correction of Boltzmann and sample coil resistance effects.

and Q corrections as above, and then if there was a residual negative slope for the bulk plateau, to calibrate the temperature dependence of each run, fitting the temperature dependence of the signal from bulk plateau (see appendix D), and extrapolating the correction to lower temperatures.

Since this sensitivity calibration (for either system) was performed for each run, using the known mass of total liquid in the sample as a reference, it gave a direct conversion from measured signal E.M.F. {Volts} to mass of cryoporometric liquid {g}, and hence using standard values for the density of the liquid, to measured values for the pore volumes {l}.

7.3.5 NMR relaxation effects on volumetric calibration.

Sensitivity variations due to T_1 changes were in the main avoided by repeating sufficiently slowly, and, although there is then a trade-off between signal to noise and relative pore volume calibration within a pore size distribution, runs were performed with a sufficiently slow repeat time (usually 4s to 10s) that this was not considered a problem. (The data transfer from the oscilloscope to the computer limited the capture rate to 1 trace every four seconds.) When preparing samples a repetitive freeze/pump/thaw cycle (commonly used when measuring relaxation times to remove dissolved paramagnetic oxygen) was deliberately not used, to keep the T_1 lower, and increase the signal averaging available.

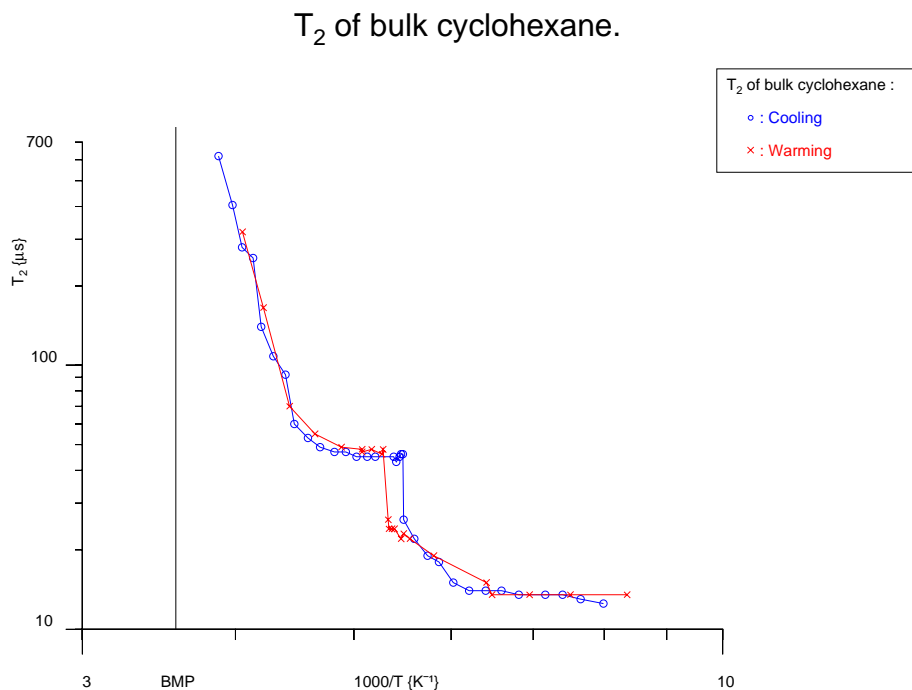


Figure 28: Measured T_2 of cyclohexane in the bulk, on warming and on cooling.

There is little problem in discriminating between bulk water and ice, as there is a large change in T_2 as the ice melts. With cyclohexane the situation is not so simple, as cyclohexane has both a rigid lattice structure at low temperature (with a very short T_2) and a plastic crystal phase (with a T_2 that is of the order of one millisecond just below the melting temperature) (see figures 28, 29).

As the T_1 and T_2 of bulk liquid cyclohexane is typically about one second, the amplitude of the echo as a function of time is only limited by diffusion; thus there is in principle little problem in distinguishing between solid (plastic) cyclohexane and bulk liquid cyclohexane, using a 2τ time of between say 4ms and 40ms, when the signal from the plastic phase will have decayed, but that from the liquid will be little affected. As we shall see, we will wish to use the shorter times in the smaller pores, but the longer one when measuring in large pores at temperatures that are very near the bulk melting point (where the plastic phase has the longest decay time).

The main remaining problem, that has a substantial effect on the correct calibration of measured pore volume, is due to the change of T_2 of the liquid and the solid from its value in the bulk, to that found in pores.

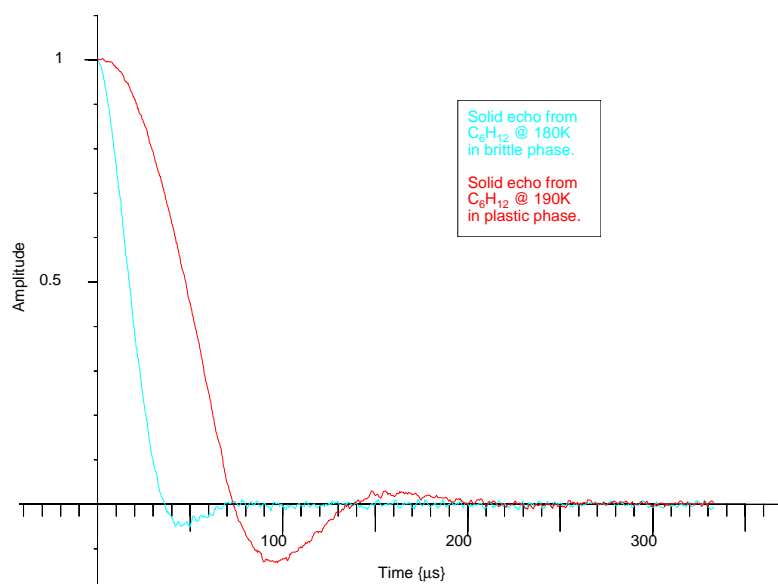
Solid echo from bulk C_6H_{12} in brittle and plastic phases

Figure 29: Solid echoes from bulk cyclohexane in the brittle and plastic phases.

Exhaustive work has been performed, measuring the T_2 of water and cyclohexane in sol-gel silica pores (both fully and partly filled) [Booth and Strange, 1998, Allen et al., 1997, 1998]. There is much further work to do in the case of other porous structures.

For fully filled pores (which pertains to the current work} one may summarise the main effects in larger sol-gel silica pores as being : A) a surface relaxation at the pore wall, that, by rapid exchange within the pore, results in a reduced T_2 for the liquid in the pore (this effect is increased if there are paramagnetic materials in the pore walls); and B) diffusion effects in field gradients due to susceptibility variation in the porous structure (this effect is increased if there is say iron in the pore wall).

These effects modify the relaxation of the liquid in the pore; however the longer percolation time required to reach the bulk liquid around the grains results at short τ in little reduction for the T_2 of this bulk liquid. (We may indeed then make further deductions regarding this percolation path distance).

In small partially filled pores the process is complicated by the tendency for the liquid/solid to actually form a disordered state, where the T_2 s of the liquid and solid tend towards one another, but the work in this thesis is restricted to fully filled pores.

In principle it might be possible to go from the measured T_2 values to the deduced cryoporometric behaviour, as a function of 2τ time; in practice the route that was followed (as the above T_2 results were not available at the time this work was performed) was to directly perform cryoporometric measurements on reference sol-gel silicas filled with water or cyclohexane, at a number of different 2τ times (chapters 7.5, 7.4).

NMR relaxation effects.

For sol-gel silica measured using cyclohexane, if we examine a typical melting point curve (figure 27a), we see that after the above Boltzmann and Q corrections, the bulk plateau has nearly zero slope, but the plateau from the liquid in the pores has a definite positive slope. This could be attributed to melting in very large pores, but it is far more probable that the slope is due to an increase in the T_2 of the liquid in the pores as the sample warms. (If it were due to a contribution from the signal from solid, we would expect a far more rapid change in slope near the bulk melting point – see figure 28).

We have a question then as to what the correct volumetric normalisation is, as a function of pore size, for such a material. This is particularly acute with regard to measuring the median pore size, as for this we need to have a value for the total pore volume (which we wish to divide by two).

If we believe that the slope of the plateau reflects the change in T_2 , and that this may be extrapolated to lower temperatures, then we conclude that if we project a line of half the amplitude (and half the slope) until it intersects (a smoothed line through) the melting point curve, this will then be a melting point that can be transformed using the Gibbs-Thomson equation (2) to give the true median pore diameter.

NMR diffusion effects : pore gradients.

If on the other hand we examine the Boltzmann and Q corrected plateau between the liquid melting step in the pores and the bulk melting step for cement, we see that rather than having a positive slope as in the silica case, it is now negative. We may explain this if we remember that these materials have large internal gradients, due to iron in the pore walls and susceptibility effects. This produces diffusional gradient attenuation of the NMR signal. Thus, as the pore liquid becomes warmer, the diffusional rate increases, and as a result the NMR echo becomes more attenuated.

The solution in both the above cases is to use a Carr-Purcell-Meiboom-Gill sequence – in the diffusional case it will mitigate the effect of diffusion, and in both cases it will allow the establishment of a T_2 corrected amplitude. We note, however, that in general we will have bulk liquid as well as liquid in the pore, and thus we must use the technique given in the next section.

7.3.6 Corrections for T2 relaxation.

Provided 2τ is sufficiently short that exchange between the pore and bulk liquid is negligible on the timescale of the experiment, but sufficiently long that spin-locking effects are negligible (these conditions are satisfied for the $2\tau = 4\text{ms}$ to 40ms times used in this work), we may perform cryoporometric measurements at a number of different 2τ times, and correct for the loss of magnetisation in the pore liquid. We may thus obtain accurate values for the volume of the pores, both in total and as a function of pore diameter.

In appendix E we show that even if the pore liquid and bulk liquid have different relaxation times, we may measure the ratio of the pore to total signal $\frac{V_{PL}}{V_{TL}}(t)$ and plot $\frac{1}{\frac{V_{PL}}{V_{TL}}(t) - 1}$ to obtain a function with a single decay time and a y intercept of α , and may then write for the pore volume :

$$v_P = \frac{1}{\rho_L} \cdot \frac{M_{TL}}{1 + \frac{1}{\alpha}} \quad \{l\}$$

where we have measured the total mass of the liquid in the sample M_{TL} and know the liquid density ρ_L .

Using the data obtained for the cryoporometric calibrations (chapters 7.4, 7.5) we may plot figures 37, 38, and thus deduce the true normalised total pore volume of the various silicas (table 7).

This allowed calibration of the cryoporometric constants, and provided direct information on regions of operation where self consistent results could be obtained. It was noticed in particular with water that considerable loss of signal intensity (as a result of T_2 attenuation) could be tolerated, without significantly changing the measured melting point, and hence measured pore size (see chapter 7.5.4).

7.4 Calibration of melting point depression of cyclohexane in porous silica.

7.4.1 Sample preparation.

16 samples were made using 8 different porous silicas from a number of sources, of nominal pore diameter 40Å, 60Å, 100Å, 140Å, 200Å and 500Å, making two samples of each silica.

The Unilever (A) 60Å, 200Å and 500Å had been characterised by Dr. D.Ward of Unilever by gas adsorption as having the following pore diameters, the mean values being used for calibration purposes :

Silica	Adsorption	Desorption	Average
C60	52.0 Å	46.5 Å	49.3 Å
C200	222.1 Å	180.7 Å	191.4 Å
C500	491.8 Å	419.1 Å	455.5 Å

Table 4:

Pore diameters for Unilever (A) silica samples as characterised by gas-adsorption.

The pores were filled with anhydrous cyclohexane in a dry glove box; for all these samples the filling factor of the cyclohexane exceeded 100% – i.e. there was excess cyclohexane outside the pores in the intergranular space; this was confirmed later by checking that there was a step in the cryoporometric melting curve due to bulk liquid. Weighings were made of empty tubes + caps, then with the dried silica, then with the added liquid; then the samples were flame sealed (see chapter 6).

7.4.2 Cryoporometric measurements.

89 cryoporometric runs were made using these samples. i.e. the amplitude of the NMR echo at 2τ was measured as a function of the sample temperature, using a thermocouple soldered to a copper foil wrapped around the sample, while the sample was slowly warmed from a state of all liquid frozen to all liquid melted.

Measurements were made with 2τ values of 4ms, 10ms, 20ms and 40ms, to determine the effect that the liquid T_2 had on the results – shorter times were difficult to measure, due to the tendency of the residual FID following the 180° pulse to extend into the echo time; for longer τ times the echo suffered undue attenuation due to T_2 decay.

Some measurements were also made at different values of warming rate; most of the measurements were made with a warming rate of $0.5\text{C}^{\circ}\cdot\text{min}^{-1}$, being as slow a rate as could be reliably used with the Lindacot liquid nitrogen injection cooling (see chapter 5.1), without temperature reversals becoming common; some measurements were made at $1.0\text{C}^{\circ}\cdot\text{min}^{-1}$ and $0.2\text{C}^{\circ}\cdot\text{min}^{-1}$ for comparative purposes.

7.4.3 Melting point depression calculation.

The melting point curves were corrected for receiver gain compression (chapter 7.2), for the Boltzmann variation of magnetization with temperature (chapter 2.3), and receiver coil resistance with temperature (chapter 7.3.1); the bulk melting point found interactively, and the median melting point determined :

A interactive routine, *mpdsteps*, was written in *Apl68000* to read in turn from file all those data sets that matched the sample directory and name templates, convert the raw thermocouple readings to temperature (using a 17 part 7th order polynomial fit to the latest ITS90 thermocouple tables from the National Bureau of standards), apply receiver gain compression corrections (not really necessary) using the routine *nmrrxcor*, perform Boltzmann and receiver coil Q corrections using the routine *nmrbqcor*, save the data and graph it to the screen (see appendix D).

For a given (overfilled) sample of porous silica, as the temperature rises, the melting point curve rises to a plateau when all the liquid in the pores has melted; there is then a further rise to a new plateau when the bulk liquid in the inter-granular void space melts.

Six cursor positions were then read, allowing the user to mark the start and end temperatures of the two plateau and of the step. Each section was then linearly least square fitted, and used to derive a measured value of bulk melting point for a particular sample and warming rate. The plateau were then extrapolated to this bulk melting point, to give the amplitudes of the signal from the liquid in the pores and of all the liquid in the sample (due to a measured mass of liquid).

The ratio of the total liquid in the sample to the (maximum possible) liquid in the pores is then the liquid filling factor; for these measurements where fully filled pores were used, this filling factor was then always in excess of 100%. (The few samples where it was less than 100% were rejected from the measurement process, as these would not then reflect the true pore diameter.)

This procedure gave melting point curves whose bulk plateau were very close to horizontal; however the plateau due to melted liquid in the pores in many cases had positive slopes, presumably due to T_2 changes in the liquid cyclohexane as a function of temperature. To get the true median pore size for a given silica, we need to correct for this; thus a line with half the amplitude and half the slope of the fit to the pore plateau was generated. A band of the melting point distribution around where this half amplitude line intersected the melting point distribution was fitted with a line, and the solution of the precise intersection of the half amplitude line and this fitted line found.

If the variable *Coefs* is a two row two column array, each row containing the coefficient of a line, then we may use the *Apl* expression $X \leftarrow - \div / -/[1] \text{ Coefs}$ to obtain the X value of the intersection of the lines, giving the median melting point depression of the distribution.

This was repeated for all the pore size distributions containing good data.

For $2\tau = 4\text{ms}$, and at a warming rate of $0.5\text{C}^\circ \cdot \text{min}^{-1}$ for the larger pore diameter silicas, and $1\text{C}^\circ \cdot \text{min}^{-1}$ for the smaller ones (due to the time involved in warming over the wider temperature range), we obtain for the median melting point depressions as a function of nominal pore diameter the 34 results plotted in figure 30.

From this it can be seen that the results for each type of silica are for the most part tightly clustered. We see that the Unilever (B) results are clearly distinct from the Unilever (A) results (for at least the 60\AA and 200\AA silicas); thus it is inappropriate to use the Unilever (A) nominal pore diameters for the Unilever (B) silicas; hence we exclude the Unilever (B) data from the fit. Even if we also exclude the 40A Merck silica, as their results fall far off the best fit line, we still find that this best fit line has a Y intercept that is 2.3 degrees above zero.

Since the bulk melting point for each measurement had been adjusted to better than 0.1C° , this is at first surprising. A way of correcting this behaviour is to introduce curvature to the fit; early in this project, when examining such melting point depression curves, it was noticed that the large pore diameter silicas were well fitted by a straight line, but that the departure seemed to increase for small pore diameter silicas. Thus rather than use a simple quadratic fit of constant curvature, it was proposed that the melting point depression might be represented by a modified Gibbs-Thomson equation of the form :

$$\Delta T = \frac{k}{x-2 \cdot Sl}$$

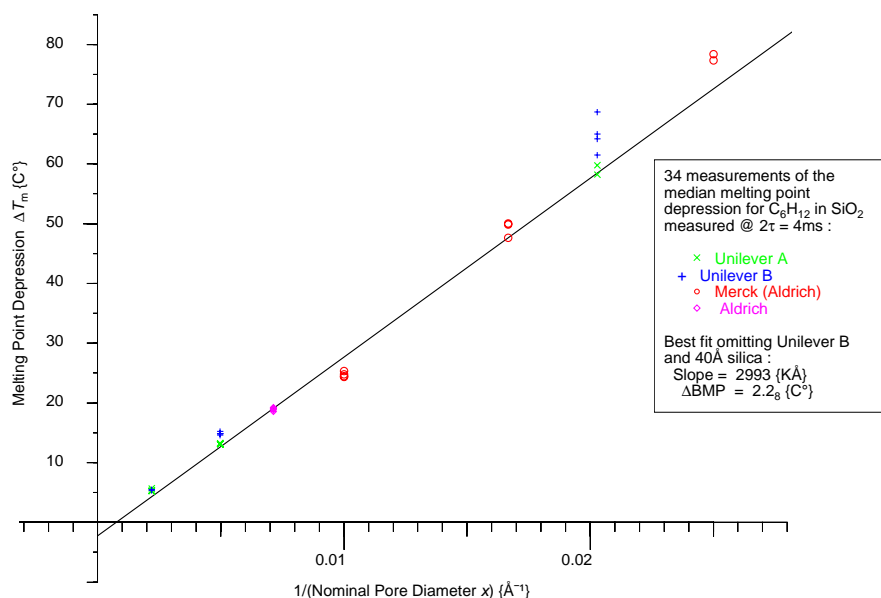
Melting point depression for C_6H_{12} in SiO_2 for $\tau = 2ms$ 

Figure 30:

Measured median melting point depression for cyclohexane in 8 different porous silicas, for $2\tau = 4ms$, plotted against inverse nominal pore diameter – linear fit.

i.e. that the melting crystal behaved thermodynamically as though it had a radius that was less than that measured by gas adsorption by an amount $Sl = SurfaceLayer$.

On discussion, such a modified equation appears to have found some favour, and has been employed in work published elsewhere [Hansen et al., 1996, Jehng et al., 1996].

If we employ such an equation, and adjust the surface layer such that a straight line fit passes through the origin we obtain, for $2\tau = 4ms, 10ms, 20ms, 40ms$ figures 31, 32.

Thus we see such an equation does indeed model the data well. However reservations must be expressed regarding the physical interpretation, since we see from the constants required for these fits (table 5) that the so called surface layer thickness is τ dependent.

There is no apparent way that the effective radius and hence thermodynamic melting properties could depend on the NMR measurement time scale; probably what we are seeing is a result of T_2 changing more in small pores [Booth and Strange, 1998], in a way that is just consistent with the modified Gibbs-Thomson equation. None the less this equation is a convenient method of modeling the non-uniform curvature with just one extra parameter.

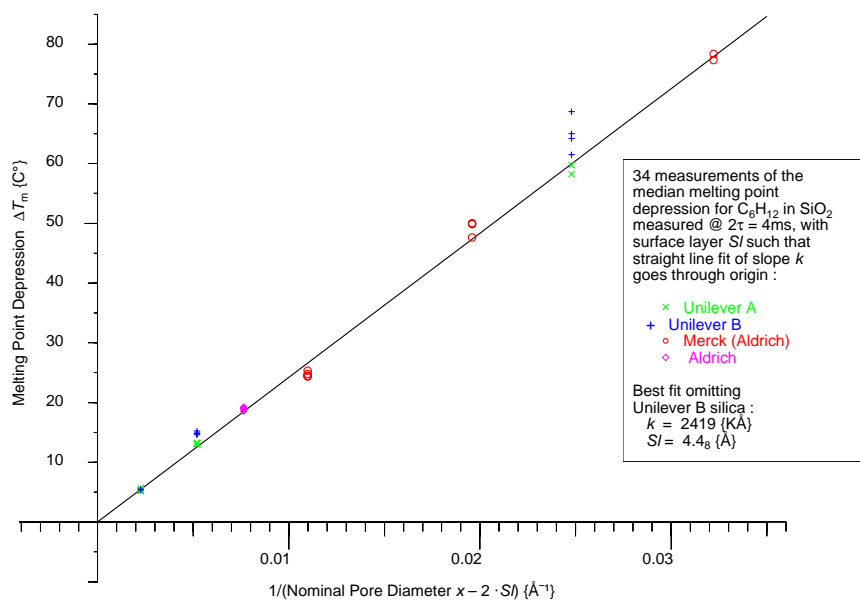
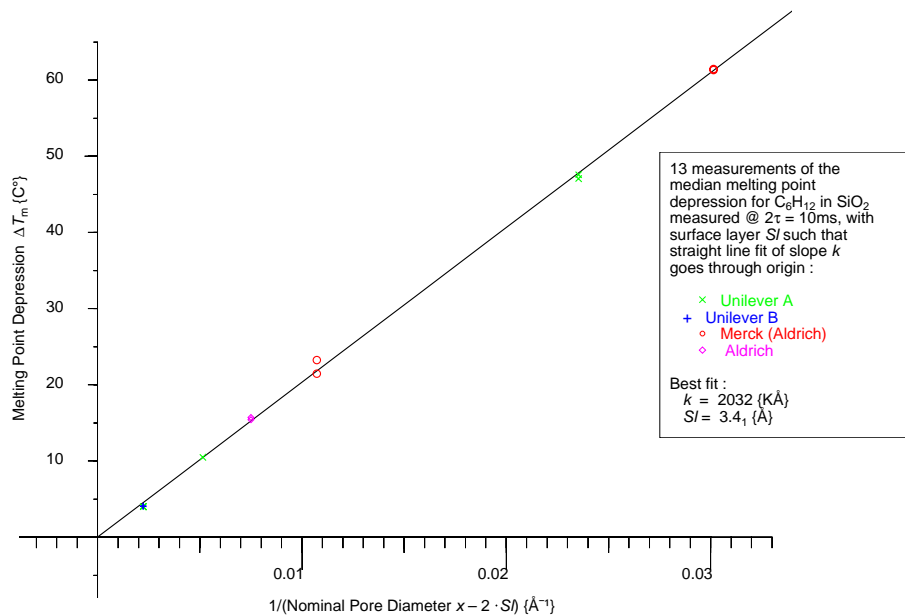
Melting point depression for C_6H_{12} in SiO_2 for $\tau = 2ms$ Melting point depression for C_6H_{12} in SiO_2 for $\tau = 5ms$ 

Figure 31:

Measured median melting point depression for cyclohexane in porous silica, @ $2\tau = 4ms$, $10ms$, plotted against inverse (nominal pore diameter - $2 \times$ surface layer); i.e. fitted to a modified Gibbs-Thomson equation.

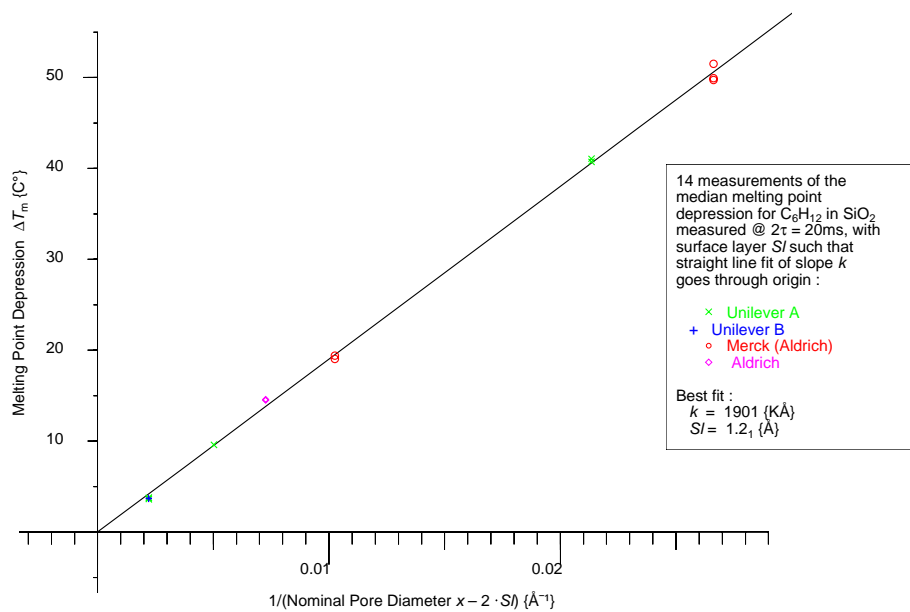
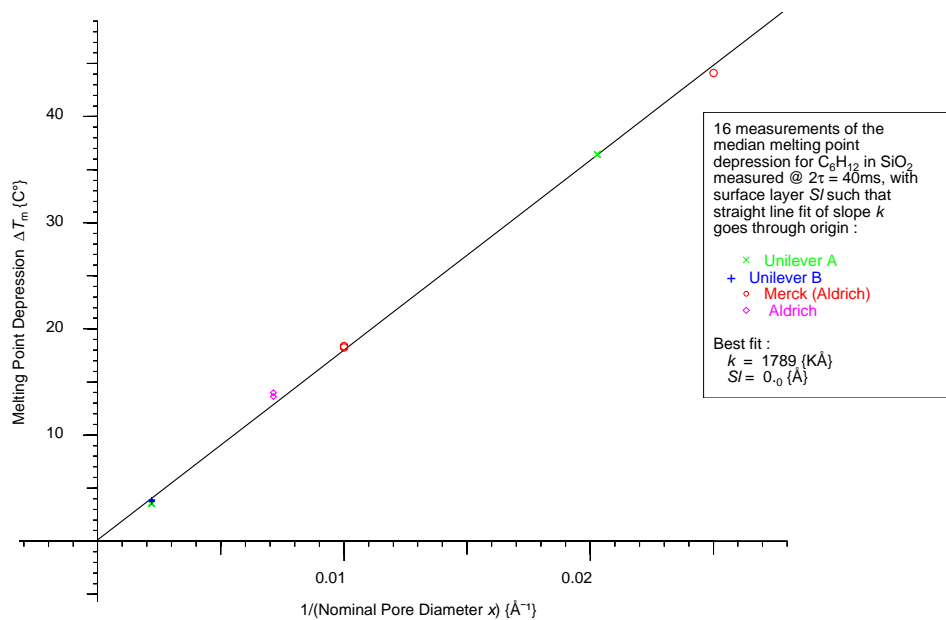
Melting point depression for C_6H_{12} in SiO_2 for $\tau = 10ms$ Melting point depression for C_6H_{12} in SiO_2 for $\tau = 20ms$ 

Figure 32:

Measured median melting point depression for cyclohexane in porous silica, @ $2\tau = 20ms, 40ms$, plotted against inverse (nominal pore diameter $- 2 \times$ surface layer); i.e. fitted to a modified Gibbs-Thomson equation.

2τ {ms}	k {KÅ}	Sl {Å}
4	2419	4.47 ₆
10	2032	3.40 ₇
20	1901	1.21 ₄
40	1789	0.00 ₀

Table 5: Slope k of melting point depression, and surface layer Sl , for cyclohexane in sol-gel silica, measured at time 2τ .

We see that the slope k of the melting point depression is dependent on τ . Graphing this dependency, we find that it varies inversely with a fraction power of τ ; thus we generate a log-log graph of k vs. τ (figure 33). Fitting this we deduce that for cyclohexane in porous sol-gel silica

$$k \approx 1627 + 1256.6 \cdot \tau^{-0.68_0}$$

We conclude that we have obtained a calibration for the melting point depression of cyclohexane in sol-gel silica, valid when measuring at 2τ from 4ms to 40ms, and that we may measure down to at least 40Å in pore diameter with good calibration.

Slope k variation with τ for C_6H_{12}

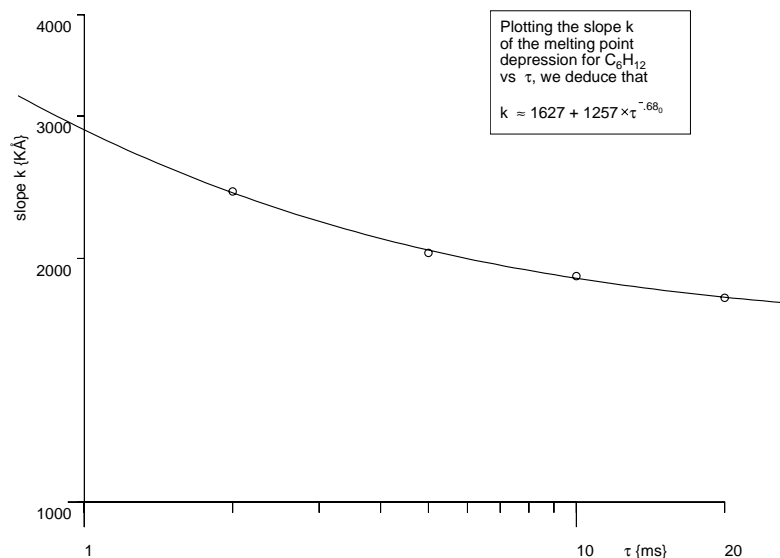


Figure 33: Slope k of melting point depression for cyclohexane in porous silicas, as a function of τ .

7.5 Calibration of melting point depression of water in porous silica.

7.5.1 Sample preparation.

20 samples were made using 10 different porous silicas from the same sources as for the cyclohexane calibration, of nominal pore diameter 25Å, 40Å, 60Å, 100Å, 140Å, 200Å and 500Å, making two samples of each silica. The Unilever (A) 60Å, 200Å and 500Å had been characterised by Dr. D.Ward of Unilever by gas adsorption; from the cyclohexane calibration we may deduce approximate values for the Unilever (B) silica :

Silica	Unilever (A)	Unilever (B)
C60	49.3 Å	46.3 ± 1.5 Å
C200	191.4 Å	171.5 ± 2.5 Å
C500	455.5 Å	453 ± 5 Å

Table 6: Pore diameters for Unilever (A) silica samples as characterised by gas-adsorption, and for Unilever (B) silica as deduced from cyclohexane cryoporometry. The uncertainty quoted for Unilever (B) silica is just the RMS scatter in the measured results using the cyclohexane calibration.

The pores were filled with filtered, reverse osmosis exchanged deionised water, which was shewn to have a conductivity of about 10% of the available singly distilled water; for all these samples the filling factor of the water exceeded 100% – i.e. there was excess water outside the pores in the intergranular space; this was confirmed later by checking that there was a step in the cryoporometric melting curve due to bulk water. Care was taken not to greatly overfill these samples, as otherwise the expansion of the water on freezing shatters the tubes.

Weighings were made of empty tubes + caps, then with the dried silica, then with the added water; then the samples were flame sealed (see chapter 6).

7.5.2 Cryoporometric measurements.

108 cryoporometric runs were made using these samples. i.e. the amplitude of the NMR echo at 2τ was measured as a function of the sample temperature, using a thermocouple soldered to a copper foil wrapped around the sample.

Measurements were made with 2τ values of 4ms, 10ms, 20ms and 40ms, to determine the effect that the water T_2 had on the results – shorter times were difficult to measure,

due to the tendency of the residual FID following the 180° pulse to extend into the echo time; for longer τ times the echo suffered undue attenuation due to T_2 decay.

Some measurements were also made at different values of warming rate; most of the measurements were made with a warming rate of $0.5\text{C}^\circ\cdot\text{min}^{-1}$, being as slow a rate as could be reliably used with the Lindacot liquid nitrogen squirt cooling (see chapter 5.1), without temperature reversals becoming common; some measurements were made at $1.0\text{C}^\circ\cdot\text{min}^{-1}$ and $0.2\text{C}^\circ\cdot\text{min}^{-1}$ for comparative purposes.

7.5.3 Melting point depression calculation.

The interactive routine *mpdsteps* was used to analyse these results, as in the case for the cyclohexane calibration.

For $2\tau = 4\text{ms}$, and for $0.5\text{C}^\circ\cdot\text{min}^{-1}$ (for all but the 25\AA pore diameter silica, due to the time involved in warming over necessary wide temperature range), we obtain the 61 results plotted in figure 34.

From this it can be seen that the results for each type of silica are for the most part tightly clustered.

If we do a linear least squares fit we obtain a best fit line with a slope of $573 \{\text{K}\cdot\text{\AA}\}$.

The results are clustered fairly close to the best fit line; there is no noticeable deviation even for the 25\AA nominal pore diameter silica. Thus we conclude that any surface layer effect must be less than 0.5\AA . Other workers report a surface layer of 1.75\AA for water [Hansen et al., 1996].

7.5.4 The effect of pore size dependent T_2 .

The cryoporometric melting curves for values of τ greater than 2ms show that for the smaller values of pore diameter there is a progressive loss of signal intensity due to the shorter values of the liquid T_2 in the pores, to the point where measurements of the melting point depression are of reduced accuracy in say 40\AA pore diameter silica with $2\tau \geq 20\text{ms}$ (figure 35).

None the less, if we plot the values that we can obtain (figure 36), we obtain values for 60\AA and greater pore diameter that are in good agreement with the values measured with $2\tau = 4\text{ms}$.

We conclude that the results we obtain using water in pore diameters of 50\AA and greater are not highly sensitive to the value of τ chosen. Unless there is some other reason that

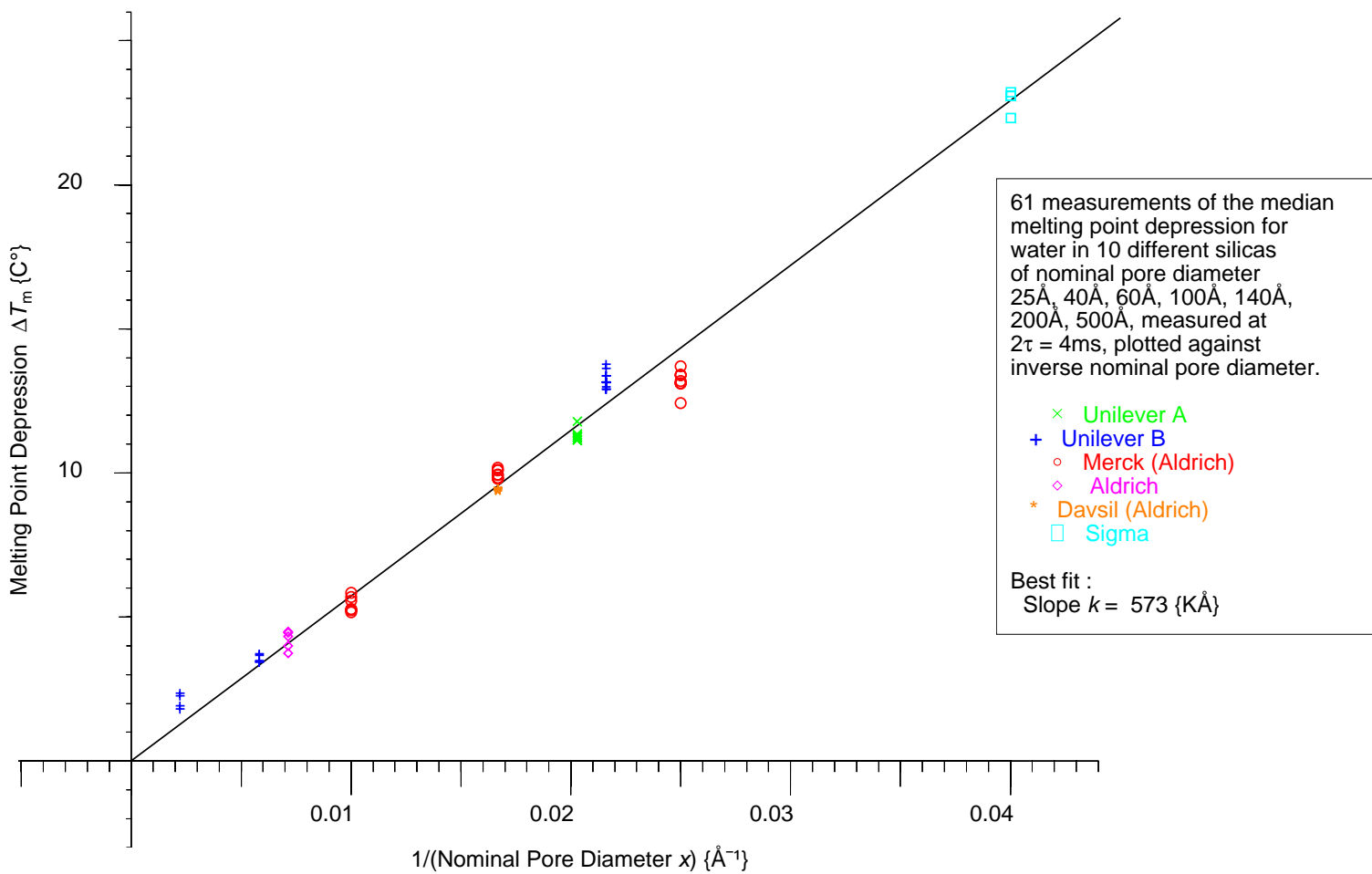
Melting point depression for H₂O in SiO₂ for $\tau = 2\text{ms}$ 

Figure 34:

Measured median melting point depression for water in 10 different porous silicas, for $2\tau = 4\text{ms}$, plotted against inverse nominal pore diameter.

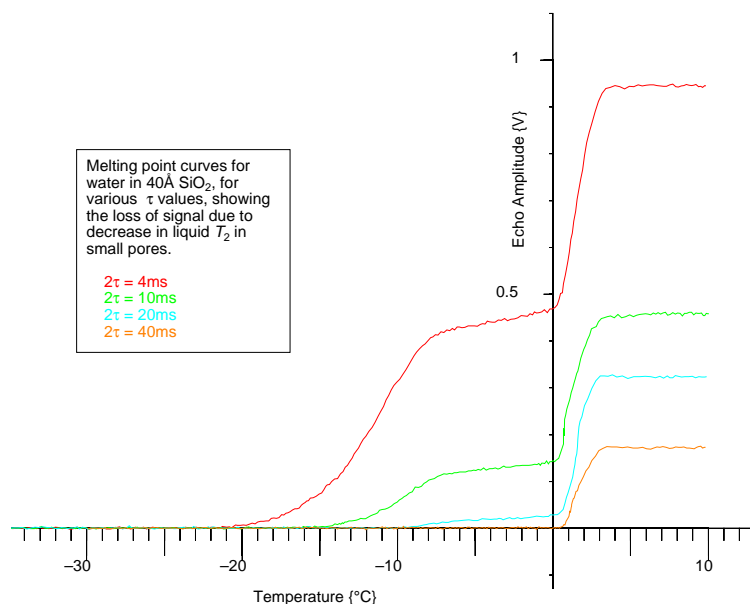
Melting point curves for water in 40Å silica vs. τ .

Figure 35: Melting point curves for water in 40Å silica, for various τ values, showing effect of short T_2 in small pores.

precludes its choice (such as an anomalously short T_2), 2ms is thus a good value to choose for τ , as the pore diameters obtained are in not in disagreement with those from longer values of τ , and in silica glasses at least, a wide range of pore diameters (down to at least 25Å) can be measured without the reduction of the liquid T_2 in the small pores noticeably affecting the results.

7.5.5 Calibrated porosity measurement.

We have seen that for water at least, down to 50Å pore diameter, the measured median pore size is relatively independent of the measuring τ , over the range $2\tau = 4\text{ms}$ to 40ms. What is clearly more dependent on τ is the apparent porosity, as measured at one particular value of τ . The following procedure was used to generate porosities corrected for signal loss resulting from T_2 decay.

For a given (overfilled) sample of porous silica, as the temperature rises, the melting point curve rises to a plateau when all the liquid in the pores has melted; there is then a further rise to a new plateau when the bulk liquid in the inter-granular void space melts.

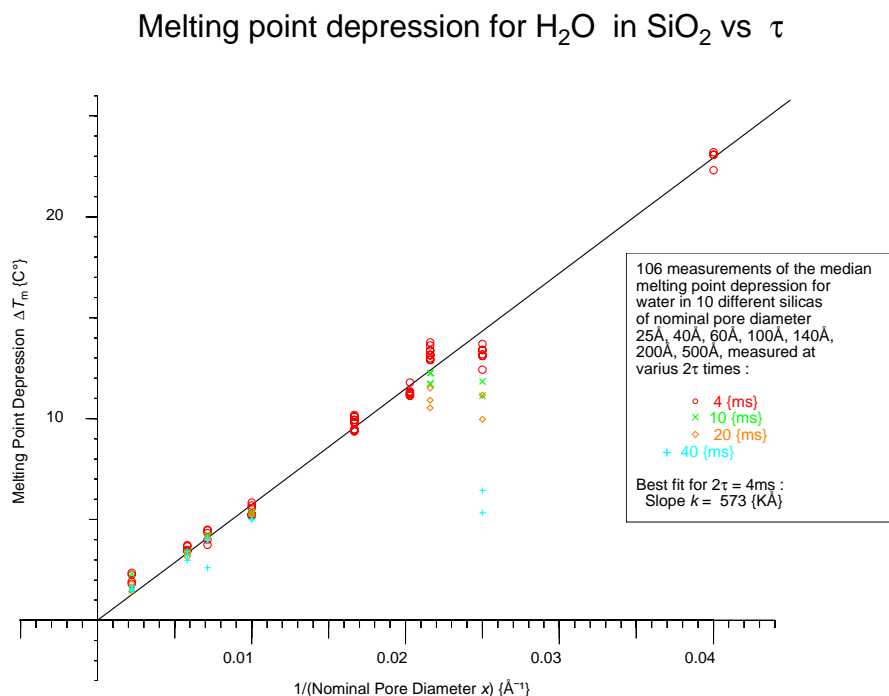


Figure 36: Median melting point depression for water in porous silica, for $2\tau = 4\text{ms}$, 10ms , 20ms , 40ms . Straight line is the best fit line for $2\tau = 4\text{ms}$.

Thus the interactive routine *mpcstep* (see appendix D) was used to measure the amplitude of the plateaus and then extrapolate them to the measured bulk melting point, to give the amplitudes of the signal from the liquid in the pores and of all the liquid in the sample (due to a measured mass of liquid).

The ratio of the total liquid in the sample to the (maximum possible) water in the pores is then the liquid filling factor; for these measurements where fully filled pores were used, this filling factor was then always in excess of 100%.

Since the routine *mpcstep* is passed the measured mass of the dry porous matrix and the mass of added liquid, it then calculates volumetric melting curves, normalised to the dry matrix mass, from which the routine *mpc2psd* calculates pore volume as a function of pore diameter using the Gibbs-Thomson relation 2 (chapter 3.1).

This routine employs a routine *monotonic* that applies a constraint that the signal from the melting liquid should only increase monotonically as the temperature increases – this provides a remarkable increase in signal to noise, and ensures that the differentiated signal (and hence pore volume) can not go negative due to noise.

As we have seen in figure 35, the filling factor and pore volumes as measured above will

be incorrect if there is relaxation due to T_2 , as the relaxation will be greater in the water in the pores than in the bulk liquid.

If however we perform cryoporometric measurements at more than one τ value, and plot the log of the inverse of $1 - \text{filling factor}$, i.e. of $\frac{V_{PL}}{V_{BL}}(2\tau)$, against 2τ , for these measurements of water in silica we obtain figures 37, 38.

Thus although the measured signal depends on the signal from bulk liquid and from pore liquid, which have different T_2 s, if we adopt the protocol in chapter 7.3.6 and appendix E, we obtain relationships with a single exponential decay (see figures 37, 38).

If we denote the y intercept on these graphs $\alpha = \frac{V_{PL}}{V_{BL}}(0)$, we may then write for the normalised pore volume (i.e. per gram of dry silica) :

$$v_{Pore} = \frac{1}{\rho_L} \cdot \frac{1}{1 + \frac{1}{\alpha}} \cdot \frac{M_{TL}}{M_S} \quad \{l \cdot g^{-1}\}$$

where (appendix E) $M_{TL} = \text{Mass of Total Liquid}$, $M_S = \text{Mass of Silica}$.

Thus we see that there is little change for the larger pore values, such that for 500Å silica $\alpha = \frac{V_{PL}}{V_{BL}}(0)$ falls within the scatter of $\frac{V_{PL}}{V_{BL}}(2\tau)$. However the for small pores the correction obtained by extrapolating the exponential decay back to zero time is substantial (see graph for 40Å silica in figure 37). Such corrections are important when calculating the calibrated volume for pore size distributions.

Silica	α	$1/(1+1/\alpha)$	M_{TL}/M_S	v_{Pore} {ml·g ⁻¹ }
25Å Sigma	0.5892	0.3708	0.919	0.341
40Å Merck	2.254	0.6927	0.853	0.591
60Å Merck	3.168	0.7601	0.930	0.707
60Å UnileverB	3.153	0.7592	1.121	0.677
100Å Merck	2.12	0.6795	1.397	0.950
140Å Aldrich	1.74	0.6350	1.854	1.177
200Å UnileverB	4.09	0.8035	2.093	1.681
500Å UnileverB	4.03	0.8012	1.955	1.567

Table 7: Calculation of the normalised pore volume v_{Pore} for eight porous silicas, from y intercept of ratio α of signal from pore liquid to signal from bulk liquid V_{PL}/V_{BL} , as measured by cryoporometry as a function of 2τ time, and from the ratio of mass of total liquid to mass of silica M_{TL}/M_S .

Thus in table 7 we list $\alpha = \frac{V_{PL}}{V_{BL}}(0)$ as measured from figures 37, 38, the deduced factors $\frac{1}{1+\frac{1}{\alpha}}$, the measured $\frac{M_{TL}}{M_S}$, and hence the calculated normalised pore volumes v_{Pore} (i.e.

τ dependence of measured pore to bulk signal for H₂O in SiO₂

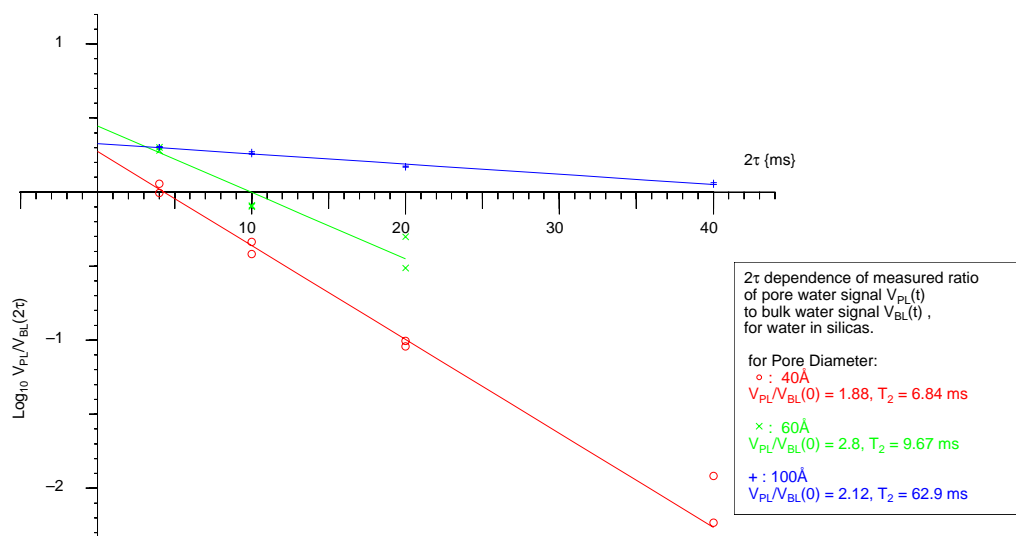


Figure 37:

τ dependence of measured pore to bulk signal for water in 40Å, 60Å, 100Å diameter porous silica.

τ dependence of measured pore to bulk signal for H₂O in SiO₂

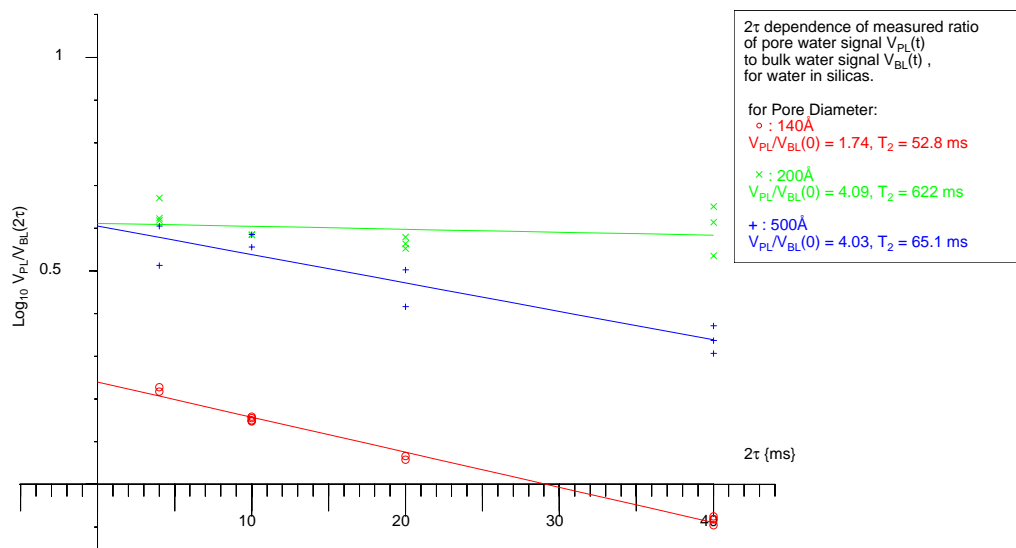


Figure 38:

τ dependence of measured pore to bulk signal for water in 140Å, 200Å, 500Å diameter porous silica.

per gram of dry silica) from the above equation, for eight porous silicas.

For water, the above data is used in chapter 11.5 for the calculations of pore volume, silica filling factor and (voidless) silica matrix density for the various silicas.

It should be emphasised that these graphs only serve to obtain the corrected filling factors for these particular samples; a full study of the effect of both filling factor and relaxation times was not part of this study, though clearly of great importance [Allen et al., 1997, 1998, Booth and Strange, 1998].

It would be possible to obtain the information for this correction in a single cryoporometric run, by measuring the heights of a chain of echoes from a Carr-Purcell-Meiboom-Gill sequence, at each temperature; the current design of the measurement software is not configured for such a measurement as the limited number of points (1008) transferred from the digital scope is a major constraint with the existing apparatus, particularly where signal to noise is of importance.

Chapter 8

Multidimensionally Resolved Pore Size Distributions.

As part of this project a novel method was developed of determining median pore size and pore size distributions as a function of spatial position inside a porous sample. Pore sizes were measured with 1, 2 and 3-dimensional spatial resolution, using NMR cryoporometry in conjunction with magnetic resonance imaging techniques [Strange and Webber, 1995, Strange, Webber, and Schmidt, 1996, Strange and Webber, 1997a,b].

Nuclear Magnetic Resonance was used both as a convenient technique for measuring the fraction that was liquid, deep inside the porous material, and as a way of spatially encoding the pore size density to produce pore size distribution maps and median pore size maps.

8.1 Spatially resolved cryoporometry.

The frequency of the NMR signal is proportional to the magnetic field in which the nuclei are precessing (chapter 2.2).

Thus the addition of space encoding magnetic field gradients to the sample volume allows spatial localisation of the region of sample from which the signal is being produced. Both frequency and phase encoding may be used, with a (multi-dimensional) Fourier transform providing 1, 2 and 3 dimensional localisation of the signal producing regions [Callaghan, 1993].

8.2 1D NMR Cryoporometry.

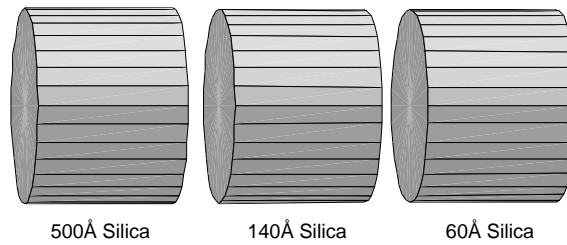
For the measurements with 1 dimensional spatial resolution the spectrometer developed for bulk Cryoporometric measurements was used.

Structured samples were prepared (Fig. 39a), in 5mm diameter tubes, each consisting of three layers of porous silica of 60Å, 140Å and 500Å nominal pore diameter, separated by PTFE spacers (giving no proton signal). Water or cyclohexane was added to the silica, to give approximately 110% filling of the pores. i.e. 10% more liquid was added to the porous media than necessary to just fully fill the pore volume, the excess going to fill the inter-granular space.

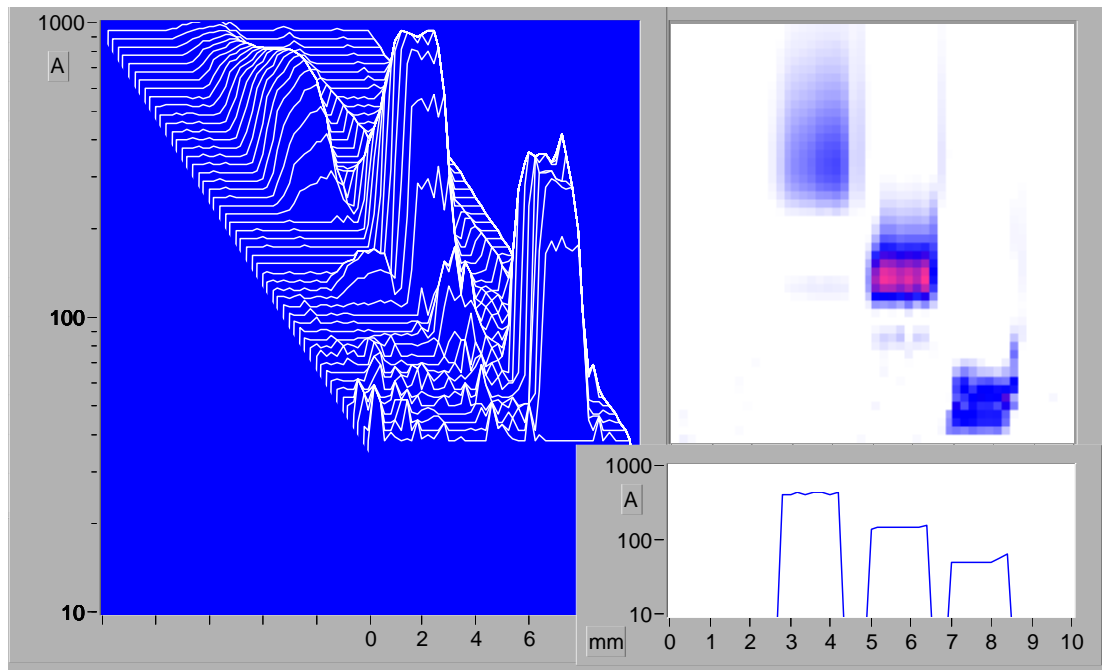
To obtain 1D spatial resolution of the pore size distribution frequency encoding of the NMR signal was used. The main B_0 field was along the Z axis, and a constant magnetic field gradient $G_y = \delta B_z / \delta y$ was applied in the perpendicular Y direction along the axis of the NMR sample tube, to obtain frequency encoding of the axial position. The gradient was generated by four current carrying wires plus return wires, suitably spaced [Kroon, 1968, Rahman, 1991] to minimise all but the linear gradient term G_y .

Since the NMR precession frequency is proportional to the magnetic field B_0 , the frequency of the NMR signal varied linearly with axial position. The space between the magnet pole faces (34mm pole gap) and the Dewar of the variable temperature probe was limited, thus the gradient set was constructed from four one-turn rectangular coils cut from copper sheet, and mounted on drafting film. A DC current of 7A produced a gradient of $0.05 \text{ T}\cdot\text{m}^{-1}$, sufficient to render the magnet's B_0 inhomogeneity negligible. Rather than recording just the peak amplitude of the echo at each temperature as in normal NMR cryoporometry, the complete echo envelope from a $90^\circ_x\text{-}\tau\text{-}180^\circ_y\text{-}\tau\text{-echo}$ sequence was captured. Figure 40 shows the particularly simple sequence, with the static gradient $G_y = \delta B_z / \delta y$. Since the linear field-gradient allows a linear mapping from frequency space to y -dimension, the Fourier transform of the echo in the gradient then gives a 1D profile of the liquid component at this temperature.

The sample temperature was measured with a copper/constantan thermocouple soldered to a grounded copper foil wrapped round the sample, providing temperature uniformity, inside the R.F. coil. (Provided the foil does not form a closed turn it also aids R.F. homogeneity, and hence the ability to obtain precise 90° and 180° precession throughout the sample volume).



(a:) 1D porous silica phantom with axial structure in the y direction.

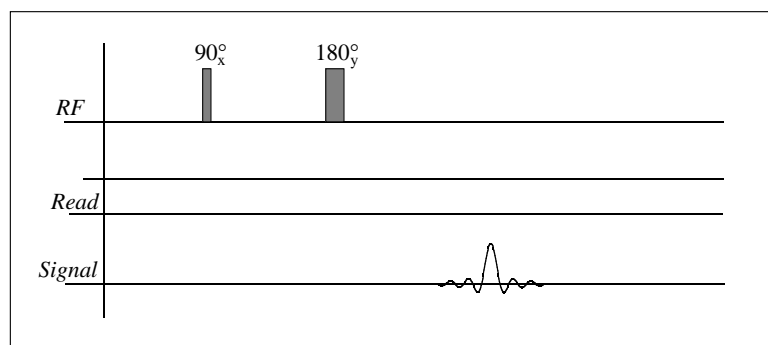


(b:) 1D resolved porosity.

Figure 39: 1D Cryoporometry.

(a) Test sample constructed from layers of 60Å, 140Å and 500Å nominal pore size silica. (b) Measured porosity resolved as a function of axial position ($0 \rightarrow 10$ mm) and logarithmic pore diameter ($40 \rightarrow 1000$ Å). The data is plotted both as a surface plot and as an intensity map.

The lower right graph is a plot of the median pore size as a function of axial position.



1D spin echo sequence with static read gradient $G_y = \delta B_z / \delta y$.

Figure 40: 1D imaging sequence.

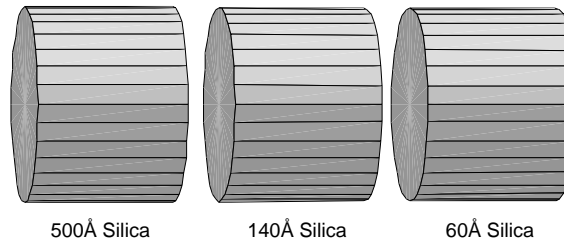
To make a measurement the test sample was cooled until all the liquid was frozen, and there was no signal. It was then slowly allowed to warm naturally at approximately one degree per minute or less. With a sample size of $5 \times 10\text{mm}$ one can estimate the temperature variation over the sample as less than 1C° at -50C° and 0.3C° at 0C° , where the temperature rises much more slowly. The corresponding error in pore size determination is within 5% due to temperature gradients across the sample.

A succession of 1D profiles was captured, averaging 16 times, as the sample warmed. Initially all the sample was frozen, and there was no signal. The liquid in the 60\AA silica melted first, then that in the 140\AA silica, followed by that in the 500\AA silica, and finally any bulk liquid outside the pores.

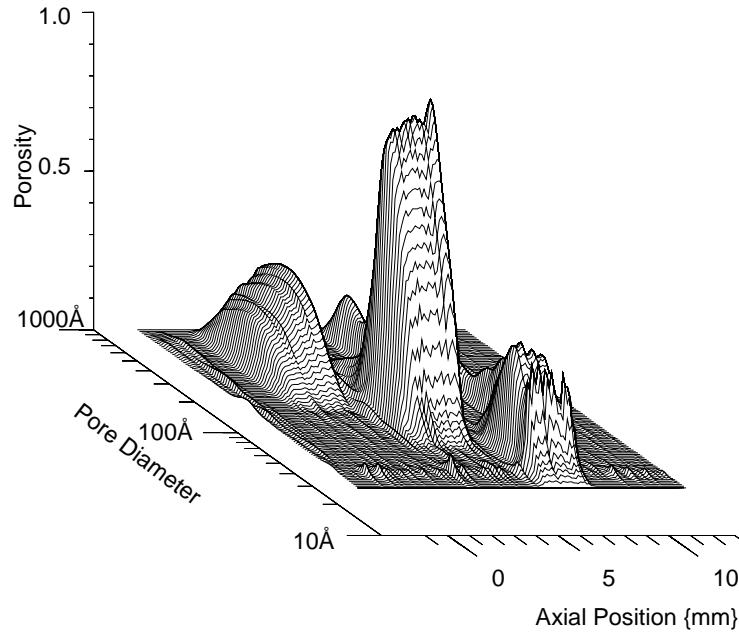
When the temperature run was complete, the data was analysed using LabVIEW (*1dporous*) and Apl (*porous1d*). First the oscilloscope traces were Fourier transformed, and then the standard cryoporometric differentiation and re-mapping according to the Gibbs-Thomson equation was performed along the temperature axis, for each array point in the sample.

This re-mapped data is presented as a surface map, and as an intensity map, in figure 39b, giving the porosity within the sample as a function of pore diameter and axial position. This shows that the porosity is successfully resolved with good spatial resolution and pore size resolution comparable with that from a standard cryoporometry run. The median pore size was also calculated, for each point in the 1D sample (figure 39b, lower right).

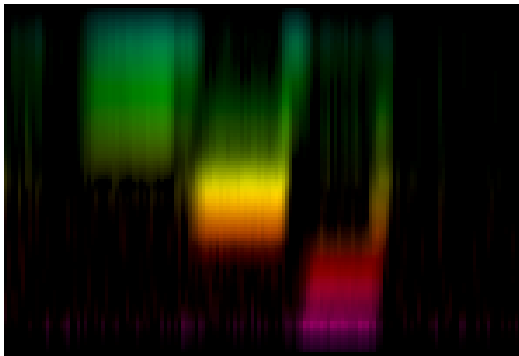
A second measurement was made on a three part sample, as shown in figure 41. As



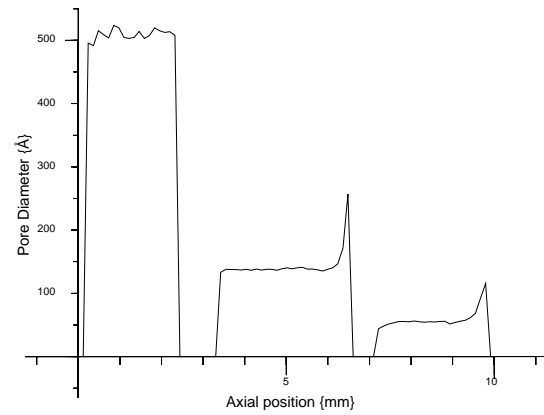
(a:) 1D porous silica phantom with axial structure in the y direction.



(b:) 1D resolved porosity for 3 part phantom.



(c:) Colour map of Pore Size.



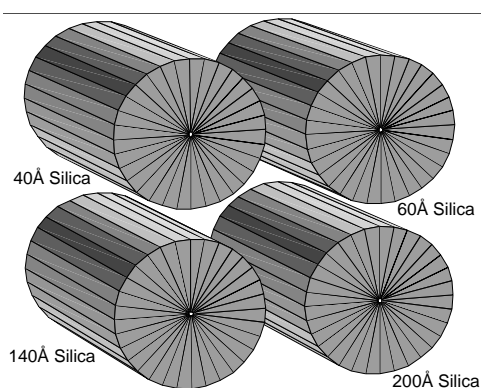
(d:) Median pore size as a function of axial position, for the phantom constructed from nominal 500Å, 140Å and 60Å silicas.

Figure 41: 1D Cryoporometry.

before, as surface map of Log_{10} Pore Diameter vs. Axial Position is shown (figure 41b), as is a colour coded map (figure 41c) and a graph of median pore size (figure 41d), which shows very good agreement with the nominal pore diameters of the silicas used.

8.3 2D Resolved Pore Size Distributions

A test phantom (figure. 42) was constructed with 2D structure, consisting of four 5mm high-resolution thin walled glass tubes, containing 40Å, 60Å, 140Å, and 200Å pore diameter porous silica, arranged in a square array.



2D silica phantom with axial uniformity in the z direction.

Figure 42: 2D Cryoporometry sample with xy porous structure

Anhydrous cyclohexane was added to the dried silica in a glove box under a nitrogen atmosphere, and the tubes evacuated and flame sealed.

The samples were inserted into the neck of the dewar. Silicon grease was used to keep them in thermal contact with a cylinder of Pyrophyllite, used as an insulating thermal mass. A copper/constantan thermocouple was embedded in a hole in the Pyrophyllite cylinder, to allow the temperature to be monitored. The neck of the dewar was filled with foam, to provide additional thermal insulation.

The sample was cooled with liquid nitrogen, and 32 images were recorded as a function of temperature, as the phantom warmed up naturally. At each temperature, a 2 dimensional cross-sectional image of the liquid was obtained using Fourier reconstruction. A single slice of 20mm was selected along the Z direction of the magnetic field using soft pulses. This slice was positioned so as to exclude the silicon grease from the image.

The imaging sequence used (*secho.ppr,ppl*) was modified from being a gradient echo sequence (figure 43a), to one using a $90^\circ_x - \tau - 180^\circ_y - \tau$ -echo sequence (Fig. 43b), with a

2τ of 14ms, as this time was greater than the T_2^* of the wide-bore magnet used and was suitably between the decay time in the solid (up to 2ms) and the decay time in the liquid (100ms). The X Y phasing ensures that the echo maintains the same relative phase as the FID. Here X and Y are understood to cycle round through all combinations of $\pm X$, $\pm Y$ as required by the CYCLOPS [Hoult and Richards, 1975] sequence, preserving their relative orientation.

CYCLOPS phase cycling was used to eliminate D.C. offsets and ghosting due to receiver channel gain differences. The CYCLOPS sequence rotates the basic sequence used through 0° , 90° , 180° , 270° phase offsets: a change of 180° inverts the phase of the signal, thus by subtracting the $\pm X$ and $\pm Y$ signals $I_X - I_{-X}$, $I_Y - I_{-Y}$, one removes any D.C. offset (and hence zero frequency spikes in the image); similarly a rotation of 90° swaps the real and imaginary signals $\Re(I)$, $\Im(I)$ between the receiver U and V channels, thus by adding the resultant X, Y signals one eliminates ghosting due to receiver U and V channel gain (A) differences; finally one has $\Re(I) \cdot 2 \cdot (A_U + A_V)$, $\Im(I) \cdot 2 \cdot (A_U + A_V)$.

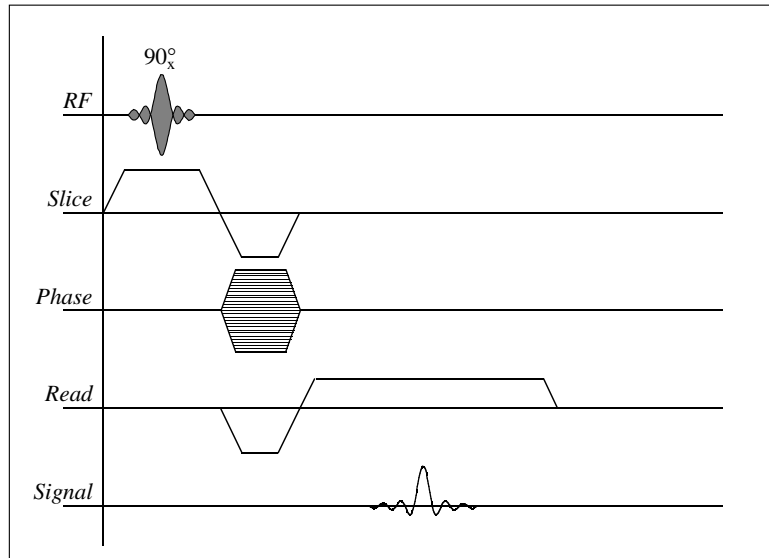
Averaging, with a repeat time of 1 second limited by T_1 , was kept to the minimum of 4 required by the CYCLOPS sequence, giving a slice imaging time of 4.3 minutes .

Data was captured as one read frequency encode (4 times oversampled), and one phase encode, for a resolution of 128×32 , but reconstructed into 32 maps of 64×64 images. Fourier reconstruction of the 2D data sets for each temperature was performed on the Digital Signal Processor of the SMIS console PC.

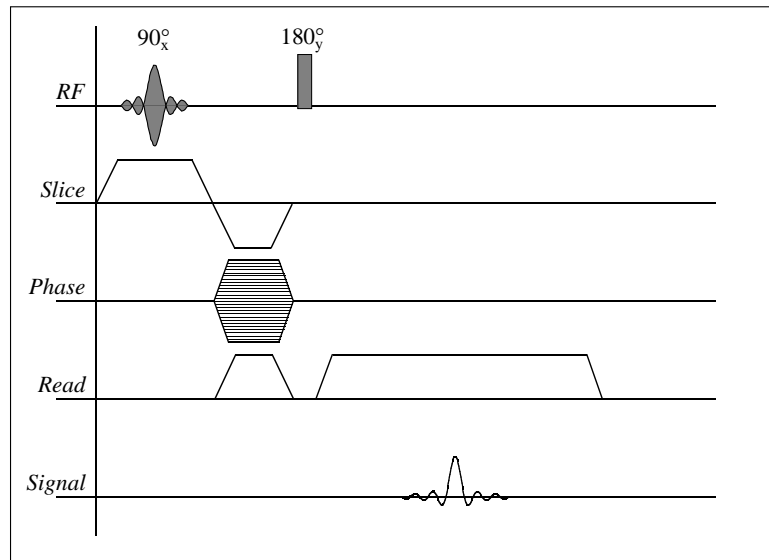
32 images were recorded as a function of temperature, as the phantom warmed up. The resulting $N_X \times N_Y \times N_T$ data set was stored as 32 maps of 64×64 integer images, which occupies 0.5 MByte for the temperature run. This data set was then transferred to an 4 MByte Atari running Mint multitasking and Apl68000, but no floating point accelerator.

Selected images are shown in figure 44 where the sequential melting of the liquid in the 40\AA , 60\AA , 140\AA and 200\AA pore diameter silicas can be seen as the image signal of the liquid.

Applying the constraint along the temperature axis that a noiseless signal should only increase in amplitude as the temperature increases and the sample melts (*monotonic*), gave a marked improvement in signal to noise (figures 44, 45). This is particularly important as the next step in the analysis is differentiation along the temperature axis. The 32 images (averaged in pairs for display purposes) are shown in figure 46. The

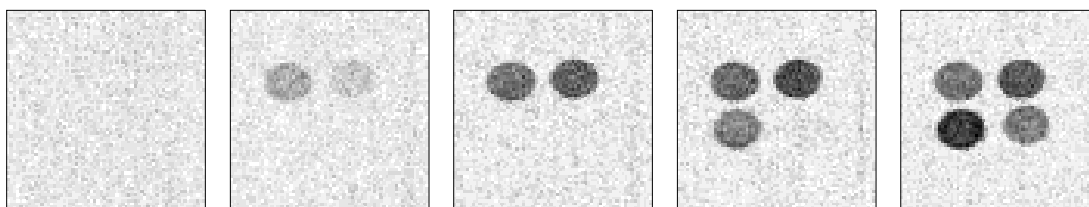


a) 2D gradient echo sequence.



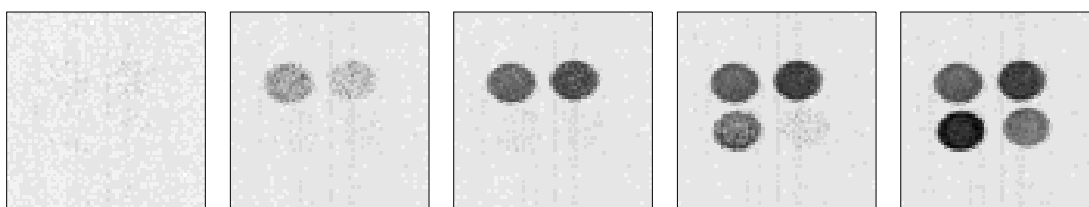
b) 2D spin echo sequence with slice select gradient $G_z = \delta B_z / \delta z$, phase encode gradient $G_y = \delta B_z / \delta y$, and read gradient $G_x = \delta B_z / \delta x$.

Figure 43: 2D imaging sequences.



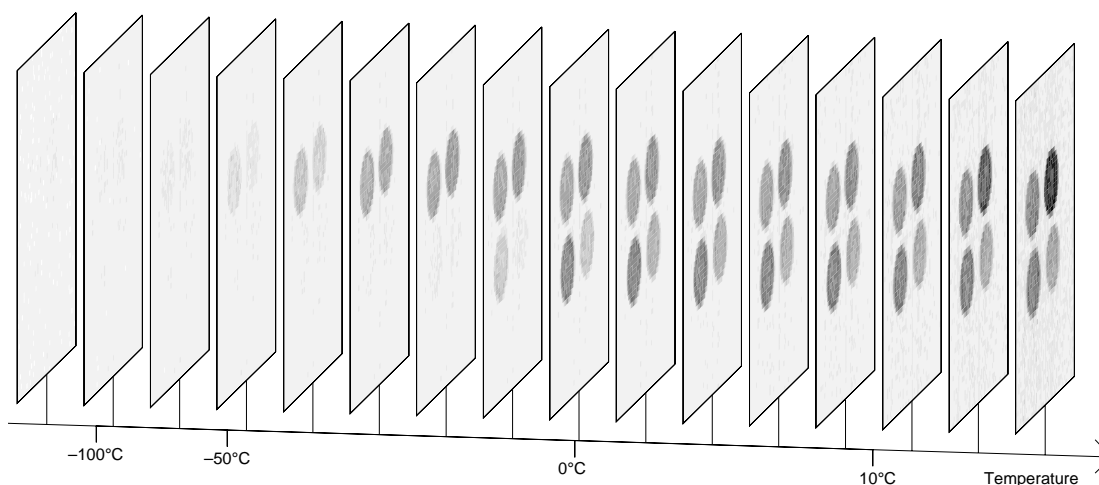
Map 2: $-135^{\circ}C$ Map 9: $-38^{\circ}C$ Map 12: $-22^{\circ}C$ Map 16: $-6^{\circ}C$ Map 20: $5^{\circ}C$
 Raw intensity maps showing the sequential melting of the liquid in the 40\AA , 60\AA , 140\AA
 and 200\AA pore diameter silicas.

Figure 44: Selected intensity maps from the temperature run.



Map 2: $-135^{\circ}C$ Map 9: $-38^{\circ}C$ Map 12: $-22^{\circ}C$ Map 16: $-6^{\circ}C$ Map 20: $5^{\circ}C$
 Improved signal to noise after application of the constraint of monotonicity in melting.

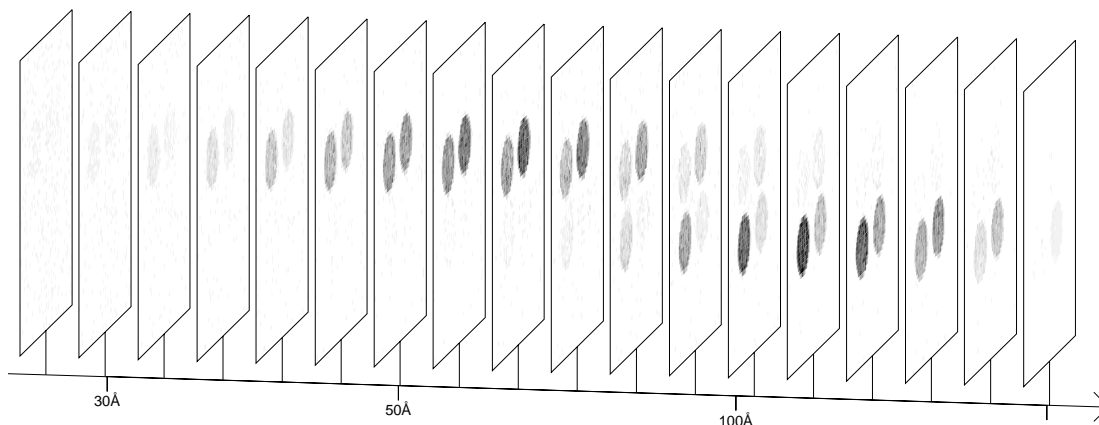
Figure 45: Monotonic intensity maps from the temperature run.



Liquid proton density images showing the melting of the liquid in larger pore sizes at
 higher temperatures.

Figure 46: Liquid Proton Density images vs. Temperature.

cryoporometric differentiation with respect to temperature and re-map according to the Gibbs-Thomson equation was then applied to each xy pixel of the data set in figure 46 (*porous2d*). The resulting porosity maps as a function of pore diameter and xy position are shown in figure 47.



Porosity resolved as a function of pore diameter and xy location, obtained from figure. 46 by cryoporometric differentiation w.r.t. temperature and re-mapping.

Figure 47: Porosity maps vs. Pore Diameter.

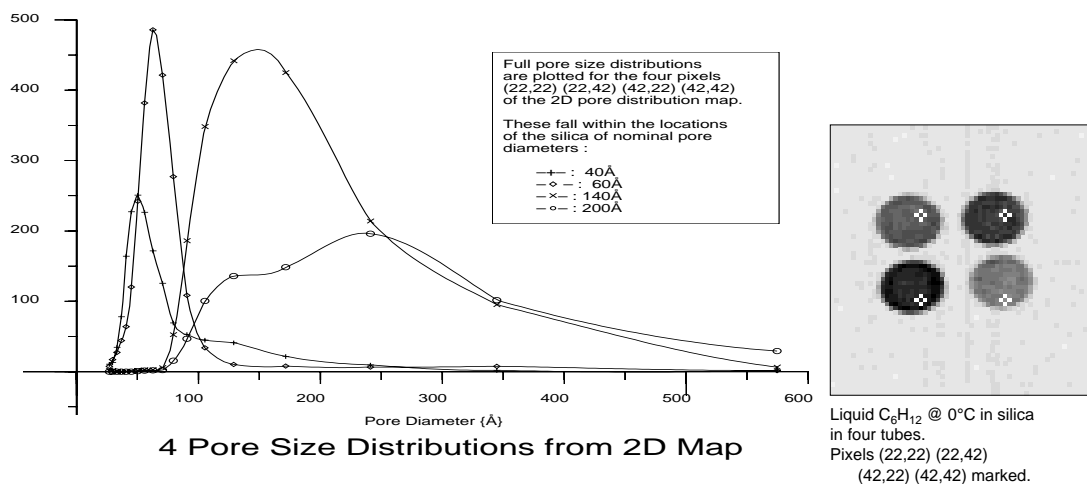
The routine that plots the poresize distribution as a set of angled planes was written in a way that saves filespace and printing time, by deliberately restricting the number of printed shades to 21.

For each plane, the commonest shade is found, by a random sampling, and this is written as the background shade. Then, each row is examined for adjacent patches of the same shade using fast integer vector functions, and if the shade in a row is constant, adjacent rows are examined. The resulting rectangle is saved, unless the shade is the background shade, in which case it is thrown away. For all the planes in the 3D volume, the XY coordinates are converted to Homogeneous coordinates, with the Z coordinate for each plane stepped along from the next. First scaling, then 3D rotations around the Y axis and X axis are applied, before projecting back onto the $Z=0$ plane. The resulting parallelograms are then filled with the appropriate shading.

Axes are generated by the polynomial fitting of graphs of the x -ordinates vs. the corresponding integers, and the resulting polynomial then evaluated at the required ordinates

to generate the axis markings. 3D scaling, rotation and projection generated the appropriate coordinates. Routines that paint on the screen (*plotgm*, *showsur*, *showsax*) and that generate postscript (*psplotgm*, *pshowsur*, *pshowsax*) were written. A naive implementation of the above 18 slice picture would have generated a postscript file 4.4MByte in size; the final one produced is 420kByte, saving creation and printing time in proportion.

It is possible to pick individual pixels from the data structure of figure 47, and plot the full pore size distributions for these pixels. This has been done for the four pixels (22,22) (22,42) (42,22) (42,42) (figure 48). Pore size resolution is comparable with that obtained with standard cryoporometry runs, except at large pore sizes where it can be improved by warming more slowly, thus reducing the thermal gradients that can act to blur the pore size information.



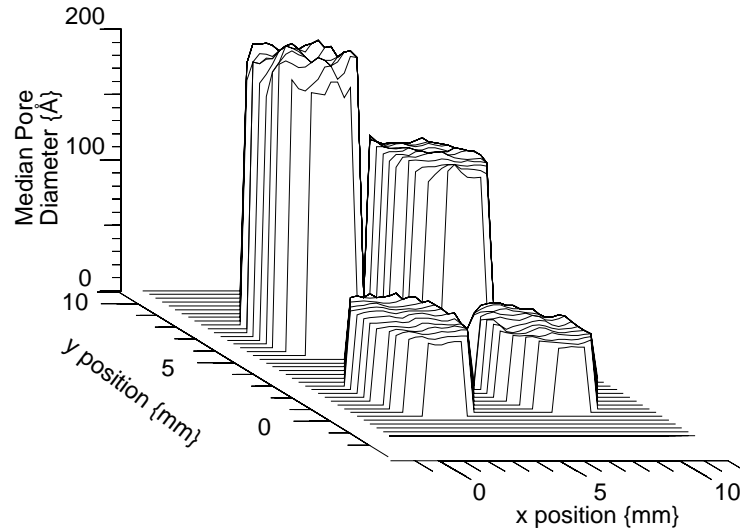
Localised pore size distributions are extracted from the data in figure 47, for four pixels. The peaks of the distributions agree well with the nominal pore sizes.

Figure 48: Localised Pore Size Distributions.

A plot of median pore size for each pixel in figure 47 has also been generated (figure 49). This provides a concise summary of the average pore sizes present, though containing less information. The measured median poresizes correspond closely to the nominal silica pore diameters.

An alternative way of viewing the same information, that may be of use when the sample is less structured, is given in figure 50, where Log_{10} median pore diameter is displayed as colour Hue, with colour Saturation set to 1 and Luminosity set to 0.5 (where Luminosity

= 1 gives all white). (Here colours are viewed in the HLS representation of a double cone, white at the apex, L=1, black at the basal peak, L=0, and saturated colours S = 1 around the waist where the two cones meet.) HLS colours were mapped to RGB (*hlstorgb*) as part of (*i2rgb*), and then a postscript colour map generated using a colour version of the sparse mapper described previously (*psplotcm*).



A map of the Median Pore Size for the four tube phantom, rotated for ease of viewing.

Figure 49: 2D map of Median Pore Size.

8.4 3D Resolved Pore Size Structure

A test phantom with 3D structure was prepared in a 10mm diameter tube, that visually appears to be just 15mm of silica powder in the bottom of the tube.

The sample was actually prepared, using dry 60Å and 500Å nominal pore diameter silica, as follows : about 5mm of 60Å silica was placed in the bottom of the 10mm tube, then 20mm of 60Å silica was placed in a 5mm tube, which was then up-ended and pushed to the base of the 10 mm tube. 500Å silica was added as a collar, to a further depth of about 5mm.

The 5mm tube was then carefully withdrawn, while tapping, hopefully leaving a central column of 60Å silica, the excess then spilling over the 500Å silica, to a further depth of about 5mm. The ideal shape of the 500Å and 60Å silica, ignoring mixing of the dry powders, hand shake, etc. is given in figure 52a. The phantom was then fully dried, and

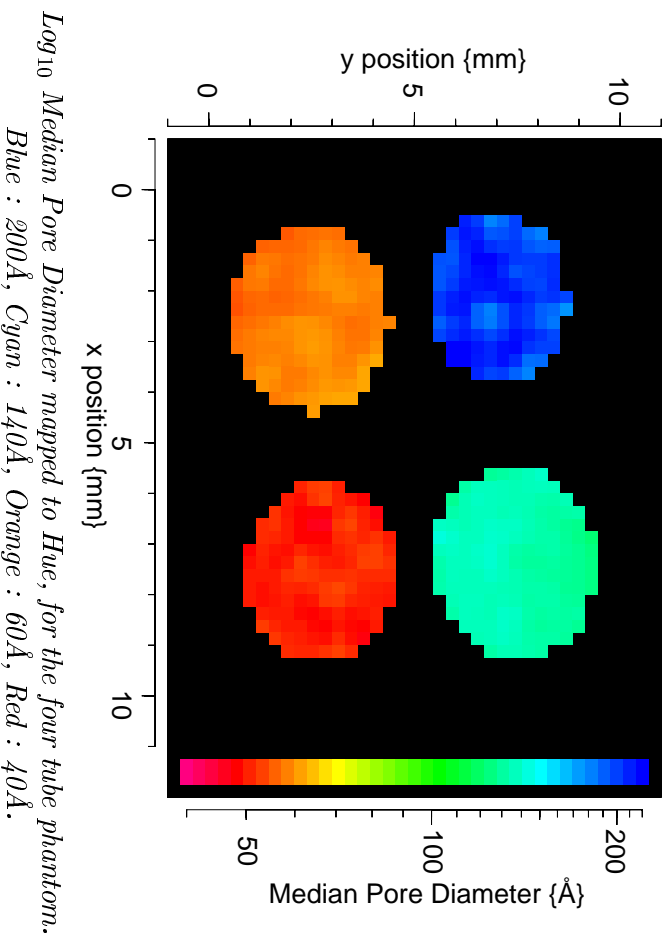
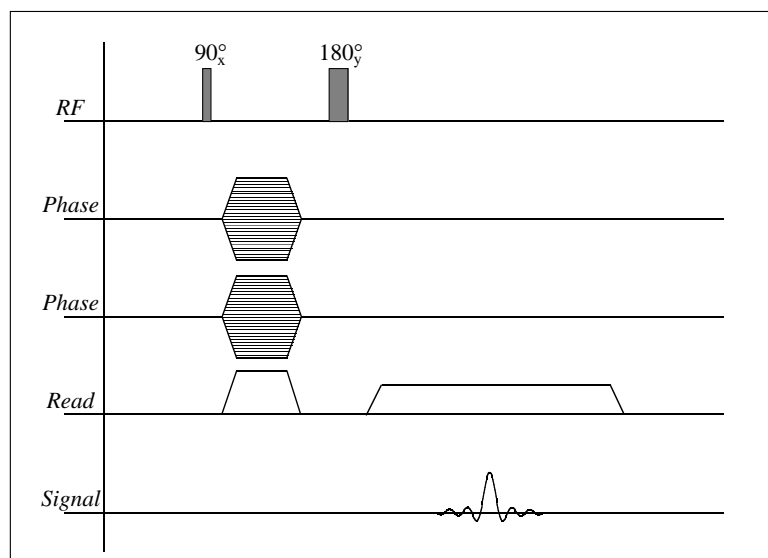


Figure 50: Colour map of Median Pore Size.

anhydrous cyclohexane injected into the silica with a hypodermic needle (to facilitate an homogeneous distribution of the cyclohexane), under dry nitrogen in a glovebox. The phantom was cooled, and 3D image sets captured as a function of temperature. The imaging sequence used (*3d_fse_ppr_ppf*) (figure 51) was a 3D Fourier transform sequence (one read frequency encode, and two phase encodes), for a resolution of $128 \times 32 \times 32$, but reconstructed into $(64 \times 64) \times 32$ slices at each temperature. Again a spin echo sequence was used, with a 2τ of 14 ms, with CYCLOPS phase cycling.

Averaging was kept to the minimum of 4 required by the CYCLOPS sequence; each 3D image data set took about 60 minutes to acquire, with a repeat time of 1 second. As with the 2D case, improvements are required in the control of the sample temperature. The quantity of data required is large if one is to obtain full pore size distributions throughout a 3D volume, as one has to capture a data set $N_X \times N_Y \times N_Z \times N_T$ in size.

For the purposes of this study N_T was restricted to 2, one measurement in a temperature range where the cyclohexane in the 60Å silica was liquid, but that in the 200Å silica was frozen (250°K to 265°K), the other at room temperature. Strictly the latter



3D spin echo sequence with phase encode gradients $G_x = \delta B_z / \delta x$ and $G_y = \delta B_z / \delta y$, and read gradient $G_z = \delta B_z / \delta z$.

Figure 51: 3D imaging sequence.

measurement should have been made just below the bulk melting point of the cyclohexane, to exclude bulk liquid, but the temperature control was at that time not sufficiently precise. (It has since been upgraded, first using a Control and Readout temperature controller, and later a Bruker Variable Temperature Unit.)

A thermal time-constant of some hours, when liquid N_2 was injected into the dewar, facilitated the lower temperature measurement. There is clearly a possible problem with thermal gradients when using such large samples.

The frequency axis was oriented longitudinally, to aid axial positioning of the sample in the magnet bore.

Fourier reconstruction of the 3D data sets for each temperature was performed on the digital signal processor of the SMIS console. The resulting $N_X \times N_Y \times N_Z$ data set at each temperature was set at $64 \times 32 \times 64$, stored as 32 slices of 64×64 integer images, which occupies 0.5 MByte for each temperature.

The data was then transferred to a 4 MByte Atari running Mint multitasking and Apl68000TM, but no floating point accelerator.

A 3-dimensional data set was then obtained for the 500Å silica on its own, using Apl : The data sets were first brought into register (there was noticeable displacement along

the frequency axis). The data set intensities were compared with suitable amplitudes, and a 3D bit array generated for each temperature, and then the following tri-state logical operation performed :

$$\text{Silica500} \leftarrow 1 = (\text{Warm} - \text{Cold})$$

This bit data set, when constructed as a shaded 3D image, gives a very cleanly selected image, but shows the abrupt steps in the logical bits very clearly. Thus the bit data set was used in a multiplicative operation to select the relevant intensities from the original Warm integer data set. Finally a 3D three point smoothing was applied, that performs a Gaussian-like three point smoothing along each of the principle axes, and all of the 3D diagonals. This then generated a 3D data set that the surface rendering could operate on with a minimum of artifacts.

3D rendering was performed using routines written at our laboratory by Tristan Green [Green, 1994], for an M.Sc.

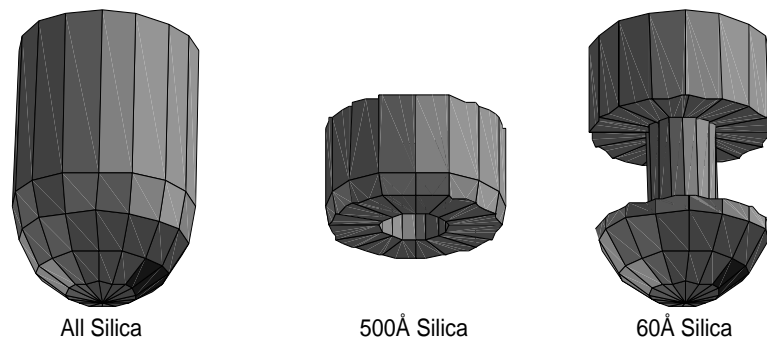
These routines can be compiled for any UnixTM host, and were run on a PC running Linux, with XV as a viewing window. The images were generated into a 512×512 window, and cropped. Three point 2D smoothing was applied, with a 24bit colour table. Colour postscript images were generated (figure 52b). The left hand image is of all the silica powder, with no discrimination. The middle image shows just the 500Å silica, the right hand image is of just the 60Å silica. The linear features mark where silica powder has been displaced by the hypodermic needle.

It is possible to view the 3D data sets from any direction; a view from below the sample shows the collar of 500Å silica more clearly (Fig. 52c).

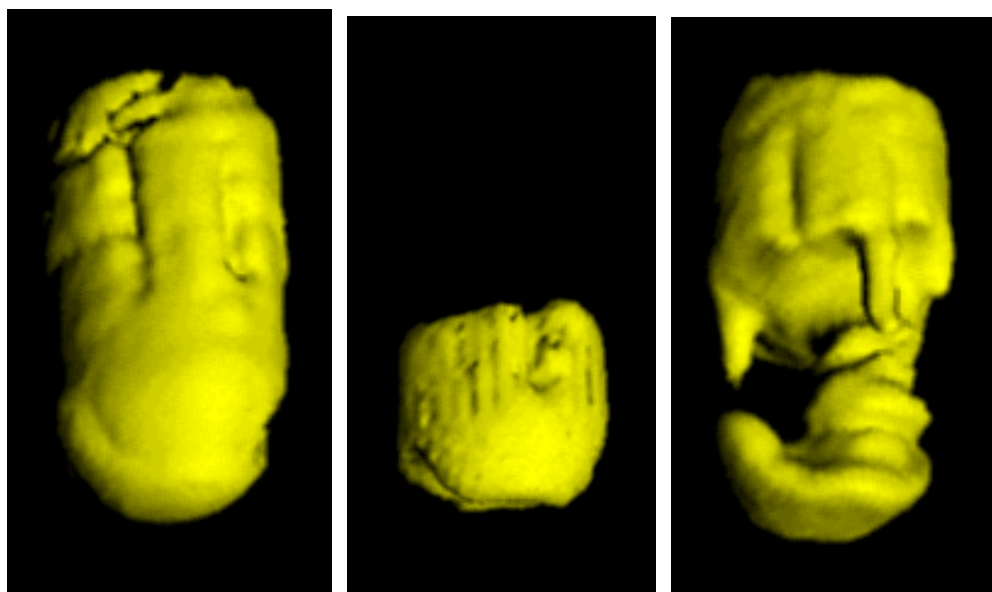
A second sample was constructed in a similar manner, except that the cyclohexane was allowed to diffuse in over a few days, rather than being injected. A similar set of measurements was performed, as shown in figure 53.

This ability to take a porous solid and to generate images of just those regions whose pore sizes fall within a particular range is a novel capability that must have wide applications in physical, chemical and biological studies. We have since gone on to apply the technique to imaging the pore structure of faulted rock cores.

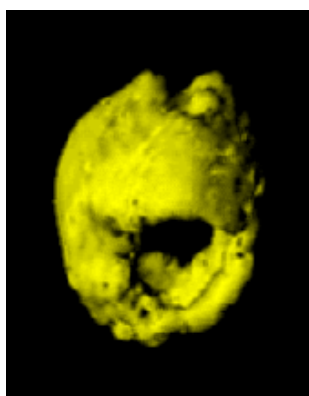
To perform a full 3D pore size distribution run would require the ability to maintain the temperature stable to a fraction of a degree for the time to acquire each full 3D data set (currently 1 hour, though other imaging sequences could reduce this).



(a:) *Idealised 3D Structure of 500Å plus 60Å silica phantom.*

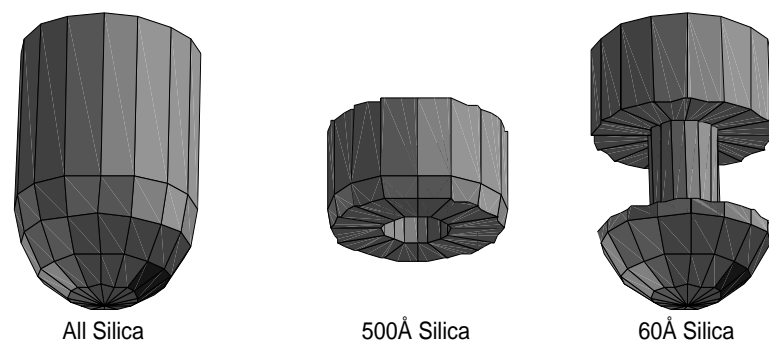


(b:) *3D resolved Pore Size Structure.*

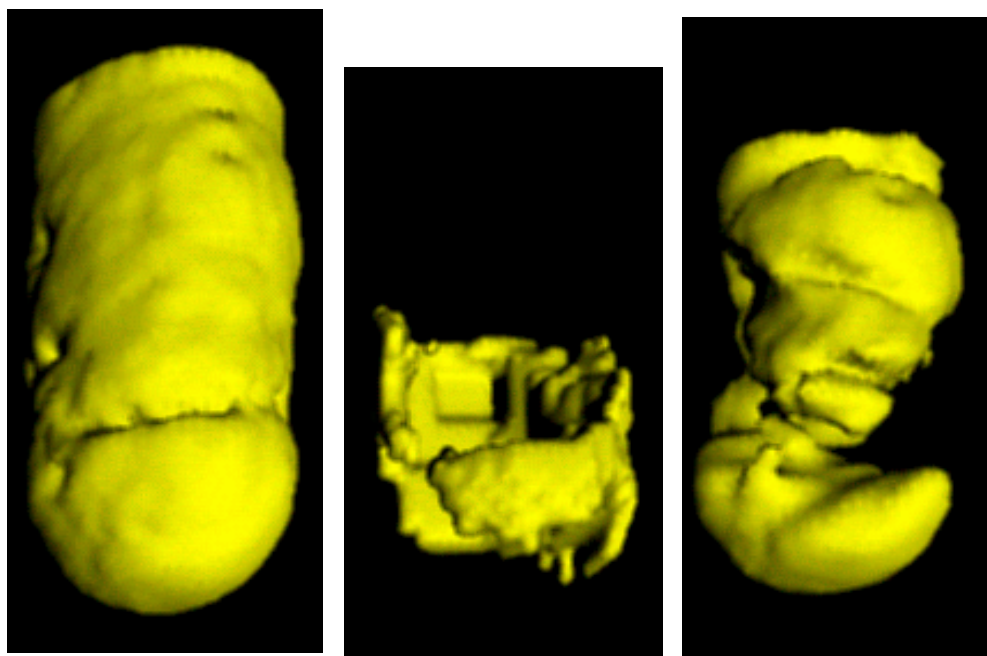


(c:) *Underneath view of 500Å Silica.*

Figure 52: 3D porous sample resolved into 500Å and 60Å components



All Silica 500Å Silica 60Å Silica
 (a:) Idealised 3D Structure of 500Å plus 60Å silica phantom.



Undifferentiated Silica 500Å Silica 60Å Silica
 (b:) 3D resolved Pore Size Structure.



(c:) Top view of 500Å Silica.

Figure 53: 3D porous sample resolved into 500Å and 60Å components

The full data set is $N_X \times N_Y \times N_Z \times N_T$ in size. For the dimensionless poresize distribution measurement, we usually set N_T to be 300 for bulk cryoporometry, but even if we use 32, a data set $64 \times 64 \times 32 \times 32$ in size occupies 16MByte. The Monotonic and PoreVolume data sets will be similar sizes. If one is not to perform the operation by repeatedly reading the arrays in from disk, and operating on only a tiny subsection, one needs at least 32MByte of RAM memory, assuming that one writes out and deletes from memory data sets as soon as they are finished with – say 48 to 64MByte with operating system, program and additional temporary storage; more will make programming quicker and simpler.

It is not at all clear what is the best way of displaying the full pore size distribution data for a 3D object, as this then is a 4D data set. The median pore size data could be displayed as colour coded slices, as for the single slice in the previous 2D data (chapter 8.3). Alternatively, when discrete regions have different median pore sizes, one could represent them as shaded surfaces, as in this work.

8.5 Conclusion

A method for determining the full pore size distribution and median pore size for any point in a 1 or 2-dimensional sample has been presented. Measurement and shaded surface representation of 3-dimensionally resolved pore size structures has also been demonstrated.

This method offers a uniquely non-destructive method of obtaining the full pore size distribution or median pore size at any point inside a bulk sample.

Chapter 9

Cryoporometric measurements on large pore porous materials at various warming rates, and the deduction of probe and liquid characteristics.

Cryoporometric runs were performed on large pore size sol gel silicas and on Trisopor porous glass, the pore sizes respectively being near the upper end of that resolvable with water and cyclohexane. Measurements were performed at a number of different warming rates, using the gas flow cooler. These measurements provided the first reliable cryoporometric measurements of the pore size distribution in the larger Trisopor glasses, to be compared with the nominal pore diameters obtained from mercury intrusion. They also served as a commissioning test of the gas flow cooler for use with cryoporometry; they allowed evaluation of the cryoporometric method at large pore sizes; they provided data to test a method of deducing the correct value of the bulk melting point to be used for a particular liquid at a particular warming rate, for a particular probe; they provided data that could be used to deduce the cryoporometric resolution of the existing probe as a function of pore diameter, liquid, and probe warming rate.

9.1 Sample preparation.

Samples were prepared of dried Trisopor[®] porous glass of nominal pore diameter 158Å, 250Å, 480Å, 1000Å and 1930Å slightly overfilled with cyclohexane. Weighings were made of the empty tube plus cap, then with added porous glass after drying, then after adding the anhydrous cyclohexane in a nitrogen filled glovebox. The samples were flame sealed on a vacuum line.

The sample of 200Å sol gel silica had previously been made for the calibration of the water melting point depression.

9.2 Measurement runs.

Cryoporometric runs were performed on the samples using the newly implemented gas flow cooler (chapter 5.3) at various warming rates (see table 8). The first runs on 1930Å and 1000Å silica provided information as a function of warming rate, and allowed deduction of warming rates suitable for resolving the other Trisopor samples.

Pore Diameter {Å}	Warming rate {C°·min ⁻¹ }
158	0.5, 0.2
250	0.1
480	0.05
1000	0.1, 0.05
1930	0.05, 0.02, 0.01
200	0.2, 0.1, 0.05

Table 8: Warming rate of measurements performed on cyclohexane in Trisopor porous glass and on water in 200Å sol gel silica.

Runs took about 2 to 4 hours, with the exception of the one at 0.2C°·min⁻¹ on 158Å Trisopor, which took about 7 hours, due to the depth of cooling required.

9.3 Cryoporometric results.

Examination of the melting point data shows that the gas flow cooling system gives a high uniformity of warming, even at 0.01C°·min⁻¹, with no noticeable tendency to the temperature reversals that occur frequently with the Lindacot system below

$0.5\text{C}^\circ\cdot\text{min}^{-1}$. This was the main impetus to implement gas flow cooling, and as such seems to have succeeded well.

Pore size distributions (figures 54, 55, 56) were calculated using the method described below. We notice that all the pore distributions appear reproducible and well resolved, with the exception of that at $0.05\text{C}^\circ\cdot\text{min}^{-1}$ using 1930Å Trisopor, where the warming rate was too fast for adequate resolution. For the larger pore sizes the distributions appear somewhat sharper than is common with sol gel silicas. The 250Å sample is decidedly bi-modal; some of the other distributions suggest that they are composed of a slight overlap of intrinsically very sharp distributions.

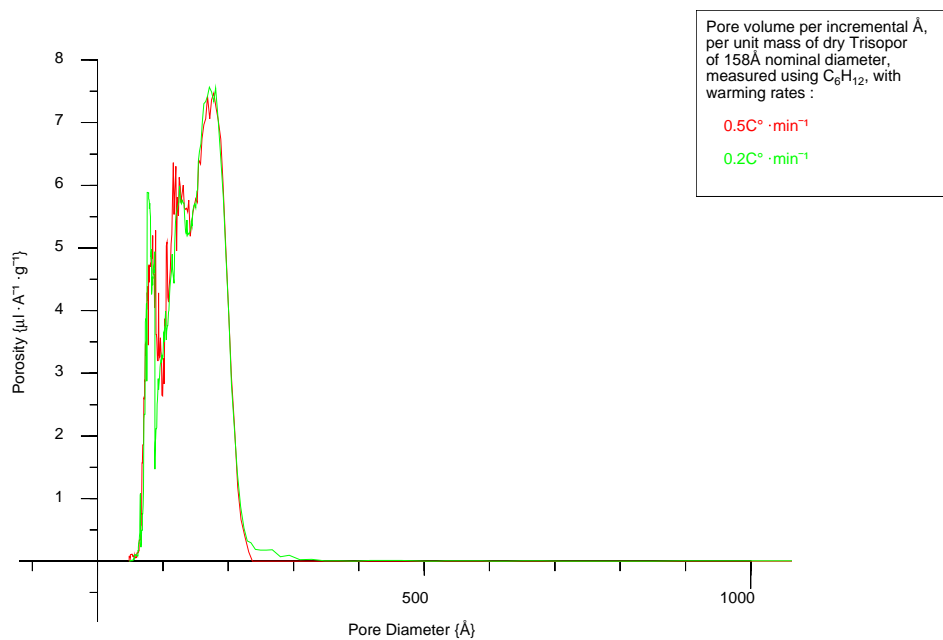
The measured peaks in Trisopor are all larger than the nominal pore sizes; this may be due to sensitivity to pore geometry, but is most likely due to the fact that the cryoporometric calibration of the melting point depression factor k for cyclohexane has been performed in terms of sol gel silicas calibrated by gas adsorption, which measures surface area to volume of the pores, whereas the Trisopor samples have been calibrated by mercury intrusion, which measures pore throat sizes, and can thus be expected to give lower results.

9.4 Calibrations as a function of warming rate.

We wish to consider the thermal behaviour of a scanning cryoporometer, where the body of the probe (by default) is programmed to linearly ramp in temperature. We note that while the bulk liquid around the grains of porous silica is melting, the liquid will be at a constant temperature. The temperature that we actually measure at the thermocouple will however change, due to the thermal resistances in the probe (see appendices D, G). As a result, if pore size distributions are calculated for melting point curve data measured at differing probe warming rates and using the same value of bulk melting point for all the calculations, the displacement in temperature due to the time required to melt a mass of solid (at constant warming rate of the probe) results in a relative displacement of the calculated pore distribution peaks.

If T_u, T_l are the upper and lower limits of the step in the melting point curve caused by the melting of the bulk liquid around the porous grains of silica, one would expect that if one chose the mid-point of T_u, T_l , one would correct for this displacement; in fact this over-compensates. It had been noticed when doing cryoporometric runs at

158Å Trisopor pore size distribution.



250Å Trisopor pore size distribution.

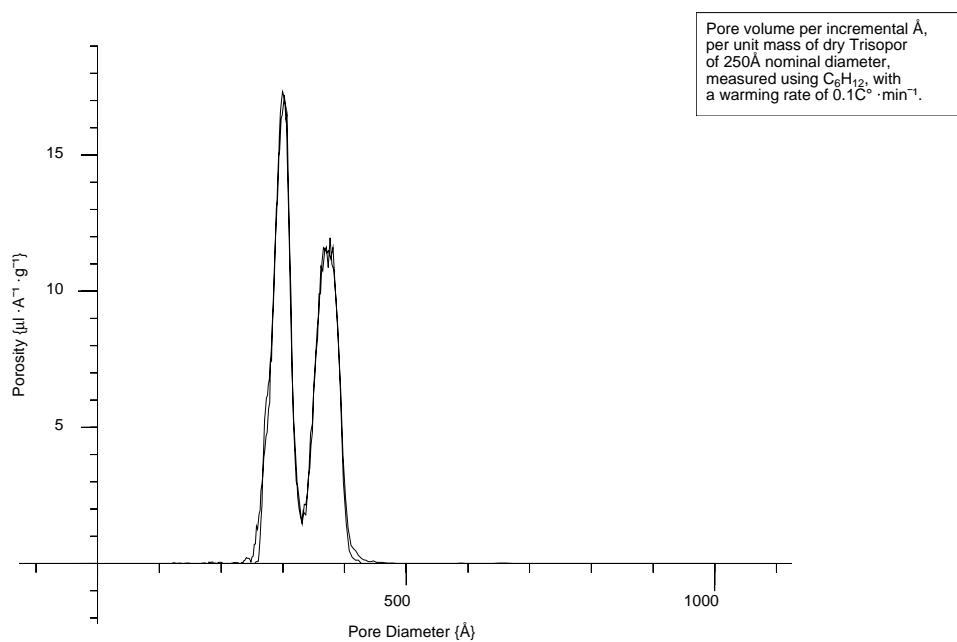
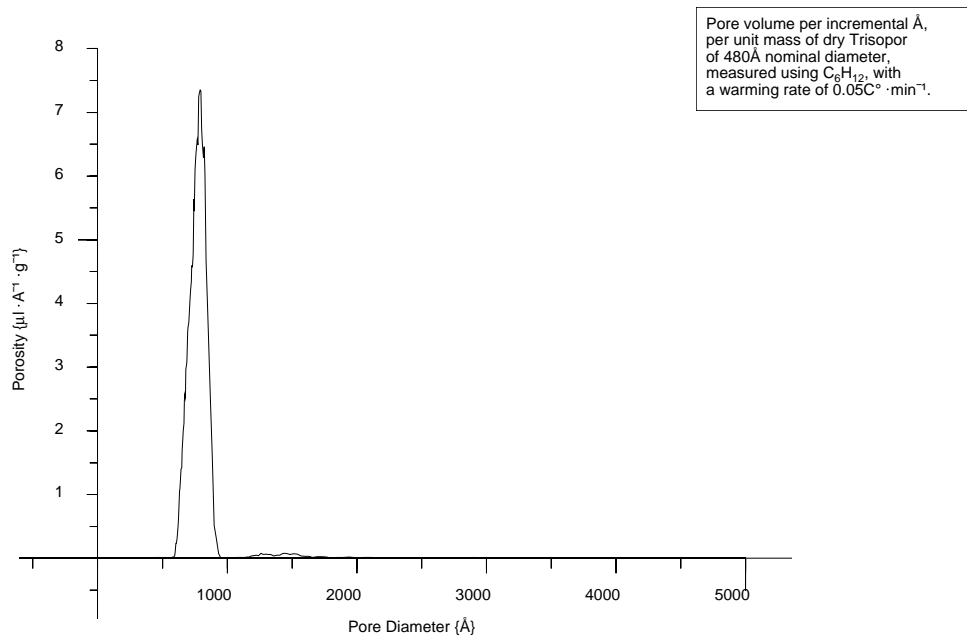


Figure 54:

Cryoporometric pore size distributions measured using cyclohexane in 158Å, 250Å Trisopor, for various warming rates.

480Å Trisopor pore size distribution.



1000Å Trisopor pore size distribution for 2 warming rates.

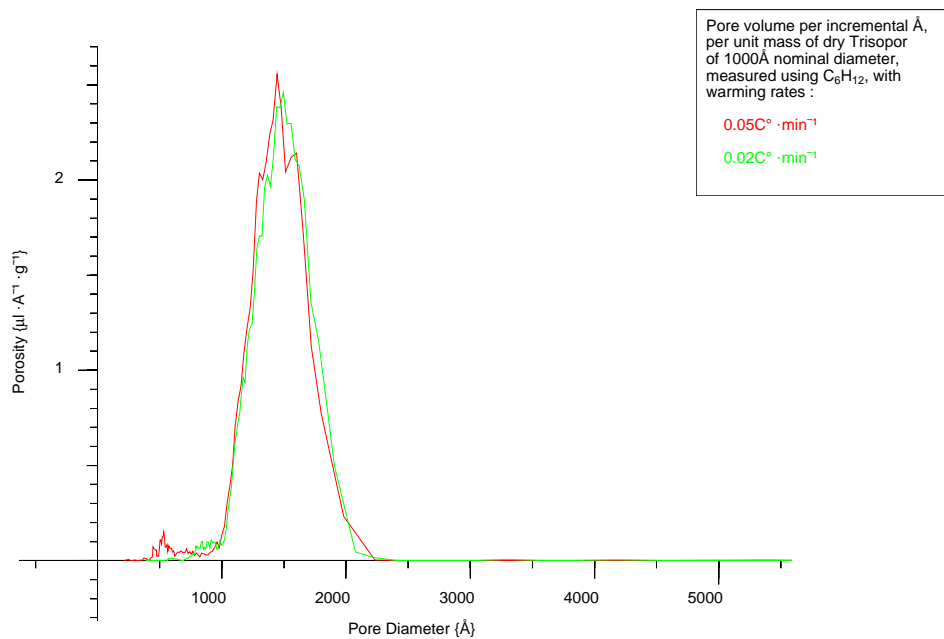


Figure 55:

Cryoporometric pore size distributions measured using cyclohexane in 480Å, 1000Å Trisopor, for various warming rates.

1930Å Trisopor pore size distribution for 3 warming rates.

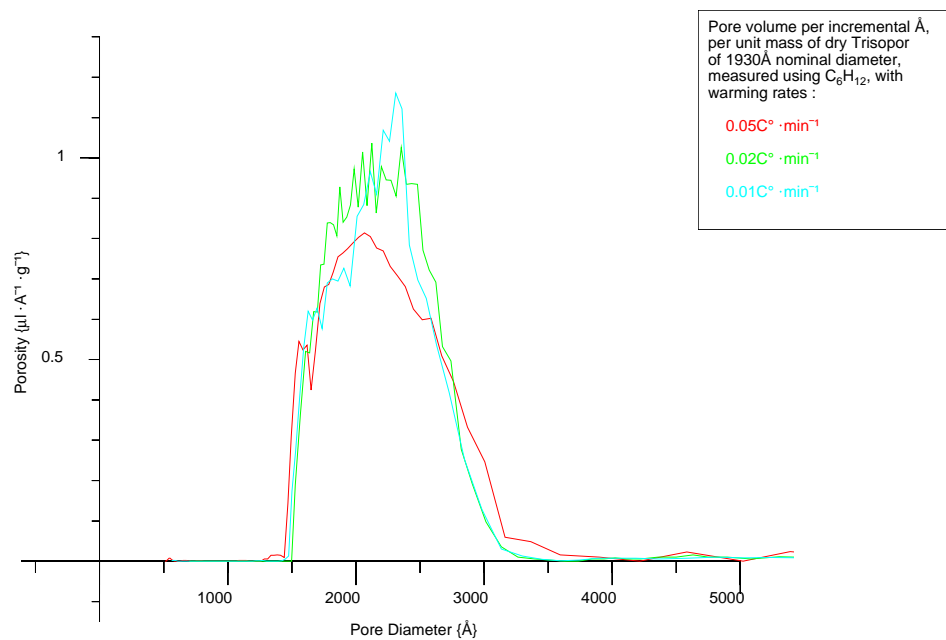
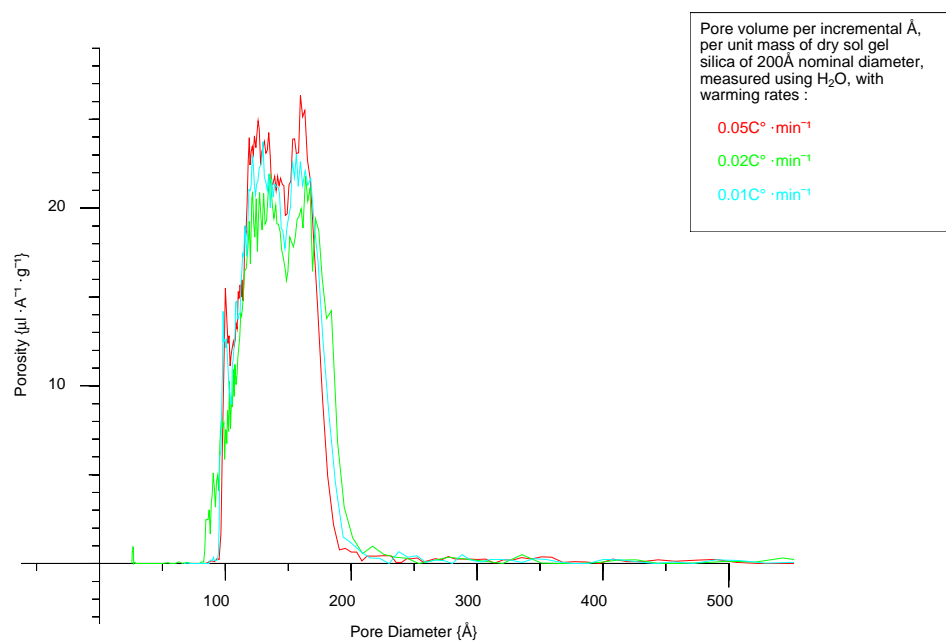
200Å sol gel silica pore size distribution using H₂O.

Figure 56:

Cryoporometric pore size distributions measured using cyclohexane in 1930Å Trisopor, and water in 200Å sol gel silica, for various warming rates.

relatively large warming rates that the best value of bulk melting point to choose to match nominal to measured pore diameters corresponded to about 1/3 way up the bulk melting step.

In appendix D we consider Δt_m , the time required for a sample of liquid undergoing an isothermal phase transition to melt, and its dependence on the mass of liquid melting ΔM_b and the size of the heat flux into the sample $W_s = W_{s0} \cdot \left(\frac{dT}{dt}\right)^p$ (where $p \approx 0.5$), and (given a uniform probe warming rate) deduce the total temperature range $\Delta T_b = T_u - T_l$ that is actually measured for the transition by the sample thermocouple

$$\Delta T_b = \Delta T_s + \frac{L_f \cdot \Delta M_b}{W_{s0}} \cdot \left(\frac{dT}{dt}\right)^{1-p}$$

where L_f = Latent Heat of Fusion of the solid to liquid transition.

In this appendix we describe routine *mpcstep*, which uses user interaction and linear least squares fitting to obtain T_u, T_l from the melting point curve data, and with these calculates a measured value for the bulk melting point at this particular warming rate

$$T_{bulk} = T_l + \frac{1}{3} \cdot (T_u - T_l);$$

The routine then proceeds to calculate the volume normalised pore size distribution for the corresponding data, using this value, then plots and saves the distribution.

Using this approach, the graphs in figures 54, 55, 56 were calculated, which show reasonable independence of heating rate for all but the case of $0.05 \text{C}^\circ \cdot \text{min}^{-1}$ in cyclohexane in 1939\AA pore size, where there is degraded resolution due to the warming rate.

9.5 Cryoporometric resolution.

Using the measured value for the residual temperature difference ΔT_s along the sample (appendix D figure 124), we may calculate the resultant best resolution as a function of pore diameter and cryoporometric liquid slope constant k . We may go further, if we use the measured proportionality (with slope β) of the total bulk melting point step ΔT_b to $\left(\frac{dT}{dt}\right)^{1-p}$ (where $p \approx 0.5$) (appendix D), we may deduce from the Gibbs-Thomson equation the corresponding full width resolution broadening function =

$$\begin{aligned} \phi(k, \text{Diameter}, \frac{dT}{dt}) &= \frac{k}{\pm \frac{1}{2} \cdot \Delta T_b + \frac{k}{\text{Diameter}}} \\ &= \frac{k}{\pm \frac{1}{2} \cdot \left(\Delta T_s + \beta \cdot \left(\frac{dT}{dt}\right)^{1-p}\right) + \frac{k}{\text{Diameter}}} \end{aligned}$$

which we may express in Apl as :

$-/[1] k \div (-1.1 \times 0.5 \times CoefCT1k93 \text{ genlin WarmingRate} * 1-p) \circ. + k \div Diameter$
 Plotting this for warming rates of 1, 0.1, 0.01 $\text{C}^\circ \cdot \text{min}^{-1}$, for pore sizes from 50Å to 2000Å, we obtain using $k_{cyclohexane} = 1825$, figure 57a for cyclohexane, and using $k_{water} = 495$, figure 57b for water.

The majority of cryoporometry measurements in this work have been made using the Lindacot temperature controller (see chapter 5.1), at a warming rate of 0.5 or 1 $\text{C}^\circ \cdot \text{min}^{-1}$; it can be seen from figure 57a that with the existing probe, cyclohexane measurements at 0.5 $\text{C}^\circ \cdot \text{min}^{-1}$ are then limited to be below about 1000Å, as at this pore size the full width broadening is comparable with the pore diameter.

Measurements using gas flow cooling (see chapter 5.3) were made mainly with warming rates in the region of 0.1 to 0.01 $\text{C}^\circ \cdot \text{min}^{-1}$. With cyclohexane at 0.01 $\text{C}^\circ \cdot \text{min}^{-1}$ the full width broadening with the existing probe is comparable with the pore diameter at about 10000Å = 1μm, assuming that no other factors intrude.

One such factor may be a residual broadening of the liquid melting curve due to impurities. However for both the anhydrous Sureseal[®] cyclohexane from Aldrich and the filtered/reverse osmosis/ion exchanged water that were used, this should be considerably less than the measured value of $\Delta T_s \approx 0.06 \text{ C}^\circ$.

If we wish to improve on this resolution, we see from the above equation for ΔT_b that it is important to reduce the residual temperature difference along the sample ΔT_s . However we also see that we can improve the resolution at larger warming rates either by reducing L_f or ΔM_b , or by increasing W_s .

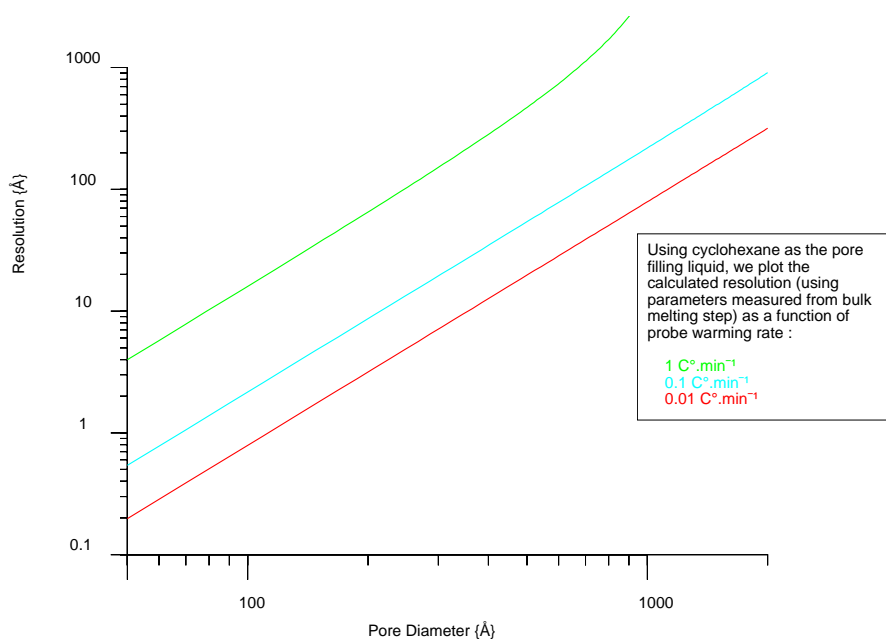
Thus we can see that we need to warm much slower when using water as the cryoporometric liquid, not only by the ratio of the melting point depression factors $\frac{k_{water}}{k_{cyclohexane}}$, but also take into account the higher latent heat of fusion L_f of water compared with cyclohexane.

The approach of reducing the mass of the sample is commonly used in Differential Thermal Analysis (DTA), and may be possible with NMR as at slow warming rates there is as much as a day available for averaging the NMR echo amplitudes.

Attempts to increase the heat flux W_s into the sample may conflict with the requirement to keep the total temperature range along the sample ΔT_s as small as possible.

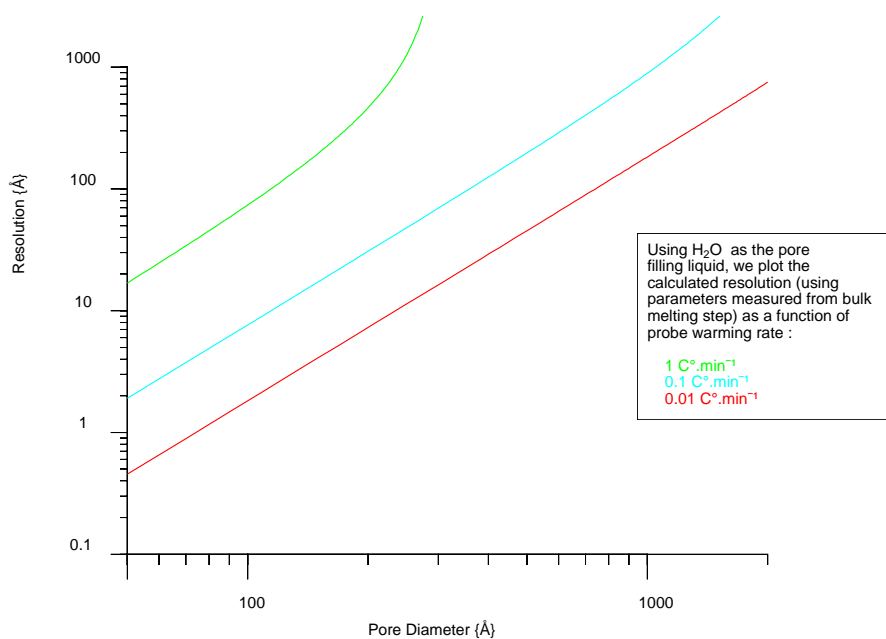
Even without further changes we see from figure 57a that the introduction of the gas flow cooler, by allowing warming rates to be reduced by a factor of 50, has improved the resolution at a given pore diameter by a factor of 10, (more at large pore sizes);

Calculated cryoporometric probe resolution using cyclohexane.



(a:) Calculated pore size resolution for cyclohexane.

Calculated cryoporometric probe resolution using water.



(b:) Calculated pore size resolution for water.

Figure 57: Calculated probe pore size resolution for cyclohexane and water, as limited by residual temperature gradients in the sample, and by probe warming rates (parameters measured from bulk step as a function of warming rate).

alternatively, for the same resolution we can now study pores that are $\sqrt{10}$ larger. Studying comparative pore size distributions, we see that the practical difference is even greater, perhaps a factor of 10, as the temperature fluctuations with the Lindacot cooling system badly distort the resultant pore size distributions at large pore sizes.

9.6 Conclusion.

Thus we have deduced an expression describing the cryoporometric resolution for a scanning cryoporometer. We have shown that provided we warm no faster than specified in the cryoporometric resolution graphs in figure 57, using gas flow cooling with cyclohexane as the indicator liquid, we obtain highly repeatable pore size distribution graphs up to 2000Å pore diameter (figures 54, 55, 56).

Chapter 10

Naturally porous materials exhibiting a fractal pore size distribution.

NMR cryoporometric measurements of pore size distributions have been made for underfired clay, and for chalk, We show that in a sample of underfired clay, for a ratio of pore sizes of 25, the pore size distribution has a self-similarity that follows a fractal characteristic. In a chalk sample the porosity for a decade ratio of pore sizes at small pore diameters exhibits a self-similar distribution, but at larger pore diameters for a decade shows a self-similar distribution with a higher than extrapolated porosity.

10.1 Self similarity and Fractal dimension.

If one considers space-dividing fractured curves that form self-similar shapes [Mandelbrot, 1983, Ch:II,6], we see that a whole interval $0 \leq x < X$ on a straight line of Euclidean dimension 1 may be 'paved' by $N = b$ 'parts'. If these 'parts' are the intervals $(k - 1)X/b \leq x < kX/b$ where k goes from 1 to b , then each part can be deduced from the whole by applying a scaling ratio $ScalingRatio(N) = 1/b = 1/N$.

Similarly for a rectangle on a plane one obtains $ScalingRatio(N) = 1/N^{1/2}$ and for a rectangular parallelepiped one obtains $ScalingRatio(N) = 1/N^{1/3}$

Thus in general, for D-dimensional parallelepipeds we obtain

$$ScalingRatio(N) = \frac{1}{N^{1/D}}$$

or

$$N \cdot \text{ScalingRatio}^D = 1$$

Mandelbrot considered the possibility of fractal dimension D becoming non-integer.

We have here two variables, the ratio of scales 'ScalingRatio' over which we are measuring self-similarity, and N , which is in effect a scaling parameter telling us what fraction of the whole (maximum) we find.

Suppose we consider the measurement of a parameter P at two length scales x_1, x_2 , such that we measure $P(x_1), P(x_2)$.

It is then clear that we may map

$$\begin{aligned} \text{ScalingRatio} &\Leftrightarrow \frac{x_2}{x_1} \\ N &\Leftrightarrow \frac{P(x_2)}{P(x_1)} \end{aligned}$$

where we consider $x_2 > x_1$, and $P(x_2) > P(x_1)$ in agreement with the above discussion.

We may then describe the self-similarity in parameter $P(x)$ in terms of a fractal relationship :

$$\begin{aligned} N \cdot \text{ScalingRatio}^D &= 1 \\ \therefore \frac{P(x_2)}{P(x_1)} \cdot \left(\frac{x_2}{x_1}\right)^D &= 1 \\ \therefore D \cdot \text{Ln} \left(\frac{x_2}{x_1}\right) &= \text{Ln} \left(\frac{P(x_1)}{P(x_2)}\right) \end{aligned}$$

10.2 Self similarity in measured pore size distributions.

We have measured the the pore size distribution (by which we mean the incremental pore volume per Ångstrom increase in pore diameter, per gram of dry porous material) for a number of naturally porous materials, by NMR cryoporometry.

We plot in figure 58 the pore size distribution for Obergrafenhain clay fired at 850°C and in figure 59 we plot the pore size distribution for Flamborough chalk.

We see that for a length scale change from 80Å to 2000Å (a factor of 25) the log-log plot for the clay exhibits deviations from a straight line that only have the characteristics of measurement noise.

Fractal porosity in underfired clay.

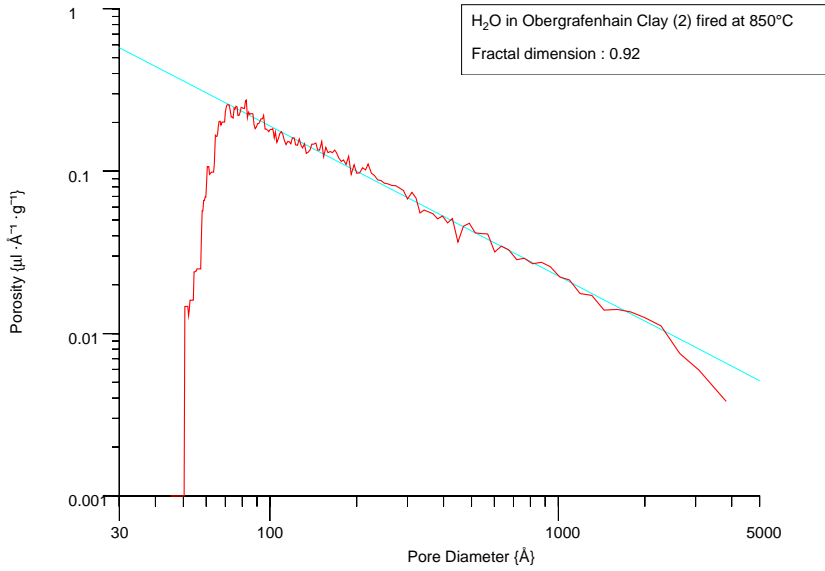


Figure 58: Cryoporometry pore size distribution for Obergrafenhain (2) clay fired at 850°C.

Fractal porosity in chalk.

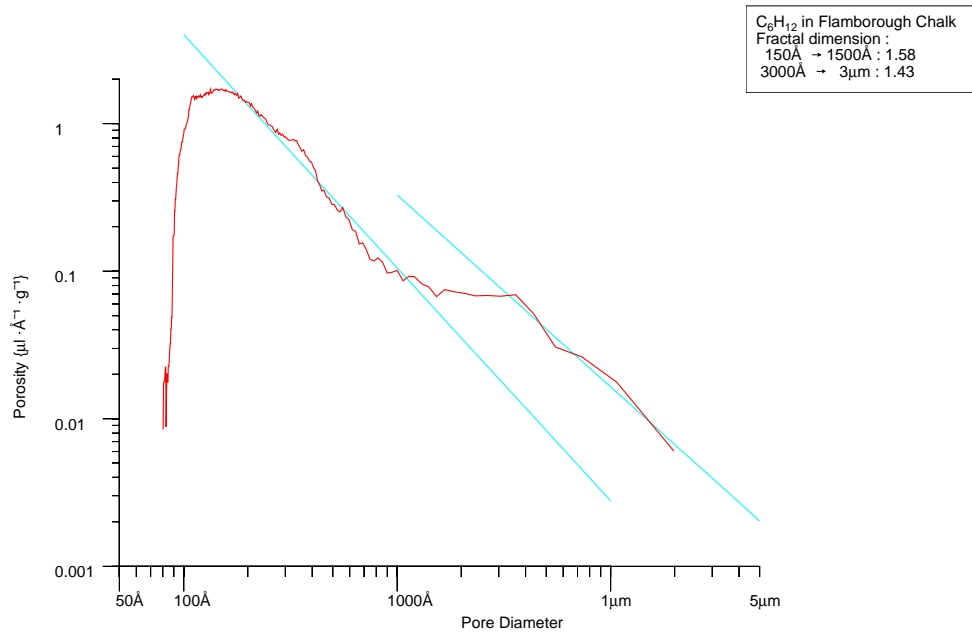


Figure 59: Cryoporometry pore size distributions for Flamborough chalk.

Suppose we write for our parameter $P(x)$ the measured incremental porosity as a function of pore diameter x , then we have (with -ve slope β) :

$$\begin{aligned} \ln(P(x)) &= \alpha + \beta \cdot \ln(x) \\ \therefore \ln(P(x_2)) - \ln(P(x_1)) &= \beta \cdot (\ln(x_2) - \ln(x_1)) \\ \therefore \ln\left(\frac{P(x_2)}{P(x_1)}\right) &= \beta \cdot \ln\left(\frac{x_2}{x_1}\right) \\ \therefore -\ln\left(\frac{P(x_1)}{P(x_2)}\right) &= \beta \cdot \ln\left(\frac{x_2}{x_1}\right) \\ \therefore \frac{P(x_1)}{P(x_2)} &= \left(\frac{x_2}{x_1}\right)^{-\beta} \\ \therefore \frac{P(x_2)}{P(x_1)} \cdot \left(\frac{x_2}{x_1}\right)^{-\beta} &= 1 \end{aligned}$$

Hence we conclude that the pore size distribution for the clay from 80Å to 2000Å has a self-similarity that is fractally related, such that the negative of the slope β of the log-log plot gives us the fractal dimension D of the self-similarity of the porosity. Thus for the clay we obtain $D \approx 0.90$.

For the chalk we see one region of linear behaviour on the log-log plot, from 150Å to 1500Å, implying a self-similar behaviour with a fractal dimension of $D \approx 1.6$. However from 3000Å to 3μm we find a displaced line with a higher porosity than expected from an extrapolation of the first line, with $D \approx 1.4$. One possible explanation of this is that the nano-porosity is in the form of porous cemented grains, with additional porosity in the inter-granular voids on a micron scale.

It should be emphasised that this behaviour is a property of the materials studied, and that the NMR cryoporometer used for these measurements has been shown to have good resolution over the range 25Å to 1μm both by direct measurement and by deduction from the width of the step in the melting curve when any bulk liquid melts.

Chapter 11

Densities and solid-solid density correlations in dry porous silica systems: measured by weighing, imbibation, neutron scattering and nuclear magnetic resonance; interpreted using analytic and Monte-Carlo models of porous systems.

Neutron Scattering measurements of $S(Q)$ for $0.0008 \leq Q \leq 17$ providing information on the radial density correlations in the porous media and Nuclear Magnetic Resonance cryoporometric measurements of pore size distributions for mean pore diameters $25\text{\AA} \leq D_{\text{void}} \leq 2000\text{\AA}$ are presented for sol-gel porous glasses. To interpret this information, density distributions in model silicas are evaluated by analytic and Monte-Carlo methods for $r \leq 21 \times \text{LatticeSpacing}$, and $G(r)$, $d(r)$, $L(l)$ and $I(Q)$ calculated. S.E.M. micrographs and bulk density and imbibation measurements provide additional constraints on the models.

11.1 Introduction.

Sol-gel silicas and some micelle templated silicas were studied by density and imbibation measurements, NMR cryoporometry and neutron scattering. We wish to provide a consistent explanation of the observed measurements; thus models of porous structures were generated.

Initial consideration is given to simple systems of porous structures that model the average behaviour of sol-gel and micelle templated silicas – realistic models are shown to be constrained by simple bulk density measurements on the silicas.

Then the detailed behaviour of the solid-solid radial density correlation $G(r)$ for uniform pores on a regular lattice is considered, before examining the behaviour of ensembles of pores with statistical variation in pore diameter and lattice spacing. For these Monte-Carlo modelling of the porous structure is used [Hammersley and Handscomb, 1964], using the above geometric models. The mean densities given by the analytic calculations provide stringent tests that we have correctly implemented the geometry in the Monte-Carlo models.

Constraints are placed on the models and their parameters, using information derived from the neutron scattering and NMR cryoporometric measurements, to generate more realistic models. This helps to greatly improve the calculation efficiency.

We also find that we need to model the scattering from a planar slab; thus $G(r)$ is calculated for a plane slab by analytic, numerical and Monte-Carlo integration.

The $G(r)$ radial distribution information is calculated for a number of porous structure models as a function of two parameters, $D_{void}/LatticeSpacing$ and $LatticeSpacing Variance = \sigma^2$, and transformed to scattering intensity $I(Q)$. It is then compared with the measured scattering intensity, using linear scaling of the amplitude and the Q scale. i.e. we transform from a scale in which the $LatticeSpacing$ is normalised to unity, to one in which it is measured in Å. We find these parameters are sufficient to obtain a quite detailed representation of the measured scattering over some decades of scattering intensity and length scale.

11.2 Model porous systems: constraints and simplifications.

We wish to consider porous systems, such as are formed in silica using the sol-gel process and those such as MCM-41 and MCM-48 formed by a micelle templating process.

By porous we mean that they have the ability to absorb liquids, and thus will in the main exclude systems containing primarily blind pore void space. At the other extreme we can exclude geometries where the pore void is so large that the structure loses cohesion. We will apply constraints on the geometries, using information gained from Scanning Electron Microscope (SEM) micrographs, bulk density and imbibation measurements, and NMR Cryoporometry and Neutron Scattering experiments.

11.2.1 Structural length scales observed in porous silica systems.

First we wish to consider the length scales on which the porous silica shows structure. Many models have been proposed for porous silica structure, some fractal in nature [Stanley and Ostrowsky, 1986]. In this work the density and spatial structure of a number of porous silicas has been studied using Neutron Scattering diffraction and small angle scattering (SANS) over length scales 0.34\AA to $0.75\mu\text{m}$; using NMR Cryoporometry over length scales 10\AA (using water as the cryoporometric liquid) to perhaps $10\mu\text{m}$ (using cyclohexane); using Pulsed Magnetic Field (PFG) diffusion measurements and NMR fringe field diffusion measurements (using water in the silica pores) over length scales $0.3\mu\text{m}$ to $30\mu\text{m}$; with SEM micrographs over length scales $0.5\mu\text{m}$ to 1mm ; and average bulk properties of the silica powder, grain and silica matrix studied using bulk density and liquid imbibation measurements.

With the exception of sintered porous silica and aerogel, which are available as solid blocks, most porous silicas are made in the form of fine porous grains.

If we examine Scanning Electron Microscope (SEM) micrographs of silica grains for 100\AA pore diameter sol-gel silica (figures 60, 61), we see that the grains are typically of size $100\mu\text{m} \rightarrow 200\mu\text{m}$. Further examination of the micrographs shows that on a micron scale we have approximately spherical structures on the surface of the silica, with a diameter of about $2.2\mu\text{m}$. However if we examine the exposed silica edges in figure 61, we do not see any actual porosity between the domains. For a structure composed of random packed spheres it is possible to see into the lattice to the third layer, and

even with Hexagonal Close Packing second or third layers may be visible, depending on orientation (see figure 70); this is not apparent in the micrographs.

If we examine the intensity of neutron scattering from sol-gel silicas as a function of Q (see figure 85), we see structure that for a simple analysis seems to suggest structure on two length scales (see figures 99, 100, 101). However a more thorough analysis based on the calculation of the scattering from the radial density distribution for model pore structures shows that we can obtain similar scattering from models that contain a single Gaussian shaped distribution of spherical pores (see chapters 15, 16).

NMR cryoporometry using cyclohexane as the cryoporometric liquid with the gas-flow cooling system, with variable warming rate to give a uniform resolution on a log scale (see appendix F), can now resolve porosity on a micron scale, and with reduced resolution up to possibly $10\mu\text{m}$. Such measurements on porous silicas show little porosity other than the expected porosity distributed around the nominal pore diameter.

Diffusion measurements made on liquids in sol-gel silica powders using both NMR Pulsed Field Gradient (PFG) techniques and superconducting magnet Fringe Field Gradient techniques, as a function of temperature, are both consistent with the presence of structure on a $100\mu\text{m}$ (grain) scale, but not at $2\mu\text{m}$. However these measurements require additional confirmatory studies and are not presented further here.

Thus we tentatively conclude that the unconstrained silica prefers to grow into spherical shapes with diameters of about $2.2\mu\text{m}$ (themselves porous on a scale of 100\AA), but that the body of the silica is probably filled with touching polyhedral domains of porous silica, with little or no additional porosity on a $1\mu\text{m}$ scale.

We have seen that the Neutron Scattering measurements of the scattering from porous silica (performed as part of this work) show structure that depends on pore diameter; we will discuss this further in chapters 16, 17.

NMR cryoporometric measurements performed as part of this work have shown that for the sol-gel silicas that are being considered, the normalised pore size distribution is 20% to 50% wide, with an approximately Gaussian distribution, (figure 62), and that of the micelle templated silicas is considerably less. This pore size distribution is thus much different from the fractal distribution that is sometimes posited.

Thus for our models we will limit our consideration to pores characterised by a mean pore diameter and a Gaussian statistical variation. This greatly constrains both the shape of the pores and the geometry of the 3D spatial repetition of the pores, for a self

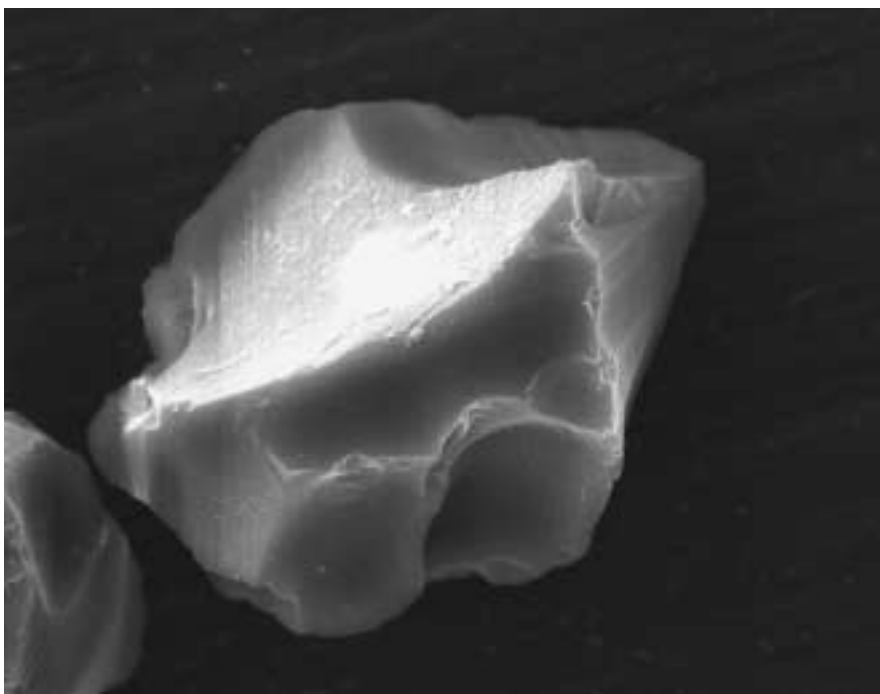


Figure 60:

SEM micrograph of typical sol-gel silica grain of about $150\mu\text{m}$ dimensions, porous on a scale of 100 \AA . The notch of the 'crevasse' near the 'peak' is shown in figure 61.

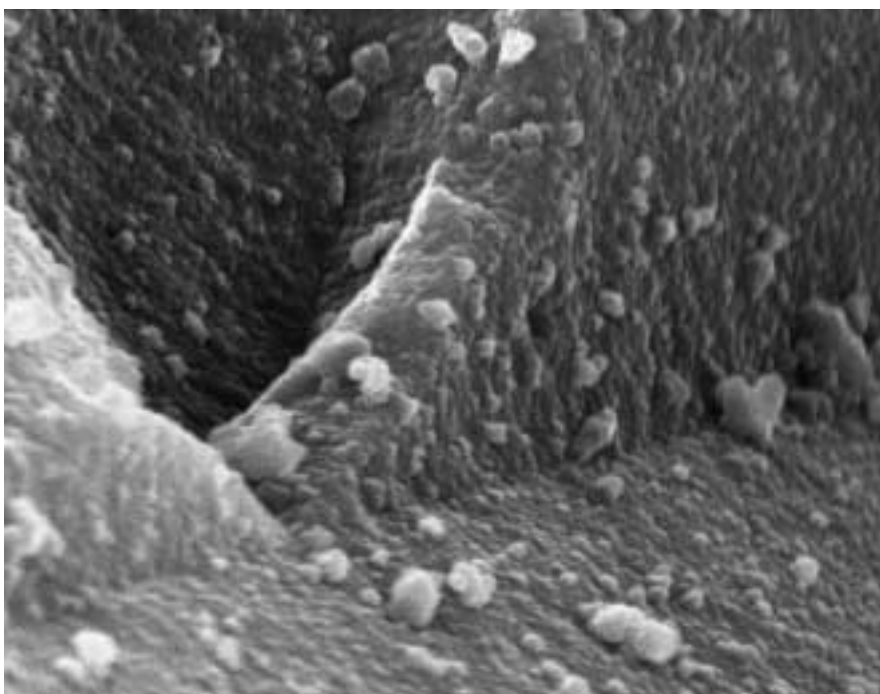


Figure 61:

SEM micrograph of the silica grain in figure 60, porous on a scale of 100 \AA , showing spherical structures with a diameter of about $2.2\mu\text{m}$, but no inter-domain void space.

Normalised pore volume distributions for sol-gel silicas.

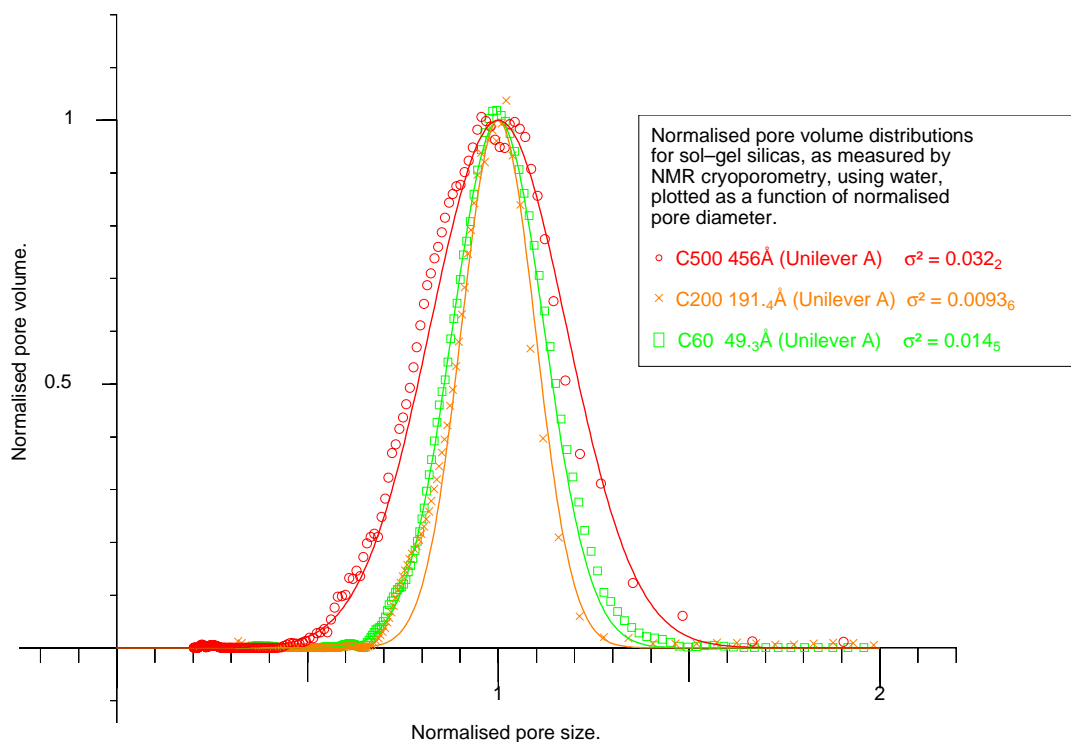


Figure 62:

Normalised pore volume distributions for sol-gel silicas, with fitted Gaussians, showing Full Width at Half Maximum values of 20% to 50%.

consistent lattice.

Neutron scattering measurements made as part of this work show that whereas the pores in the micelle templated silicas are arranged in a highly regular manner, giving moderately sharp Bragg peaks, (figure 63), the scattering from the sol-gel silicas shows just broad small-angle scattering, with little sign of Bragg scattering from a regular lattice of pores (figure 85). Thus one concludes the pores in the sol-gel silicas, although of a fairly regular size, are arranged in an essentially random manner with little long range order. One is then limited to suitable packing geometries for the above pores that can satisfy the measured bulk densities and radial distributions.

Next we consider if there is possible nano-scale structure in the silica – i.e. is the silica from which the pores are excised also structured ?

NMR cryoporometric measurements on sol-gel silicas in the range $25\text{\AA} \rightarrow 2000\text{\AA}$ mean

pore diameter show negligible porosity below that of a Gaussian like distribution around the mean pore diameter, down to the lower limit of about 10\AA (using water).

With Neutron Scattering we note that we do not see any additional structure between the scattering that changes with pore diameter, and the scattering from the atomic structure, such as might be due to nano-porosity, (figures 63, 85).

Scattering from Hexagonal Silica measured on D17 + D4

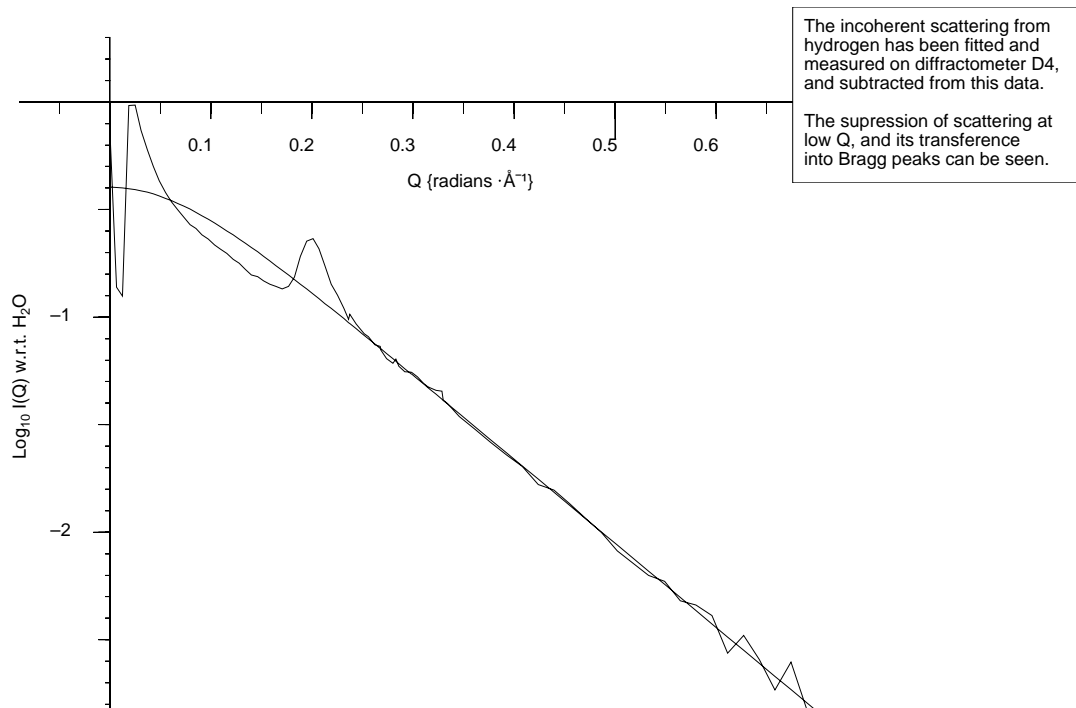


Figure 63:

Neutron scattering from dry porous silica MCM-41, showing peak at low Q and Bragg peak at $0.2 \{\text{radians} \cdot \text{\AA}^{-1}\}$, with pore structural intensity falling two orders of magnitude before atomic structural peak at $Q \sim 1.5 \{\text{radians} \cdot \text{\AA}^{-1}\}$.

11.2.2 Continuum simplification.

Thus an important simplification for our models comes from the fact that we see from the neutron scattering from even those silicas with small pore structure, such as MCM-41 or 40\AA sol-gel silica, that the scattering intensity from the pore structure falls some orders of magnitude before the first atomic structural peak at about $1.5 \{\text{radian} \cdot \text{\AA}^{-1}\}$ (see figures 63, 85).

Thus we may model our pores as holes cut from a continuum, rather than having to model discrete silicon and oxygen atoms; this reduces by many orders of magnitude the amount of information we have to store and manipulate for a large three-dimensional representation of a porous solid.

11.2.3 Bulk density constraints on simple pore and lattice geometries.

Simple measurement of the porous silica density allows one to deduce information that constrains the range of possible pore geometries within the silica. They also enable us to normalise the radial density correlation graphs obtained from measured neutron scattering from the silicas.

We have seen that the porous silicas being considered are made in the form of fine porous grains. Thus when considering the densities of the porous silica structure, one must take into account the packing densities of the grains. This is clearly variable, as can be seen by first pouring silica powder into a measuring cylinder, and then repeatedly tapping it, when a compression of a few percent is observed. However the grains soon reach a state of consistent maximum compression.

For hard spheres of a uniform size, close random packing density for has been shown by experiment [Finney, 1970] to be 0.6366 ± 0.0004 , i.e. about 64%, compared with a maximum possible density of $\frac{\pi}{3\sqrt{2}}$ (hexagonal close packed or face centered cubic) i.e. about 74%. Clearly grains with a wide range of sizes will pack more densely, but the mesh sizes claimed for the sol-gel silicas studied cover only a moderate range of sizes. Thus a packing density of 64% will initially be assumed for the grains of the standard sol-gel silicas. Imbibation experiments combined with NMR Cryoporometry experiments (section 11.5) allow us to measure this ratio. On the other hand there is evidence that the very fine grained templated silicas studied are much less than optimally packed, in that there is a volume reduction to about 80% when liquid is added to the dry powder, suggesting that the dry packing density may be about 50%, perhaps due to a ‘fluffy’ grain shape.

Density and imbibation experiments give us an additional check on the possibility of microporosity, as discussed in the preceding section: If the grains were microporous, in the form of random packed spheres, there would in effect be two nested sets of random

void packing outside the (25Å to 2000Å diameter) pores, such that we would have

$$\frac{V_{pore} + V_{silica}}{V_{pore} + V_{silica} + V_{micropacking} + V_{grainpacking}} \approx 0.64^2$$

$$\approx 0.41$$

In section 11.5 we measure values of between about 0.6 and 0.67 for the inter-grain packing fraction that are consistent with approximately random packing, with insufficient void space outside the pores to account for a large degree of microporosity.

Density and imbibation experiments also give us an additional check on the possibility of nanoporosity, as discussed in the preceding section: We have seen that we do not in the neutron scattering results see evidence of nano-structure on a scale between the atomic and pore dimensions ($\sim 10\text{\AA}$).

We will see in section 11.5 that we find a value of about 2.0 for the specific density of the (voidless) silica lattice. If this had a nano-structure of random packed spheres, this would imply a specific density of over 3.1 for the silica; fused silica has typical specific density of between 2.1 and 2.2, and even quartz crystal is only 2.6 [Kaye and Laby, 1966].

11.3 Models of simple porous systems.

Thus in constructing models of porous structures, we have to consider the shape of the pores themselves, the structure on which the pores are arranged, and the packing of the grains of the porous material.

These models will allow us to establish relationships, for each model, between pore diameter D_{void} (as measured say by NMR Cryoporometry), and lattice spacing a (to which one would *a priori* expect Neutron Scattering experiments to be primarily sensitive).

A number of pore geometries will be considered, and possible maximum and minimum density and silica filling factors evaluated and compared with experimental values as measured by density and imbibation measurements. Some of the geometries are chosen for their initial simplicity (rather than any expectation that they model reality), or because they form an extreme limit to the likely variation of real silica geometries, between which we may then interpolate.

We thus use as initial simple models of the pores, uniform pores distributed on a regular lattice. We then proceed to considering pores on ensembles of regular lattices with

statistical variations in diameter and spacing. Ideally one would like to treat pores on truly random lattices, but this step has not yet been made; there would be a substantial step in the computation required.

For initial bulk density considerations, we may clearly consider a porous structure composed of pores *all* with the average size, shape and spacing.

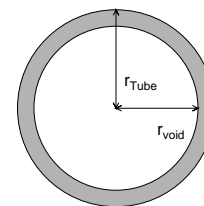
Further, for bulk density considerations we may simplify the geometry – i.e. when considering a simple geometric model of a regular lattice of cylindrical pores, we will also be treating with reasonable precision (for bulk density considerations) those templated silicas that are formed of intertwined cylinders, as well as the MCM-41 that is accurately modeled by cylinders on a hexagonal lattice.

In comparing the calculated densities with the measured ones, we need to know the density of the (voidless) silica lattice – examining bulk densities for silica [Kaye and Laby, 1966] initially led to the fairly arbitrary choice of 2.2 for the specific density; however measurements of the density of silica dry and filled with water, and of the total pore volume by NMR enable us to calculate the specific density of the silica lattice to be close to 2.0 (section 11.5) so will pre-empt those measurements and use that value here.

11.3.1 Single cylindrical tube.

The simplest such porous system we can consider is an isolated tube (figure 64) (thus deferring the problem of how the pores are packed).

If the inner void and outer tube radii are R_{void} , R_{Tube} , the length is L , and the density is ρ_{silica} , then we have :



$$\begin{aligned}
 \text{Total Mass of Tube} &= M_T = \pi L (R_{Tube}^2 - R_{void}^2) \cdot \rho_{silica} \\
 \text{Total Volume of Tube} &= V_T = \pi L R_{Tube}^2 \\
 \therefore \text{Density} &= \rho_T = \frac{R_{Tube}^2 - R_{void}^2}{R_{Tube}^2} \cdot \rho_{silica} \\
 \therefore \text{Volume Fraction for Tube} &= f_T = \frac{\rho_{Tube}}{\rho_{silica}} \\
 &= 1 - \frac{R_{void}^2}{R_{Tube}^2} \\
 \therefore \text{Tube radius} &= R_T = (1 - f_{Tube})^{-1/2} \cdot R_{void}
 \end{aligned}$$

Figure 64: Isolated tube geometry.

Thus if we were to pack such tubes into say a square array (figure 65), the lattice spacing a would be $(1 - f_{Tube})^{-1/2} \times D_{void}$ (the pore diameter). i.e. Just by measuring the density we are able to form a relationship between the pore diameter (as say measured by gas adsorption or cryoporometry) and the pore repetition spacing (as say measured

by X-ray scattering or neutron scattering). This seemingly simple step is flawed though, in that we are neglecting the void space outside the tubes; however we do now have a simple formula that now gives us the form of the relationship between the lattice spacing a and the silica filling factor f , for cylindrical voids.

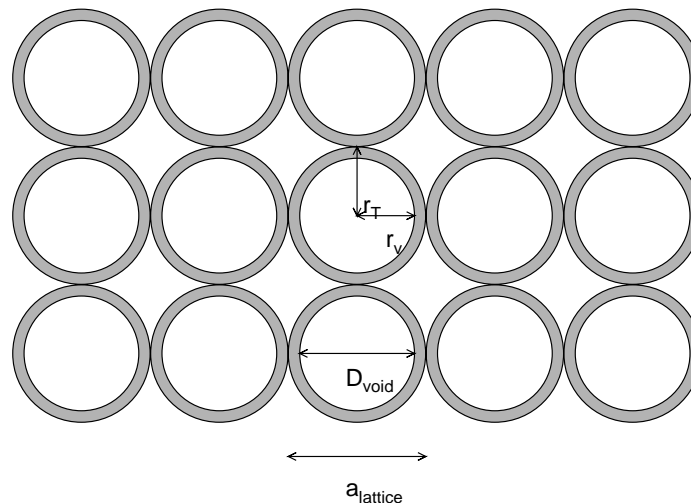


Figure 65: Lattice of tubes – a flawed model.

11.3.2 Cylindrical voids.

A more realistic model is to consider a solid matrix of silica, out of which is excised pore void volume on a regular array. We will initially consider two variants on the above : a regular square array of cylindrical voids; and a regular hexagonal close packed array of cylindrical voids. The latter is that with the greatest possible void space, and the former is probably lower than any likely randomised structure.

Square array of cylinders.

If now we take N lattice units of length L and lattice spacing a , with a cylindrical pore of radius R_{void} in each lattice unit (figure 66), then :

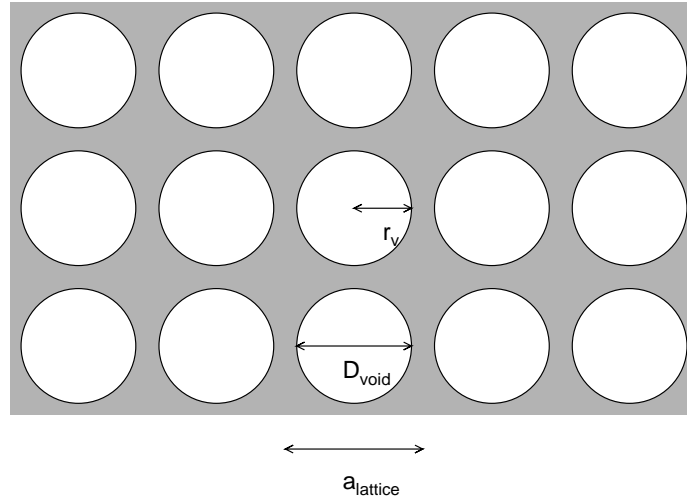


Figure 66: Square lattice of cylindrical voids.

$$\text{Total Mass} = M_{cs} = ((N \times L \times a^2) - (N \times L \times \pi \times R_{\text{void}}^2)) \cdot \rho_{\text{silica}}$$

$$\text{Total Volume} = V_{cs} = N \times L \times a^2$$

$$\therefore \text{Density} = \rho_{cs} = \left(1 - \pi \frac{R_{\text{void}}^2}{a^2}\right) \cdot \rho_{\text{silica}}$$

$$\therefore \text{Volume Fraction} = f_{cs} = 1 - \frac{\pi}{4} \left(\frac{D_{\text{void}}}{a}\right)^2$$

$$\therefore \text{Lattice Spacing} = a_{cs} = \left(\frac{\pi}{4} \cdot (1 - f_{cs})^{-1}\right)^{1/2} \cdot D_{\text{void}}$$

We may note that for $D_{\text{void}} \geq a$ the structure loses cohesion; i.e. there is a minimum grain density of

$$\rho_{cs_{\text{min}}} = \left(1 - \frac{\pi}{4}\right) \cdot \rho_{\text{silica}} = 0.215 \times 2.0 = 0.43 \{\text{g} \cdot \text{cm}^{-3}\}$$

As we can see, this is sufficient to eliminate this structure from consideration for some templated porous silicas (whose structure we know anyway). Ordinary sol-gel materials have specific grain densities which may (in large pore silicas) be below 0.4; even allowing for the uncertainty of the measurements we would expect them to be on the limit of structural cohesion, and very friable, which is not what we observe.

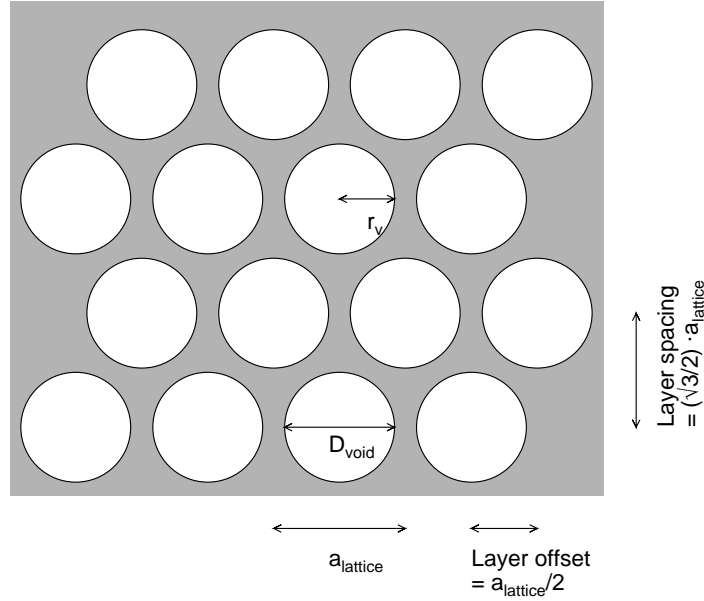


Figure 67: Hexagonal lattice of cylindrical voids.

2D hexagonal close packed array of cylinders.

This should closely model the MCM-41 hexagonal micelle templated silica. The hexagonal unit cell contains one cylindrical pore, but is skewed; thus we shall find it more convenient to consider a rectangular cell of dimensions a , $\sqrt{3}a$, containing two cylinders of radius R_{void} (figure 67).

For N of these of length L :

$$\begin{aligned} \text{Total Mass} &= M_{ch} = ((N \times L \times a \times \sqrt{3} \times a) - (2 \times N \times L \times \pi \times R_{\text{void}}^2)) \cdot \rho_{\text{silica}} \\ \text{Total Volume} &= V_{ch} = N \times L \times a \times \sqrt{3} \times a \\ \therefore \text{Density} &= \rho_{ch} = \left(1 - \frac{2\pi}{\sqrt{3}} \cdot \frac{R_{\text{void}}^2}{a^2}\right) \cdot \rho_{\text{silica}} \\ \therefore \text{Volume Fraction} &= f_{ch} = 1 - \frac{\pi}{2\sqrt{3}} \left(\frac{D_{\text{void}}}{a}\right)^2 \\ \therefore \text{Lattice Spacing} &= a_{ch} = \left(\frac{\pi}{2\sqrt{3}} \cdot (1 - f_{ch})^{-1}\right)^{1/2} \cdot D_{\text{void}} \end{aligned}$$

For $D_{\text{void}} \geq a$ the structure loses cohesion; i.e. there is a minimum grain density of

$$\rho_{ch_{\min}} = \left(1 - \frac{\pi}{2\sqrt{3}}\right) \cdot \rho_{\text{silica}} = 0.0931 \times 2.0 = 0.186 \{\text{g} \cdot \text{cm}^{-3}\}$$

This is well matched by the measured minimum grain density of the templated silicas.

We also conclude that it is possible to construct hexagonal structures of cylinders that

match measured sol-gel silica grain densities.

Random packed array of parallel cylinders.

Random arrays of cylinders have not yet been treated, but we would expect the grain densities to be between the previous two cases (which was the reason for treating the unlikely model of a cubical array). This is thus a possible model that satisfies the observed grain densities.

11.3.3 Spherical Geometries.

There are two possible ways of constructing porous structures with spherical geometry. The first is to have touching spheres of silica, with the pores being the inter-sphere voids. The second is to have intersecting spherical voids in a solid silica matrix. This is effectively the inverse of the first case, but there is the additional degree of freedom in that the intersecting pores may have radii greater than that of the corresponding touching silica spheres. Thus the intersection of the cavities in the second structure with pore diameter $D_{void} > a_s$ (lattice spacing, spherical) will give rise to porosity. It is also worth noting that since the walls can not be of infinite thinness, porosity can also be expected for D_{void} slightly less than a_s . As in the cylindrical case, there is an upper limit beyond which the lattice loses cohesion.

For convenience of display we will represent both the case of silica spheres on a lattice and silica (touching) voids on a lattice as solid spheres.

We will again start with a lattice with a lattice packing density lower than is likely in a real system :

Cubic array of silica spheres.

For a cubic lattice of silica spheres, D_{silica} must equal lattice spacing a (figure 68).

$$\begin{aligned}
 \text{Total Mass} &= M_{ssc} = \left(\frac{4}{3} \cdot N \times \pi \times \left(\frac{a}{2} \right)^3 \right) \cdot \rho_{silica} \\
 \text{Total Volume} &= V_{ssc} = N \times a^3 \\
 \therefore \text{Density} &= \rho_{ssc} = \left(\frac{4\pi}{3} \cdot \frac{(a/2)^3}{a^3} \right) \cdot \rho_{silica} \\
 &= \frac{\pi}{6} \cdot \rho_{silica} \\
 \therefore \text{Volume Fraction} &= f_{ssc} = \frac{\pi}{6}
 \end{aligned}$$

i.e. the grain density is fixed at a constant $\frac{\pi}{6} \cdot \rho_{silica} \approx 0.524 \times \rho_{silica} \approx 1.05 \{g \cdot cm^{-3}\}$

This may be relevant to certain sintered porous glasses, but is too high for sol-gel glasses. Other more likely packing geometries than cubical, such as Hexagonal Close Packed or random, will have even higher grain densities.

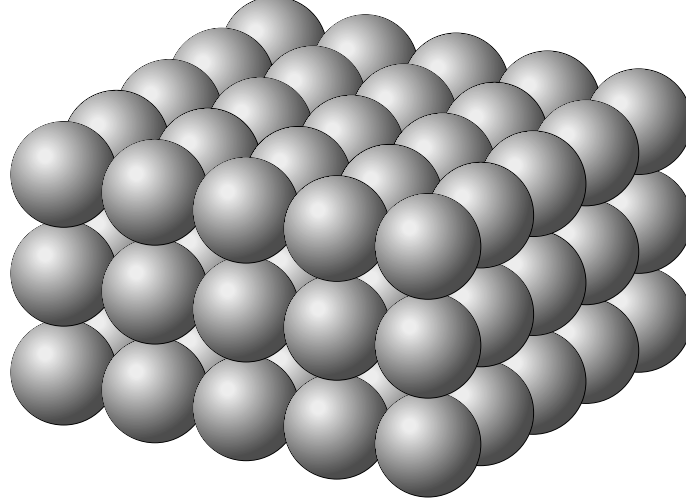


Figure 68: Solid silica spheres on a cubic lattice; this also represents touching spherical voids on a cubic lattice.

Cubic array of spherical voids.

If now we take N lattice units of cubical lattice spacing a , with a spherical void of radius R_{void} centered on each lattice unit (figure 68), and allow R_{void} to exceed $a/2$, we note that we must take care to not include in the calculation of the void volume that part of the sphere that falls outside the lattice cube.

First, for $R_{void} \leq a/2$:

$$\begin{aligned} \text{Total Mass} &= M_{sc} = \left((N \times a^3) - \left(\frac{4}{3} \cdot N \times \pi \times R_{void}^3 \right) \right) \cdot \rho_{silica} \\ \text{Total Volume} &= V_{sc} = N \times a^3 \\ \therefore \text{Density} &= \rho_{sc} = \left(1 - \frac{4\pi}{3} \cdot \frac{R_{void}^3}{a^3} \right) \cdot \rho_{silica} \\ \therefore \text{Volume Fraction} &= f_{sc} = 1 - \frac{\pi}{6} \left(\frac{D_{void}}{a} \right)^3 \\ \therefore \text{Lattice Spacing} &= a_{sc} = \left(\frac{\pi}{6} \cdot (1 - f_{sc})^{-1} \right)^{1/3} \cdot D_{void} \end{aligned}$$

Now, for $a/2 \leq R = R_{void} \leq \sqrt{2}a/2$, the excluded volume that projects beyond the $+x$

face of the lattice cube is given by (see appendix I) :

$$\begin{aligned} V_E &= \int_{a/2}^R \pi(R^2 - x^2) dx \\ &= \pi \left[R^2 x - \frac{1}{3} x^3 \right]_{a/2}^R \\ &= \pi \left(\frac{2}{3} R^3 - \frac{a}{2} R^2 + \frac{1}{24} a^3 \right) \end{aligned}$$

Thus

$$\begin{aligned} V_{void} &= \frac{4}{3} \pi R^3 - 6 \cdot V_E \\ &= \pi \left(-\frac{8}{3} R^3 + 3aR^2 - \frac{1}{4} a^3 \right) \end{aligned}$$

Hence

$$\begin{aligned} \text{Total Mass} &= M_{sc} = ((N \cdot a^3) - (N \pi (-\frac{8}{3} R_{void}^3 + 3a \cdot R_{void}^2 - \frac{1}{4} a^3))) \cdot \rho_{silica} \\ \text{Total Volume} &= V_{sc} = N \cdot a^3 \\ \therefore \text{Density} &= \rho_{sc} = \left(1 - \left(\pi \left(-\frac{8}{3} \left(\frac{R_{void}}{a} \right)^3 + 3 \left(\frac{R_{void}}{a} \right)^2 - \frac{1}{4} \right) \right) \right) \cdot \rho_{silica} \\ \therefore \text{Volume Fraction} &= f_{sc} = 1 - \left(\pi \left(-\frac{1}{3} \left(\frac{D_{void}}{a} \right)^3 + \frac{3}{4} \left(\frac{D_{void}}{a} \right)^2 - \frac{1}{4} \right) \right) \\ \therefore \text{Lattice Spacing} &= a_{sc} \approx (0.689 + 0.76 f_{sc} - 0.251 f_{sc}^2) \cdot D_{void} \end{aligned}$$

where the expression for a_{sc} has been obtained by numerical reversion and inversion of the preceding line.

Figure 69 shows f_{sc} as a function of D_{void}/a . This represents the likely upper bound of the density for spherical voids.

For $D_{void} \geq \sqrt{2} \cdot a$ the silica structure loses cohesion;

\therefore for $R = \sqrt{2}a/2 = a/\sqrt{2}$ the excluded volume is given by :

$$\begin{aligned} V_{E_{min}} &= \frac{\pi}{6} \cdot \left(\sqrt{2} - \frac{5}{4} \right) \cdot a^3 \\ \therefore V_{void_{min}} &= \frac{4}{3} \pi R^3 - 6 \cdot V_E \\ &= \pi \cdot \left(\frac{5}{4} - \frac{2}{3} \cdot \sqrt{2} \right) \cdot a^3 \\ &= 0.965 a^3 \\ \therefore \rho_{sc_{min}} &= \left(1 - \pi \cdot \left(\frac{5}{4} - \frac{2}{3} \cdot \sqrt{2} \right) \right) \cdot \rho_{silica} \end{aligned}$$

This minimum density of $0.0349 \times \rho_{silica} \approx 0.070 \text{ \{g}\cdot\text{ml}^{-1}\}}$ is far lower than is seen in sol-gel silicas (even for such a loose packing geometry of the pores as cubic) and is more typical of aerogel silicas.

Filling factor for spherical voids on a cubic lattice

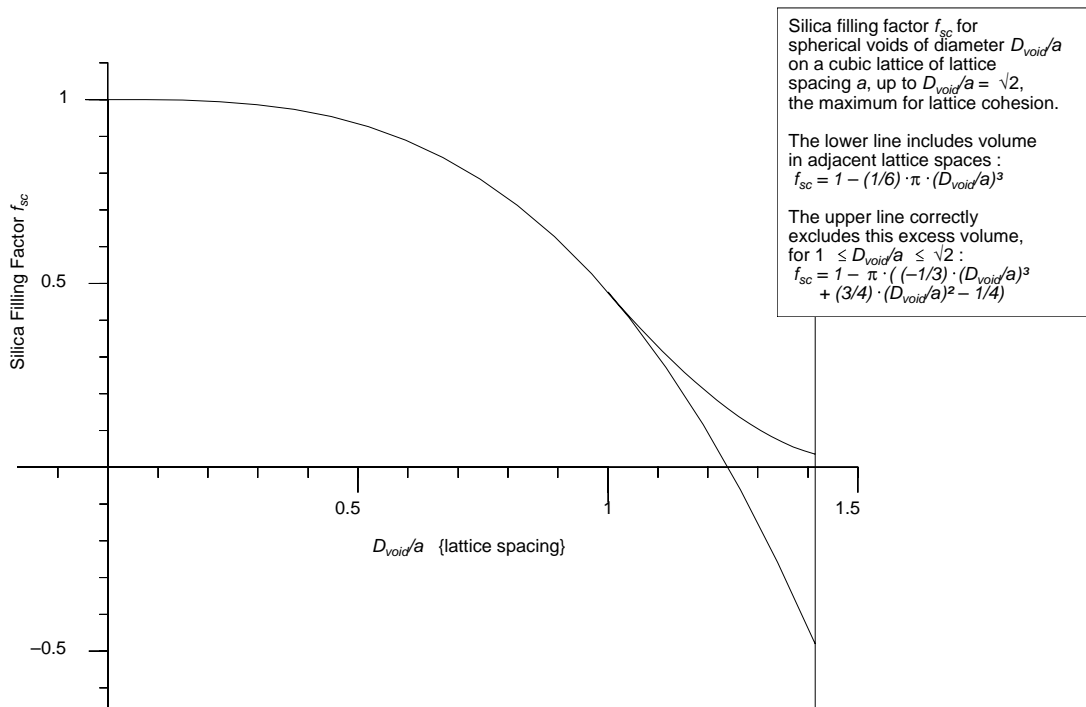


Figure 69: Silica filling factor for spherical voids on a cubic lattice, as a function of $D_{void}/LatticeSpacing$.

Thus we may immediately conclude that if the pores are spherical then the process of formation of sol-gel silicas prevents the generation of mean pore sizes up to the lattice cohesion limit.

Hexagonal Close Packed array of spherical voids.

For spherical voids on a hexagonal close packed array (figure 70), we must again take care to not include in the calculation of the void volume that part of the sphere that falls outside the unit cell.

First, for $R_{void} \leq a/2$:

$$\begin{aligned}
\text{Total Mass} &= M_{sHcp} = \left(\left(\frac{N \times a^3}{\sqrt{2}} \right) - \left(\frac{4}{3} \cdot N \times \pi \times R_{void}^3 \right) \right) \cdot \rho_{silica} \\
\text{Total Volume} &= V_{sHcp} = \frac{N \times a^3}{\sqrt{2}} \\
\therefore \text{Density} &= \rho_{sHcp} = \left(1 - \frac{8 \cdot \pi}{3 \cdot \sqrt{2}} \cdot \frac{R_{void}^3}{a^3} \right) \cdot \rho_{silica} \\
\therefore \text{Volume Fraction} &= f_{sHcp} = 1 - \frac{\pi}{3 \cdot \sqrt{2}} \cdot \left(\frac{D_{void}}{a} \right)^3 \\
\therefore \text{Lattice Spacing} &= a_{sHcp} = \left(\frac{\pi}{3 \cdot \sqrt{2}} \cdot (1 - f_{sHcp})^{-1} \right)^{1/3} \cdot D_{void}
\end{aligned}$$

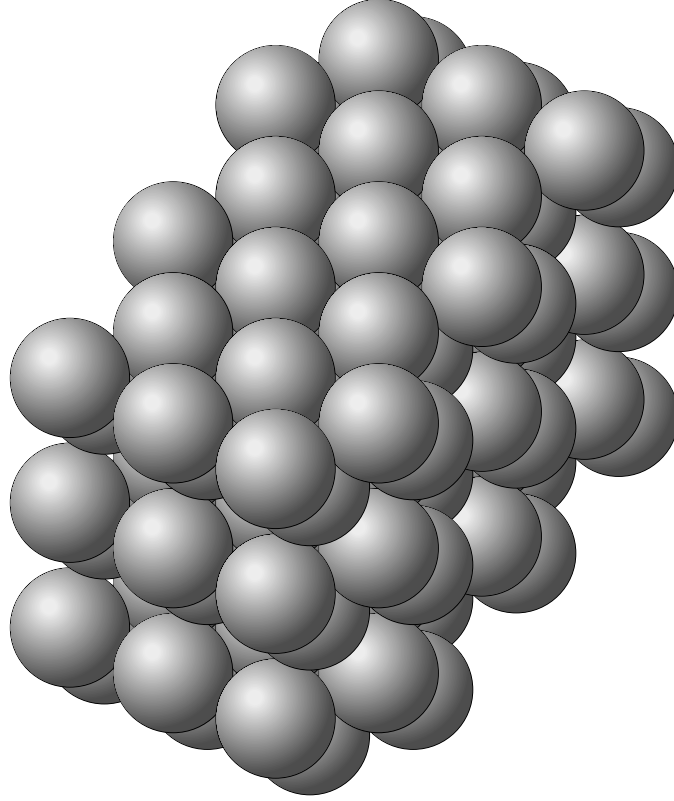


Figure 70: Touching spherical voids on an Hexagonal Close Packed lattice.

For $R_{void} > a/2$ an exact analytic evaluation of the excluded volume is not easy. Since a Monte Carlo calculation of $G(r)$ for spherical voids on an HCP lattice had already been performed for $0.45 \leq \frac{R_{void}}{a} \leq 0.6$, the most straight forward method of obtaining the mean silica filling factor f_{sHcp} over this range was by averaging $G(r)$ for large r . However we may also note that since each unity diameter sphere on an HCP lattice touches 12 other spheres, then up to the lattice cohesive limit we may describe the void volume as

D_{void}/a	$f_{analytic}$	f_{mean}
0.90	0.46019	0.46017
0.94	0.38497	0.38500
1.00	0.25952	0.25953
1.04	0.17801	0.17795
1.10	0.08551	0.08551
1.14	0.04576	0.04575
1.20	(0.02257)	0.01743

Table 9: Monte Carlo values for mean silica filling factor f_{mean} , compared with known analytic values $f_{analytic}$, for spherical voids on an HCP lattice. $D_{void}/a = 1$ corresponds to touching spheres, $D_{void}/a = 2/\sqrt{3} \approx 1.1547$ corresponds to the cohesive limit, above which this analytic description fails.

$$\begin{aligned} V_{void} &= \frac{4}{3}\pi R^3 - 12 \cdot V_E \\ &= \pi \left(-\frac{20}{3}R^3 + 6aR^2 - \frac{1}{2}a^3 \right) \end{aligned}$$

Hence

$$\begin{aligned} \text{Total Mass} &= M_{sc} = \left(\left(\frac{N \cdot a^3}{\sqrt{2}} \right) - N\pi \cdot \left(-\frac{20}{3}R_{void}^3 + 6a \cdot R_{void}^2 - \frac{1}{2}a^3 \right) \right) \cdot \rho_{silica} \\ \text{Total Volume} &= V_{sc} = \frac{N \cdot a^3}{\sqrt{2}} \\ \therefore \text{Density} &= \rho_{sc} = \left(1 - \left(\frac{\pi}{\sqrt{2}} \cdot \left(-\frac{20}{3} \cdot \left(\frac{R_{void}}{a} \right)^3 + 6 \cdot \left(\frac{R_{void}}{a} \right)^2 - \frac{1}{2} \right) \right) \right) \cdot \rho_{silica} \\ \therefore \text{Volume Fraction} &= f_{sc} = 1 - \left(\frac{\pi}{\sqrt{2}} \cdot \left(-\frac{5}{3} \cdot \left(\frac{D_{void}}{a} \right)^3 + 3 \cdot \left(\frac{D_{void}}{a} \right)^2 - 1 \right) \right) \end{aligned}$$

Thus we obtain the values in Table 9, where we see the failure of this analytic description above the lattice cohesive limit. Figure 71 shows f_{sHcp} as a function of D_{void}/a .

Good approximation over the range $0.9 \leq \frac{D_{void}}{a} \leq 1.2$ are given by quintic polynomials:

$$\begin{aligned} \therefore \text{Volume Fraction} &= f_{sHcp} \approx 84.111 - 475.173 \cdot D/a + 1055.798 \cdot (D/a)^2 \\ &\quad - 1144.893 \cdot (D/a)^3 + 605.921 \cdot (D/a)^4 - 125.506 \cdot (D/a)^5 \end{aligned}$$

$$\begin{aligned} \therefore \text{Lattice Spacing} &= a_{sHcp} \approx (0.808 + 1.752f_{sHcp} - 8.245f_{sHcp}^2 \\ &\quad + 23.891f_{sHcp}^3 - 32.063f_{sHcp}^4 + 17.129f_{sHcp}^5) \cdot D_{void} \end{aligned}$$

$$\therefore \text{Minimum Density} = f_{sHcp(min)} \cdot \rho_{silica} \approx 0.03511 \times \rho_{silica} \approx 0.07022 \{g \cdot cm^{-3}\}$$

This is surprisingly close to the value for a cubic lattice.

Filling factor for spherical voids on an HCP lattice

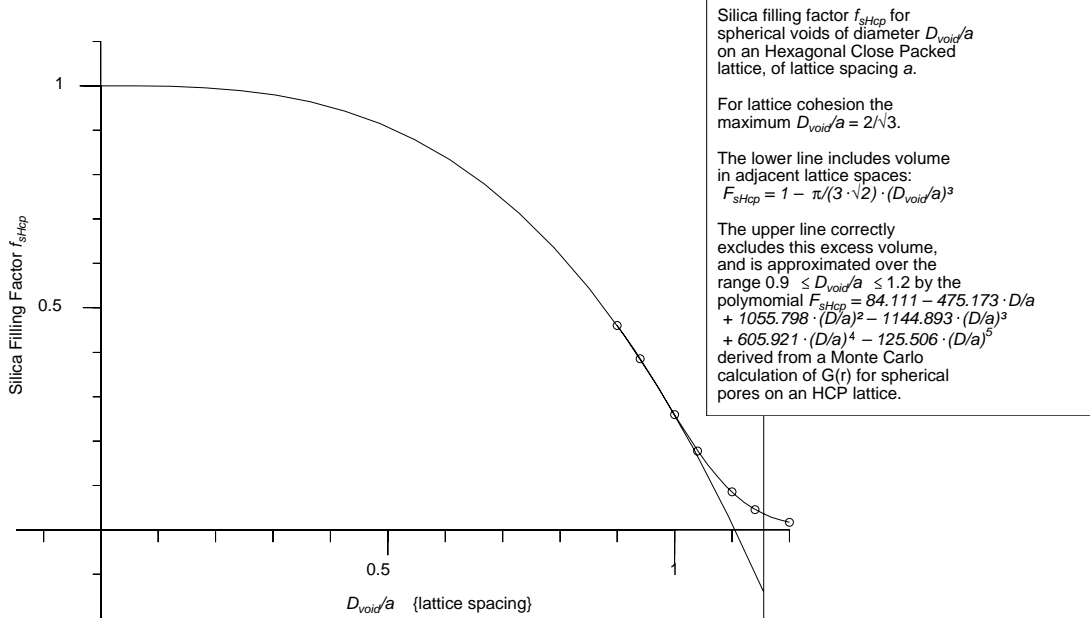


Figure 71: Silica filling factor for spherical voids on an Hexagonal Close Packed lattice, as a function of $D_{void}/LatticeSpacing$.

Random arrays of spherical voids.

First, for $R_{void} \leq a/2$:

If we consider spheres of diameter a packing as random packed spheres, each containing an (initially non-intersecting) pore of diameter D_{void}

$$\begin{aligned} \text{Volume Fraction} &= f_{sr} = 1 - 0.64 \cdot \left(\frac{D_{void}}{a}\right)^3 \\ \therefore \text{Lattice Spacing} &= a_{sr} = (0.64 \cdot (1 - f_{sr})^{-1})^{1/3} \cdot D_{void} \end{aligned}$$

For $R_{void} \geq a/2$:

Considering the filling factors for cubic, random and Hexagonal Close Packed arrays of spherical voids f_{sc} , f_{sr} , f_{sHcp} , for $0 \leq \frac{D_{void}}{a} \leq 1$

$(1 - f_{sc})$, $(1 - f_{sr})$, $(1 - f_{sHcp})$ maintain constant proportions :

$$\begin{aligned} f_{sc} &= 1 - \frac{\pi}{6} \cdot \left(\frac{D}{a}\right)^3, & 1 - f_{sc} &= \frac{\pi}{6} \cdot \left(\frac{D}{a}\right)^3 \approx 0.52 \cdot \left(\frac{D}{a}\right)^3 \\ f_{sr} &= 1 - 0.64 \cdot \left(\frac{D}{a}\right)^3, & 1 - f_{sr} &\approx 0.64 \cdot \left(\frac{D}{a}\right)^3 = 0.64 \cdot \left(\frac{D}{a}\right)^3 \\ f_{sHcp} &= 1 - \frac{\sqrt{2} \cdot \pi}{6} \cdot \left(\frac{D}{a}\right)^3, & 1 - f_{sHcp} &= \frac{\sqrt{2} \cdot \pi}{6} \cdot \left(\frac{D}{a}\right)^3 \approx 0.74 \cdot \left(\frac{D}{a}\right)^3 \end{aligned}$$

Filling factor for spherical voids on various lattices.

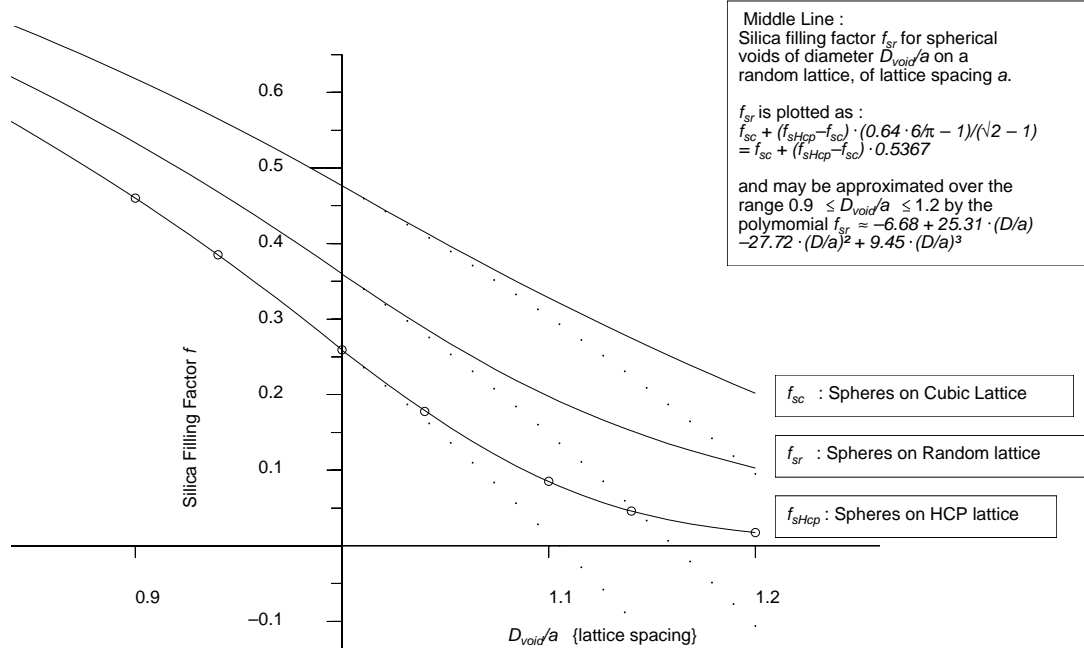


Figure 72:

Filling factors for spherical voids on cubic, random and Hexagonal Close Packed lattices as a function of $D_{void}/LatticeSpacing$.

If we assume that this behaviour is continued for $\frac{D_{void}}{a} > 1$, such that the spheres now intersect, up to the lattice cohesion limit, we may write :

$$(1 - f_{sr}) = \left(\frac{0.64 - \frac{\pi}{6}}{\frac{\sqrt{2} \cdot \pi}{6} - \frac{\pi}{6}} \right) \cdot ((1 - f_{sHcp}) - (1 - f_{sc})) + (1 - f_{sc})$$

$$\begin{aligned} f_{sr} &= \left(\frac{0.64 \cdot \frac{\pi}{6} - 1}{\sqrt{2} - 1} \right) \cdot (f_{sHcp} - f_{sc}) + f_{sc} \\ &= 0.537 \cdot (f_{sHcp} - f_{sc}) + f_{sc} \\ &\approx -131.53 + 600.974 \cdot D/a + 1085.214 \cdot (D/a)^2 \\ &\quad + 976.854 \cdot (D/a)^3 - 440.696 \cdot (D/a)^4 + 79.972 \cdot (D/a)^5 \end{aligned}$$

Although this is an approximation of unknown accuracy, it offers us our best estimate of the silica filling factor f as a function of D_{void}/a for a random lattice, without having to construct an ensemble of self-consistent random lattices, a non-trivial task.

Figure 72 shows f_{sc} , f_{sr} and f_{sHcp} as a function of D_{void}/a .

$$\begin{aligned} \text{Lattice Spacing} = a_{sr} \approx & (0.694 + 1.81f_{sr} - 5.367f_{sr}^2 + 10.558f_{sr}^3 \\ & - 10.162f_{sr}^4 + 4.605f_{sr}^5) \cdot D_{void} \end{aligned}$$

Since spherical voids on both a cubic lattice and an HCP lattice have nearly the same minimum f (0.035) we surmise that the value for a random lattice is the same.

Random arrays of spherical voids in nanoporous silica.

In section 11.2.1 we demonstrated that the neutron scattering data showed no signs of structure indicating that the body of the silica out of which the voids are excised is nanoporous. However if for completeness we will consider such a model, in which the nanoporosity is due to the silica being in the form of small spheres with a diameter in the 10Å region. If we take this model, and assume the spheres are of approximately uniform diameter, and randomly packed, the average density out of which the larger voids is excised will be $\approx 0.64 \times \rho_{silica}$.

Thus the fractional void volume required to match a measured density will be lower in the nanoporous case than in the bulk silica case, by a factor 0.64, and hence the pore lattice spacing could be expected to be increased (with a simple model), for a given D_{void} , by $0.64^{-1/3} = 1.16$.

Such a factor would also apply if, rather than being nanoporous, the silica was microporous on the scale of around $2\mu\text{m}$ diameter, for which we have also found little evidence.

11.4 Density measurements: sol-gel and templated silicas.

Simple measurement of the porous silica density provides information that constrains the range of possible pore geometries within the silica. Given such geometries, we may then use pore diameters as measured by gas adsorption and NMR cryoporometry to deduce likely pore lattice spacings, and pore number densities. This information may then be used to derive calculated neutron scattering data, which we may then compare with measured scattering.

11.4.1 Porous silica density measurements.

Dried silica powder was added to a weighed measuring cylinder, and tapped repeatedly to obtain maximum density, a compression of a few percent being typically observed.

The volume was measured, and the cylinder plus silica re-weighed after further drying. Three measurements were made for each silica. The measured density of the porous silica powder ρ_m was then calculated.

11.4.2 Grain densities and silica filling factors.

Random packing of equal sized spheres is known to give a packing fraction of 0.6366 [Finney, 1970]; particles with a range of sizes will pack more densely, but since the mesh range given by the makers of the sol-gel silicas was fairly tight, an approximate value of 64% was initially assumed for the grains. Thus the calculated density inside the silica grains = $\rho_g \approx \rho_m/0.64$. {g.ml⁻¹}

It was noticed that the templated Behrens silicas compressed by an additional fraction (~0.8) when liquid was added to them, so lower packing fractions were assumed (~50%) Thus for these calculated density inside the silica grains $\rho_g \approx \rho_m/0.5$. {g.ml⁻¹}

Silica	Compression Factor.	Packing Fraction.
Cub14	0.92	0.59
Cub18	0.80	0.51
LMU14	0.67	0.43
LMU16	0.87	0.56
LMU18	0.83	0.53

Table 10: Compression of Behrens silicas on addition of liquid, and deduced grain packing fraction.

These measured densities and packing fractions were then used to calculate the mean density ρ_g in the porous silica grains.

To obtain the filling factor of the silica in the grain f_g , ρ_g was divided by the density of the (voidless) silica lattice, for which a value of 2.2 {g.cm⁻³} was initially assumed. However when we imbibe liquids into porous silicas and measure the density of the (voidless) silica lattice (section 11.5) we find values close to 2.0, thus we use that value here.

The densities of 13 silicas were measured, and their grain silica filling fractions f_g calculated, as shown in table 11. The uncertainties were derived from the likely errors and the root mean square deviations in repeated measurements.

Silica	D_p	ρ_m	ρ_g	f_g
25Å Sigma	25	0.767	1.198	0.599
40Å Merck	40	0.570	0.891	0.445
C60 Unilever B	46.3	0.477	0.745	0.373
60Å Merck	60	0.507	0.792	0.396
100Å Merck	100	0.419	0.655	0.327
140Å Merck	140	0.352	0.550	0.275
C200 Unilever B	171.5	0.272	0.425	0.213
C500 Unilever B	453	0.284	0.444	0.222
Cub 14	24	0.117	0.234	0.091
Cub 18	28	0.168	0.336	0.131
LMU 14	26	0.129	0.258	0.101
LMU 16	28	0.116	0.232	0.091
LMU 18	30	0.106	0.212	0.083
uncertainty		± 0.03	± 0.06	± 0.04

Where, for porous material *Silica*, we have :

D_p : nominal pore diameter. {Å}

ρ_m : measured density of silica powder. {g.ml⁻¹}

ρ_g : calculated density inside the silica grains $\approx \rho_m/0.64$. {g.ml⁻¹}

for templated silicas $\approx \rho_m/0.5$. {g.ml⁻¹}

f_g : filling fraction of silica inside the grain $\approx \rho_g/2.0$.

Table 11: Densities and silica fractions for porous silicas.

It is immediately noticeable that the smaller pore diameter sol-gel silicas are about three times as dense as the ones with the largest pore diameters, and that the micelle templated silicas are about half as dense as even the largest pore diameter sol-gel silicas. It is not clear whether the latter ratio is due to the grain packing density for the templated silicas still being over-estimated.

Any realistic model of the silica porous structure must be consistent with the deduced grain silica filling factors. These measured silica filling factors may be compared with the calculated minimum silica filling factors for the various geometries that have been considered (table 12).

We see that the templated silicas are well matched by cylinders on a hexagonal lattice as expected; that solid silica spheres on a cubic lattice are denser than any but the 25Å silica (and any likely lattice will be even denser) and that the limiting values for the other geometries are far lower than the values measured for the sol-gel silicas and are more typical of aero-gels. We conclude that in sol-gel silicas there is some process that

Pores Lattice	Cylinders Square	Cylinders Hexagonal	S.Spheres Cubic	V.Spheres Cubic	V.Spheres HCP	V.Spheres Random
fmin	0.215	0.0913	0.514	0.0349	0.0351	0.035 ?

Table 12: Minimum silica fraction f for given pore geometries. (S.Spheres : Solid silica spheres, V.Spheres : Spherical voids.)

limits the minimum density achievable. We consider the structure of sol-gels further in section 11.5.3.

11.4.3 Lattice spacings.

Thus we are now able, given the densities of the various sol-gel silicas, and their nominal pore diameters D_{void} , to deduce the corresponding lattice spacing a , for cubic, HCP and (most importantly for the sol-gel silicas) random lattices, in both uniform and nanoporous silica.

Reverting and inverting the expressions for

$$f\left(\frac{D_{void}}{a}\right) \text{ to obtain } \frac{a}{D_{void}}(f)$$

we obtain the coefficients of the quintic polynomials in f :

$$\frac{a_{sc}}{D_{void}} : 0.672 \quad 1.173 \quad -2.996 \quad 7.557 \quad -9.796 \quad 5.59$$

$$\frac{a_{sr}}{D_{void}} : 0.694 \quad 1.81 \quad -5.367 \quad 10.558 \quad -10.162 \quad 4.605$$

$$\frac{a_{sHcp}}{D_{void}} : 0.808 \quad 1.752 \quad -8.245 \quad 23.891 \quad -32.063 \quad 17.129$$

$$\frac{a_{srn}}{D_{void}} : 0.682 \quad 1.329 \quad -3.074 \quad 4.848 \quad -4.01 \quad 1.457$$

where the first term is the constant.

These are valid over the ranges

$$0.8 \leq \frac{a_{sc}}{D_{void}} \leq 1.1 \quad 0.8 \leq \frac{a_{sr}}{D_{void}} \leq 1.1 \quad 0.7 \leq \frac{a_{sHcp}}{D_{void}} \leq 1.1 \quad 0.8 \leq \frac{a_{srn}}{D_{void}} \leq 1.1$$

In chapter 11.5 we will use these polynomials to obtain the lattice spacing a for the

various silicas and lattice geometries, (tables 16 and 17), from the nominal pore diameter D_{void} , as measured by gas adsorption, and the measured silica grain filling factor f_g , as measured by density and imbibation measurements on silica powders.

11.5 Imbibing liquids into porous silicas to determine mean porous parameters by measuring densities and by NMR cryoporometry.

By imbibing liquids into porous silica and measuring the density we may measure the density of the (voidless) silica lattice. By combining information from NMR cryoporometry we may separate the total liquid content into a fraction that is in the pore and a fraction that is in the void space around the silica grains, and thus obtain measured values for the silica and void filling factors inside the grain, and for the packing fraction of the grains.

11.5.1 Silica (voidless) lattice density.

Bulk silica has a range of specific densities of up to 2.6 (quartz crystal), but fused silica is usually in the range 2.1 to 2.2 [Kaye and Laby, 1966].

We may determine the mean density ρ_{silica} of the (voidless) silica lattice in porous sol-gel silicas by the following protocol.

The volume V_{dry} and mass M_{dry} of a quantity of dry porous silica was measured in a 5ml measuring cylinder after repeated tapping to achieve a state of maximum density; then :

$$\begin{aligned} V_{silica} + V_{pore} + V_{packdry} &= V_{dry} \\ \rho_{silica} \cdot V_{silica} &= M_{dry} \end{aligned}$$

Where V_{silica} , V_{pore} , $V_{packdry}$ are respectively the volumes of the (voidless) silica lattice, the pores and the packing void around the dry porous silica grains.

Excess liquid of known density ρ_{liquid} was added, such that all open pore and grain packing void space was filled. The measuring cylinder was inverted repeatedly to remove trapped air bubbles, and then left overnight to allow the silica grains to settle. Excess liquid was then removed with a pipette and cotton wool buds, to just leave the liquid in pore and packing void space. The volume V_{wet} and mass M_{wet} were then measured.

The volumes dry and wet were slightly different – this does contain useful information, in that it tells us that the packing dry and wet are slightly different; we may obtain both.

Then :

$$\begin{aligned} V_{silica} + V_{pore} + V_{packwet} &= V_{wet} \\ \rho_{silica} \cdot V_{silica} + \rho_{liquid} \cdot (V_{pore} + V_{packwet}) &= M_{wet} \end{aligned}$$

Hence we have :

$$\begin{aligned} \rho_{liquid} \cdot (V_{pore} + V_{packwet}) &= M_{wet} - M_{dry} \\ \therefore V_{pore} + V_{packwet} &= \frac{M_{wet} - M_{dry}}{\rho_{liquid}} \\ \therefore V_{silica} &= V_{wet} - \frac{M_{wet} - M_{dry}}{\rho_{liquid}} \\ \therefore \rho_{silica} &= \frac{M_{dry}}{V_{silica}} \\ &= \frac{M_{dry}}{V_{wet} - \frac{M_{wet} - M_{dry}}{\rho_{liquid}}} \end{aligned}$$

These measurements were performed on seven porous silicas; the results and the calculated density of the (voidless) silica lattice is shown in table 13. We see that we find a density of 2.02 ± 0.09 {g·ml⁻¹} for all the silicas with the exception of the two largest pore Unilever B silicas, which have densities of 1.82, 1.81. It is probable that these results are reliable to at least two significant figures, but this can only be established by repeating the measurements.

Silica	M_{dry} {g}	V_{dry} {ml}	M_{wet} {g}	V_{wet} {ml}	V_{silica} {ml}	ρ_{silica} {g·ml ⁻¹ }
25Å Sigma	1.0	1.41	1.9743	1.47	0.497	2.01
40Å Merck	1.0	1.78	2.5179	2.02	0.504	1.98
60Å Unilever B	1.0	2.00	2.6858	2.20	0.517	1.93
60Å Merck	1.0	2.32	2.2314	2.75	0.516	1.94
100Å Merck	1.0	2.34	3.2075	2.68	0.474	2.11
200Å Unilever B	1.0	3.32	5.3540	4.90	0.550	1.82
500Å Unilever B	1.0	3.28	4.0050	3.56	0.553	1.81

Table 13: Wet and dry porous silica masses and volumes, normalised to unity dry silica mass, and deduced volumes and densities for the (voidless) silica lattices.

11.5.2 Measuring pore and packing void volume.

The above protocol can not on its own separate pore and packing void volume. However if we also use NMR cryoporometry, where we freeze the liquid and make use of the fact that liquid in the small pores melts at a different temperature from the liquid in the larger packing void space around the grains, we may with care obtain accurate values for the total pore volume V_{pore} of the silica (table 7). It is necessary to correct for the different relaxation times for the liquid in the pores compared with that in the inter-grain void space by measuring at more than one τ time (see chapter 7.1 and appendix E). Thus we obtain the dry and wet packing volumes for seven porous silicas (table 14).

Silica	V_{dry} {ml}	V_{wet} {ml}	V_{silica} {ml}	V_{pore} {ml}	V_{pkd} {ml}	V_{pkw} {ml}
25Å Sigma	1.41	1.47	0.497	0.34	0.57	0.63
40Å Merck	1.78	2.02	0.504	0.59	0.69	0.93
60Å Unilever B	2.00	2.20	0.517	0.71	0.78	0.98
60Å Merck	2.32	2.75	0.516	0.68	1.13	1.56
100Å Merck	2.34	2.68	0.474	0.95	0.92	1.26
200Å Unilever B	3.32	4.90	0.550	1.68	1.09	2.67
500Å Unilever B	3.28	3.56	0.553	1.57	1.16	1.44

Table 14: For a unity mass of dry silica we may measure from imbibation measurements the dry and wet total volumes, and the volumes of the silica matrix, and from NMR Cryoporometry the total pore volume (table 7); hence we may deduce the dry and wet packing volumes for seven porous silicas.

Thus we now know V_{silica} , V_{pore} , $V_{packwet}$, $V_{packdry}$ and hence may obtain measured values for the silica fraction inside the porous grain f_g and for the grain packing fraction f_{pack} (both wet and dry) :

$$f_g = \frac{V_{silica}}{V_{silica} + V_{pore}}$$

$$f_{pack} = \frac{V_{silica} + V_{pore}}{V_{silica} + V_{pore} + V_{pack}}$$

We notice a decrease in silica fraction in the grain with larger pore diameter (with the exception of 500Å pore diameter, which is consistently out of sequence); if we compare these values with those in table 11, where we assumed a grain packing density of 0.64, and a silica density of 2.0, we see that we have a fractional difference in f_g that ranges from 1% in the case of the 25Å silica to around 17% in the case of the 200Å and 500Å

Silica	f_g	f_{pkd}	f_{pkw}
25Å Sigma	0.593	0.594	0.570
40Å Merck	0.460	0.615	0.542
60Å Unilever B	0.423	0.612	0.556
60Å Merck	0.432	0.514	0.434
100Å Merck	0.333	0.608	0.531
200Å Unilever B	0.246	0.672	0.455
500Å Unilever B	0.261	0.646	0.595

Table 15: From imbibation measurements and from NMR Cryoporometry we may deduce the silica fraction in the grain f_g and the dry and wet grain packing fractions f_{pkd} , f_{pkw} , for seven porous silicas.

silicas. We note that we measure a substantially lower density for the silica in the last two cases than was assumed.

We see that 500Å silica dry packs very close to the theoretical random packing of spheres, 200Å silica packs more densely, but the remainder pack less densely at around 95% of random packing density, with 60Å Merck only packing at 80% of random packing density. Again, probably 2 figures are significant.

The less dense wet packing implies a linear increase in grain spacing of a few percent; for 100Å Merck SiO₂ it is 5% and, as the S.E.M. micrographs showed that the average grain diameter was about 150μm, this implies an interfacial layer of water between the grains of about 7μm, if uniform.

In section 11.3 we derive relationships between the pore diameter D_{void} and the lattice spacing a for various pore packing geometries. Inserting measured grain silica filling factors f_g into these we obtain table 16.

Silica	D_{void}	D_v/a_{ch}	D_v/a_{sc}	D_v/a_{sr}	D_v/a_{sHcp}
25Å Sigma	25	0.67	0.92	0.86	0.82
40Å Merck	40	0.77	1.01	0.94	0.90
60Å Unilever B	46.3	0.80	1.04	0.97	0.92
60Å Merck	60	0.79	1.03	0.96	0.91
100Å Merck	100	0.86	1.10	1.01	0.97
200Å Unilever B	171.5	0.91	1.16	1.07	1.01
500Å Unilever B	453	0.90	1.15	1.06	1.00

Table 16: From measured grain silica filling factors f_g we obtain ratios of pore void diameter D_{void} to lattice spacing a for various pore packing geometries, for seven porous silicas.

We see that for the case of cylinders on a hexagonal lattice D_v/a_{ch} is consistently less than unity, implying a cohesive lattice; permeability is ensured by the cylindrical pores, so this is a viable structure.

For the extreme case of spherical voids on a cubical lattice D_v/a_{sc} is mostly above unity, ensuring permeability.

At first sight the fact that for the cases of spherical pores on a random lattice and the extreme case of spherical pores on an HCP lattice D_v/a_{sr} and D_v/a_{sHcp} are in many cases below unity would seem to imply impermeability; however if we note that in practice a silica wall can not be infinitely thin, we may obtain permeability in practice. The minimum thinnesses required are 3.5\AA in the random packing case, and 5\AA in the HCP case.

In table 17 we show the corresponding pore lattice spacings – one might expect scattering experiments to be more sensitive to lattice spacing rather than pore diameter.

Silica	D_{void} {\AA}	a_{ch} {\AA}	a_{sc} {\AA}	a_{sr} {\AA}	a_{sHcp} {\AA}
25\AA Sigma	25	37.3	27.2	29.1	30.5
40\AA Merck	40	51.9	39.6	42.3	44.5
60\AA Unilever B	46.3	57.9	44.7	47.9	50.4
60\AA Merck	60	75.8	58.3	62.5	65.6
100\AA Merck	100	116.6	91.2	98.5	103.5
200\AA Unilever B	171.5	188.5	147.6	161	170.4
500\AA Unilever B	453	503	394	429	453

Table 17: Lattice spacing a deduced from silica grain filling factor f_g , for various pore geometries, for seven porous silicas.

11.5.3 Deducing pore throat diameters.

If we plot the data in table 17, such that we plot lattice spacing a against pore diameter D_{pore} for the various pore packing models, we obtain reasonable straight line relationships; fitting, we find the lines intercept the y axis at small finite positive values :

$$a_{ch} : 8.2 \{\text{\AA}\}, \quad a_{sc} : 5.2 \{\text{\AA}\}, \quad a_{sr} : 4.9 \{\text{\AA}\}, \quad a_{sHcp} : 4.8 \{\text{\AA}\}$$

In the case of a_{ch} (cylinders on a hexagonal lattice) the 8.2\AA may represent a genuine minimum wall thickness between the cylinders. However if this were the case for the

spheres we would have little permeability; since we know that they are permeable we thus make the assumption that these figures are telling us about the minimum silica wall thickness that can stand between two pores.

In figure 73 we model two average pores for 40Å Merck silica, assuming spherical pores on a random packed lattice, with a 5Å minimum wall thickness; we see we obtain permeability where we would not otherwise expect it. We may deduce by Pythagoras the diameter of the throats between the pores for the various models and silicas :

$$D_{throat} = (D_{void}^2 - (a - Wall_{min})^2)^{\frac{1}{2}}$$

as shewn for the case of spheres on a random packing in table 18.

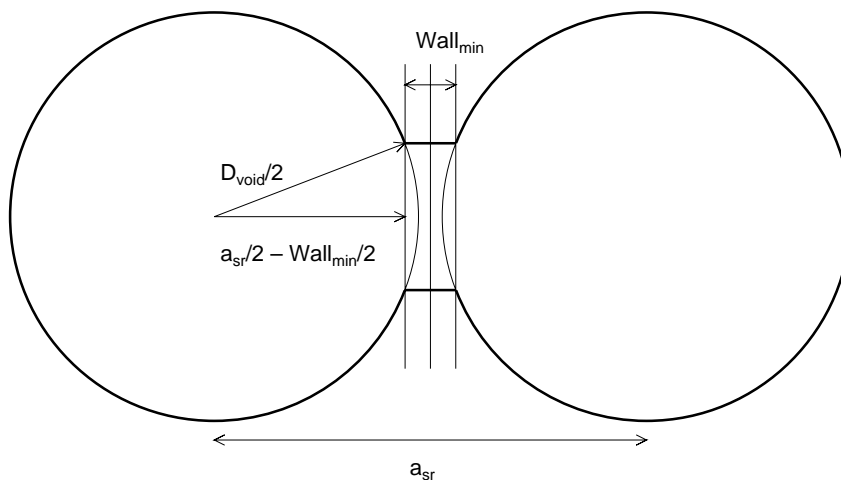


Figure 73: Idealised model of throat between two pores in 40Å Merck SiO₂, assuming spherical pores on a random packed lattice, and assuming a minimum silica wall thickness of 5Å.

We see that the throat diameters are, with some variation, a fairly constant one third of the pore diameters. i.e. with this constraint and the assumption of a minimum silica wall thickness of about 5Å we may 'construct' porous media whose density changes by a factor of 3 over the range of pore diameters 25Å → 500Å, as does the real sol-gel silica, and yet maintain permeability.

We may thus substitute

$$D_{throat} = \frac{1}{3} \cdot D_{void}$$

Silica	D_{pore} {Å}	a_{sr} {Å}	D_{throat} {Å}	D_{th}/D_p {%}
25Å Sigma	25	29.1	6.78	27
40Å Merck	40	42.3	14.3	36
60Å Unilever B	46.3	47.9	17.3	37
60Å Merck	60	62.5	17.3	29
100Å Merck	100	98.5	35.4	35
200Å Unilever B	171.5	161	71.3	42
500Å Unilever B	453	429	160	35

Table 18: For seven silicas covering a $1 \rightarrow 20$ range in pore diameter D_{pore} we tabulate the lattice spacings for spheres on a random lattice a_{sr} , the deduced pore throat diameters D_{throat} , and the ratio of these to the pore diameters D_{th}/D_p .

into the above expression, and hence may deduce for lattice spacing

$$a = Wall_{min} + \frac{2\sqrt{2}}{3} \cdot D_{void}$$

We note that for a pore on an HCP lattice there will be twelve 'throats' to neighbouring pores – we might assume that this would be slightly reduced in the case of a random packed lattice – this would reduce the surface area of the pore to about 50% of that of an intact sphere of the same diameter, if the pore throats are about $1/3$ of the pore diameter as deduced above.

An experiment was performed in which large pore diameter Trisopor silica was filled with a precursor, which was then decomposed to MgO. This was then heated to 500°C , to form nanocrystals, with an expected volume reduction to $1/5^{th}$. NMR cryoporometry runs were performed on the initial and final material, see figure 74. (We note that the nominal diameter of the Trisopor is measured using mercury intrusion, not gas adsorption.) The pore volume was shown to reduce by about 19%, while the pore diameters reduced by about 24% (peaks) to 25% (medians). This is consistent with the MgO being deposited on the pore wall uniformly in a layer of thickness about $1/8^{th}$ of the pore diameter, over an area about 44% of the area of the sphere – this in turn is consistent with there being an average of ten throats, of diameter $1/3^{rd}$ pore diameter according to the above model, excised out of the pore wall.

1614Å Trisopor pore size distribution, + filled with MgO.

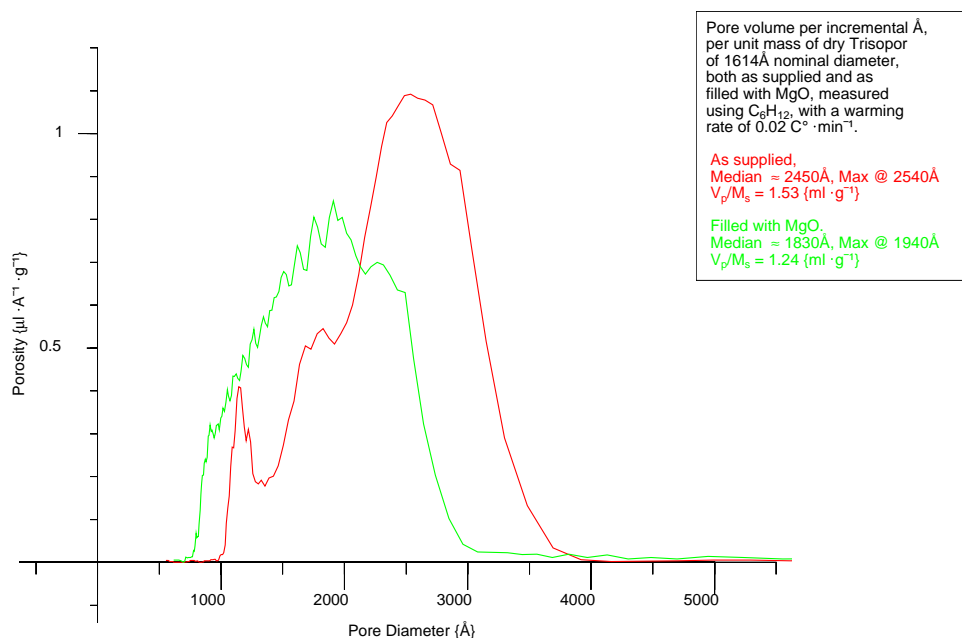


Figure 74: Large pore silica pore size distributions as measured by NMR Cryoporometry, before and after depositing MgO nanocrystals.

11.6 Summary.

Thus we now have evaluated the mean properties of a range of possible model pore structures; we have evaluated the likely range of silica filling factors f_{silica} , for comparison with measured bulk values and as a check by comparison with the mean values we shall generate by Monte-Carlo methods for models with variance around the mean.

Using pore diameters as measured by gas adsorption and NMR Cryoporometry we have calculated likely values for the pore lattice spacings for the various models, for comparison with neutron scattering results.

We have measured the density of the (voidless) silica matrix, and shown that it is unlikely to be either nano or micro porous, other than the known measured ($25\text{Å} \rightarrow 2000\text{Å}$) pores. We have measured the grain packing fractions for dry and wet grains.

We have shown that we may construct model silicas that mimic measured sol-gel silica densities with the constraints that the minimum pore wall thickness is 5Å , and the pore throat diameters are about $1/3^{rd}$ of the pore diameters.

Chapter 12

Neutron scattering theory.

12.1 Wave – Particle duality.

Particles and waves have properties such that it is possible to treat either as particles or as waves [De Broglie, 1929]. Thus a particle with momentum \mathbf{p} also has a wave vector \mathbf{k} , such that [Planck, 1929] :

$$\mathbf{k} = \mathbf{p} \frac{2\pi}{h} = \frac{\mathbf{p}}{\hbar}$$

and

$$|\mathbf{k}| = k = \frac{2\pi}{\lambda} = \frac{p}{\hbar}$$

Thus neutrons scatter from nuclei in matter; interference between the wave vectors gives us spatial information such that short range (atomic) spacings give rise to neutron diffraction, and longer range variations in the distribution of matter give rise to small angle scattering neutron scattering (SANS).

12.2 Scattering and density distribution relationships.

We wish to study the density distributions in porous silica; thus we consider the elastic scattering of neutrons from an instantaneous distribution of scattering centres.

The observed scattering has incoherent and coherent components. For hydrogen the scattering intensity shows little variation in the small-angle region; thus water makes a good small-angle calibration standard (see section 14.1). For dry silica the coherent scattering dominates and we may use the intensity variation in the scattering to determine the spatial structure on an atomic and mesoscopic scale.

If one has an incident plane monochromatic wave $A_i \exp(i\mathbf{k}_i \cdot \mathbf{r})$ of neutrons with wave vector \mathbf{k}_i , that is scattered through angle θ_s so that one has a final wave vector \mathbf{k}_f , then one has a scattering vector (see figure 75)

$$\mathbf{Q} = \mathbf{k}_i - \mathbf{k}_f$$

and a resulting wave [Cowley, 1975]

$$A_i \exp(i\mathbf{k}_i \cdot \mathbf{r}) + \frac{A_i b}{r} \exp(i\mathbf{k}_f \cdot \mathbf{r})$$

where b has dimensions length, and is called the "scattering length".

Thus for elastic scattering through angle θ_s , $|\mathbf{k}_i| = |\mathbf{k}_f|$, and we have [Newport et al., 1988]

$$|\mathbf{Q}| = Q = 2 \cdot |\mathbf{k}_i| \cdot \sin \frac{\theta_s}{2} = \frac{4 \cdot \pi}{\lambda} \cdot \sin \frac{\theta_s}{2}$$

where λ is the wavelength.

When the scattering is from a lattice, we have the Bragg relationship. For scattering by two features separated by a distance d_B , where the neutron is scattered through twice an angle θ_B (see figure 76), we have for order m of the scattering :

$$d_B = \frac{m \cdot \lambda}{2 \cdot \sin \theta_B} = \frac{m \cdot \lambda}{2 \cdot \sin \frac{\theta_s}{2}} = \frac{m \cdot \lambda}{2 \cdot Q \cdot \frac{\lambda}{4\pi}} = \frac{2\pi \cdot m}{Q}$$

Thus the relationship between the Bragg scattering length d_B and Q (the modulus of the scattering vector) is given by :

$$\frac{d_B}{m} \{\text{\AA}\} = \frac{2\pi \{\text{radians}\}}{Q \{\text{radians} \cdot \text{\AA}^{-1}\}}$$

It is vital to remember the presence of the 2π , if we are to obtain correctly scaled reciprocal relationships; it is conventional to give Q the dimensions $\{\text{\AA}^{-1}\}$, but this implies one might just take the reciprocal to obtain a length scale. Thus here we will use the units $\{\text{radians} \cdot \text{\AA}^{-1}\}$ to remind us of the presence of the 2π .

Thus in the weakly scattering (Born) approximation, for a scattering field $\phi(\mathbf{r})$ we seek

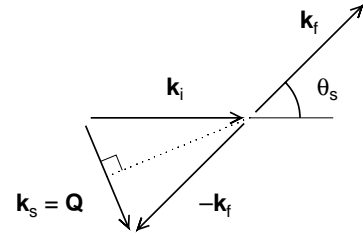


Figure 75: Vector diagram for elastic scattering.

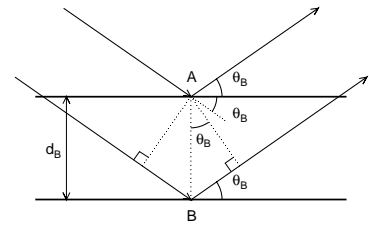


Figure 76: Bragg scattering.

as a solution of the wave equation [Feigin and Svergun, 1987]

$$\left(\nabla^2 + k_i^2 + \nu\phi(\mathbf{r})\right)\Psi(\mathbf{r}) = 0$$

the scattered wave $\Psi(\mathbf{r})$, where ∇^2 is the Laplace operator, and ν gives the strength of the interaction.

We note that the dimensions of the nuclei that are scattering are far smaller than the wavelengths of the neutrons we are using, and the scattered waves are spherical and isotropic.

We can not measure the amplitude and phase of the scattered wave directly, just the flow of energy or number of scattered particles, proportional to the square of the scattering amplitude at large distances :

$$\frac{d\sigma}{d\Omega} = \frac{A_i^2}{r^2}|f(\mathbf{q})|^2 = \frac{A_i^2}{r^2}I(\mathbf{q})$$

where Ω is a solid angle, and $I(\mathbf{q})$ is the scattering intensity or differential cross section, and has the dimensions length squared, and

$$f(\mathbf{q}) = \frac{\nu}{4\pi} \cdot \int_V \phi(\mathbf{r}) \exp(i\mathbf{q}\mathbf{r}) d\mathbf{r}$$

is the amplitude of the elastic scattering due to field $\phi(\mathbf{r})$ (i.e. in our case, $\rho(\mathbf{r})$).

We define a number of representations of the number density distribution in the scattering body, where r is always measured from an existing atom [Newport et al., 1988]

$$\begin{aligned} \rho_n(r) &= \text{number of atoms per unit volume at radius } r. \\ \rho_{\infty n} &= \langle \rho_n(r) \rangle = \text{mean number of atoms per unit volume.} \\ J(r) &= 4\pi r^2 \rho_n(r) = \text{radial distribution function.} \\ J_{\infty}(r) &= 4\pi r^2 \rho_{\infty n}(r) = \text{the smooth curve about which } J(r) \text{ oscillates.} \\ g(r) &= \frac{J(r)}{J_{\infty}(r)} = \text{pair distribution function.} \end{aligned}$$

Similarly we may define a number of representations of the continuous density distribution in the scattering body, where r is always measured from a point in the solid [Feigin

and Svergun, 1987]:

$$\begin{aligned}
 \rho(r) &= \text{mass per unit volume at radius } r. \\
 \rho_\infty &= \langle \rho(r) \rangle = \text{mean density.} \\
 P(\mathbf{r}) &= \rho(\mathbf{r}) * \rho(-\mathbf{r}) = \text{Patterson function.} \\
 \gamma(r) &= \langle \rho(r) * \rho(-r) \rangle = \text{density correlation function.} \\
 G(r) &= 1 + \langle \frac{\rho(r)}{\rho_\infty} * \frac{\rho(-r)}{\rho_\infty} \rangle = \text{normalised density correlation function.}
 \end{aligned}$$

where * represents convolution.

Thus $\gamma(r)$ represents the averaged self-convolution of the density distribution.

Then we have

$$I(\mathbf{q}) = \int_V P(\mathbf{r}) \exp(i\mathbf{q}\mathbf{r}) d\mathbf{r}$$

Since the Patterson function is even (symmetric) we note that

$$\begin{aligned}
 \int_{-\infty}^{\infty} f_s(\theta) \cdot \exp(i\theta) d\theta &= \int_{-\infty}^{\infty} f_s \cdot \cos(\theta) d\theta + \int_{-\infty}^{\infty} f_s \cdot i \cdot \sin(\theta) d\theta \\
 &= \int_{-\infty}^{\infty} f_s \cdot \cos(\theta) d\theta + 0 \\
 \therefore I(\mathbf{q}) &= \int_V P(\mathbf{r}) \cos(\mathbf{q}\mathbf{r}) d\mathbf{r}
 \end{aligned}$$

The porous silica we are scattering from is in the form of fine grains of random orientation, and thus we must perform a spherical average :

$$\begin{aligned}
 I(q) &= \frac{1}{4\pi} \int_{\Omega} I(\mathbf{q}) d\Omega \\
 &= \frac{1}{4\pi} \int_0^\infty \int_0^{4\pi} r^2 dr d\omega \int_0^{4\pi} d\Omega P(\mathbf{r}) \cos(\mathbf{q}\mathbf{r}) \\
 &= \int_0^\infty r^2 dr \int_0^{4\pi} P(\mathbf{r}) d\omega \frac{1}{4\pi} \int_0^{4\pi} \cos(\mathbf{q}\mathbf{r}) d\Omega \\
 &= 4\pi \int_0^\infty r^2 \gamma(r) \frac{\sin(q \cdot r)}{q \cdot r} dr
 \end{aligned}$$

where we note that averaging $\cos(\mathbf{q}\mathbf{r})$ over all orientations gives us :

$$\langle \cos(\mathbf{q}\mathbf{r}) \rangle = \int_0^\pi \cos(qr \cdot \cos(\phi)) \cdot \frac{\sin(\phi)}{2} d\phi = \frac{\sin(qr)}{qr}$$

and that

$$\gamma(r) = \frac{1}{4\pi} \cdot \int_0^{4\pi} P(\mathbf{r}) d\omega = \langle \rho(\mathbf{r}) * \rho(-\mathbf{r}) \rangle = \langle \int_V \rho(r') \rho(r' + r) dr' \rangle$$

where * denotes convolution.

We thus obtain the transform pair [Newport et al., 1988] [Feigin and Svergun, 1987] :

$$\begin{aligned} I(q) = S(q) - 1 &= 4\pi \cdot \rho_\infty \cdot \int_0^\infty r^2 \cdot (G(r) - 1) \cdot \frac{\sin(q \cdot r)}{q \cdot r} dr \\ \frac{\gamma(r)}{\rho_\infty} = G(r) - 1 &= \frac{1}{2\pi^2 \cdot \rho_\infty} \cdot \int_0^\infty q^2 \cdot (S(q) - 1) \cdot \frac{\sin(q \cdot r)}{q \cdot r} dq \end{aligned}$$

where the constants have been adjusted so that a complete cycle of transformation returns the initial function.

Thus we have :

$$I(q) = S(q) - 1 = \frac{2\pi \cdot \rho_\infty}{q} \cdot \int_{-\infty}^\infty r \cdot (G(r) - 1) \cdot \sin(q \cdot r) dr$$

Since $G(r)$ is even (symmetric), $r \cdot G(r)$ is odd (anti-symmetric), thus we note that

$$\begin{aligned} \int_{-\infty}^\infty f_a(\theta) \cdot \exp(i\theta) d\theta &= \int_{-\infty}^\infty f_a(\theta) \cdot \cos(\theta) d\theta + \int_{-\infty}^\infty f_a(\theta) \cdot i \cdot \sin(\theta) d\theta \\ &= 0 + \int_{-\infty}^\infty f_a(\theta) \cdot i \cdot \sin(\theta) d\theta \\ \therefore \int_{-\infty}^\infty f_a(\theta) \cdot \sin(\theta) d\theta &= -i \cdot \int_{-\infty}^\infty f_a(\theta) \cdot \exp(i\theta) d\theta \end{aligned}$$

$$\begin{aligned} \therefore I(q) = S(q) - 1 &= -i \cdot \frac{2\pi \cdot \rho_\infty}{q} \cdot \int_{-\infty}^\infty r \cdot (G(r) - 1) \cdot e^{i \cdot q \cdot r} dr \\ \therefore \frac{\gamma(r)}{\rho_\infty} = G(r) - 1 &= -i \cdot \frac{1}{4\pi^2 \cdot \rho_\infty \cdot r} \cdot \int_{-\infty}^\infty q \cdot (S(q) - 1) \cdot e^{i \cdot q \cdot r} dq \end{aligned}$$

and we now have our relationships expressed in terms of standard Fourier transforms, the imaginary results of which give us $S(q) - 1$, $G(r) - 1$.

We may note that we can also express the above two transforms in the form :

$$\begin{aligned} I(q) &= \frac{2\pi}{q} \cdot \frac{\partial}{\partial q} \int_{-\infty}^\infty \gamma(r) \cdot e^{i \cdot q \cdot r} dr \\ \gamma(r) &= \frac{1}{4\pi^2 \cdot r} \cdot \frac{\partial}{\partial r} \int_{-\infty}^\infty I(q) \cdot e^{i \cdot q \cdot r} dq \end{aligned}$$

12.3 Scattering from porous media.

The above relationships are effectively expressed in a form where the mean density of the solid is normalised to unity. However we wish to consider porous media, where we have in effect three densities to consider, as discussed in sections 11.2.1, 11.2.3, 11.4, 11.5 : the bulk (as macroscopically measured) powder density ρ_m , the average density within the grains ρ_g , and the density of the (voidless) silica matrix ρ_s . It is the last two that are relevant on the scale of neutron scattering.

We thus see that the bulk density for porous media is not a convenient constant to normalise to, as it will vary with the porous structure that we are trying to measure. We identify ρ_∞ in the above equations with the grain density ρ_g , and obtain as a useful characteristic of a porous silica :

$$f_g = \text{fraction of grain filled with silica} = \frac{\rho_g}{\rho_s} = \frac{\rho_\infty}{\rho_s}$$

For porous media it is reasonable to assume ρ_s is reasonably constant; thus we obtain :

$$I(q) = S(q) - 1 = 4\pi \cdot \rho_s \cdot \int_0^\infty r^2 \cdot (f_g \cdot G(r) - f_g) \cdot \frac{\sin(q \cdot r)}{q \cdot r} dr$$

We note [Feigin and Svergun, 1987]

$$\gamma(0) = \rho_\infty^2 \cdot V$$

where V is the volume. Thus we write :

$$\gamma_0(r) = \frac{\gamma(r)}{\gamma(0)} = \frac{1}{4\pi} \cdot \int_0^{4\pi} d\omega \frac{1}{V} \cdot \int_0^\infty \frac{\rho(r')}{\rho_\infty} \frac{\rho(r' + r)}{\rho_\infty} dr'$$

$\gamma_0(r)$ is thus the characteristic function [Porod, 1951] for a structure excised out of a constant density material, and depends only on the spatial distribution of the material. For our models of porous silica we have in effect normalised ρ_s to unity.

$\gamma_0(r)$ thus represents the probability of finding a solid region within the porous structure at distance r from a given point within the solid. Thus at $r = 0$ we must be in the solid, and $\gamma_0(r) = 1$; for a finite body of maximum dimensions D , $\gamma_0(r > D) = 0$. In appendix K we calculate $F(r, R) = \gamma_0(r)$ for a sphere, and in appendix L $\gamma_0(r)$ for an infinite plane slab.

In a porous medium $\gamma_0(r)$ will decrease (possibly with oscillations) from 1 at $r = 0$ to an average value of $\frac{\rho_\infty}{\rho_s} = f_g$ at $r = \infty$. Thus we use $\gamma_0(r)$ as a convenient expression to evaluate in chapter 15, where we calculate the normalised solid-solid density correlation function for a number of idealised porous structures, with density ρ_s and lattice spacing a normalised to unity. We see good agreement between the calculated $\gamma_0(r)$ at large r and f_g calculated analytically. We note that $\gamma_0(r)$ s calculated by Monte-Carlo integration go to f_g at large r , while measured $\gamma(r)$ s, $\gamma_0(r)$ s go to zero, and must have $\rho_\infty = \gamma_g$ restored using measured densities.

In section 16.2 we transform measured $I(q)$ scattering data for dry porous silicas to $\gamma(r)$, and restore the densities as measured in chapter 11.5; thus we plot $G_\rho(r) = (\rho_s - \rho_g) \cdot \gamma_0(r) + \rho_g$, where the density varies from ρ_s at $r = 0$ (fairly constant for most silicas) to $\rho_g = f_g \cdot \rho_s$ at large r . The latter values vary widely with the construction of the silica. We will often for convenience just use the symbol $G(r)$ to represent both the function $G_\rho(r)$ and the Monte-Carlo case with ρ_s normalised to unity.

In practice we know our porous structures are actually constructed from atoms; thus the scattering we actually measure will consist of diffraction from the structure of the discrete atomic distributions at large q , with small angle scattering from the larger scale porous structure at lower q . As we see in sections 11.2.2, 16.1, even for the smallest pore diameter studied, the scattering from the pores falls by many orders of magnitude before the onset of scattering from the molecular structure, and thus we may treat our model porous structures as though excised from a uniform continuous medium.

12.4 The Guinier approximation.

For randomly oriented density variations we have for the intensity of scattering

$$I(q) = 4\pi \cdot \int_0^\infty r^2 \cdot \gamma(r) \cdot \frac{\sin(q \cdot r)}{q \cdot r} dr$$

At very low angles $\phi = q \cdot r$, we may expand the sinc term in the above as a Maclaurin series :

$$\frac{\sin(q \cdot r)}{q \cdot r} \approx 1 - \frac{1}{3!} \cdot (r \cdot q)^2 + \frac{1}{5!} \cdot (r \cdot q)^4 - \frac{1}{7!} \cdot (r \cdot q)^6 + \dots$$

then for small ϕ we may write a quadratic approximation :

$$I_q(q) = I(0) \cdot \left(1 - \frac{1}{3} \cdot R_g^2 \cdot q^2\right)$$

where for a particle of maximum dimensions D , volume V , with second moment M_2 :

$$I(0) = 4\pi \cdot \int_0^D r^2 \cdot \gamma(r) dr = 4\pi \cdot D^{2+1} \cdot M_2$$

with R_g being the radius of gyration of the scatterer;

$$R_g^2 = \frac{1}{2} \cdot \frac{\int_0^D r^4 \cdot \gamma(r) dr}{\int_0^D r^2 \cdot \gamma(r) dr} = \frac{\int_V r^2 \cdot \rho(r) dr}{\int_V \rho(r) dr}$$

Thus we may write our approximation in terms of a moment expansion :

$$\begin{aligned} \frac{I_q(q)}{I(0)} &= 1 - \frac{1}{3} \cdot \frac{1}{2} \cdot \frac{\int_0^D r^4 \cdot \gamma(r) dr}{\int_0^D r^2 \cdot \gamma(r) dr} \\ &= 1 - \frac{D^2}{6} \cdot \frac{M_4}{M_2} \cdot q^2 \end{aligned}$$

which for a sphere of uniform density, radius R , diameter D , becomes :

$$\frac{I_q(q)}{I(0)} = 1 - \frac{D^2}{20} \cdot q^2, \quad \text{since for a sphere } R_g^2 = \frac{3}{5} \cdot R^2 = \frac{3}{20} \cdot D^2$$

A better approximation for $I(s)$ in this low $\phi = q \cdot r$ region is a Gaussian approximation given by the Guinier equation [Guinier, 1939] :

$$I_g(q) = I(0) \cdot \exp\left(-\frac{1}{3} \cdot (R_g \cdot q)^2\right) = I(0) \cdot \exp\left(-\frac{1}{20} \cdot (D \cdot q)^2\right)$$

where we have

$$\exp\left(-\frac{1}{3} \cdot (R_g \cdot q)^2\right) \approx 1 - \frac{1}{3} \cdot (R_g \cdot q)^2 + \frac{1}{18} \cdot (R_g \cdot q)^4 - \frac{1}{162} \cdot (R_g \cdot q)^6 + \dots$$

In terms of a moment expansion we obtain :

$$\frac{I_g(q)}{I(0)} \approx 1 - \frac{D^2}{6} \cdot \frac{M_4}{M_2} \cdot q^2 + \frac{D^4}{72} \cdot \frac{M_4^2}{M_2^2} \cdot q^4 - \frac{D^6}{1296} \cdot \frac{M_4^3}{M_2^3} \cdot q^6 + \dots$$

which for a sphere of uniform density becomes :

$$\frac{I_g(q)}{I(0)} \approx 1 - \frac{D^2}{20} \cdot q^2 + \frac{D^4}{800} \cdot q^4 - \frac{D^6}{48000} \cdot q^6 + \dots$$

This gives us a closer approximation to the full expansion of the correct sinc expression :

$$\frac{I(q)}{I(0)} \approx 1 - \frac{D^2}{6} \cdot \frac{M_4}{M_2} \cdot q^2 + \frac{D^4}{120} \cdot \frac{M_6}{M_2} \cdot q^4 - \frac{D^6}{5040} \cdot \frac{M_8}{M_2} \cdot q^6 + \dots$$

which for a sphere of uniform density becomes :

$$\frac{I(q)}{I(0)} \approx 1 - \frac{D^2}{20} \cdot q^2 + \frac{3 \cdot D^4}{2800} \cdot q^4 - \frac{D^6}{155040} \cdot q^6 + \dots$$

In chapter 16.1 we note that scattering from porous sol-gel silicas is well fitted by sech curves, up to the point where there is a q^{-4} departure. Thus we may write

$$I_s(q) = I(0) \cdot \text{sech}(R_s \cdot q) = I(0) \cdot \text{sech}\left(\frac{\sqrt{2}}{\sqrt{3}} \cdot R_g \cdot q\right)$$

where we identify a radius R_s such that

$$R_s^2 = \frac{2}{3} \cdot R_g^2, \quad \text{and for a sphere} \quad R_s^2 = \frac{2}{5} \cdot R^2 = \frac{1}{10} \cdot D^2.$$

$$\begin{aligned} \therefore I_s(q) &= I(0) \cdot \frac{2}{e^{q \cdot R_s} + e^{-q \cdot R_s}} \\ &\approx I(0) \cdot \left(1 - \frac{1}{2} \cdot \frac{2}{3} \cdot (R_g \cdot q)^2 + \frac{5}{24} \cdot \frac{4}{9} \cdot (R_g \cdot q)^4 - \frac{61}{720} \cdot \frac{8}{27} \cdot (R_g \cdot q)^6 + \dots \right) \end{aligned}$$

In terms of a moment expansion we obtain :

$$\frac{I_s(q)}{I(0)} \approx 1 - \frac{D^2}{6} \cdot \frac{M_4}{M_2} \cdot q^2 + \frac{5 \cdot D^4}{276} \cdot \frac{M_4^2}{M_2^2} \cdot q^4 - \frac{61 \cdot D^6}{2430} \cdot \frac{M_4^3}{M_2^3} \cdot q^6 + \dots$$

which for a sphere of uniform density becomes :

$$\frac{I_s(q)}{I(0)} \approx 1 - \frac{D^2}{20} \cdot q^2 + \frac{D^4}{480} \cdot q^4 - \frac{61 \cdot D^6}{720000} \cdot q^6 + \dots$$

We see that all these expansions are the same to the quadratic term; that the sech expansion fits a sphere less well than the Guinier expansion – however it fits the data better. This tells us that we are probably seeing scattering from a $G(r)$ that is not that

of a sphere.

The sech expansion encodes the measured $I(s)$ data well; by equating moments it is possible to obtain them to high order; however the convergence of a moment expansion is very slow, and a standard Fourier transformation of $I(s)$ to $G(r)$ is preferred.

12.5 The Porod law.

For a particle of constant density and with a smooth closed boundary of surface area S we may show that [Porod, 1951, Feigin and Svergun, 1987]

$$\left. \frac{d\gamma(r)}{dr} \right|_{r=0} = \frac{1}{4\pi} \cdot (-\pi) \cdot \int_S \rho^2 dS = -\frac{\rho^2 \cdot S}{4}$$

If we consider the behaviour of $I(q)$ as $q \rightarrow \infty$, for a particle of maximum dimensions D we have $\gamma(D) = 0$. Expanding $I(q)$ in terms of derivatives of $\gamma(r)$ we find that

$$I_P(q) = -\frac{8\pi}{q^4} \cdot \left. \frac{d\gamma(r)}{dr} \right|_{r=0} + O$$

where other terms O are oscillating, and divided by q^3 , q^4 . (We see this behaviour in $I(q)$ for a sphere, see figure 102, where we plot the average $I(q)$ for an ensemble of spheres with a Gaussian distribution.)

Thus in this high q limit we obtain the Porod law :

$$I_P(q) \approx \frac{2\pi}{q^4} \cdot \rho^2 \cdot S$$

such that on a log-log plot of $I(q)$ for dry porous silicas we obtain a straight line with a gradient around -4 (see chapter 16.1).

12.6 Combining the Guinier and Porod descriptions.

We wish for a description of $I(q)$ that is valid in both the low and high q limits. Consider inhomogeneities in liquids with random fluctuations. These may be described with correlations that as a first approximation decay exponentially, with a correlation length ξ . The Fourier transform of an exponential is a Lorentzian (Ornstein-Zernike equation), such that

$$I_{OZ}(q) = I_0 \cdot \frac{1}{1 + \xi^2 q^2}$$

In the limit $\xi^2 q^2 \ll 1$ we may take a Maclaurin expansion.

$$(1+x)^\alpha = 1 + \alpha x + \frac{\alpha(\alpha-1)}{2!} x^2 + \frac{\alpha(\alpha-1)(\alpha-2)}{3!} x^3 + \dots$$

Thus this Ornstein-Zernike equation may be written

$$I_{OZ}(q) \approx I_0 \cdot (1 - \xi^2 q^2 + \xi^4 q^4 - \xi^6 q^6 + \dots)$$

For a random mixture of two phases with a sharp boundary we find [Mountjoy, 1999, Li and Ross, 1994, Teubner and Strey, 1987, Martin et al., 1986, Hurd et al., 1987]

$$I_{GP}(q) = I_0 \cdot \frac{1}{(1 + \beta^2 q^2)^{\frac{d}{2}}}$$

In the limit $1 \ll \beta^2 q^2$ for agreement with the Porod law we want a behaviour $\propto q^{-4}$ thus we conclude $d = 4$.

In the limit $\beta^2 q^2 \ll 1$

$$I_{GP}(q) \approx I_0 \cdot \left(1 - \frac{d}{2} \beta^2 q^2 + \dots\right)$$

Thus for agreement with the Guinier equation we want

$$\frac{d}{2} \beta^2 = \frac{1}{3} R_g^2, \quad \therefore \beta^2 = \frac{1}{6} R_g^2$$

Thus we obtain one possible equation that agrees with the Guinier and Porod equations in their respective regions of validity, if we write :

$$I_{GP}(q) = I_0 \cdot \frac{1}{\left(1 + \frac{R_g^2}{6} \cdot q^2\right)^2}$$

which is a Lorentzian².

For a sphere of uniform density and diameter D this becomes :

$$I_{GP}(q) = I_0 \cdot \frac{1}{\left(1 + \frac{D^2}{40} \cdot q^2\right)^2}$$

Other expressions have been derived in the literature that behave differently in the transition between these limits [Li and Ross, 1994, Teubner and Strey, 1987, Schmidt, 1991], with varying applicability to sol-gel porous media. None of these functions fit the

observed scattering from sol-gel silicas as well as the empirical sech function discussed above, with a small admixture of a random mixture of two phases as just discussed.

12.7 Obtaining $G(r)$ for these scattering forms.

In appendix M we use the algebraic language *Maple* to obtain analytic expressions for $\gamma(r)$ for these standard neutron scattering $I(q)$ functions : Guinier (Gaussian), Porod (q^{-4}), Orstein-Zernike (Lorentzian), Guinier-Porod (Lorentzian²), and for the porous media form of sech.

12.8 Babinet's Theorem.

We saw in section 12.2 that we are not directly sensitive to the amplitude $f(\mathbf{q})$ and phase of the scattered wave, but only to the intensity $I(\mathbf{q}) \propto |f(\mathbf{q})|^2$.

Babinet [Francon, 1966] showed that this implies that two phase complementary screens scatter in a way that can not be distinguished :

If one has an unobstructed aperture that gives rise to a scattering pattern of amplitude $f_0(u, v)$, and alternately place in front of it two 2D complementary screens whose scattering amplitudes are $f_1(u, v)$, $f_2(u, v)$, then we have :

$$f_2(u, v) = f_0(u, v) - f_1(u, v)$$

However the scattering amplitude from the unobstructed aperture at finite scattering angles will be very small (in practical neutron scattering terms, all the amplitude will be lost in the beam-stop), thus

$$\begin{aligned} f_2(u, v) &= -f_1(u, v) \\ \therefore I_2(u, v) &= |f_2(u, v)|^2 = |-f_1(u, v)|^2 = |f_1(u, v)|^2 = I_1(u, v) \end{aligned}$$

12.9 Chordal analysis.

Babinet's theorem shows the importance of the interfacial area when considering the scattering from a two phase medium, such that a uniform void and a uniform voidless solid will both give no detectable scattering.

Suppose we consider the distribution of chords $L(l)$ between random points on the surface of a simple convex body (or void) of uniform density and maximum dimensions D , embedded in a medium of uniform density.

There then exists relationships between $\gamma_0(r)$ and $L(l)$ [Feigin and Svergun, 1987, p46] (quoted without derivation or proof).

$$\begin{aligned}\gamma_0(r) &= \frac{\int_r^D (l-r) \cdot L(l) dl}{l_0 = \int_0^D l \cdot L(l) dl} \\ \frac{L(r)}{l_0} &= \frac{\partial^2 \gamma_0(r)}{\partial r^2}\end{aligned}$$

We may understand these relationships if we write the integrals in the form of a convolution like that for $\gamma(r)$, where we consider the density ρ as being uniform between r and D and zero elsewhere :

$$\int_r^D \rho(l-r) \cdot \rho(l) dl$$

Hence we deduce that the relationships are not applicable to the general cases of concave bodies, multiple bodies, and porous media in general. There is the comment in the text of reference [Feigin and Svergun, 1987] that the relationships are not very useful to examine experimental data due to the noise making the second derivative meaningless. This is none the less useful as a way of deducing $\gamma_0(r)$ for simple structures that satisfy the above conditions. Numerical integration of $L(l)$ is in effect only 2D, and is some orders of magnitude faster than that required for 3D evaluation of $\gamma_0(r)$. The forms of $L(l)$ are in general much simpler than that for the averaged, convoluted $\gamma_0(r)$ – that for a sphere is a simple straight line $\propto l$ between $0, D$ and zero elsewhere - this often allows analytic forms to be obtained by inspection of numerically calculated $L(l)$ data. We may with care also use these relationships as an informative guide in porous media, for radii less than that of a pore radius, such that the dominant terms will be inter-pore and not traverse both pore void and solid (see figure 111).

Further we find that the experimental scattering data from ILL SANS apparatus D22 is, with careful processing, quite able to give meaningful chordal information, by both numerical Fourier transformation and analytic transformation, offering much greater structure discrimination than the averaged, convoluted $G(r)$ data (see chapter 12.9).

Chapter 13

Neutron scattering from silica.

13.1 Neutron scattering apparatus.

Measurements of the intensity of neutron scattering from porous silica were performed at the Institut Max von Laue – Paul Langevin (ILL) in Grenoble. For a schematic of the reactor core, moderators and instrument lay-out at ILL see figure 77.

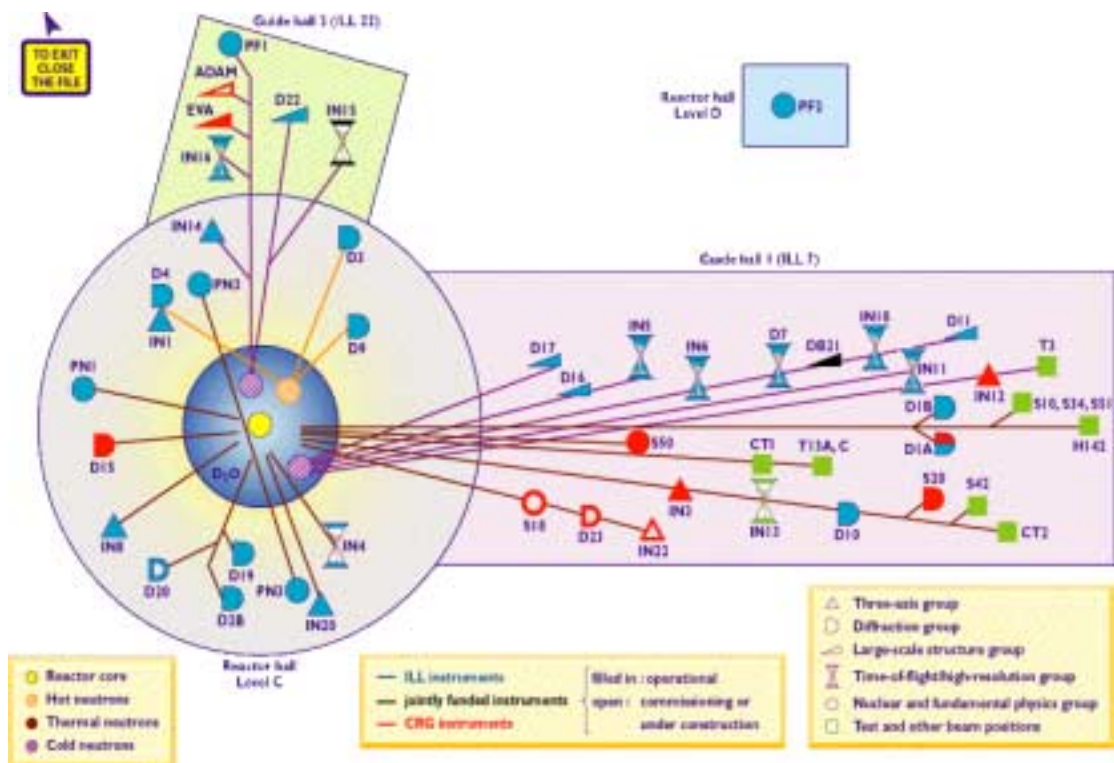


Figure 77: Schematic of the reactor core, moderators and instrument lay-out at ILL.

13.1.1 Neutron production, thermalisation and monochromatisation.

Neutrons for scattering experiments are commonly produced either in nuclear reactors specially designed for producing high fluxes of neutrons (as at ILL), or by impinging accelerated pulses of protons onto heavy metal targets (as at ISIS at the Rutherford Lab.).

In both cases the neutrons are conventionally moderated or thermalised, using hot graphite (for short wavelength neutrons) as on ILL D4, which then uses a copper monochromator ($0.35\text{\AA} \leq \lambda \leq 0.7\text{\AA}$), or cooled baths of hydrogen containing liquid – typically methane (for long wavelength neutrons) as on ILL D22, which then uses a Dornier velocity selector (a rotating cylinder with helical slots) ($3\text{\AA} \leq \lambda \leq 20\text{\AA}$).

For a Maxwellian (thermalised) distribution of the speeds of N particles travelling in all directions (i.e. a solid angle of 4π) we have [Reif, 1965, Landau and Lifshitz, 1965]:

$$F(v)dv = 4\pi N \cdot \left(\frac{m}{2\pi k_b T} \right)^{\frac{3}{2}} \cdot v^2 \cdot e^{-\frac{mv^2}{2k_b T}} dv$$

Hence the distribution for N neutrons emerging from a moderator through solid angle $\Delta\Omega$ must be the same; i.e. :

$$F(\alpha)d\alpha = 4\pi N \cdot \left(\frac{E}{\pi k_b T} \right)^{\frac{3}{2}} \cdot e^{-\frac{E}{k_b T}} \frac{d\alpha}{\alpha}$$

Where symbol ' α ' can be any of v, k, λ since :

$$p = mv = \hbar k = \frac{h}{\lambda}, \quad \frac{dv}{v} = \frac{dk}{k} = -\frac{d\lambda}{\lambda}$$

$$E = \frac{1}{2}mv^2 = \frac{p^2}{2m} = \frac{\hbar^2 k^2}{2m} = \frac{h^2}{2m\lambda^2}$$

Thus for λ we get :

$$F(\lambda)d\lambda = 4\pi N \cdot \left(\frac{1}{2\pi m k_b T} \right)^{\frac{3}{2}} \cdot h^3 \cdot \lambda^{-4} \cdot e^{-\frac{h^2}{2m\lambda^2 k_b T}} d\lambda$$

We graph this in figure 78.

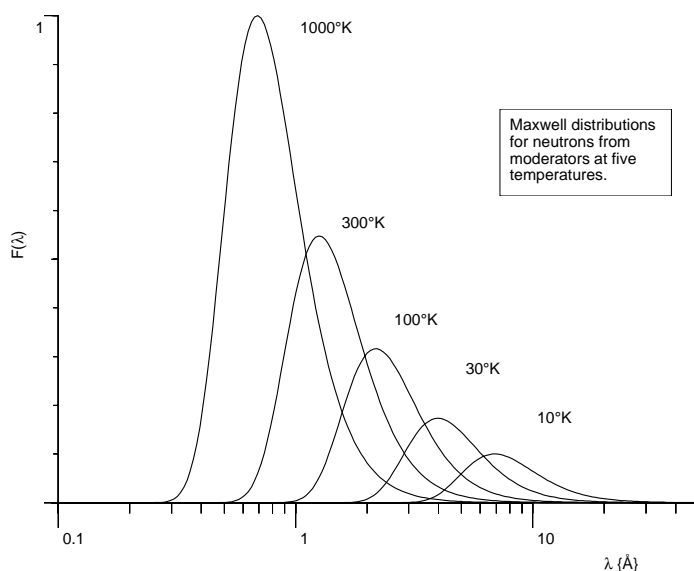
Maxwell Distribution $F(\lambda)$ for neutrons.

Figure 78: Maxwell distributions $F(\lambda)$ for neutrons from moderators at 1000K, 300K, 100K, 30K, 10K.

13.1.2 Apparatus for Neutron Scattering Diffraction – D4B.

D4B is located in the reactor hall, near the reactor core shielding. The neutrons from the moderator and monochromator are collimated and then scattered off the sample, which is placed in a 5mm dia. thin walled vanadium tube mounted in vacuum. The scattered neutrons are detected by two 64 cell linear multidetectors that move in arcs on air pads. The neutron path is nearly all maintained in a vacuum. See figures 79, 80. The instrument is controlled from a DEC Alpha computer (D4) running Unix, via VME racks, with data analysis being performed on an SGI computer (D4sgi) running Unix. Normalisation, background and sample tube subtraction, conversion to Q and sin-cos Placzek correction was performed using standard D4 Unix routines written in *C*. Additional routines to perform windowing and sech Placzek correction were written in *Apl* [Iverson, 1962], translated to *C* [Budd, 1988, Sirlin, 1988..1999], and compiled to executable code, while at ILL. The programs were added to the other general user programs on D4sgi.



Figure 79: View of D4B neutron diffractometer, showing sample vacuum chamber and the two multidetector housings.

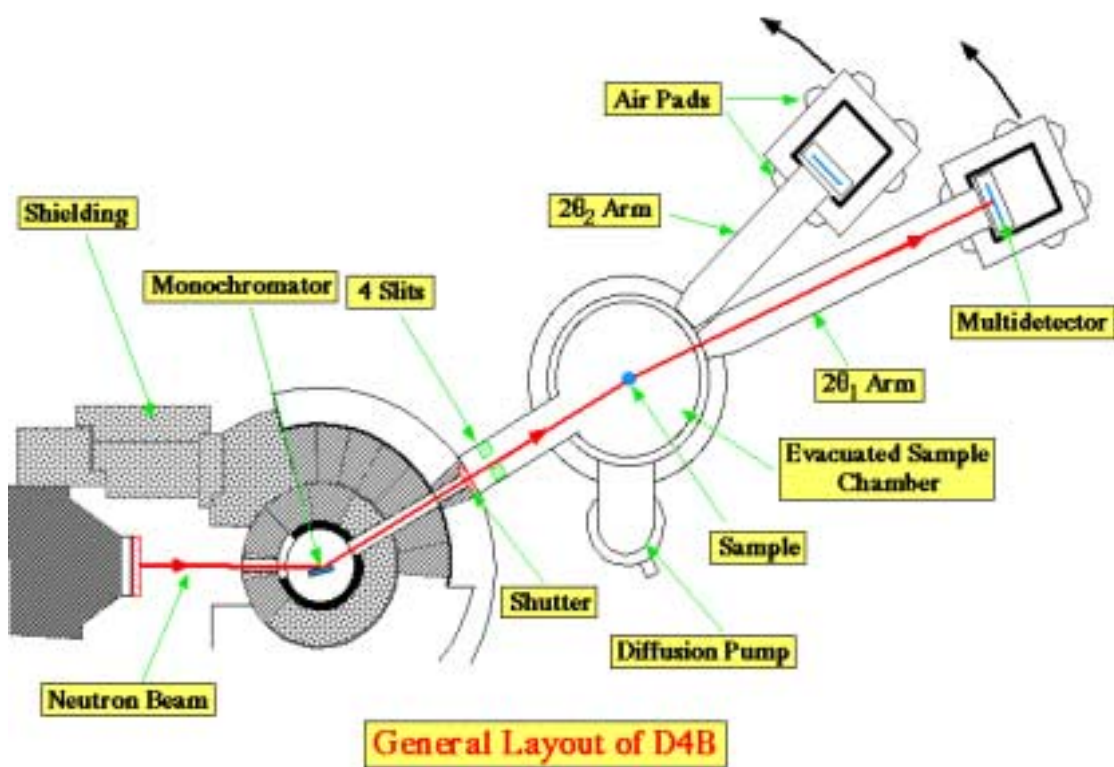


Figure 80: Schematic for D4B neutron diffractometer.

13.1.3 Apparatus for Small Angle Neutron Scattering – D22.

D22 occupies the length of guide hall 2, outside the reactor containment hall (see figures 77, 81).

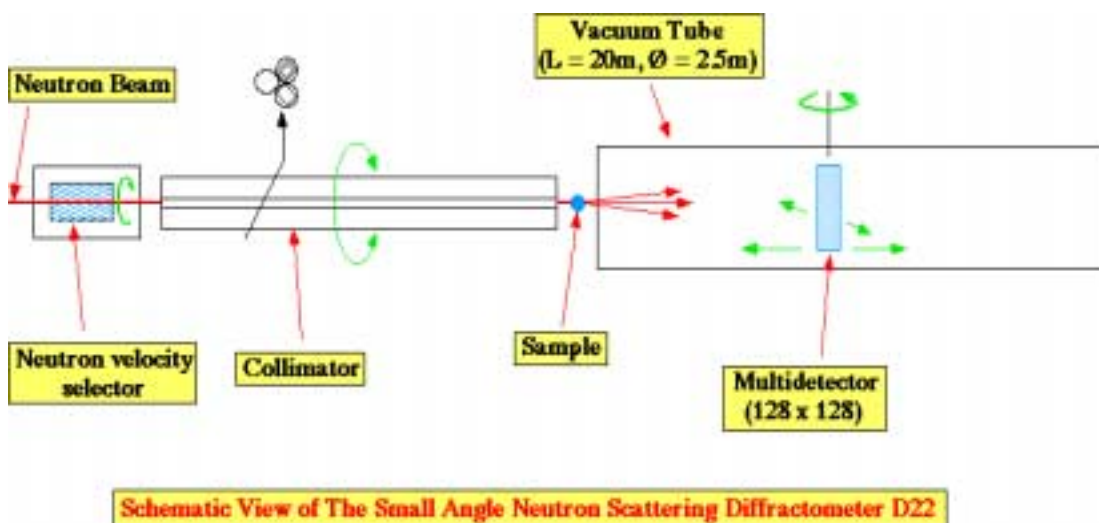


Figure 81: Schematic of D22 small angle diffractometer, showing Dornier monochromator, 18m long collimator, and multidetector in 20m long vacuum chamber.

The collimator has 8 evacuated guide sections, with source to sample distances variable from 1.4m to 17.6m. There is a choice of 4 attenuations. See figure 82.

The porous silica samples were placed in a flat quartz Helma cell – sample thickness was 1mm. These were placed in a multi-sample sample changer, with multiple degrees of freedom, allowing the samples to be changed rapidly under computer control.

The detector is a 128×128 element multidetector, $96\text{cm} \times 96\text{cm}$, and moves inside a 20m long evacuated chamber, under computer control, with sample to detector distance adjustable from 1.43m to 18m. The detector can also be displaced sideways by 500mm, giving an offset beam centre on the detector, allowing higher Q ranges to be reached. See figure 83.

The instrument is controlled from a DEC Alpha computer (D22) running Unix, via VME racks, with data analysis being performed at ILL on an SGI computer (D22sgi) running Unix, and at a later date on a 200MHz Pentium running Linux, using a program written in *Apl*, translated to *C*, and compiled to executable. The program (*DoD22*) was ported to the SGI, and placed on D22sgi for others to use.



Figure 82: View of D22 neutron collimator and attenuators.



Figure 83: View of D22 multidetector in 20m long vacuum chamber.

13.2 Sample Preparation.

Seven porous silica samples with nominal pore diameters of 25Å (Sigma), 40Å (Merck), 60Å (Merck), 46.3Å (C60 Unilever B), 100Å (Merck), 171.5Å (C200 Unilever B), 453Å (C500 Unilever B) were pre-dried over-night at 120°C, before going to ILL. Before measurement they were transferred into 5mm dia. thin walled vanadium tubes for measurement on D4, and into 1mm sample thickness Helma cells for measurement on D22. The samples were then re-dried for a few hours at 120°C, stoppered, and then gently tapped to consolidate the silica grains.

13.3 Measurement of Scattering Intensity.

For D4, measurements were made of the scattering from an empty vanadium tube, a solid 5mm vanadium rod, and a tube containing distilled water and tubes containing the silicas.

They were placed one at a time in the sample changer, which was then evacuated, and both detectors scanned over their full θ range, giving a Q coverage of 0.2 to 17 {radians·Å⁻¹}.

For D22 the silica samples were then placed in the sample changer, together with a position containing B₄C neutron absorber for measuring the background, an empty sample holder for measuring the beam intensity, an empty Helma cell, for measuring the transmission and scattering of the container, and a Helma cell containing distilled water, for intensity normalisation.

Measurements were made of all these samples with the detector at positions of 1.43m sample-detector distance (350mm offset), 1.43m (centred), 5m (centred), 18m (centred), measuring both transmission and scattering. This gave a Q range of 0.0008 to 0.3 {radians·Å⁻¹}.

For the transmission measurements, attenuator 3 was inserted, and the beam stop moved off-centre. For the scattering measurements attenuator 1 was used at 1.43m and some 5m measurements, and no attenuator used for 18m and other 5m measurements, and the beam stop position adjusted to give good blocking of the direct beam.

Two long duration measurements were made of the water scattering, at 1.43m (offset and centred) to measure the detector efficiency.

Chapter 14

Neutron Scattering Analysis.

14.1 Neutron Scattering from water.

The neutron scattering from hydrogen is dominated by incoherent scattering and is very flat in the small-angle region, showing mainly Placzek fall-off above 1 {radian·Å⁻¹} due to the recoil of the light hydrogen nuclei. A measurement of the scattering from water made on D4 shows this clearly (see figure 84). We show an empirical fit to the incoherent scattering such that the two parameter sech + cubic approximation :

$$Norm(q) \approx \frac{2}{e^{\frac{q}{Q_0}} + e^{-\frac{q}{Q_0}}} + \alpha \cdot q^3$$

acts to correct for Placzek fall-off. i.e. it models the incoherent scattering. Also shown is the residual (rescaled) coherent scattering, after subtraction of the incoherent scattering. The use of sech has the advantage that we have a description of the Placzek fall-off in terms of a single main parameter, the fall-off width Q_0 , with the cubic parameter α just acting as a fine adjustment at high Q .

We see that it is reasonable to assume the scattering intensity in the small angle region is nearly constant, and we may thus use water as a normalisation standard.

14.2 Calibration and normalisation for small angle scattering.

Measurements of the scattering from water on D22 with the detector centred and offset at 1.43m allowed the measured scattering from the two 2D water scattering intensity

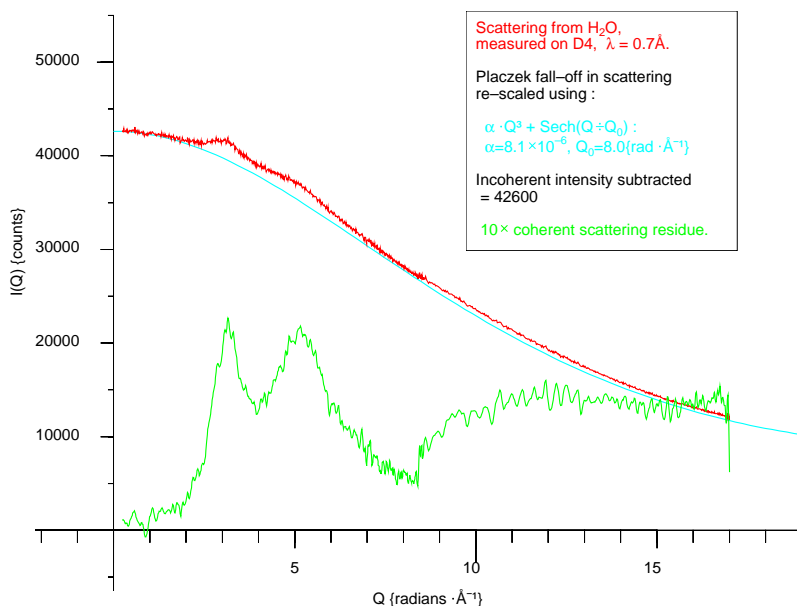
Sech fitted as Placzek Correction for H₂O.

Figure 84: Placzek fall-off of the neutron scattering from water, showing a Sech approximation to the incoherent scattering, and the residual coherent scattering.

maps to be separated into three components: a detector efficiency map, a geometric fall off $\text{Geom}(\theta_s)$ due to the scattering $I(\theta_s)$ being detected by a flat detector, and an attenuation $\text{Atten}(\theta_s)$ due to the angled scattering passing through a longer (attenuating) path length in the sample (see appendices N, O and figure 88). It must be noted that a different $\text{Geom}(\theta_s)$ is required for each detector position and $\text{Atten}(\theta_s)$ is different (but calculable) for the calibrating water sample, and each measured sample, being dependent on the direct path attenuation.

The detector efficiency map calculated at the closest detector distance of 1.43m was used at all distances, as this has the best signal to noise. The water maps at all detector distances and offsets were then used to provide intensity normalisation and to calculate the geometric fall-off for the relevant measurements – although the latter was close to the theoretical geometric behaviour (see appendix N) there was measurable deviation, and thus even fourth order polynomials $\varphi^4(\theta) = \alpha + \beta \cdot \theta^2 + \gamma \cdot \theta^4$ were used to model $\text{Geom}(\theta_s)$, after multiplication of the water scattering map by the appropriate $\text{Atten}(\theta_s)$ map.

All measurements were initially normalised to 10^5 monitor counts; then for normalised

measurement intensity maps :

- B : Background
- $EC_{T,S}$: Empty Cell (Transmission, Scattering)
- $W_{T,S}$: Water (Transmission, Scattering)
- $S_{T,S}$: Sample (Transmission, Scattering)

we may now calculate a corrected water scattering map :

$$W'_S = (W_S - B) - \frac{W_T}{EC_T} \cdot (EC_S - B)$$

We separate this (using the measured transmission) into calculated correction maps :

- DEM : Detector Efficiency Map
- Geom(θ_s) : Geometric fall-off Map
- AttenW(θ_s) : Water sample thickness attenuation Map

A Detector Mask Map and a Beam Stop Mask Map are also calculated.

We may now obtain corrected sample scattering maps :

$$S'_S = (S_S - B) - \frac{S_T}{EC_T} \cdot (EC_S - B)$$

It should be noted that we wish to correct all maps in the latter equation by the detector efficiency map – thus we may defer this operation (take it outside the brackets) and obtain final corrected sample scattering maps, using the Geom(θ_s) for the detector position and the sample AttenS(θ_s) :

$$S''_S = \frac{S'_S}{DEM \cdot Geom(\theta_s) \cdot AttenS(\theta_s)}$$

These maps were then converted to I(R) and the number of points reduced using a binless smoothing routine with settable resolution (default 300 radial points). This data was then remapped to I(Q).

Finally the I(Q) data measured for each sample at different detector positions was combined by polynomial fitting in the overlap regions and re-normalising to the D22 1.43m (offset) water map.

The scattering intensity measured for the seven silicas on D22 and six on D4 is shown in figure 85.

Neutron Scattering from Porous Silica

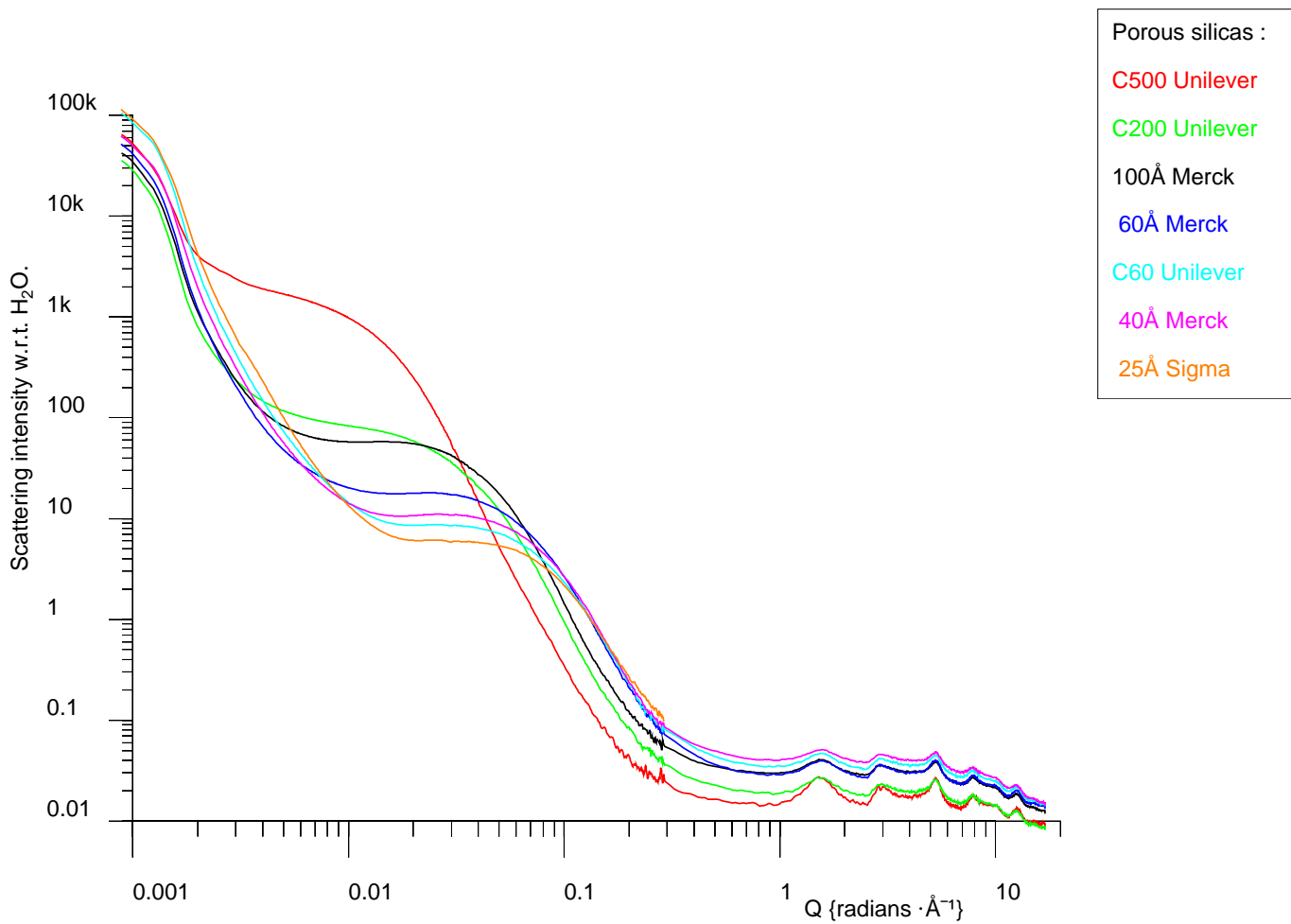


Figure 85: Scattering intensity from seven porous silicas, as measured on D22 and D4.

14.2.1 DoD22 show and analysis program.

To perform the above analysis a multiprocessing program *dod22* was written in *Apl*, and compiled to *C*. This program spawns *Tcl/Tk* windows for control buttons and edit boxes, and spawns *xterm* windows in slave mode for control and status.

It has three modes, *show*, *analyse* and fully controllable from the command window and control files, see figure 86.

In **show** mode it plots a 2D detector map, a parameter box, and an $I(Q)$ radial distribution, using the beam stop position as centre (see figure 87 for 500Å silica at 1.43m). All required parameters are read from the run parameter file. A list of ranges of Numors (Number of Run) may be specified; *Follow* mode may be specified – this plots new data as it is measured, with no further user intervention required.

For calculating the water efficiency and other maps required for calibration a command file must be executed. All required parameters are again read from the run parameter file, with the exception of the sample aperture; this together with a table of Numors (assigning the Water and Empty Cell transmission and scattering numors, etc.) is read from a pre-prepared table. One parameter that is adjustable is Beamstop Extend – this determines how much larger (all round) the Beam Stop Mask Map is than the beam stop – the default of 2 pixels is usually optimum.

Figure 88 shows the Detector Efficiency Map (overlaid with the Detector Mask Map), $\text{Geom}(\theta_s)$ geometric fall-off at 1.43m, and $\text{Atten}(\theta_s)$ for a 1mm thick flat slab of water. (It should be noted that the $1/e^{\text{th}}$ attenuation distance for 12Å neutrons in water is about 1.13mm.)

Finally, once the calibration has been performed for a particular detector position, **analyse** may be run on the appropriate ranges of sample Numors (Transmission, Scattering); this performs the analysis discussed above, reading parameters from the parameter file, and requiring no further user interaction. To calculate $I(Q)$, the beam centre position of the relevant transmission measurement is first found by integration and normalisation of the row and column sums, followed by curve fitting and solving of the resultant polynomial. A typical analysis result, for 60Å silica at 5m, is shown in figure 90. Thus analyse has corrected this for background, detector efficiency, transmission, empty cell, $\text{Geom}(\theta_s)$ and $\text{Atten}(\theta_s)$.

If we use analyse on an offset water (Transmission, Scattering) pair of measurements, we obtain figure 89; we see that the normalisation is reasonable but not complete; a further

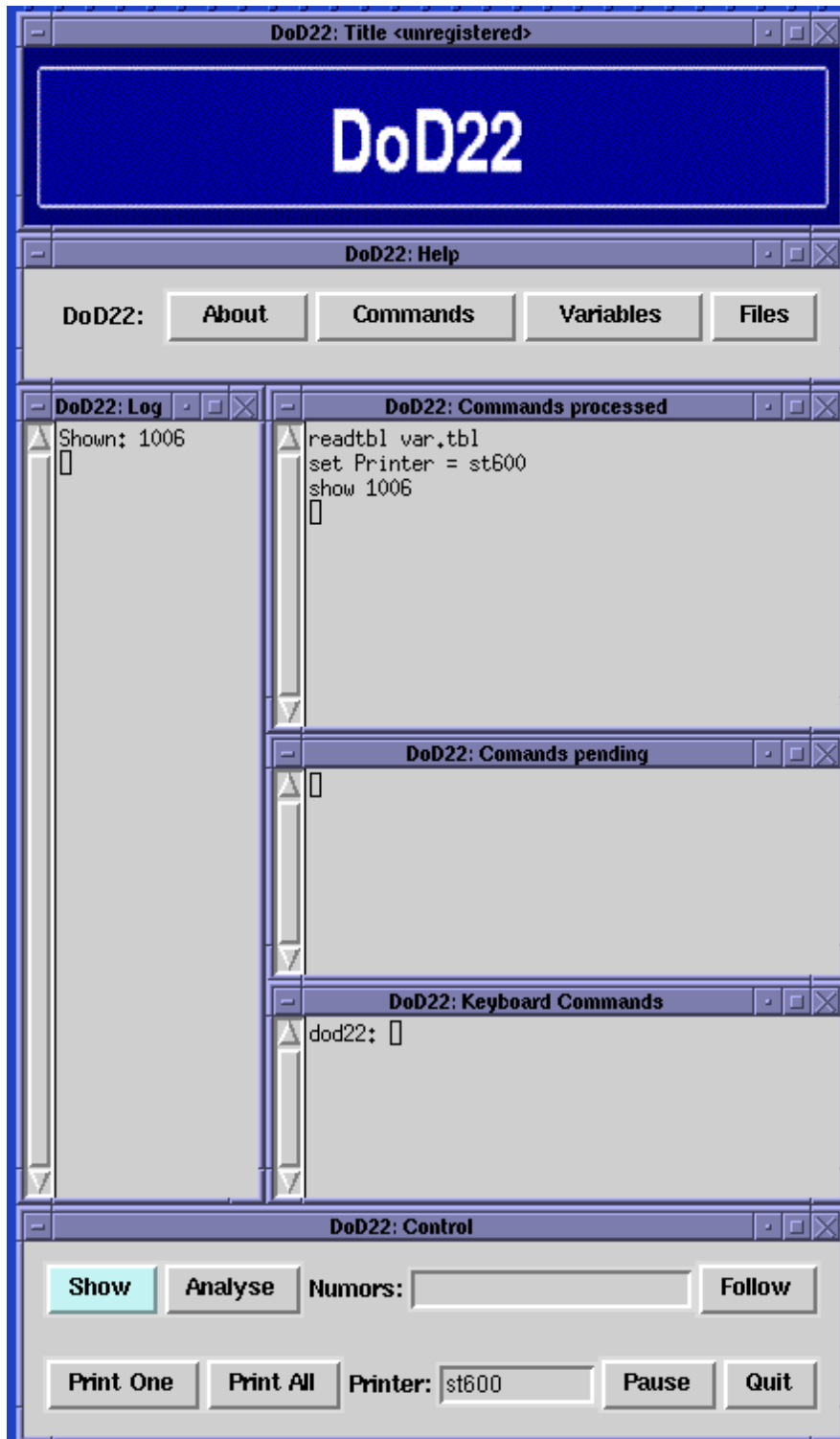


Figure 86: DoD22: Help, Command and Status windows.

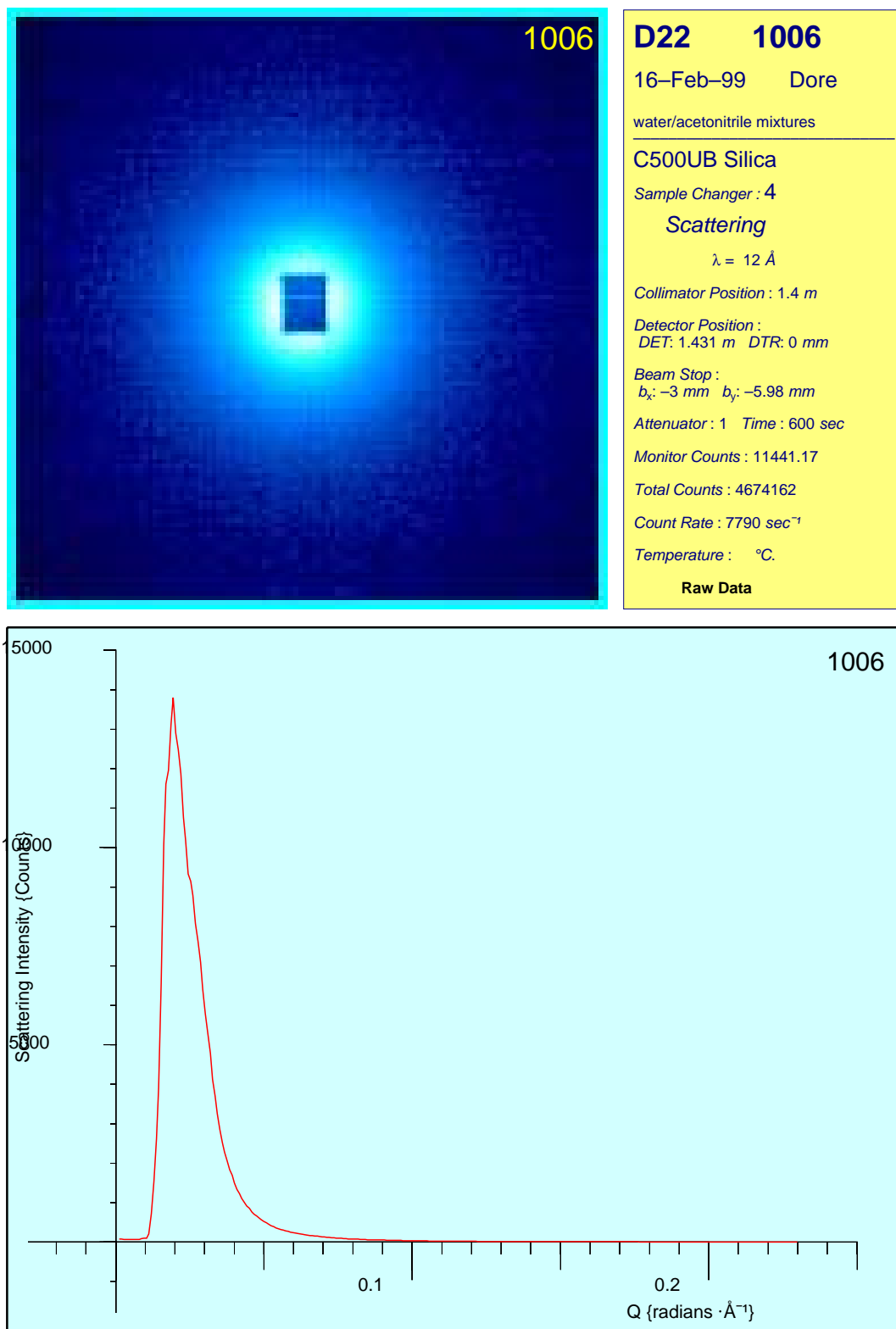


Figure 87: DoD22 show: Typical detector raw 2D I(X,Y) map, parameter table, I(Q) radial distribution.

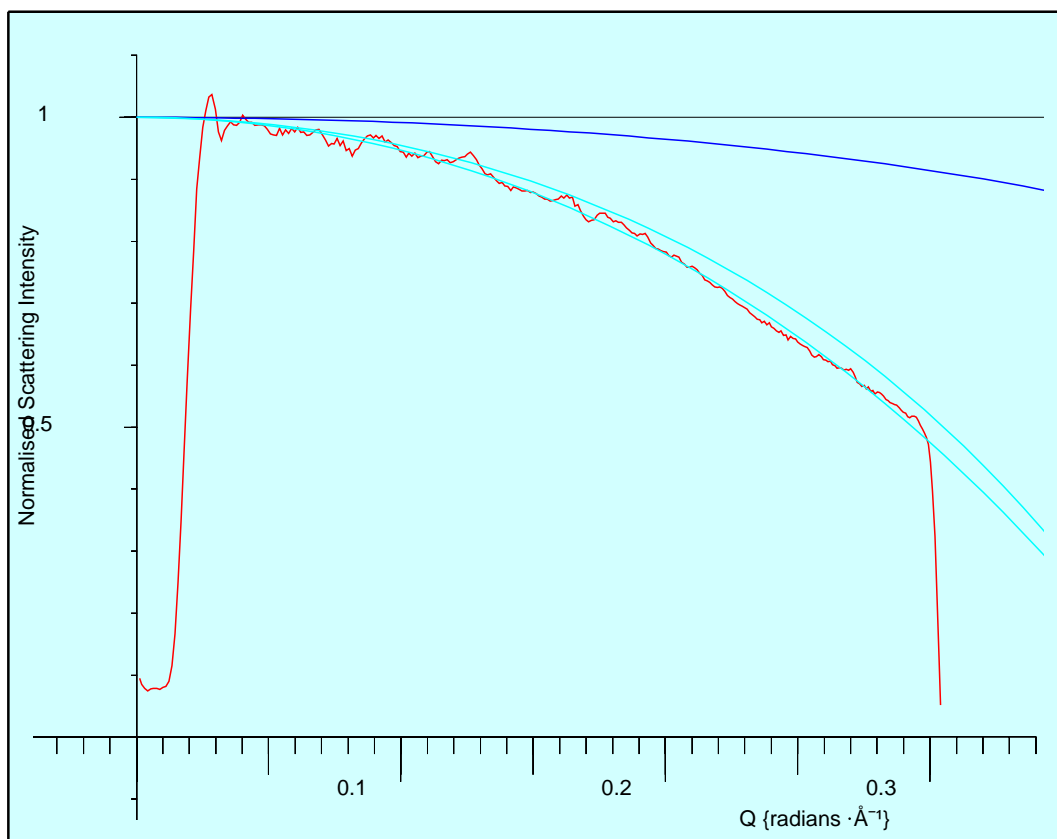
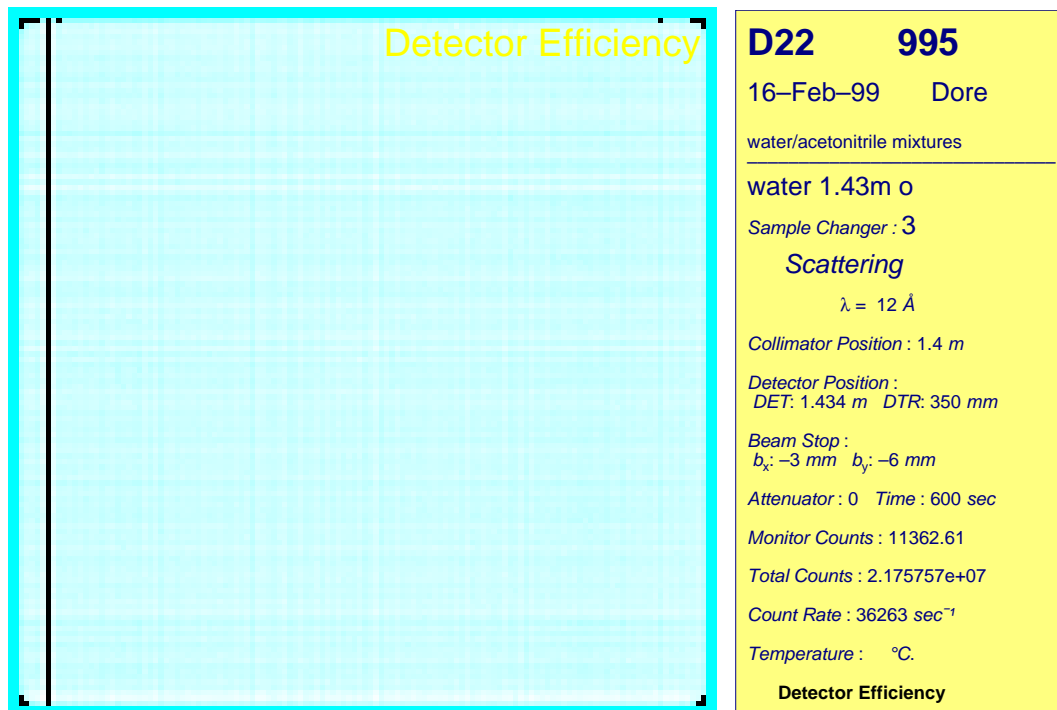


Figure 88: DoD22: Detector Efficiency Map and Mask Map, parameter table, $\text{Geom}(\theta_s)$ geometric fall off at 1.43m (cyan), and $\text{Atten}(\theta_s)$ for a 1mm water slab (blue).

iteration of normalisation may be added at a later stage. We may note the reduction in scatter brought about by the detector efficiency map correction.

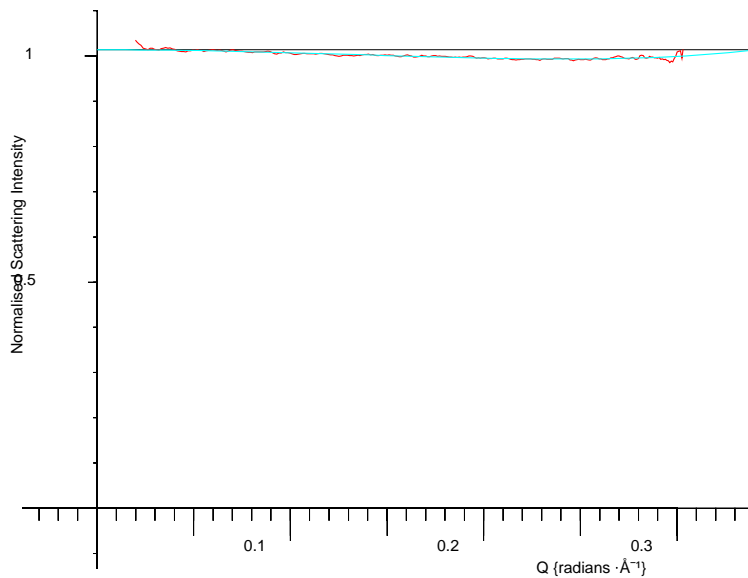


Figure 89: DoD22: Water normalisation as performed by *analyse*.

Analyse was used to prepare the individual $I(Q)$ sections for the combined porous silica scattering graph, figure 85.

The *dod22* program was originally written on a Linux PC; it has been placed on D22sgi for other users to use; postscript help panels are provided. (Note: currently *analyse* is switched off on SGIs).

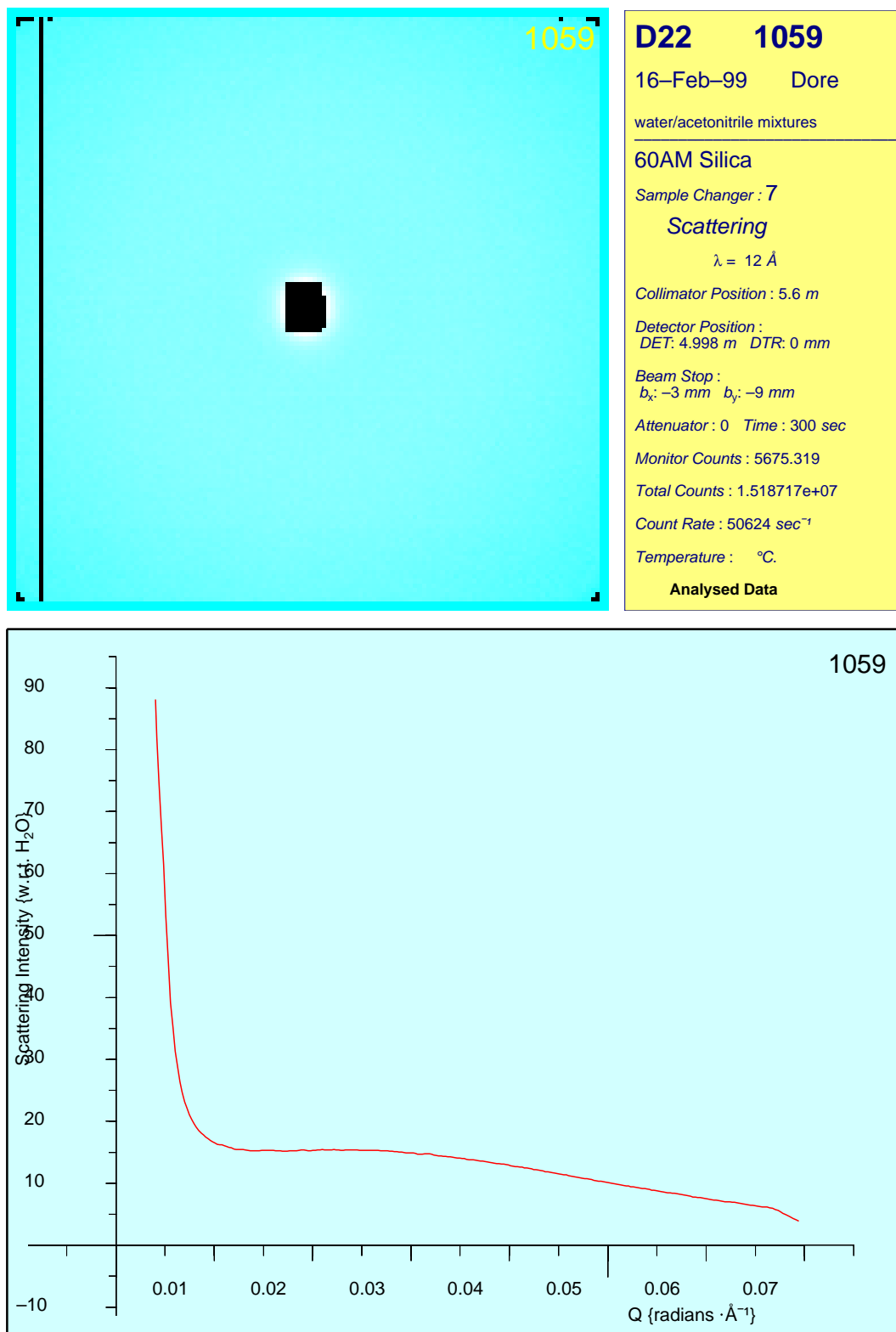


Figure 90: DoD22 *analyse*: Typical analysed 2D $I(X,Y)$ map, parameter table, $I(Q)$ radial distribution, corrected for background, detector efficiency, transmission, empty cell, $\text{Geom}(\theta_s)$ and $\text{Atten}(\theta_s)$.

Chapter 15

The calculation of the solid-solid density correlation function $G(r)$ for model porous structures.

Monte Carlo methods were used to calculate $G(r)$ for simple cylindrical pores on square and hexagonal lattices, and for spherical pores on cubic and hexagonal close packed lattices.

A uniform homogeneous medium was assumed, out of which the pores were excised. Uniform pore and lattice spacing was considered first, as appropriate to MCM templated silicas, then a statistical variation was added as found in sol-gel porous media. $G(r)$ was found to be separable into two regions : A short range structure in the calculated $G(r)$ that depends on the pore wall geometry, and a longer range oscillatory density variation around the average porous density, that depends on the lattice structure.

With higher variance, the short range structure decays smoothly with little or no oscillation into a longer range structure of very low amplitude, that then decays to the average porous density. With suitable values of variance the calculated $G(r)$ for arrays of spherical voids will be shown to match the measured $G(r)$ for sol-gel silicas.

15.1 Project aims.

Measurements had been made using a number of different techniques on porous silica sol-gel materials and liquid crystal templated silica glasses.

Measurements had been made of the density of the porous silicas; information on their nominal pore sizes was available from gas adsorption isotherms; measurements had been made of pore size distributions using Nuclear Magnetic Resonance (NMR) Cryoporometry; and finally Neutron Scattering (NS) Diffraction and Small Angle Neutron Scattering (SANS) measurements had been made to probe the spatial distributions of matter.

The intention of this project was to calculate the radial spatial distribution of matter $G(r)$ in model porous structures, and use this information to try and draw together the above information, to deduce information concerning the structure of real porous glasses.

15.2 Evaluation of scattering for porous structures.

There are two main approaches one might follow when calculating the expected scattering from porous structures :

15.2.1 Separation of scattering $I(q)$ into $P(R \cdot q)$, $S(q)$.

We note that where we have scattering from an array of identical particles of dimension R we may separate the scattering into a particle form factor $P(R \cdot q)$ and a structure factor $S(q)$ defining the spatial distribution of the particles, such that we may write :

$$I(q) = P(R \cdot q) \cdot S(q),$$

corresponding to a convolution in the real domain.

Thus for identical spheres on a lattice we may use the expression for $P(R, q)$ given in appendix K.

However we wish to model porous sol-gel silicas; we wish to model not only uniform voids on a uniform lattice, but Gaussian distributions of pore sizes on lattices with Gaussian variance; thus we require for our expression for $I(q)$ not just a single product of separable terms as for the uniform particle case but a summation or integral of terms. We note however that the problem is even more complicated, in that if we wish to model the voids as spheres we would expect them to need to intersect to give us the porosity – hence we would need to obtain an expression for $P(R, q)$ for faceted spheres (in order to avoid double counting of some of the void volume), as a function of the ratio $\frac{D_{void}}{a}$

(where a is the lattice spacing) and of the lattice geometry (determining where the facets are on the sphere).

15.2.2 Monte-Carlo integration of density correlation functions $G(r)$.

While the above is a route that might be followed in the future, the route chosen for this project was the direct (Monte-Carlo) integration of an explicit density distribution to obtain the normalised solid-solid density correlation function $\gamma_0(r)$, which may then be transformed to $I(q)$. This has the major advantage that we find that we may describe our intersecting porous structure on an infinite square or cubic lattice in only two lines (and that for hexagonal and hexagonal close packed structures in only a few more).

15.3 Project simplifications.

Clearly to fully model a real porous material would be a major task – many models have been proposed, some fractal in nature [Stanley and Ostrowsky, 1986].

The first problem is that the smallest pores studied were only about 30Å in diameter, which would at first imply that one would have to explicitly model the locations of silica atoms. However examining neutron diffraction and SANS data shows (see chapter 16.1, figures 99, 100, 101) that, even for the smallest pore structure studied, the scattering from the pore structure falls by many orders of magnitude before the start of the scattering peak from the silica lattice mean separation.

Using this information, the silica was then modelled as a uniform homogeneous medium, out of which pores were excised. As will be seen, this allows a change in modelling approach which gives rise to a major improvement in computational efficiency, providing improved statistics at fine resolution.

The other major simplification was in the construction of the porous structure modelled. Templated silicas such as hexagonal MCM-41 and cubical MCM-48 have pores on uniform lattices, which should make a simple model of the MCM-41 reasonably faithful (MCM-48 is a far more complex structure than the label ‘cubic’ would imply).

Thus initially pores were placed on a regular lattice, firstly spherical pores on a cubical lattice and cylindrical pores on a square lattice. Then hexagonal lattices of cylinders were constructed, allowing a good approximation to the structure of MCM-41. Finally spherical pores were placed on hexagonal close packed (HCP) lattices.

Sol gel glasses, though, have a statistical spread in pore sizes, and many different structures have been proposed to describe them, some fractal. Clearly to fully construct such a self-consistent model pore structure, and to measure its $G(r)$ would be a major undertaking.

Rather than construct a single porous structure containing a range of randomised pore sizes, the approach that was followed was : a) to construct an ensemble of regular porous structures, each with a statistical variation in its pore diameter and lattice spacing, and b) to interpolate between the higher and lower density Cubic and HCP lattices. NMR cryoporometry shows us that for a typical sol-gel glass the distribution in pore sizes is fairly narrow (typically 20 to 50%, see figures 62, 96), so this should be a valid approach. The $G(r)$ measured from the ensemble approach may have subtle differences from that measured for a single unified structure, but that should be to second order only.

15.4 First tests.

For an initial evaluation of algorithms, 500 points were generated at random inside a box of side $24 \times a$, where a was the intended lattice spacing. Those points outside a sphere of radius $R = 12 \times a$ were thrown away, effectively leaving a spherical grain of uniform density, sampled at 254 locations.

All pair-wise distances $\mathbf{r}_i - \mathbf{r}_j$, $i \neq j$, were evaluated, and binned in 1024 bins. This effectively gives the radial distribution function $J(r) = 4\pi r^2 \rho(r)$ for the spherical grain (figure 91). As expected the initial rise is r^2 , reflecting the surface area of each shell Δr of area $4\pi r^2$. As the surface of the grain is approached with a higher probability by larger r , the curve reaches a maximum and falls to zero, reflecting the fact that r can not be greater than $24 \times a$. We may also plot this as the pair correlation function $g(r)$ by dividing by the $4\pi r^2$ (figure 92). $g(r)$ may be given the following meaning; take an arbitrary occupied point in the test volume; $g(r)$ then represents the probability that another point at distance r is occupied. [Stanley and Ostrowsky, 1986].

The expected fall off due to the limited radius R of the sphere is calculable analytically [Steytler et al., 1983a], as shown in appendix K and is given by :

$$\gamma_0(r)_{Sph} = F(r, R) = 1 - \frac{3}{4} \cdot \frac{r}{R} + \frac{1}{16} \cdot \left(\frac{r}{R}\right)^3$$

$J(r)$ for 254 random points in uniform density sphere

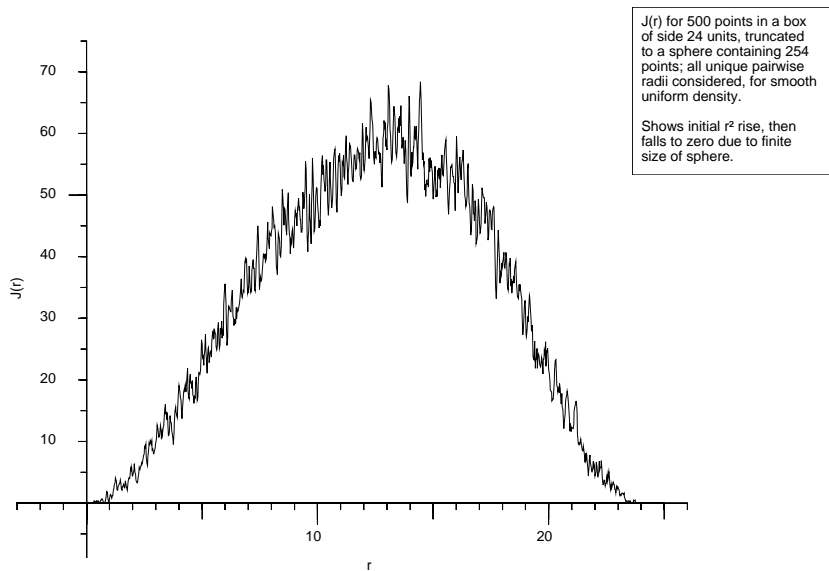


Figure 91: An initial test calculation of $J(r)$ for a sphere.

MC $g(r)$ for a sphere, with calculated $g(r)$

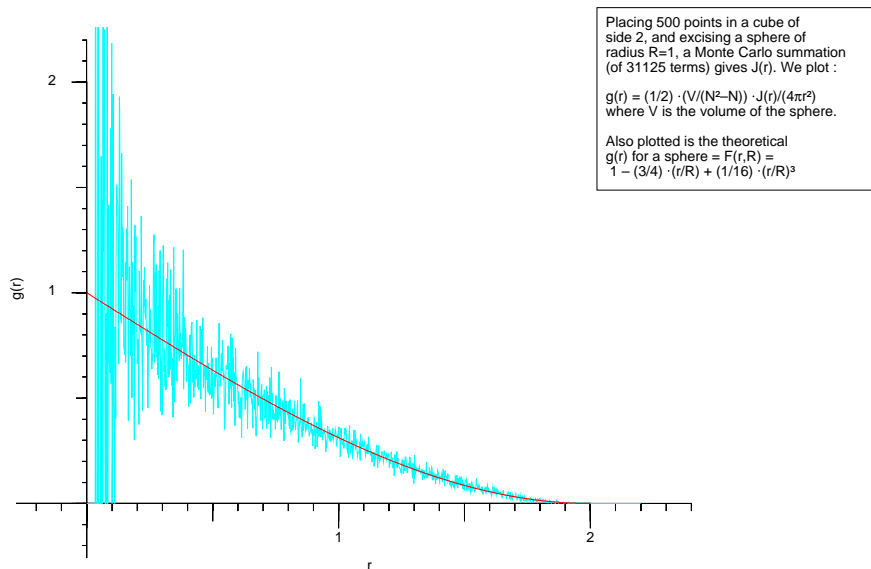


Figure 92: An initial test calculation of $\gamma_0(r)$ for a sphere.

Dividing the calculated $g(r)$ by the expected fall off $F(r, R)$ (and truncating at $20 \times a$) we get figure 93, which is a noisy but otherwise reasonable approximation to the expected uniform density.

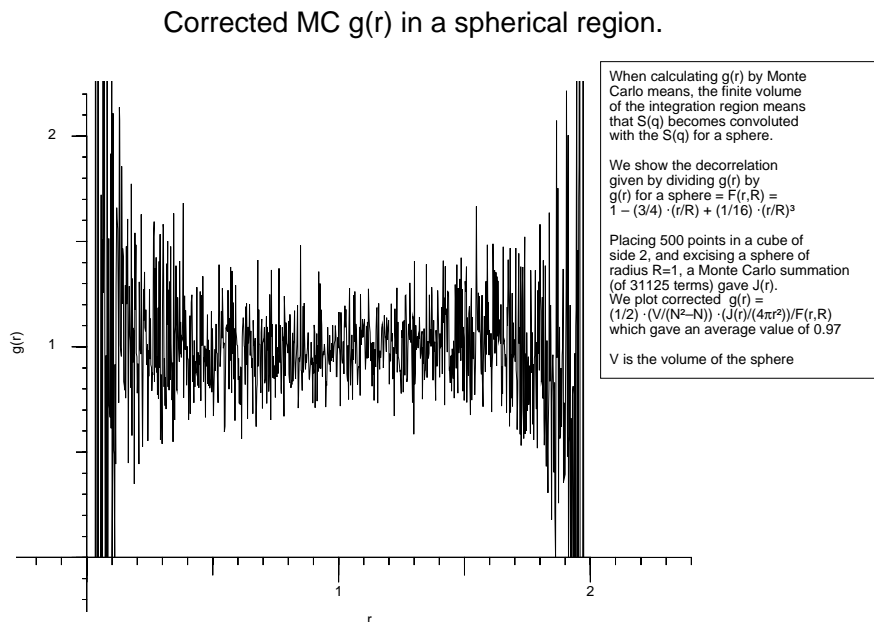


Figure 93: Corrected $G(r)$ when measuring in a finite spherical volume.

Examining this, though, we can see a number of problems. The noise in $g(r)$ gets far worse at low r , reflecting the fact that $J(r)$ was increasing with r^2 , and there is also a minimum r below which we have no information (reflecting the closest distance between any of our test points).

The corrected $g(r)$ also shows high noise at large r due to the fact that we have a finite spherical test volume – this can be overcome by using periodic boundaries, but this constrains the volume we may consider.

These problems will clearly reduce with more points and larger volumes, but to obtain fine resolution at low r this standard approach will clearly require the evaluation of a great number of radial separations, if we are to maintain information at large r . With porous structures we have the problem that we are trying to obtain information over a range of length scales.

We thus adopt a non-standard strategy.

15.5 Obtaining $G(\mathbf{r})$ in a continuous medium.

For our modified approach to calculating the spatial correlation function, we use the fact that neutron scattering shows us that we may with adequate resolution treat the density as continuous and homogeneous, except where pore void space has been excised. Thus strictly we are now calculating the solid-solid density correlation function $G(r)$, where :

$$G(r) = \frac{\rho(r)}{\rho_\infty}$$

$$\therefore G(r) = \frac{1}{V \cdot \rho_\infty} \int_v dr' \langle \rho(r') \rho(r+r') \rangle$$

where $\rho_\infty = \langle \rho(r) \rangle$ is the average density,
 V is the volume.

(see chapter 12).

Working with a continuous medium allows us to now place test point where we wish; this, used with the following algorithm, gives a great increase in calculation efficiency, resulting in better signal to noise, and reduced computation times :

We initially place N_i test points p_i at random within our test volume (which may be any shape). A test point either lands in solid occupied space, in which case it will scatter, and we will calculate the radial distribution of matter around it, or it lands in void space, in which case it is thrown away (it plays no further part, any more than would a point not within the list of scattering particles in a standard discrete Monte Carlo calculation).

We then generate a list of N_j radii, using any distribution that we choose – linear is an obvious one, but to probe small r in fine detail a partial log weighting or a Gaussian weighting can be useful; infact, since we will be interested in $r \cdot G(r)$, weightings proportional to r , r^2 are also useful (see appendices Q.2, Q.3, Q.3.1, Q.3.2).

We also generate N_j random unit vectors v_j (using von Neuman's method [Powles, 1994], see appendix Q.1), and multiply these by the radii to generate the N_j secondary test points p_j .

We now calculate the true XYZ locations of the secondary test points p_j , by adding their coordinates to those of each of the primary test points :

$$\mathbf{r}_{ij} = \mathbf{r}_i + \mathbf{r}_j$$

i.e. each point p_i is surrounded by a cloud of points p_j , at our selected but randomised radii r_j .

We next determine whether the secondary test points p_j fall within pore void space or solid material. For those that fall within solid, their radii are binned as $SolidSum(r)$; for normalisation all the test radii r_{ij} are binned separately as $RadiiSum(r)$. Then the ratio gives us :

$$G(r) = \frac{SolidSum(r)}{RadiiSum(r)}$$

This normalisation has a second most important effect on the final signal to noise – we know our sampling is statistical, and the noise in our answer will reflect this; however by binning all the test radii, $RadiiSum(r)$ then contains the information on this variation – effectively this is the answer we would get if all space was solid, which we know has a density of unity. Thus by dividing by $RadiiSum(r)$ we reduce the peak statistical noise, as we may see if we compare figure 94 with figure 92, offering a great reduction in computational effort required for a given signal to noise. The reduction is more marked at large density, as then the two sampled sets become more similar. We also see that we may now obtain $G(r)$ information to arbitrarily low r .

MC $G(r)$ for a sphere, with calculated $G(r)$

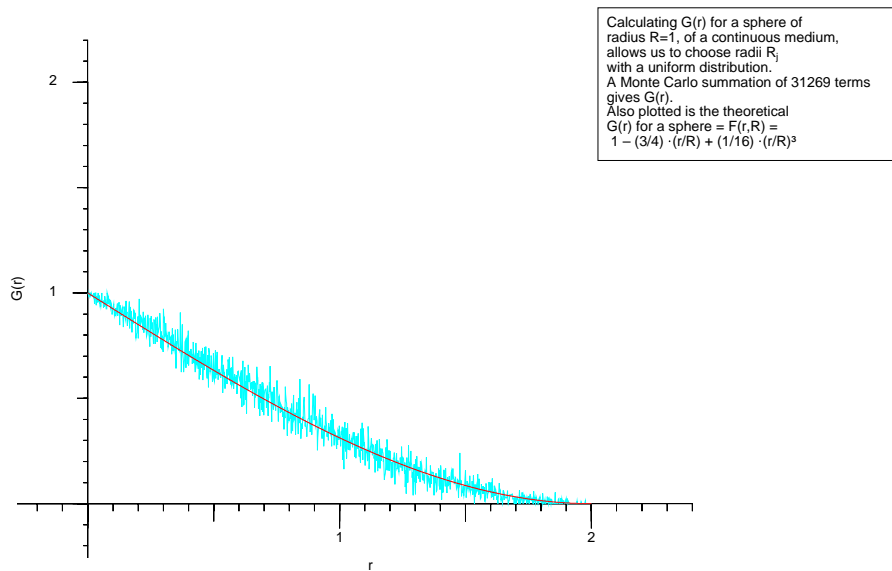


Figure 94: Calculated $\gamma_0(r)$ for a sphere constructed from a continuous medium.

Further advantages of this normalisation are correction of any non-uniformity in the

random number generator (none were found under the conditions it was used), and enabling the deliberate skewing of the random number density as described above, to facilitate measurements such as $r.G(r)$ and $d(r) = r^2.G(r)$.

In practice the above steps are repeated for many iterations, choosing first a new set of random points p_i , and then radii r_j , unit vectors v_j , to give us p_j , at each iteration. Thus there is no need to hold information on all the points in the simulation at one time.

Generating specific random radii and unit vectors and calculating the resultant x,y,z coordinates has the additional computational advantage of not requiring a square root calculation for each of many million radial distances, as required by the standard procedure.

15.6 Monte-Carlo $G(r)$ integration of simple bodies.

We may use this technique to obtain the $G(r)$ for simple and compound bodies, of finite or infinite dimension.

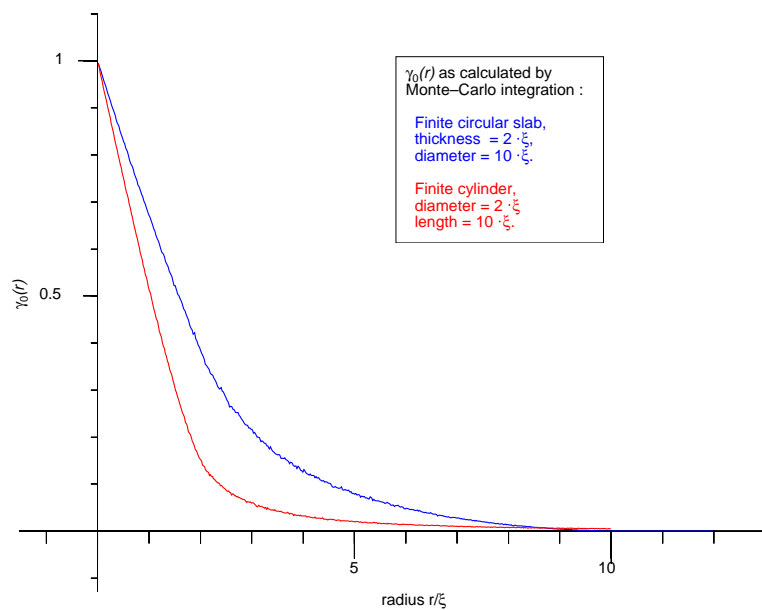
To handle a dimension in which the body is infinite, we just make the test as to whether we are in void or solid insensitive to that dimension; we must still bin over a finite range of course, and ensure that we populate that range with a reasonably dense set of test vectors.

This method was used to obtain $\gamma_0(r)$ for uniform density spheres and infinite slabs (both showing excellent agreement with theory), for finite circular slabs, for infinite and finite cylinders, and for thick shells and infinite tubes (as a model of multilayer Buckyballs and Buckytubes), see appendix L and figures 95, 110, 137.

15.7 Construction of lattices of pores.

The MCM-41 and MCM-48 templated silicas are constructed on regular lattices, thus there was a strong interest in studying pores on such lattices. Sol-gel glasses have a less ordered structure, and pose many problems in modelling their structure. Nonetheless NMR Cryoporometry shows that the pore size distribution width is typically 20% to 50% of pore diameter; we will initially model such structures by interpolation between ordered structures of different packing densities, with the introduction of disorder as a second step.

$\gamma_0(r)$ for finite circular slab and for cylinder.



$\gamma_0(r)$ for thick walled shell and infinite tube.

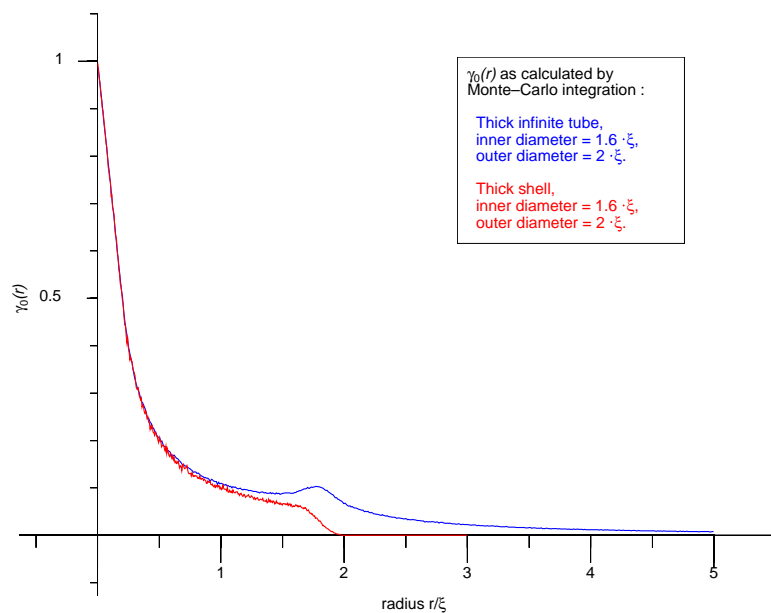


Figure 95: $\gamma_0(r)$ for some simple bodies, as calculated by Monte-Carlo integration.

15.7.1 Simulating Cubical lattices of Spherical pores.

Although spherical pores on cubical lattices represent an improbable model for the silicas on which measurements were made, they provided a valuable first step in aiding the evaluation of the algorithms, and in deciding whether to proceed to more elaborate schemes. In addition they provide a likely upper density bound to the range of densities covered by random lattices, and we will use the values we obtain to obtain those for random lattices by interpolating between the cubical case and the HCP case.

Suppose that around each of N_i test points P_i we have a cloud of N_j secondary test points P_j ; we wish to know whether the points are located in silica or void space. For an infinite cubical lattice we may just take each of our x, y, z spatial coordinates modulo the lattice spacing a ; if we normalise to the lattice spacing, this is just $1|XYZ$, where XYZ is our array of coordinates. We actually perform this twice, first to determine the number of i test points in the solid, N_{is} , when XYZ_i has dimensions $(N_i, 3)$, and secondly to determine the number of j test points in the solid, N_{js} , when XYZ_j has dimensions $((N_{is} \times N_j), 3)$.

This gives coordinates that cycle repeatedly from 0 to just under 1; subtracting a half from them gives coordinates that are zero in the centre of the pore and $\pm 1/2$ at the pore walls. Thus all that one has to do to determine if one is in pore void or solid silica is to compare the sum of the squares of the coordinates with the square of the pore radius : $PoreRadius^2 \geq (x^2 + y^2 + z^2)$.

We may combine all the above into a single *ApI* expression that tells us if we are in a pore void space :

$$SelVoid \leftarrow (PoreRadius^2) \geq + / (-0.5 + 1|XYZ)^2$$

This single expression encodes all the structure of our spherical pores on an infinite cubical lattice!

Then all we need to do is to use this to select those points in the solid :

$$PointsSolid \leftarrow (\sim SelVoid) / [1]XYZ$$

and to calculate their radial density (say by using a binning algorithm), and normalise by the radial density of the test points.

Checks were made setting the radius to $0.5 \times a$, when about half the test points fell in the solid, and then to $\sqrt{3} \times a$, when none did; this is in agreement with the analytic model.

If the radii of the pores are allowed to increase above $0.5 \times a$, the pores will intersect, and the lattice will be porous. The lattice will remain intact until the radius reaches $(1 \div \sqrt{2}) \times a$.

One should note the important difference between this periodic structure and the conventional periodic boundary conditions, is that with the latter the maximum distance over which $G(r)$ can be measured is of the order of the lattice periodicity; with this algorithm we may choose to bin over any sub-range within 0...infinity (placing our test points so as to populate this range), as it is the pores that are periodic, not the volume we are measuring within. (Later we shall relax the strict periodicity of the pores.)

15.7.2 Simulating Square lattices of Cylindrical pores.

Another simple case to test is cylindrical pores on a square lattice. Here we have just :

$$\begin{aligned} SelVoid &\leftarrow (PoreRadius^2) \geq + /(-0.5 + 1|XYZ[; 1 2])^2 \\ PointsSolid &\leftarrow (\sim SelVoid) / [1]XYZ \end{aligned}$$

15.7.3 Simulating Hexagonal lattices of Cylindrical pores.

A practical case of particular interest is templated silica MCM-41, which is constructed to have cylindrical pores on a hexagonal lattice.

The unit cell for a hexagonal lattice is skewed; this is inconvenient, thus we chose to consider a rectangular lattice containing two pores, of dimensions $(a, b) = (1, \sqrt{3}) \times a$. Thus we take $1|x$ and $(\sqrt{3})|y$, and centralise our range on $(0,0)$ by subtracting $(1, \sqrt{3}) \div 2$. Thus if a test of $PoreRadius^2 \geq (x^2 + y^2)$ evaluates true, we are definitely in pore void, as before. However we have a second pore to test for as well in the hexagonal case. For this we keep an overlapping second lattice, displaced by $(1, \sqrt{3}) \times a$. i.e. we add $(1, \sqrt{3}) \div 2$ to the x, y coordinates, before again performing the modulus, subtraction and test. If this test evaluates true we are definitely in pore void; all that remains is to *OR* the two logical vectors, and use its logical inverse to select the x, y, z locations of the points in the solid.

We may express this as :

$$\begin{aligned}
 AB &\leftarrow 1, 3^{1/2} \\
 SelVoid1 &\leftarrow (PoreRadius^2) \geq + /((-AB \div 2) + [2]AB|[2]XYZ[; 1 2])^2 \\
 SelVoid2 &\leftarrow (PoreRadius^2) \geq + /((-AB \div 2) + [2]AB|[2](AB \div 2) + [2]XYZ[; 1 2])^2 \\
 PointsSolid &\leftarrow (\sim(SelVoid1 \vee SelVoid2))/[1]XYZ
 \end{aligned}$$

15.7.4 Simulating Hexagonal Close Packed lattices of Spherical pores.

Although HCP lattices of pores are more closely packed than the average packing found in sol-gel silicas, HCP lattices of pores form a useful lower bound on the range of densities likely to be found in real sol-gel silicas.

The unit cell for an HCP lattice is skewed along two axes; this is inconvenient, thus we chose to consider a right box containing four pores of dimensions $(a, b, c) = (1, \sqrt{3}, 2 \cdot \sqrt{(2/3)}) \times a$.

We may express this as :

$$\begin{aligned}
 ABC &\leftarrow 1, 3^{1/2}, 2 \times (2 \div 3)^{1/2} \\
 SelVoid1 &\leftarrow (PoreRadius^2) \geq + /((-ABC \div 2) + [2]ABC|[2]XYZ)^2 \\
 SelVoid2 &\leftarrow (PoreRadius^2) \geq \\
 &\quad + /((-ABC \div 2) + [2]ABC|[2](ABC \times 110 \div 2) + [2]XYZ)^2 \\
 LD &\leftarrow 1 \div 3^{1/2} \\
 SelVoid3 &\leftarrow (PoreRadius^2) \geq \\
 &\quad + /((-ABC \div 2) + [2]ABC|[2](0, LD, 0.5 \times ABC[3]) + [2]XYZ)^2 \\
 SelVoid4 &\leftarrow (PoreRadius^2) \geq \\
 &\quad + /((-ABC \div 2) + [2]ABC|[2]((0, LD, 0) + ABC \div 2) + [2]XYZ)^2 \\
 SelSolidJ &\leftarrow \sim SelVoid1 \vee SelVoid2 \vee SelVoid3 \vee SelVoid4 \\
 PointsSolidJ &\leftarrow SelSolidJ/[1]XYZ
 \end{aligned}$$

LD: Layer Displacement : Y displacement between Z layers.

15.8 Ensembles of lattices with a statistical spread.

Porous structures with a wide or even fractal range of pore sizes (such that small pores and particles fit between the interstices of larger ones) are very dissimilar to regular structures, and we can not expect to model one with the other. However given that the NMR Cryoporometry indicates a typical 20% to 50% spread in pore size for the measured sol gel silicas, a reasonable first approximation is to treat them as an ensemble of regular lattices, with a statistical spread in pore and lattice sizes.

Rather than have to construct many different lattices, it was realised that they were all similar, just related by a scaling. Thus a simple scaling of our radius effectively indexes into a structure with different pore size and lattice spacing.

Thus we just generate for each of our j secondary test points p_j a value centered on unity, but with a Gaussian spread, of variance *EnsembleVariance*. Then when we calculate our relative x,y,z location for the secondary test points from the j radii r_j and j random unit vectors v_j , we scale it by *EnsembleScaleJ*, to effectively index into a structure of different size. The binning is still done at the original radius. This effectively gives us an ensemble with j different lattices.

This may be expressed as :

$$\begin{aligned} \textit{EnsembleScaleJ} &\leftarrow NJ \textit{ gauss } 1, \textit{EnsembleVariance} \\ \textit{RelativeXYZ} &\leftarrow (\textit{EnsembleScaleJ} \times \textit{RadiusJ}) \times [1] \textit{RUnitVecJ} \end{aligned}$$

Here the function *gauss* uses the Central Limit Theorem to generate a Gaussian spread, by convolving together 12 uniform distributions [Powles, 1994] (appendix Q.2).

It should be noted that the above pores are still all spherical; generating separate scalings for x,y,z would result in oblate and prolate pores as well.

To justify this approach further, although even one ball of a different size in a regular structure of otherwise identical balls can cause long range defects in the structure, in the case of a lattice of pores growing in a sol gel, if one pore starts to grow say 10% undersize, it may well be that the pores either side will grow oversize in compensation. Given the fact that we are looking for ways of arranging pores that have a 20% to 50% size spread, one likely model is one in which there is an average pore size over a reasonable volume, such that the pores can pack fairly regularly, but then this average pore size may vary by some percent in different regions. Then, within each region, there

may be a pore size variation of a few percent that is partially locally compensated by adjacent pores to preserve the packing structure.

The radial solid-solid density distribution function $G(r)$ for such a model should be well represented by that for the ensemble of regular lattices with a Gaussian distribution in lattice and pore sizes that we are calculating. Further detailed investigation may reveal that distributions other than Gaussian are more appropriate, though Gaussian is a reasonable approximation to the pore size distributions as measured by NMR Cryoporometry (figure 96).

15.9 Implementation of Monte-Carlo integration of models

The above algorithms and necessary random generation of the radii and unit vectors, and hence test points p_i and p_j were expressed in *Apl* (see appendix Q).

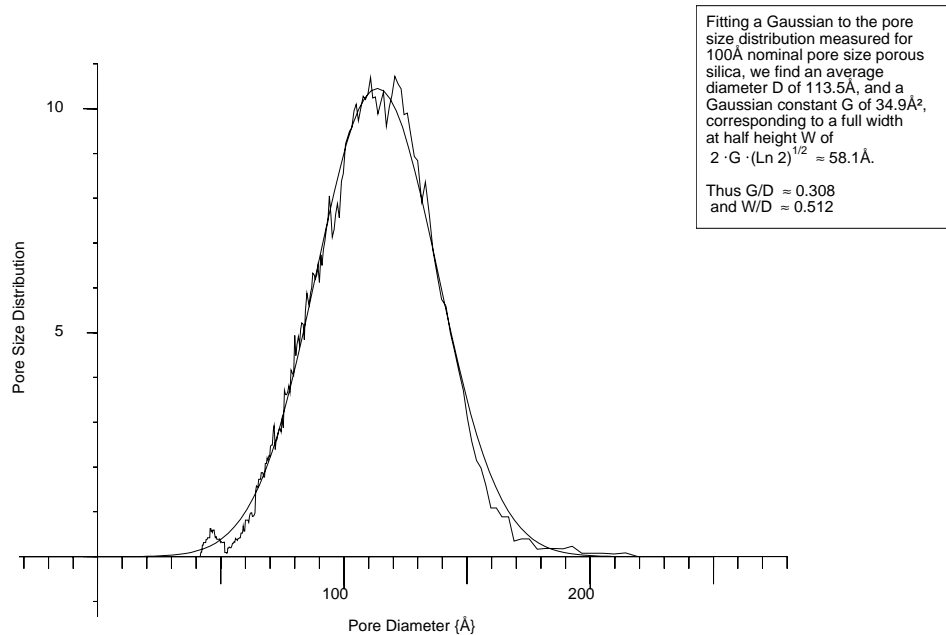
As can be seen from the code examples above, with the extreme conciseness of the algorithms one has the great advantage of being able to demonstrate 'proof of correctness by inspection', with regard to the algorithms being a faithful implementation of our geometric models.

The code was written and initially tested on an Atari TT30 30MHz computer with 14 MBytes of memory, using *Apl68000*, giving evaluations to about 3×10^8 lattice sums per integration in a week.

It was then compiled from *Apl* to *C*, using Prof. T. Budd's *Apl to C* compiler [Budd, 1988], as maintained by myself and Dr. S. Sirlin of *Nasa* [Sirlin, 1988..1999], and transferred to a DEC Alpha (with thanks to Prof. R.J. Newport and Dr. G. Mountjoy), offering calculations to 3×10^9 lattice sums in a week.

The compiler was then ported to Linux, and the Monte-Carlo integrations performed on a 200MHz Intel Pentium II MMX processor. With further code speed-up improvements, the following integrations were performed in the main out to a radius of 7.5 lattice spacings a , requiring about 3 days for 3×10^9 lattice sums. Some calculations were only done to $2 \times a$ (to investigate variations in the behaviour near the pore wall), some (to investigate the large r behaviour) out to $21 \times a$, requiring 10 or more days and $1 \rightarrow 4 \times 10^{10}$ lattice sums to achieve comparable signal to noise.

100Å Porous Silica fitted with a Gaussian.



Normalised Gaussian with half height width of 0.5.

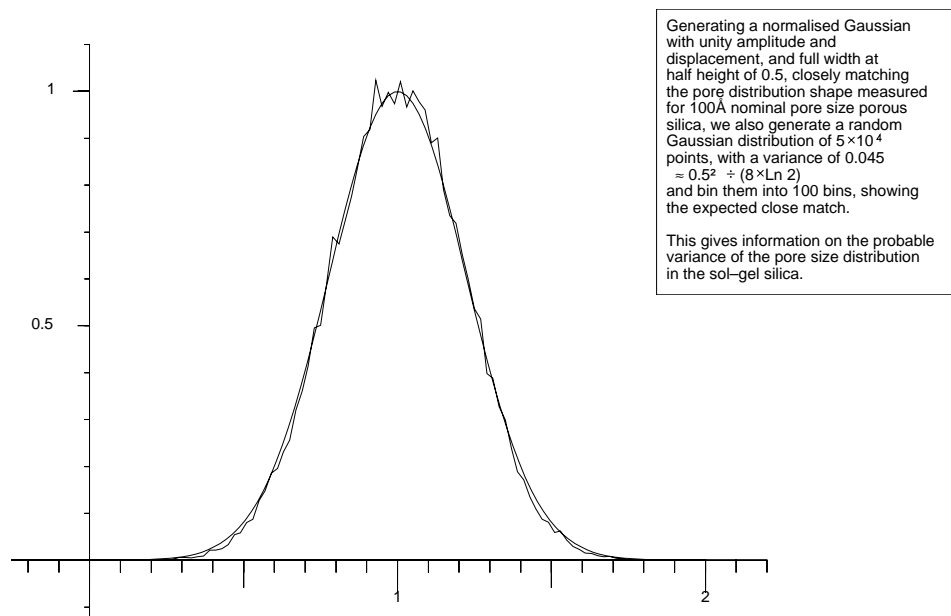


Figure 96:

Gaussian fitted to pore distribution as measured by NMR cryoporometry for 100Å Merck sol-gel silica, and Gaussian distribution generated to match fitted Gaussian, showing expected agreement.

These calculations were performed as a background Unix task with an unnoticeable impact on the foreground tasks. They only required attention a few times a week to start a new simulation with a new value of $\frac{D_{void}}{a}$ or variance.

The calculations were performed in double precision; further proof of correctness of implementation was demonstrated by showing that the generated average densities agreed with the analytic ones to four or more significant figures (e.g. see table 9), that the density went to zero at the expected ratio of $\frac{D_{void}}{a}$ and that the lattice lost cohesion at the expected ratio.

15.10 Monte-Carlo integration of porous models.

To give reasonable peak noise figures in both $G(r)$ and $r \cdot G(r)$ representations, all the following calculations were performed with random r-vectors whose density was weighted as equal parts of uniform, proportional to r and proportional to r^2 (see appendix Q.3). The final ratioing stage described above ensures this does not affect the calculated $G(r)$. Monte-Carlo integrations were performed for hexagonal lattices of cylindrical voids of diameter = $0.9 \times$ lattice spacing, for variances of 0, 0.12, 0.14.

Monte-Carlo integrations were performed for cubic lattices of spherical voids of diameter = 0.3, 0.4, 0.5, 0.6, 0.7, 0.8, 0.9, $1.0 \times$ lattice spacing, for 0 variance.

Monte-Carlo integrations were performed for HCP lattices of spherical voids of diameter = 0.2, 0.3, 0.4, 0.5, 0.6, 0.7, 0.8, 0.9, 0.94, 1.0, 1.04, 1.1, 1.14, $1.2 \times$ lattice spacing, for 0 variance (see figure 97), and for HCP lattices of spherical voids of diameter = 0.9, 0.94, 1.0, 1.04, 1.1, 1.14, $1.2 \times$ lattice spacing, for 0.005 variance.

They were also performed for HCP lattices of spherical voids of diameter = lattice spacing for variance 0, 0.005, 0.01, 0.02, 0.05, 0.1, 0.2, 0.50. It was shown that a good fit was obtained with the experimental data from sol-gel silicas for the range of variance $0.10 \rightarrow 0.20$ (chapter 16.2.4); thus a further set was calculated, with variance 0.12, 0.14, 0.16, 0.18, 0.2. See figure 98.

A set of calculations were also performed for HCP lattices of spherical voids of diameter = $0.9 \times$ lattice spacing, for variance 0, 0.005, 0.12, 0.14, 0.16. Ideally the full experimental parameter range of $\left(\frac{D_{void}}{a}, variance\right)$, should be covered, for HCP and cubic lattices. There was insufficient time for this, so one final calculation was made,

chosen to correspond to the furthest extent of the experimentally measured parameters, at diameter = $0.86 \times$ lattice spacing, variance = 0.2. This allowed an analytic fit approximation in 2D to be generated (see chapter 17).

15.11 Preliminary consideration of Monte-Carlo $G(r)$ s.

In the $G(r)$ calculated for spheres on hexagonal close packed lattices we see that near zero radius we have a measured density of nearly unity, that then falls off rapidly and nearly linearly. We understand this as follows :

We choose a test point to measure the differential scattering with respect to; this must exist and thus must be in solid (i.e. pore wall). Therefore at very short radius we will probably also be in pore wall, and so the density is nearly unity. As the radius increases there is a higher probability that we will be in void space, and thus the density falls.

At very large r we obtain the average bulk density of the model; at intermediate distances we have a periodicity that is scaled by the lattice spacing, for small variance. For larger variance the pore wall feature changes smoothly first to nearly the average density, and then slowly drops to the average density. We see in figure figure 97 that the oscillatory $G(r)$ data is asymmetric – it is thus not necessarily the case that the averaging effect of high variance will produce the same value as $G(r=\infty)$. We see this in practice, where we find a large r $G(r)$ structure in the simulated pores, that is also found in the real sol-gel silicas (see chapter 16). For this, the Monte-Carlo simulations were extended to 21 lattice spacings.

In chapter 16.2.1 and appendix L we show that we may approximate the behaviour near a pore wall as the expected $G(r)$ of a finite plane slab embedded in a medium of the average density.

Initial results for sol-gel silicas showed a better fit with experimental data for spheres than for cylinders, however as time permits it would be invaluable to extend the above limited calculations for cylinders, particularly with the MCM silicas in mind.

In chapter 16.2.4 we see that for appropriate values of $\frac{D_{void}}{a}$ and variance we may obtain good fits to $G(r)$ curves calculated from the measured scattering from sol-gel silicas. The variance changes from a value where there is a slight dip below the average density at about half the lattice spacing, to a value where there is just a smooth change to nearly the average density.

$G(r)$ for Spherical voids on an HCP Lattice

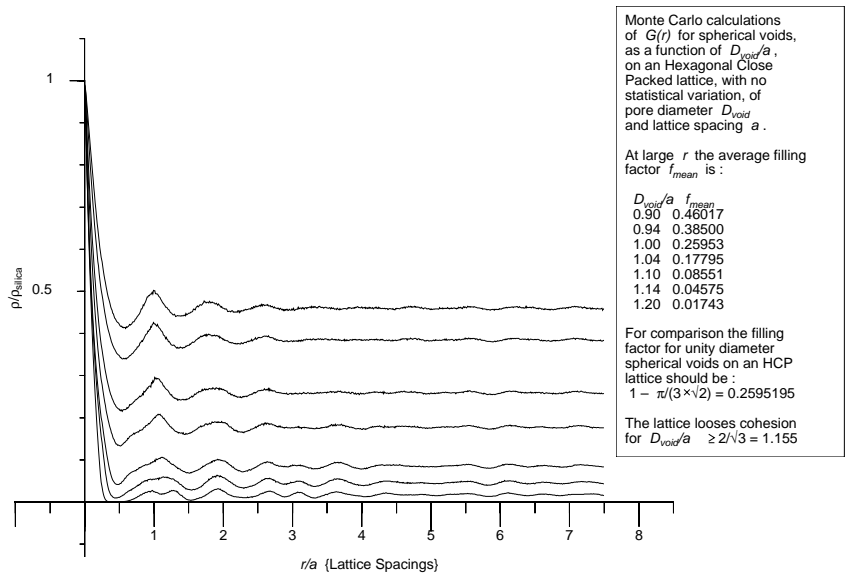


Figure 97:

$G(r)$ for spherical voids on an hexagonal close packed lattice, with zero variance, varying the ratio $\frac{D_{void}}{a}$.

$G(r)$ for Spherical voids on an HCP lattice.

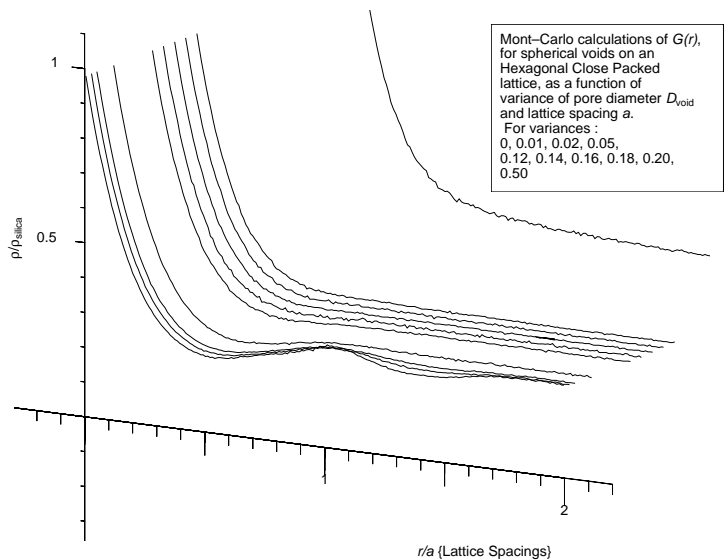


Figure 98:

$G(r)$ for spherical voids on an hexagonal close packed lattice, with $\frac{D_{void}}{a} = 1$, varying the variance.

Chapter 16

Analysis of sol-gel silica neutron scattering in q , r domains.

16.1 Analysis in q domain, comparison with Monte-Carlo data.

If we examine the measured scattering from the seven sol-gel silicas (figure 85) we have, firstly at high q , for the diffraction data measured on ILL diffractometer D4, the atomic diffraction peaks superimposed on an incoherent scattering (primarily from residual hydrogen on the silica surfaces). We see that there appears to be a larger amount of hydrogen in the small pore silicas, presumably reflecting the fact that although the pores have a area proportional to the $radius^2$, their number goes inversely with $radius^3$.

If we fit this incoherent background with a *sech* function (see section 14.1) and subtract it, we obtain figures 99, 100, 101).

We see that at high q the hydrogen subtracted data for the scattering from the pores drops monotonically with an approximately q^{-4} falloff, until the onset of atomic scattering. If we neglect the atomic scattering we obtain a form that is effectively $P(q)$ for the pores. We see, however, that we appear to have structure on two length scales, where we might assume to just have the scattering appropriate to, say, spheres the diameter of the mean pore diameter in the sol-gel silica. We do see a variation of the turn-over q for the different silicas.

We know we do not have only one pore size in our sol-gel silicas, but we have a measured pore diameter distribution from our NMR cryoporometry measurements. If we plot the

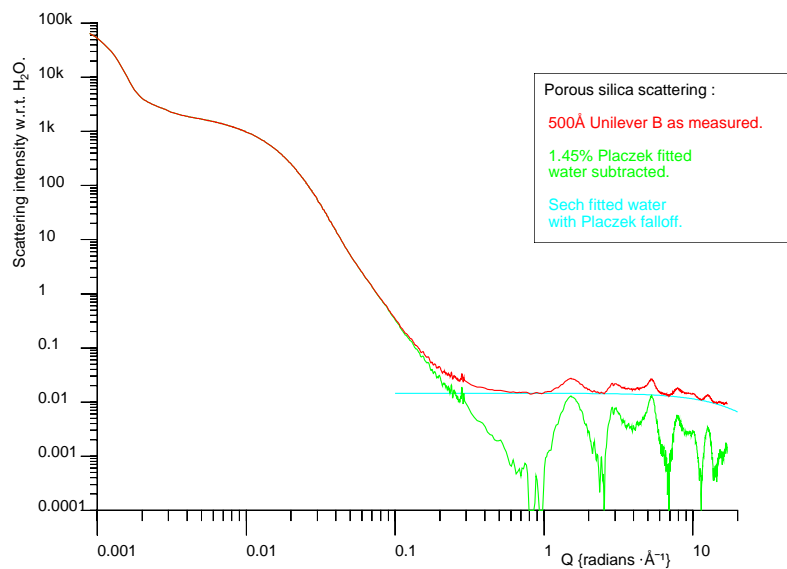
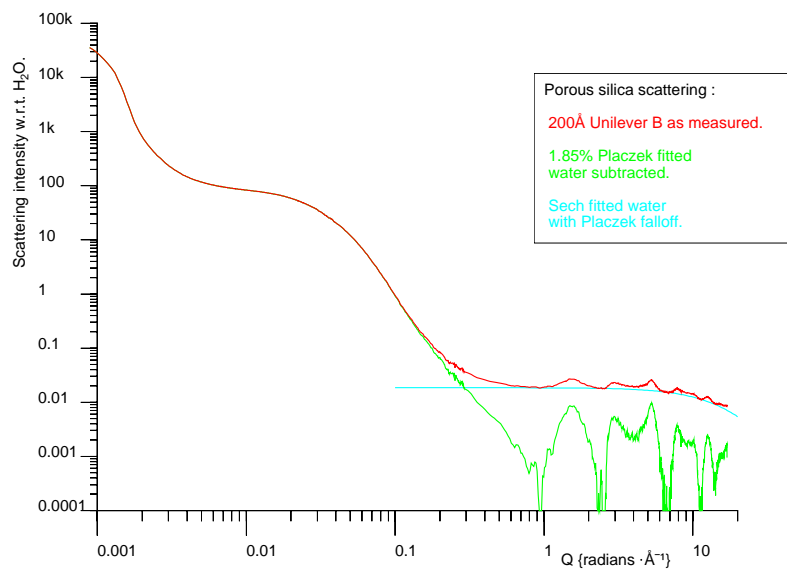
Water subtracted scattering from 500Å Unilever B SiO_2 .Water subtracted scattering from 200Å Unilever B SiO_2 .

Figure 99:

$I(q)$ for C500, C200 Unilever B SiO_2 , with Placzek fit to incoherent scattering and plot of coherent scattering residual.

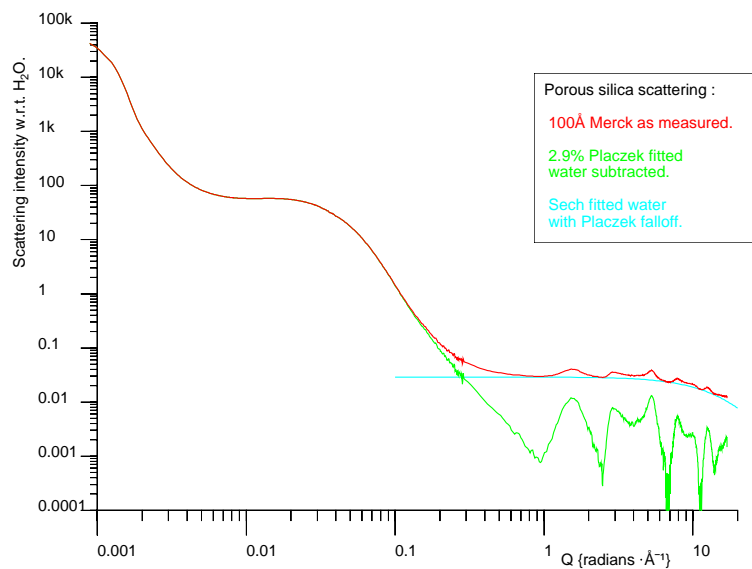
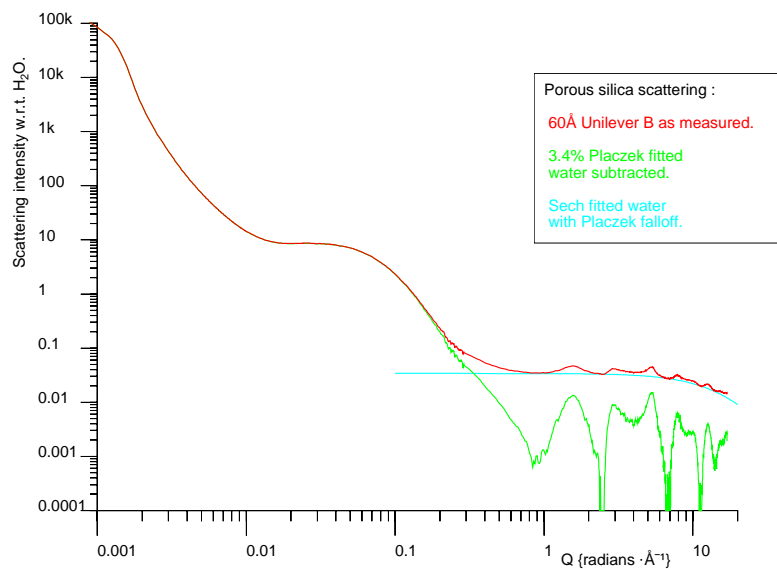
Water subtracted scattering from 100Å Merck SiO_2 .Water subtracted scattering from 60Å Unilever B SiO_2 .

Figure 100:

$I(q)$ for 100Å Merck, C60 Unilever B SiO_2 , with Placzek fit to incoherent scattering and plot of coherent scattering residual.

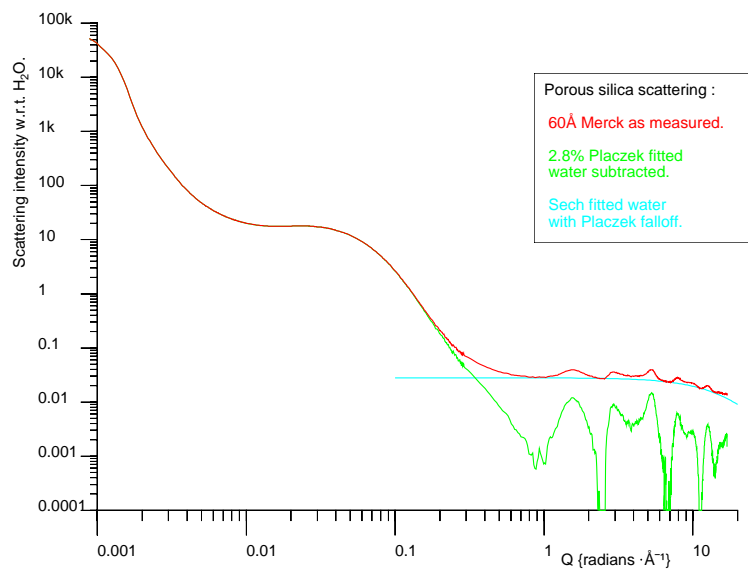
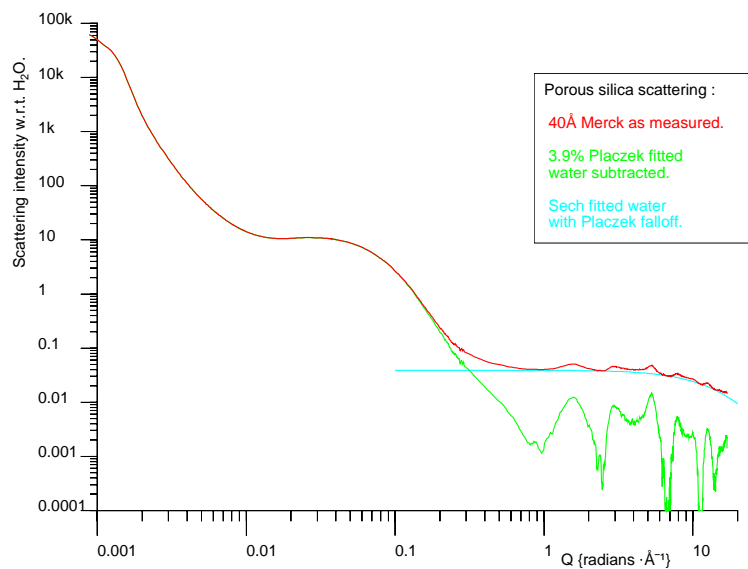
Water subtracted scattering from 60Å Merck SiO_2 .Water subtracted scattering from 40Å SiO_2 .

Figure 101:

$I(q)$ for 60Å Merck, 40Å Merck SiO_2 , with Placzek fit to incoherent scattering and plot of coherent scattering residual.

scattering expected from an ensemble of isolated spheres with the NMR measured mean and variance for Unilever C200 B silica, and compare it with the measured scattering, we obtain figure 102. We see that we appear to have scattering from structures that are both smaller and larger than expected.

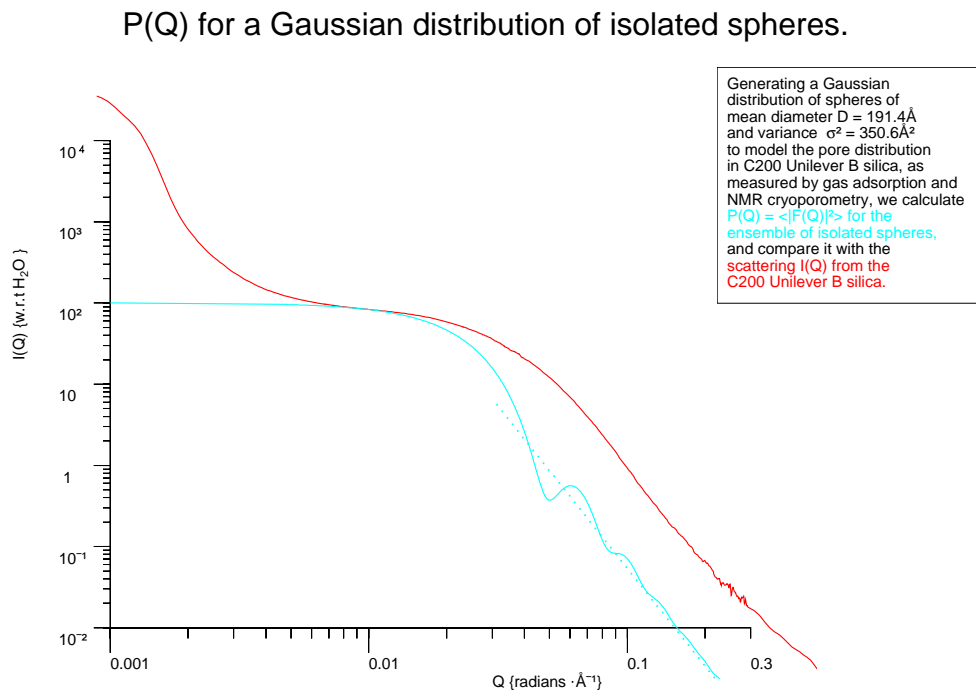


Figure 102:

Scattering from C200 Unilever B SiO_2 , with calculated scattering from a Gaussian distribution of spheres – mean and variance as measured by NMR cryoporometry.

If we initially restrict our attention to the large q feature, we may in accordance with chapter 12 fit to Guinier and Guinier-Porod equations relating to a random mixture of two phases (see figure 103). We see that we have two possible Guinier-Porod fits, one corresponding to the low q Guinier condition, the other to the high q Porod condition. These are all in broad agreement with the nominal pore diameter as measured by gas adsorption (171.5\AA), but show a spread of 30% in deduced pore diameter.

Examining the scattering in detail we see that rather than changing smoothly to a q^{-4} behaviour (as does the Guinier-Porod equation), the data for all our measured scattering curves actually have points of inflection where it changes from a steeper than q^{-4} behaviour to q^{-4} . In fact if the data for the various silicas is examined in magnification, it can be seen that beyond the point of inflection the initial behaviour is not precisely q^{-4} , but actually has a negative curvature.

$I(Q)$ for C200 Unilever B SiO_2 + Guinier, Guinier–Porod fits.

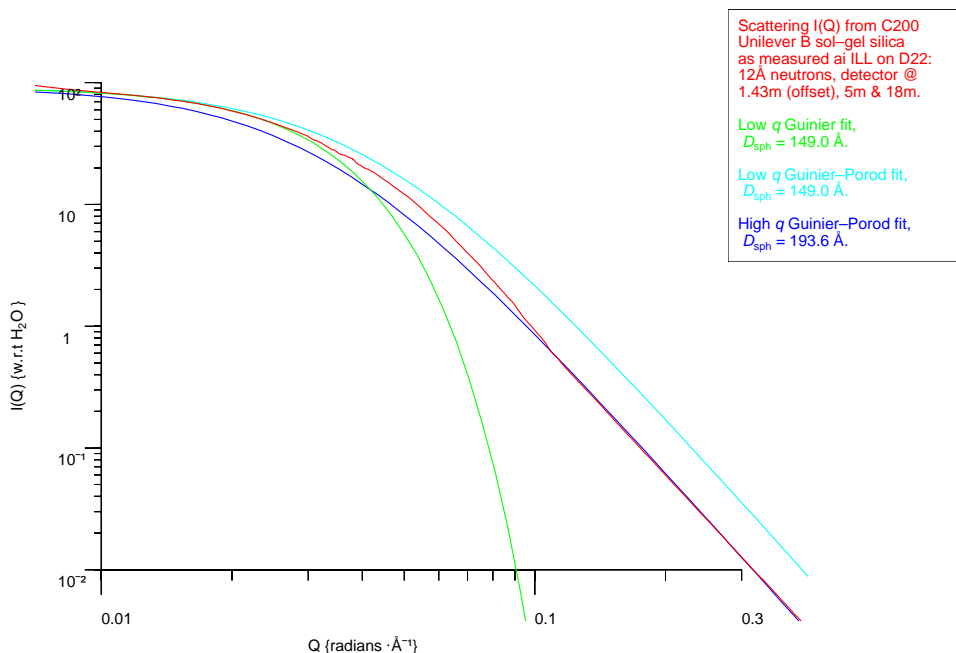


Figure 103:

Scattering from C200 Unilever B SiO_2 , with a Guinier fit and Guinier-Porod fits to the low q and high q limits.

Thus in figure 105 we plot an empirical *sech* fit (discussed in chapter 12) and a Guinier-Porod curve of $1/30^{\text{th}}$ the amplitude corresponding to a 3% addition of a random mixture of two phases. Also plotted are fits to the low- q feature, of a Guinier (Gaussian) plus a Guinier-Porod curve with approximately the same reduction in amplitude. The sum of these four components fit the observed scattering to excellent accuracy.

In figure 104 we show a similar fit for C500 Unilever B silica. We show just the high- q component, to show it to better resolution. For this silica the random mixture component is less than 1% of the total.

We will study the exact form of an isolated scatterer that gives the best fit to the measured scattering in more detail in the spatial domain, in the next section, and we note there that the excellent fit to the sum of a *sech* and Guinier-Porod is also present even in the highly sensitive chordal representation.

However we have Monte-Carlo calculated $f_g \cdot G(r)$ data for a range of models with infinite arrays of cylindrical pores on square and hexagonal lattices and of spherical pores on cubic and hexagonal close packed lattices, both with uniform pores and lattices, and

$I(Q)$ for C500 Unilever B SiO_2 , Sech + Guinier–Porod.

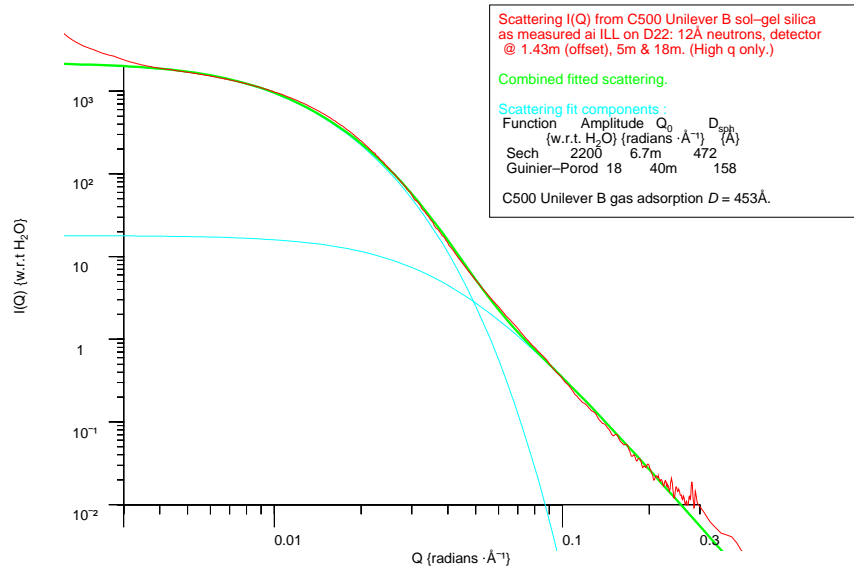


Figure 104:

Scattering from C500 Unilever B SiO_2 , with Sech + Guinier-Porod fits to the high q data.

$I(Q)$ for C200 Unilever B SiO_2 + fitted scattering.

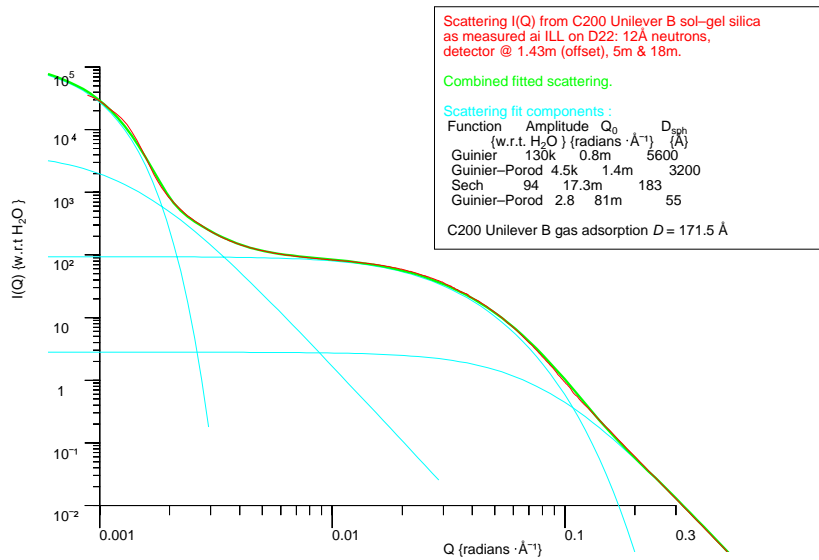


Figure 105:

Scattering from C200 Unilever B SiO_2 , with Guinier + Guinier-Porod fits to the low q data and Sech + Guinier-Porod fits to the high q data.

with variance of pore diameter and lattice spacing (see chapter 15).

We see in chapter 12.2 that we may use a Fourier transform to convert $r \cdot \gamma(r)$ data to $q \cdot I(q)$ data. Thus if we transform the data for touching spheres on hexagonal close packed lattices for various variances to $I(q)$, (see appendix P.2), and just linearly scale the vertical axis to match the measured intensity, and transform from a lattice spacing normalised to unity to one measured in angstroms we obtain figures 106, 107, 108, 109, where the Monte-Carlo calculated scattering is compared with the measured scattering for the seven sol-gel silicas.

Our only parameters for these fits are (arbitrary) amplitude, pore diameter D_{void} = lattice spacing a , and variance σ .

We see that we can match to a reasonable precision over many decades of intensity and q the observed scattering, reproducing the position of the higher q 'knee' and its abruptness and the sudden transition to a q^{-4} region (though not its exact position); most significantly we see a second structure at low q , in spite of the fact that we are constructing our lattices with structure on only one length scale.

The limitation of these fits are that our model uses an HCP lattice with variance, not a truly random one, and the plotted data are all for the case of touching spheres, whereas we know from density measurements that for the smaller pore diameter silicas in particular $D_{void} < a$. We do have Monte-Carlo data for such cases, but it has not yet been calculated at all the required values of variance – to do so would clearly be a useful advance.

The low q structure is clearly poorly resolved, even though the Monte-Carlo simulations were extended from a range of 0 to 7.5 lattice spacings out to 21 lattice spacings in an attempt to improve the resolution in this region. (Further extensions gave too degraded a signal-to-noise ratio, without extending each simulation time significantly beyond 10 days, on a 200MHz Pentium.) This long range structure could be clearly seen in $r \cdot G(r)$ plots, and is shown in the spatial domain in figure 115.

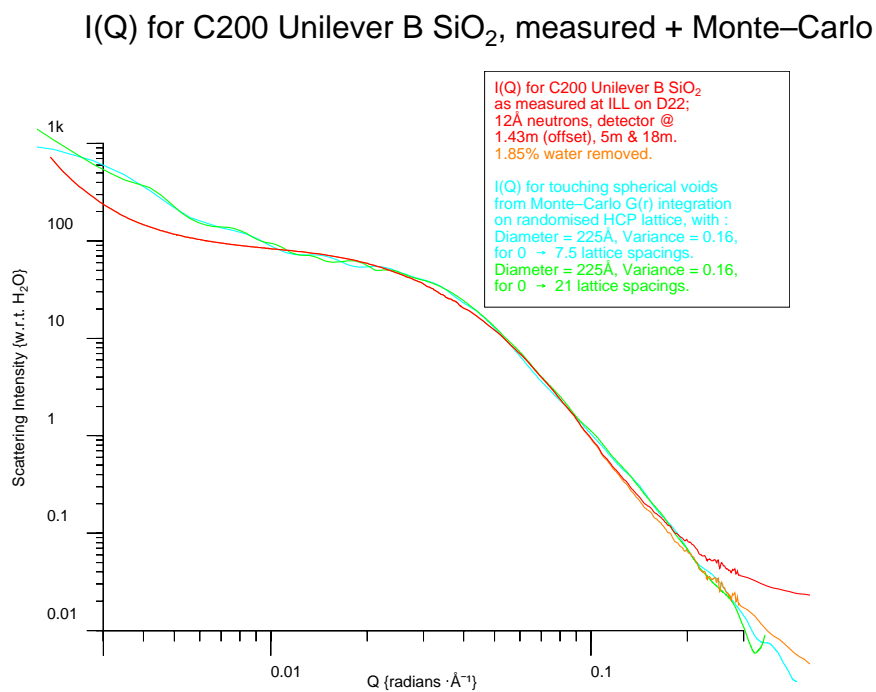
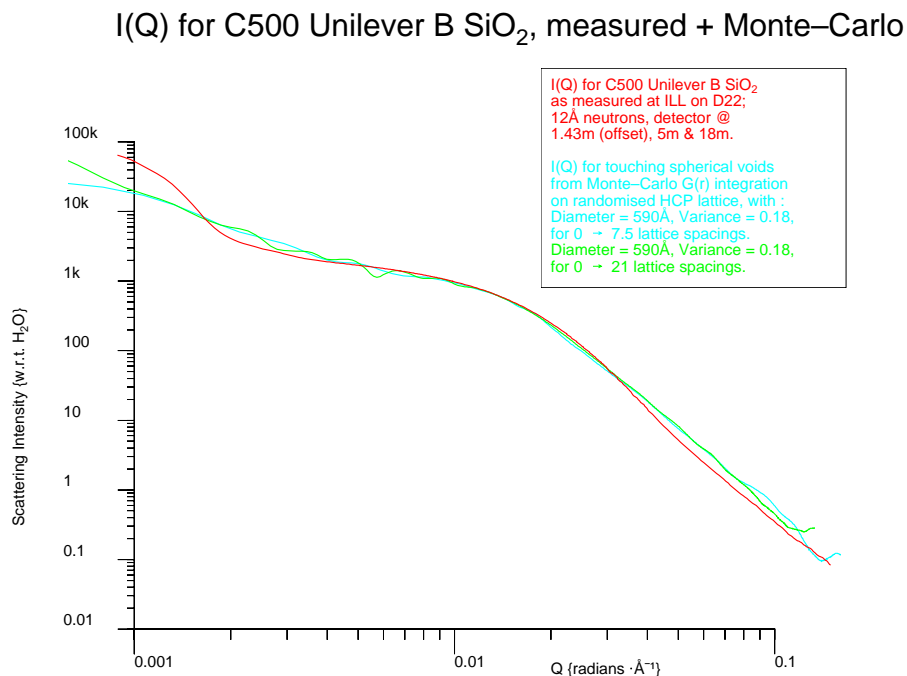


Figure 106:

$I(q)$ for C500, C200 Unilever B SiO_2 compared with calculated scattering from spherical voids on an HCP lattice with Gaussian variance of pore diameter D_{pore} and lattice spacing a .

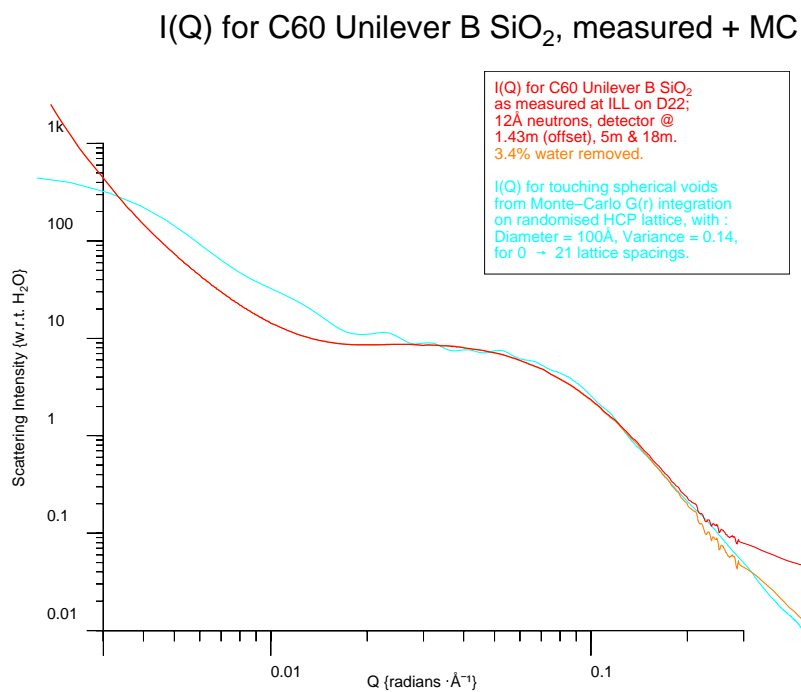
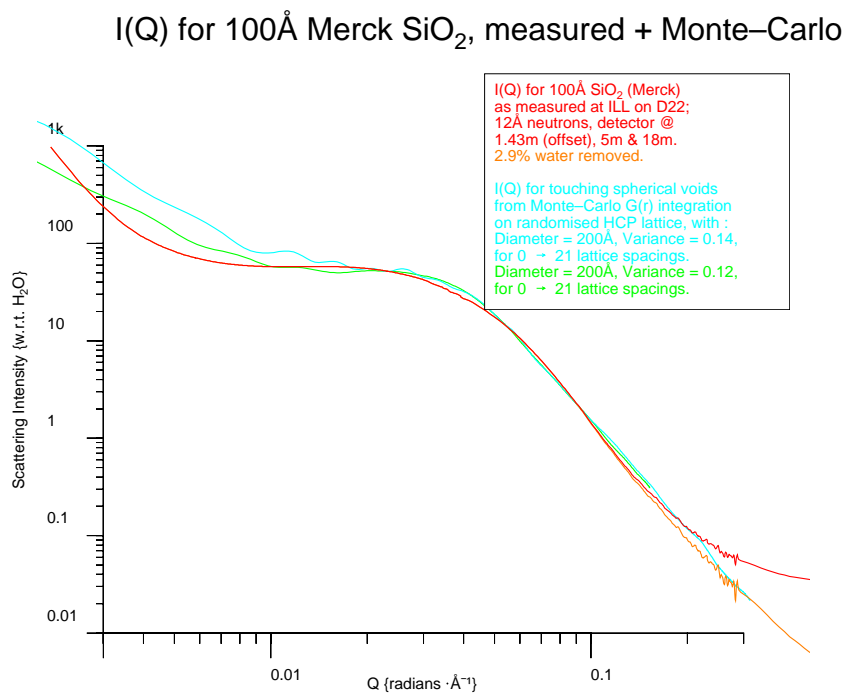
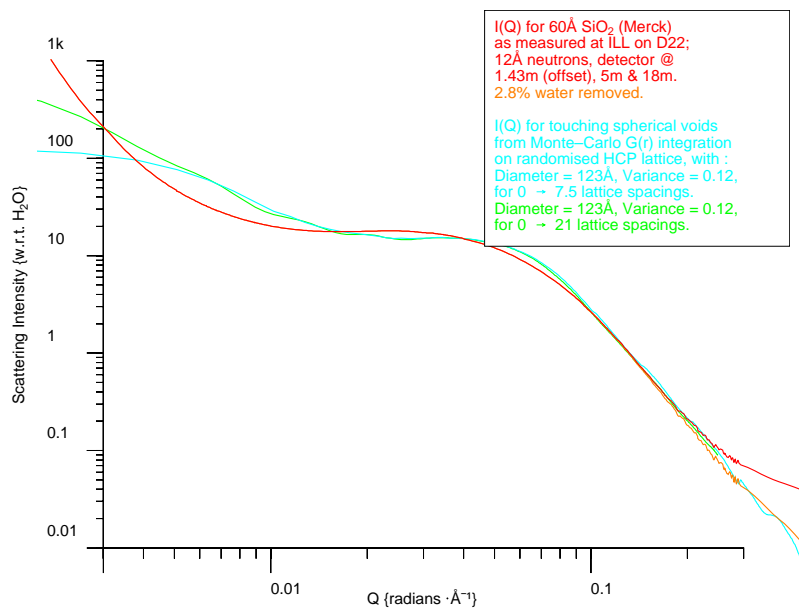


Figure 107:

$I(q)$ for 100Å Merck, C60 Unilever B SiO_2 compared with calculated scattering from spherical voids on an HCP lattice with Gaussian variance of pore diameter D_{pore} and lattice spacing a .

$I(Q)$ for 60Å Merck SiO_2 , measured + Monte-Carlo



$I(Q)$ for 40Å Merck SiO_2 , measured + Monte-Carlo

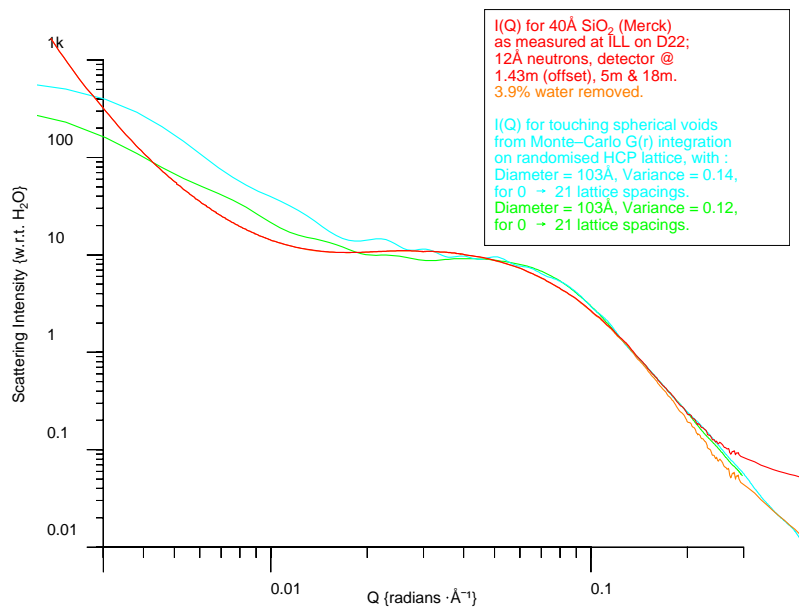


Figure 108:

$I(q)$ for 60Å, 40Å Merck SiO_2 compared with calculated scattering from spherical voids on an HCP lattice with Gaussian variance of pore diameter D_{pore} and lattice spacing a .

$I(Q)$ for 25Å Sigma SiO_2 , measured + Monte–Carlo

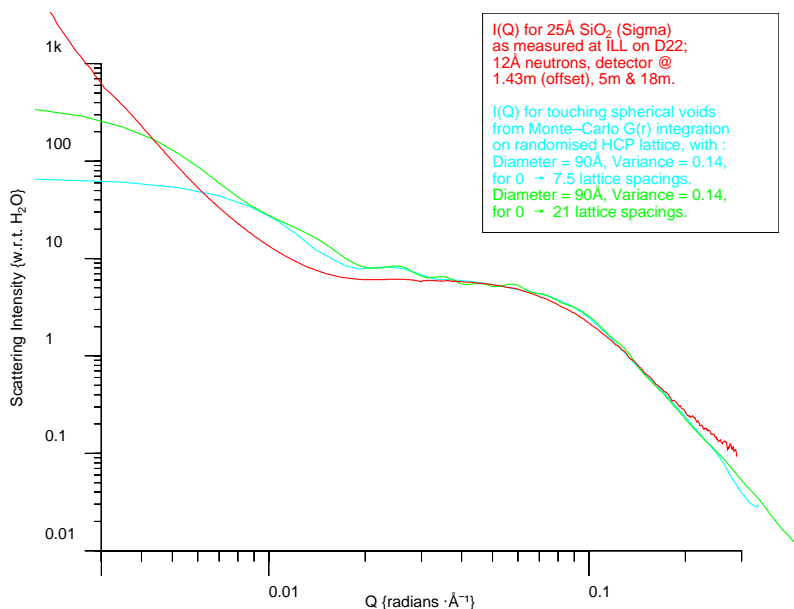


Figure 109:

$I(q)$ for 25Å Sigma SiO_2 compared with calculated scattering from spherical voids on an HCP lattice with Gaussian variance of pore diameter D_{pore} and lattice spacing a .

16.2 Analysis of silica scattering in the spatial domain.

We see in chapter 12.2 that we may use a Fourier transform to convert $qI(q)$ data to $r\gamma(r)$ data, and in appendix P.1 we summarise the steps necessary to successfully use a Fast Fourier Transform to obtain $\gamma(r)$ data.

If we perform such transformations on our measured $I(q)$ data for the seven sol-gel silicas, and examine, for example, the resulting $\gamma_0(r)$ for C200 Unilever SiO_2 at small radius, figure 110, and plot the calculated $\gamma_0(r)$ for a solid sphere of the same diameter (171.5Å) as the C200 B pore diameter as measured by gas adsorption and NMR cryoporometry, we see a very poor fit in both scaling and shape. Babinet's theorem tells us that for an isolated pore in a uniform medium we would expect the same scattering as from an isolated solid sphere of the same diameter, as we are not sensitive to phase.

However we do not have an isolated spherical void, we have an array of them, with phase relations between them.

$\gamma_0(r)$ for C200 Unilever B SiO_2 , sphere, infinite & finite slabs.

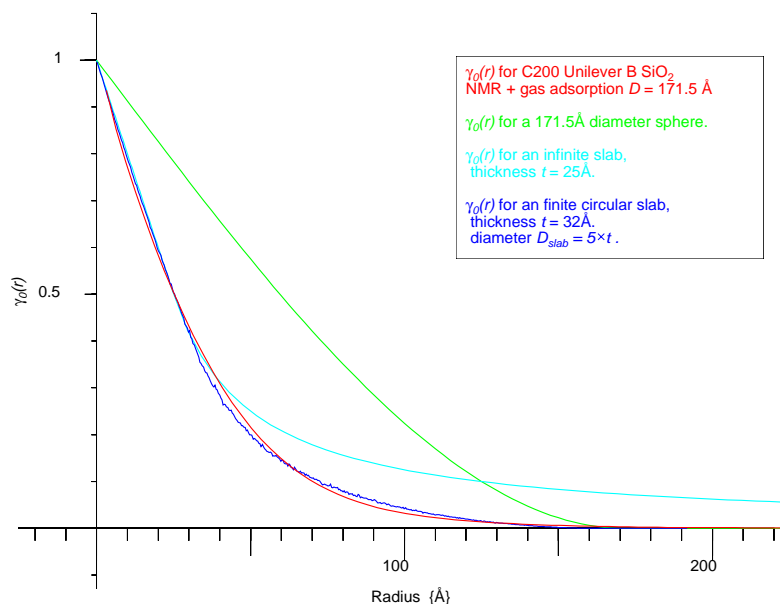


Figure 110:

$\gamma_0(r)$ for C200 Unilever B SiO_2 compared with $\gamma_0(r)$ for a matching sphere, an infinite plane slab and a finite circular slab.

16.2.1 Comparison of $G(r)$ for sol-gel silicas with that for slabs.

Further consideration of figure 110 suggests the following interpretation : $G(r)$ is measured with respect to points that exists, i.e. that are in the solid. Therefore at zero radius we are definitely in a pore wall, and the density is ρ_s ; as we go to larger r there is a higher chance we will be in pore void, and the density will fall (perhaps with oscillations); eventually at large enough r the $G(r)$ will be the average grain density ρ_g .

We note that at locations very close to the pore wall on a short enough scale the geometry will appear flat, curvature only becoming apparent at radii a significant fraction of the pore diameter. Thus we initially plot the scattering from an infinite flat plate of thickness t , as deduced in appendix L. The $\gamma_0(r)$ for an infinite plane is linear for $r \leq t$ and tends to zero for $r > t$ with an inverse r characteristic; we now see that we have gone from a structure that decays too abruptly (in the case of a sphere), to one that decays too slowly.

Thus we calculate using Monte-Carlo integration $\gamma_0(r)$ for a finite circular slab of thickness t , diameter $D_{slab} = 5 \times t$. We see that for $t = 32 \text{ \AA}$, $D_{slab} = 160 \text{ \AA}$, we obtain a

reasonable fit for such a simple model (see chapter 15.6), where we also note that the $\gamma_0(r)$ for a finite cylinder is less appropriate to that measured for the sol-gel silicas.

We wish to model a function that goes from the (voidless) silica density ρ_s at $r = 0$ to ρ_g at large r . Thus we may embed our finite slab in a uniform medium of density ρ_g .

We thus have a four parameter model describing $(\rho_s - \rho_g) \cdot \gamma_0(r) + \rho_g$, dependent on the voidless silica density ρ_s , the grain density ρ_g , (both measurable macroscopically, see chapter 11.5.2), the thickness t of the slab, and its diameter to thickness ratio ε .

We note that for $\varepsilon = 5$ we may deduce this characteristic wall thickness t from the initial slope of $\gamma_0(r)$, such that from the Monte-Carlo results we have $t = \frac{-0.6553}{\text{Slope}}$. If we perform this process on all silicas, we find pore wall thicknesses t as given in table 19.

This model should not be taken literally to suggest that we have flat slabs of these dimensions in our silica, merely that the silica walls and nodes left between the spherical voids may on a small enough scale be regarded as approximately flat surfaced slabs, and on a larger scale have an extended structure rather than a compact globular one. Thus we see that the initial linear region for $\gamma_0(r)$ for a flat slab transforms to the q^{-4} scattering behaviour at high q characteristic of smooth surfaces (see chapter 12 and appendix M).

The pore walls are not represented very well by a slab of constant thickness; we have presumably tapering walls between adjacent spheres. Further we know that we have a distribution of pore diameters, and thus presumably have a distribution of wall thicknesses and node sizes. Some initial work has been done to model these, but is not included here.

16.2.2 Conversion to density units.

We have seen that Fourier transformation of measured scattering $I(q)$ may be used to give us $\gamma(r)$ (going to zero at large r), and we may normalise this to give us $\gamma_0(r)$; in chapter 11.5 we have measured values for ρ_s (density of the voidless silica lattice) and ρ_g (density of the silica grain = $\rho_s \times f_g$). We may thus re-scale the $\gamma_0(r)$ data to density units using $G_\rho(r) = (\rho_s - \rho_g) \cdot \gamma_0(r) + \rho_g$, such that at $r = 0$ the density is the (voidless) silica density ρ_s , and at $r = \infty$ the density is the grain density $\rho_\infty = \rho_g = f_g \times \rho_s$.

We plot the resulting density scaled solid-solid density correlation function $G_\rho(r)$ for the seven sol-gel silicas in figures 113, 114. We will often just use the symbol $G(r)$ to represent both this function and the Monte-Carlo case with ρ_s normalised to unity.

16.2.3 Chordal representation.

In chapter 12.9 we consider chordal analysis in the radial domain; this offers much greater resolution than the averaged convoluted $G(r)$ representation, and is probably the right approach for any further work regarding modelling the observed scattering from arrays of pores in terms of the scattering from isolated structures.

In figure 111 we plot chordal representations of the Fast Fourier Transformed and numerically differentiated $I(q)$ data for C500 Unilever B silica (residual truncation ripple can be seen, inspite of the extended Fourier transform used), and analytically transformed and differentiated data for the Sech + Guinier-Porod approximation (see figure 104 and appendices R, M).

Chordal distribution in C500 Unilever B SiO_2 , Analytic & FFT.

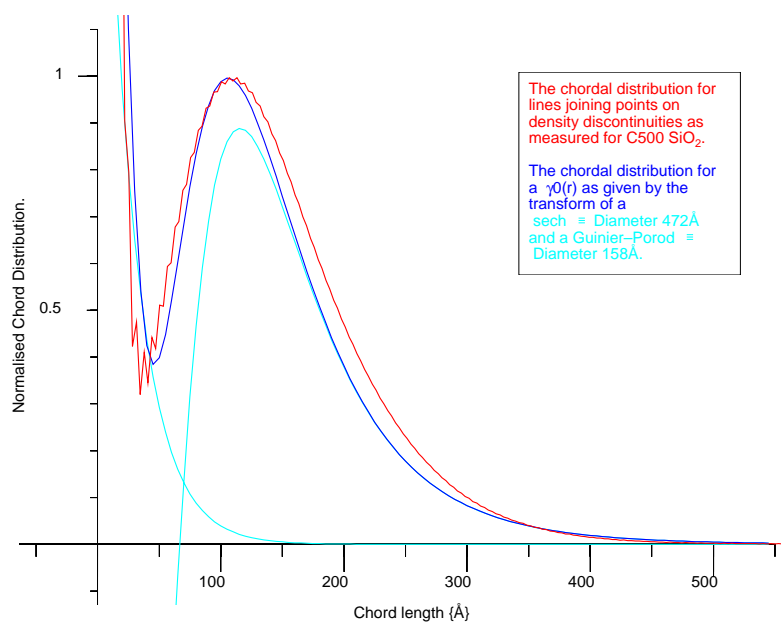


Figure 111:

Chordal $L(r)$ for C500 Unilever B SiO_2 by Fast Fourier Transformation and by analytic transformation of the Sech + Guinier-Porod approximations.

We note that we do indeed appear to have a dual function as suggested by the latter approximation, and that the short range one indeed appears to be exponential, as we would expect for the second differential of the exponential $\gamma_0(r)$ of the Guinier-Porod function (see appendix M). However we now have the resolution to see the deviation between the measured data and the transform of the empirical *sech* function.

16.2.4 Comparison with $G(r)$ data from Monte-Carlo calculations.

In chapter 15 we generate models of porous structure, and use Monte-Carlo integration to calculate their $G(r)$ curves (with ρ_s and lattice spacing a normalised to 1).

Plotting $G(r)$ for C200 Unilever B against the Monte-Carlo calculated $G(r)$ for touching spherical voids on an HCP lattice, with a 0.18 Gaussian variance in pore diameter D_{void} and lattice spacing a_{sHcp} , and setting $G(0) = \rho_s$, (figure 112), we see an excellent fit at small radius for a scaling of 220\AA pore diameter. At larger radius we see that the average density is 8.5% too high in the simulated $G(r)$ – we take this to imply that the real pores are intersecting (giving us permeability), and in table 16 we deduce that for C200 Unilever B silica for HCP and random lattices that $D_{void} = 1.01 \times a_{sHcp} = 1.07 \times a_{sr}$.

$G(r)$ for C200 Unilever B, Monte-Carlo.

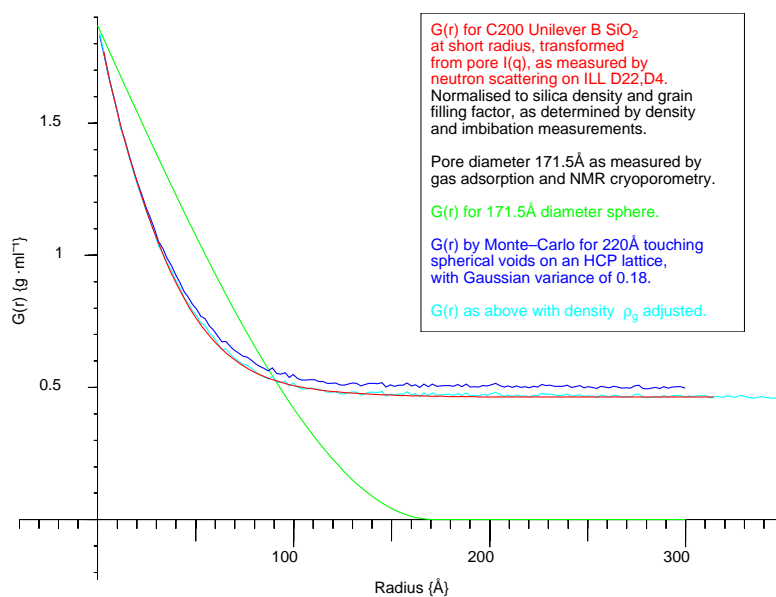


Figure 112:

Comparison of $G(r)$ for C200 Unilever B SiO_2 compared with Monte-Carlo calculation of $G(r)$ for 220\AA diameter touching spherical voids on an HCP lattice, with Gaussian variance of 0.18.

In figure 112 we also make the appropriate correction to the large r density, to obtain an improved fit, which looks excellent. However such a density reduction also implies a thinner wall between the pores (in terms of the above description); this is only of the

order of a percent or two for C200 silica, however strictly the MC calculation should be repeated with the macroscopically measured D_{void}/a ratio (chapter 11.5.2), unless we can perhaps do a linearised interpolation.

Thus we interpret this fit as implying that for our model of touching spherical voids on an HCP lattice, for a 220Å scaling of $D_{void} = a$, we obtain a similar $G(r)$ function for the inter-pore walls as for the real C200 silica, whose pore diameter as measured by gas adsorption and NMR cryoporometry is 171.5Å and for which $D_{void} \neq a$.

There is clearly an urgent need to be able to calculate $G(r)$ for a truly random lattice. We also note that we have made no allowance for the throats between pores, in our MC calculation; this will tend to bias the MC best fit to larger pore sizes, as the sub 5Å thick silica will be missing from the real porous structure (see chapter 11.5.3).

In figure 113, we plot the grain density corrected Monte-Carlo calculated $G(r)$ s for spherical voids on HCP lattices against the measured $G(r)$ s for seven sol-gel silicas, for appropriate variances of void size and lattice spacing. We see quite remarkably good fits.

In chapter 17 we use Monte-Carlo calculations to derive pore-size corrections for $D_{void} \neq a$ and interpolate between cubic and HCP lattices to obtain values appropriate to random lattices.

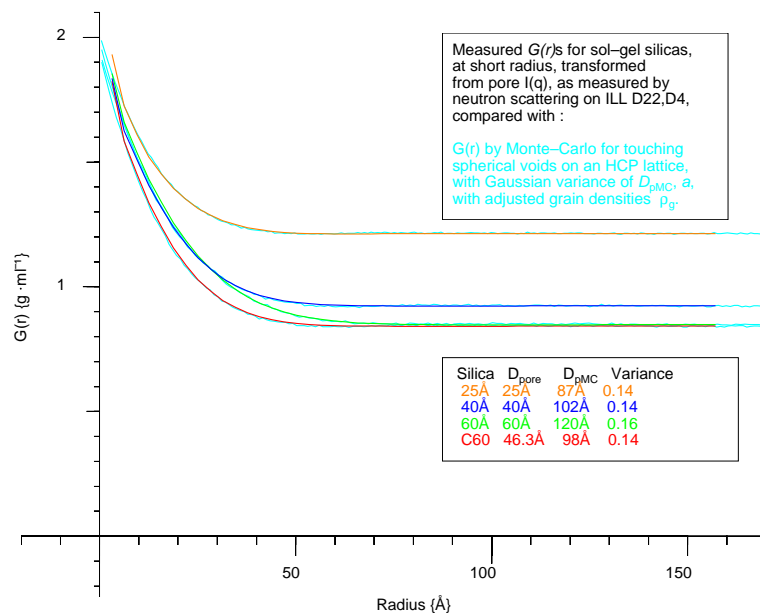
16.2.5 $G(r)$ data, Monte-Carlo $G(r)$ at large radius.

If we examine the measured $I(q)$ scattering data for the sol-gel silicas, and compare it with fitted curves (figure 105), we see that we appear to need structure on at least two scales to explain the measured scattering.

However if we compare the measured scattering with the calculated $I(q)$ curves for the Monte-Carlo simulations of spherical voids on an HCP lattice with Gaussian variation of pore diameter and lattice spacing (figures 106, 107, 108, 109), we see that we also seem to find structure on two scales, even though we are constructing our simulated porous media with regular arrays of pores with similar pore diameters. We see in the previous sections that we may identify the large q small r region with the structure of the pore walls.

In figure 114 we plot the large r behaviour of $G(r)$ for seven sol-gel silicas, and find that it is well described by a spherical region of density a few percent above the average grain density f_g , of diameter about $0.4\mu\text{m}$.

$G(r)$ for C60, 60Å, 40Å, 25Å silicas, NS + Monte-Carlo.



$G(r)$ for C500, C200, 100Å silicas, NS + Monte-Carlo.

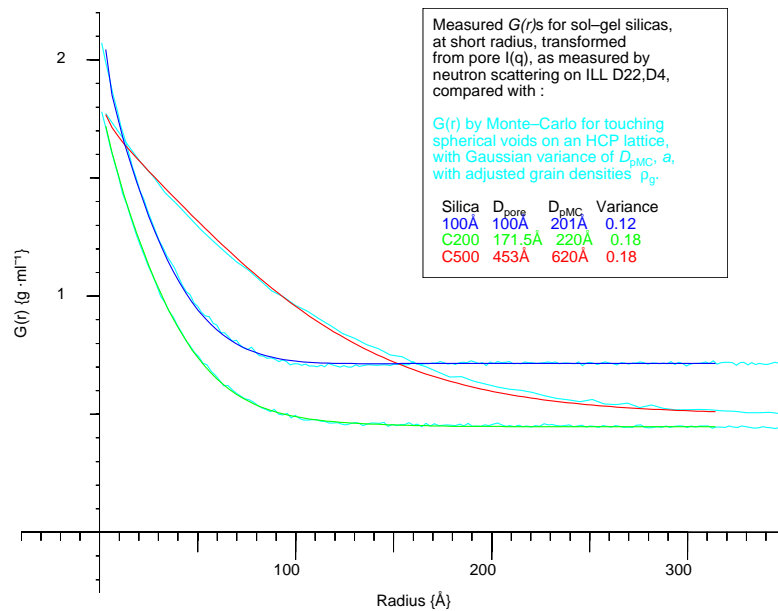
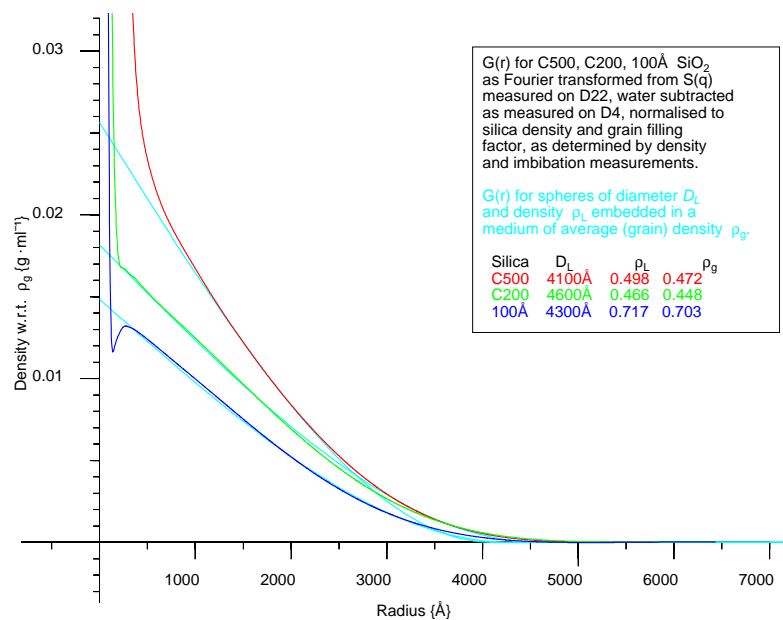


Figure 113:

$G(r)$ for C500 Unilever B, C200 Unilever B, 100Å Merck, C60 Unilever B, 60Å Merck, 40Å Merck, 25Å Sigma, SiO_2 of nominal pore diameters D_{pore} , at small radius, compared with Monte-Carlo calculation of $G(r)$ for touching spherical voids of diameter $D_{pMC} =$ lattice spacing a , on an HCP lattice, with Gaussian variance of D_{pMC} , a , with average density adjusted to match measured grain densities ρ_g .

$G(r)$ for C500, C200, 100Å SiO₂ at large radius.



$G(r)$ for C60, 60Å, 40Å, 25Å SiO₂ at large radius.

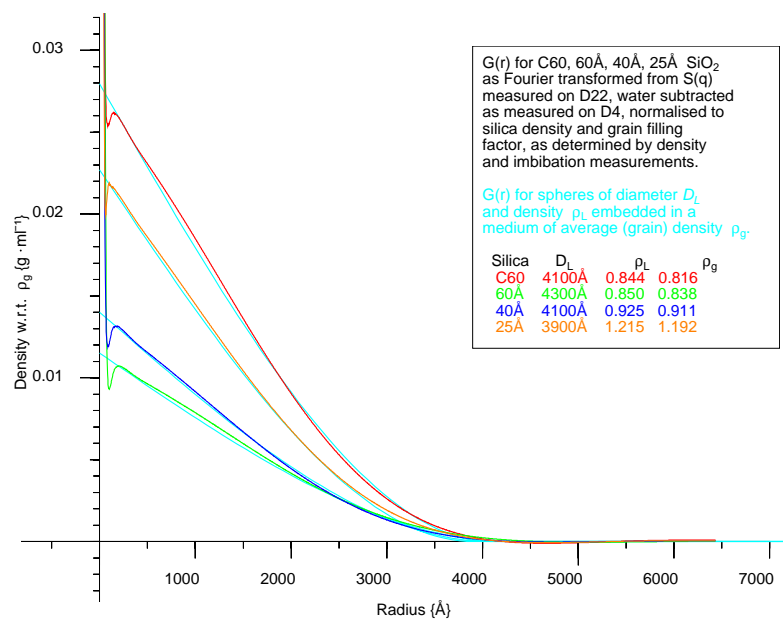


Figure 114:

$G(r)$ for C500 Unilever B, C200 Unilever B, 100Å Merck, C60 Unilever B, 60Å Merck, 40Å Merck, 25Å Sigma, SiO₂, at large radius, compared with $G(r)$ for spheres of density ρ_L embedded in measured grain densities ρ_g .

We have two possibilities. One is that we are observing an increased density that relates to the $2.2\mu\text{m}$ spherical structures observed in figure 61 (and have a scaling error). The other is that we are seeing a perturbation in the average grain density f_g caused by the porous structure itself, and its packing geometry. Evidence for the latter hypothesis is provided by figure 115 where we see the large r structure of the simulated porous media, and figures 106, 107, 108, 109, where we may compare the small q Monte-Carlo calculated scattering with the measured scattering for the seven sol-gel silicas. Although the fit is very poor, that is not surprising, given that we are simulating a random packing of pores with an ensemble of Hexagonal Close Packed lattices. The essential point is that we find that structure on two length scales is inherent in such a porous medium, and do not need to introduce an independent large scale structure or porosity.

There was clearly an interest in checking the scaling of the scanning electron microscope, and imaging other silicas, but it was then out of action for some months, and still is at the time of writing.

$G(r)$ for C200 Unilever B SiO_2 , Monte-Carlo, large radius.

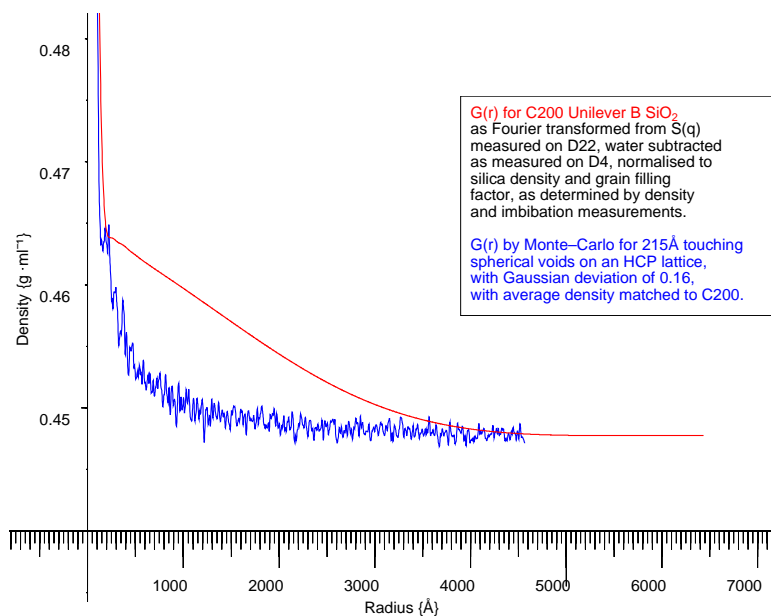


Figure 115:

$G(r)$ for C200 Unilever B SiO_2 at large radius, compared with Monte-Carlo $G(r)$ for spherical voids on an HCP lattice, with Gaussian variation of pore diameter D_{pore} and lattice spacing a .

Silica	Nominal	Voidless	Average	Water	Node +	MC	MC	Large r	Large r
	Pore Diameter D_P {Å}	Silica Density ρ_s {g·ml ⁻¹ }	Grain Density ρ_g {g·ml ⁻¹ }	Equivalent Hydrogen {%}	Wall Thickness t {Å}	Pore Diameter D_{pMC} {Å}	Gaussian Variance V_G	Sphere Diameter D_L {Å}	Sphere Density Incr. ρ_L {%}
C500	453	1.81	0.498	1.45	92.3	620	0.18	4100	5.4
C200	171.5	1.82	0.448	1.85	30.9	220	0.18	4600	4.1
100Å	100	2.11	0.703	2.9	24.9	201	0.13	4300	2.1
60Å	60	1.94	0.838	2.8	17.1	120	0.16	4300	1.4
C60	46.3	1.93	0.816	3.4	14.9	98	0.14	4100	3.4
40Å	40	1.98	0.911	3.9	15.6	102	0.14	4100	1.5
25Å	25	2.01	1.192		14.2	87	0.14	3900	1.9

Table 19: Parameters for seven sol-gel silicas.

Chapter 17

Calibration of sol-gel silica pore diameter using neutron scattering data and Monte-Carlo $G(r)$ integration of model porous structures.

We have seen that we may with reasonable precision model the shape of the density correlation function $G(r)$ measured by neutron scattering. We wish to deduce the correct calibration functions required to obtain the pore diameter of the scattering pores from the measured scattering, as a function of the ratio of pore diameter to lattice spacing, and of the pore and lattice variance.

We will see that, in spite of the fact that we are modelling our pores as spheres, we may not use the expected scaling for an isolated sphere, due to the effect of having many spheres on a lattice. Thus we use calculated scalings derived from Monte-Carlo solid-solid density correlation integrations of infinite arrays of porous structures.

We use the measured neutron scattering data, the results of density and imbibition measurements, and volumetric information derived from NMR cryoporometry to obtain the correct parameters for our real sol-gel silicas with which to access the Monte-Carlo calculated results and deduce pore diameters.

17.1 Scattering void form factors and lattice structure factors.

To deduce the pore diameter corresponding to an $I(q)$ measured by neutron scattering we note that, since we can not measure the phase of the scattered wave, we would expect Babinet's theorem to apply [Francon, 1966] (see chapter 12.8).

Babinet's theorem implies that the scattering from an isolated solid sphere would be the same as that from an isolated spherical void in an infinite solid. We find however that we have to be careful in extending this interchangeability to porous media, and not assume that a collection of spherical voids will scatter in a similar manner to an isolated sphere, as we have phase relationships between the different pores.

When one has many identical scattering objects spatially distributed, one has for the scattering

$$I(q) = P(q \cdot R) \cdot S(q)$$

where $P(q \cdot R)$ is the form factor or normalised scattering for a single isolated particle of radius R , and $S(q)$ is the structure factor for their spatial distribution.

We may note two problems with applying this relationship to porous media, both stemming from the fact that if one has more than one pore size or shape, the above equation gains more terms. The first is that we have not one size, but a Gaussian distribution of radii R ; the other is that when the voids intersect (by varying amounts) we must treat them not as spheres but as faceted spheres, to avoid multiply counting void volume.

However we start by noting that the scattering from an isolated sphere of radius R_s is given by $I(q) = P(q \cdot R_s) = |\phi(q \cdot R_s)|^2$ where [Feigin and Svergun, 1987, p14] :

$$\phi(q \cdot R_s) = 3 \cdot \frac{\sin(q \cdot R_s) - q \cdot R_s \cdot \cos(q \cdot R_s)}{q^3 \cdot R_s^3}$$

and the corresponding normalised $\gamma_0(r)$ is given by [Feigin and Svergun, 1987, p42], [Steytler et al., 1983a], see appendix K :

$$\gamma_0(r) = 1 - \frac{3}{4} \cdot \frac{r}{R_s} + \frac{1}{16} \cdot \left(\frac{r}{R_s} \right)^3$$

17.2 Characterisation by radius of $d(r)$ maximum.

Thus we find that for such a sphere, that if we differentiate $d(r) = r^2 \cdot \gamma_0(r)$ and solve equal to 0, $d(r)$ has a maximum at just over $1 \times R_s$, at $(\frac{\sqrt{3}\sqrt{7}}{\sqrt{5}} - 1) \cdot R_s \approx 1.043939R_s$.

Comparing the measured $\gamma_0(r)$ for Unilever C200 porous sol-gel silica, with the calculated $\gamma_0(r)$ for the nominal pore diameter (figure 110) we see there is a great difference in both the shape and radius scale.

In an attempt to understand this we calculate $\gamma_0(r)$ using Monte-Carlo integration (see chapter 15) for a number of model porous silicas (see chapter 11.3), both with uniform pore diameter and lattice spacing, and with variance of pore diameter and lattice spacing.

We find that the calculated $\gamma_0(r)$ for spherical voids on regular Hexagonal-Close-Packed lattices with a variance of the pore diameter and lattice spacing fit the measured data well (see figures 112, 113, 116).

However we see in figure 116 that for touching spherical voids of radius R_s , the maximum in $d(r)$ is at a radius of less than half that for an isolated sphere of the same radius.

$\gamma_0(r)$, $d(r)$ for C200 Unilever B, MC Spheres on HCP lattice, Sphere.

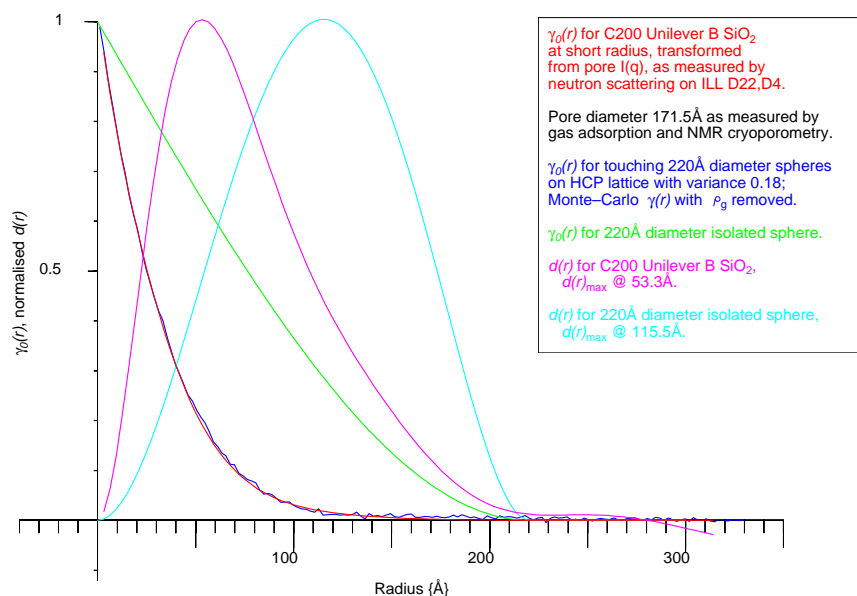


Figure 116:

Showing the good agreement for measured and Monte-Carlo $\gamma_0(r)$, but the difference between these and $\gamma_0(r)$ for a matching isolated sphere. $d(r) = r^2 \cdot \gamma_0(r)$ is also plotted.

Thus we are led to consider those structures in the models that are smaller than the spherical voids that they are constructed from, such as the silica walls between the pores and the silica 'nodes' that reside at the geometric centres of the lattice structure formed by the centres of the spheres.

17.3 Radius of $d(r)$ maximum: variation with D/a for various lattices.

If we consider a structure composed of touching spheres (solid or void) on a regular lattice (i.e. Hexagonal-Close-Packed, or Cubic), and then allow the spheres to vary in size (while keeping the sphere centres fixed on the original lattice) we see that for very small spheres separated by a large amount of space we would expect the scattering $I(q)$ (and hence $\gamma_0(r)$) to be well characterised by the $I(q)$, $\gamma_0(r)$ of an isolated sphere of the same size at small r , and by the $I(q)$, $\gamma_0(r)$ of the lattice at large r , and that as the diameter increased from 0, so the position of the maximum in the $d(r)$ due to the sphere would increase linearly with R_s .

If however we allow the sphere size to increase until there is only a small amount of silica 'node' left, we would expect the scattering to be characterised by the scattering of an individual node (and the lattice). Thus the maximum in $d(r)$ would occur at **decreasing** r as the sphere diameter was increased and the node size reduced.

If we characterise the lattice by the parameter β = distance from the geometric centre of the lattice to the centre of the spheres on the lattice, we see that for the nodes the effective 'radius' R_{se} is $\beta \cdot \frac{a}{2}$ for $\frac{D_s}{a} = 0$, $\beta \cdot \frac{a}{2} - R_s$ for $\frac{D_s}{a} = 1$, and 0 for $\frac{D_s}{a} = \beta$. Thus in this region we might expect the effective spherical radius R_{se} to vary as

$$R_{se} = \beta \cdot \frac{a}{2} - R_s$$

and hence

$$d_{Max}(r) = \left(\frac{\sqrt{3}\sqrt{7}}{\sqrt{5}} - 1\right) \cdot R_{se} = \left(\frac{\sqrt{3}\sqrt{7}}{\sqrt{5}} - 1\right) \cdot \left(\beta - \frac{2 \cdot R_s}{a}\right) \cdot \frac{a}{2}$$

In appendix H we calculate the size of the sphere that is just enclosed by a tetragon of equal sized touching spheres, thus we conclude that for an HCP lattice $\beta_{HPC} = \frac{\sqrt{3}}{\sqrt{2}}$ and a simple 3D application of Pythagoras' theorem shows that for a cubic lattice $\beta_{cubic} = \sqrt{3}$.

In section 11.3.3 we have relationships for the silica filling fraction f , such that we may deduce that

$$1-f = \frac{\pi \cdot k \cdot D_s^3}{6 \cdot a^3}$$

where :

lattice :	HCP	Random	Cubic
k :	$\sqrt{2}$	$\frac{6 \times 0.6366}{\pi}$	1

such that for $\frac{D_s}{a} = 1$, we may write :

$$\beta = \frac{\sqrt{3}}{k} = \frac{\pi \cdot 1}{6 \cdot 1-f}$$

Hence we may deduce β for a random lattice, where we do not have a fixed geometry, but we do have a known average filling factor of 0.6366 for touching equal sized solid spheres in random packing [Finney, 1970] : where :

lattice :	HCP	Random	Cubic
β :	$\frac{\sqrt{3}}{\sqrt{2}}$	$\frac{\pi \cdot \sqrt{3}}{6 \times 0.6366}$	$\sqrt{3}$

Thus we plot the expected variation for small $\frac{D_s}{a}$ and for the three cases for large $\frac{D_s}{a}$ in figure 117.

In practice the 'nodes' are not spherical, thus we would expect there to be a scaling applied to the position of the maximum, and we note that the walls directly between adjacent pores will in effect have a different scaling from that calculated for the 'nodes'. Calculating $\gamma_0(r)$ by Monte-Carlo integration for model porous structures of spherical voids with a range of diameters D_s to lattice spacing a , we obtain figure 118.

We see that we do observe an direct increase with $\frac{D_s}{a}$ at small $\frac{D_s}{a}$ but that at large $\frac{D_s}{a}$ we see a decrease as predicted.

The behaviour is not precisely as expected from the above simple model, in that the slope at large $\frac{D_s}{a}$ is not as negative as predicted. We may obtain a similar slope by averaging a proportion of the inverse function with a proportion of the direct function.

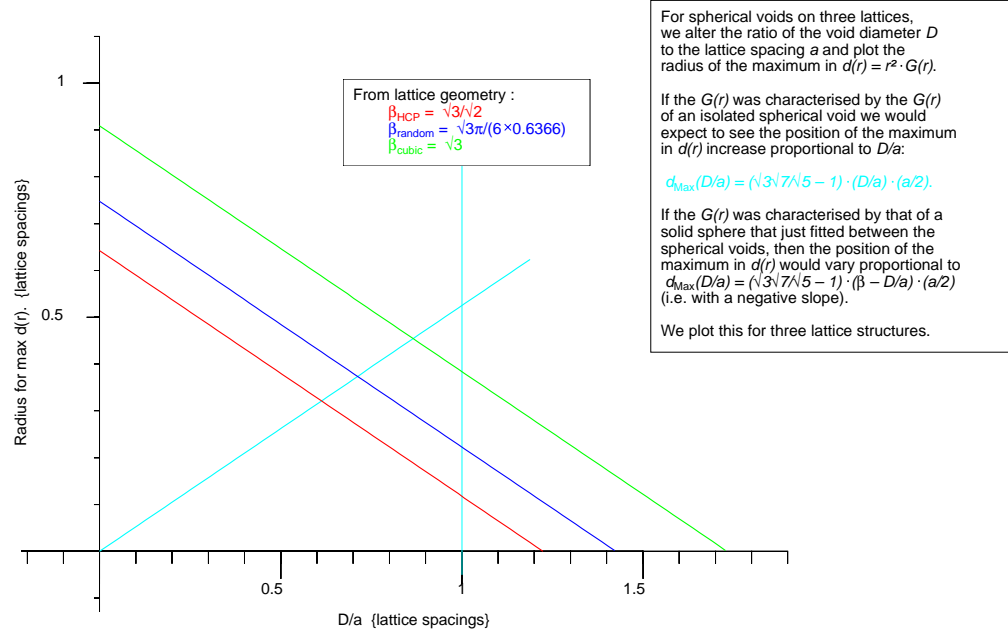
Radius of $d(r)$ maximum: variation with D/a (Theory).

Figure 117:

Theoretical variation of $d_{Max} \left(\frac{D_s}{a} \right)$ at small $\frac{D_s}{a}$, and at large $\frac{D_s}{a}$ for three lattice structures.

Thus empirically we write for the behaviour at large $\frac{D_s}{a}$ for HCP and cubic lattices :

$$r_{se} = \frac{1}{2} \cdot \left(\alpha \cdot \left(\beta - \frac{2 \cdot R_s}{a} \right) + \left(1 - \frac{\alpha}{2} \right) \cdot \frac{2 \cdot R_s}{a} \right) \cdot \frac{a}{2}$$

where the β is indeed that calculated geometrically

Since α has different values for the two lattices, we wish to express α for the lattices in terms of our lattice dependent β ; we have only two points to define the relationship – however we reject a simple linear relationship as unphysical, as it crosses the axes. Plotting the best fit values of α against β , we see that the HCP point lies on the inverse quadratic $\sqrt{2}/\beta^2$, and the cubic point close to it. We note that $\frac{\alpha_{HCP}}{\alpha_{cubic}} \approx 1 + \sqrt{2}$ within the Monte-Carlo scatter. Thus we find as one possible relationship :

$$\alpha = \frac{\sqrt{2}}{\beta^2} \cdot \frac{2}{1 + \frac{\sqrt{2}}{\sqrt{3}} \cdot \beta}$$

This allows us to deduce a value for α for the random lattice case. (This does not differ greatly from that for a simple linear relationship.) Thus we obtain the coefficients :

	HCP	Random	Cubic
$\beta :$	$\frac{\sqrt{3}}{\sqrt{2}}$ = 1.2247	$\frac{\sqrt{3\pi}}{6 \times 0.6366}$ = 1.4246	$\sqrt{3}$ = 1.73205
$\alpha :$	$\frac{2}{3} \cdot \sqrt{2}$ = 0.94281	$\frac{29.179 \cdot \sqrt{2}}{\pi^2 \cdot (1 + \frac{\pi\sqrt{2}}{3.8196})}$ = 0.64427	$\frac{2}{3} \cdot \frac{\sqrt{2}}{1+\sqrt{2}}$ = 0.39052

Table 20: Coefficients to obtain $d_{Max} \left(\frac{D}{a} \right)$ for HCP, random and cubic lattices.

We have something of a paradox, in that Babinet's theorem would lead us to believe both the above descriptions of the variation of $G(r)$ with $\frac{D_s}{a}$ are equally valid, yet the above argument and Monte-Carlo integration lead us to believe that each is more valid in a particular region. We wish to merge the description for small $\frac{D_s}{a}$ with that for large $\frac{D_s}{a}$.

We now meet a further paradox, which is not fully resolved. The above descriptions are in terms of the normalised $\gamma_0(r)$ curves; to obtain their scaled sums, we would expect to use

$$\gamma(r) = \gamma_1(r) + \gamma_2(2) = \gamma_{01}(r) \cdot \rho^2 \cdot V_1 + \gamma_{02}(r) \cdot \rho^2 \cdot V_2$$

We see that this has precisely the opposite of the effect that we want according to the above argument, selecting the inverse variation with $\frac{D_s}{a}$ at small $\frac{D_s}{a}$ and selecting the direct variation with $\frac{D_s}{a}$ at large $\frac{D_s}{a}$.

Thus we actually choose to weight according to

$$\gamma(r) \propto \frac{\gamma_{01}(r)}{V_1} + \frac{\gamma_{02}(r)}{V_2}$$

and calculate the position of the maximum in the combined $d(r)$. The resultant curves are plotted in figure 118; we see that the limiting values are well fitted, but that the above algorithm for combining the descriptions overestimates the radius for $\frac{D_s}{a} \approx 0.5$. It thus only models the actual process very poorly, and should be used with caution until a model is found that encodes the physics more correctly.

The important feature of the above analysis is that we now have an estimate for the expected value of the radius for the maximum in $d(r)$, for spherical voids on a random lattice in terms of an interpolation between the limiting cases of HCP and cubic lattices, based on an equation with a single parameter β that we derive from the geometry of the

Radius of d(r) maximum: variation with D/a.

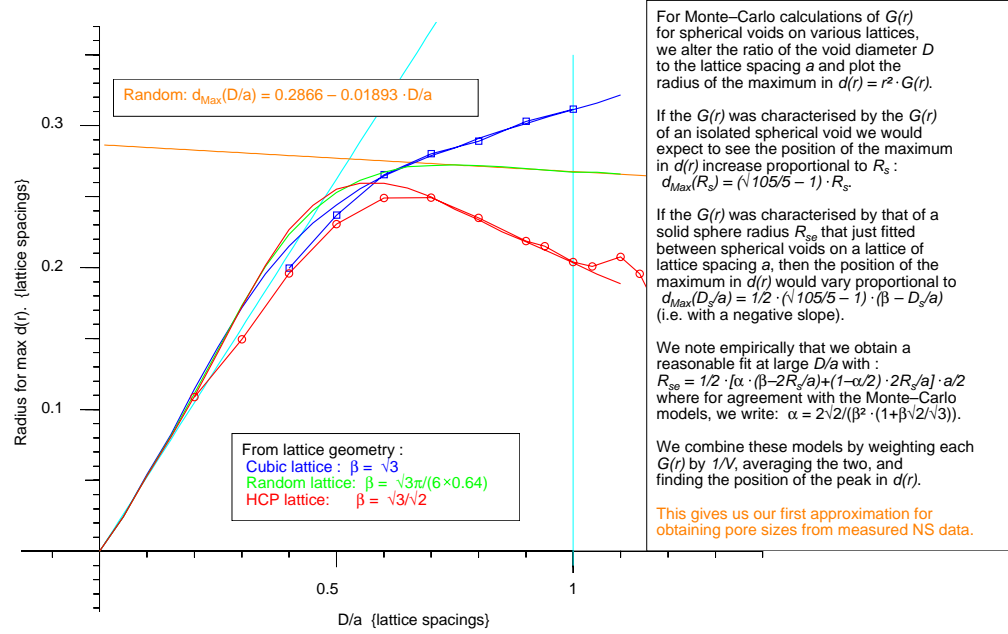


Figure 118:

Monte-Carlo variation of $d_{Max} \frac{D_s}{a}$ at small $\frac{D_s}{a}$, and at large $\frac{D_s}{a}$ for three lattice structures.

lattice. We also have an estimate of how it varies with $\frac{D_s}{a}$ - i.e. with the silica filling factor of the porous grain, which we measure in section 11.5.2.

Thus we now have a first approximation for deducing pore diameters from measured neutron scattering intensity curves.

17.4 Applying measured silica parameters to Monte-Carlo calculations.

We have just seen how we may use Monte-Carlo calculations to determine $d_{Max} \left(\frac{D_s}{a} \right)$, the expected value of the radius for the maximum in $d(r)$, for spherical voids on a random lattice as a function of $\frac{D_s}{a}$ (figure 118). We see that for practical values of $\frac{D_s}{a}$ (0.8 \rightarrow 1.1), we may approximate the variation as a linear one, giving us the first order polynomial

$$\frac{d_{Max}}{a} \left(\frac{D_s}{a} \right) = \mathcal{O}_{d_{Max}Ran} \left(\frac{D_s}{a} \right) = 0.2866 + 0.01893 \cdot \frac{D_s}{a}$$

In chapter 11.3.3 we consider models of spherical voids, and deduce a polynomial relationship (valid for both non-intersecting and intersecting pores) between the silica filling fraction f_{sr} for random lattices and $\frac{D_s}{a_{sr}}$, such that we obtain

$$\begin{aligned} \frac{a_{sr}}{D_s} = \mathcal{O}_{a_{sr}/D_s}(f_{sr}) = & 0.694 + 1.81f_{sr} - 5.367f_{sr}^2 + 10.558f_{sr}^3 \\ & - 10.162f_{sr}^4 + 4.605f_{sr}^5 \end{aligned}$$

In chapter 11.5.2 we imbibe liquids into the porous silica, and measure the dry and wet densities. We use NMR cryoporometry volumetric measurements to differentiate between liquid inside the pore and liquid around the grain, and hence measure the grain silica filling fraction f_g . If we believe that our model of spheres on a random lattice is representative of our sol-gel silica, we may equate

$$f_g = f_{sr}, \quad a = a_{sr}, \quad D_v = D_s,$$

Thus we may now write expressions for our sol-gel silica, giving us first approximations for lattice spacing a {Å} and pore void diameter D_v {Å}, in terms of d_{MaxNS} {Å} as measured by neutron scattering, lattice spacing normalised d_{MaxRan} as calculated by Monte-Carlo integration for random lattices and f_g as measured by imbibation and NMR cryoporometry volumetric measurements :

$$\begin{aligned} \frac{a}{D_v} & \approx \mathcal{O}_{a_{sr}/D_s}(f_g) \\ d_{MaxRan} \left(\frac{D_v}{a} \right) & \approx \mathcal{O}_{dMaxRan} \left(\frac{D_v}{a} \right) \\ a & \approx \frac{d_{MaxNS}}{d_{MaxRan} \left(\frac{D_v}{a} \right)} \\ D_v = \frac{D_v}{a} \cdot a & = \frac{d_{MaxNS}}{\mathcal{O}_{dMaxRan} \left(\frac{1}{\mathcal{O}_{a_{sr}/D_s}(f_g)} \right) \cdot \mathcal{O}_{a_{sr}/D_s}(f_g)} \end{aligned}$$

17.5 Neutron scattering pore diameter variance.

Examining the Monte-Carlo results we also find that d_{Max} varies slightly with the variance of the pore diameter and lattice spacing used in the calculation; this may partly be an artifact of the peak measurement, but it may be a real effect caused by the width of the Gaussians being a significant fraction of their mean; either way we should

correct for it.

Thus strictly we should replace d_{MaxRan} in the above by $d_{MaxRan}\left(\frac{D_v}{a}, Var\right)$

This two dimensional function has not as yet been fully characterised using modelling, however for HCP lattices the dependence with variance is shown for the case of $D_v = a$ in figure 119, and is encoded into the cubic polynomial

$$d_{MaxHcp}(Var) = \mathcal{P}_{drsHcpMax} = 0.2034 + 0.3489 \cdot Var - 1.688 \cdot Var^2 + 8.031 \cdot Var^3$$

Thus we need to determine the variance in the real sol-gel silicas. It was noticed that as the variance was increased in the Monte-Carlo calculations, so the maximum in $d(r)$ became increasingly asymmetric, such that the slope on the large r side could be related to the variance. This relationship is shown in figure 120, and is encoded into the cubic polynomial :

$$Slope(Var) = \mathcal{P}_{drsHcp} = -2.05305 + 2.57192 \cdot Var + 53.9955 \cdot Var^2 - 113.385 \cdot Var^3$$

such that we may numerically revert this to obtain a quadratic polynomial that allows us to determine the variance :

$$Var(Slope) = \mathcal{P}_{drsHcpR} = 0.212919 + 0.0517297 \cdot Slope - 0.0236704 \cdot Slope^2$$

Using this procedure we may thus obtain from the measured neutron scattering the variances for the real sol-gel silicas as listed in table 21. We note that the assumption here is that the lattice spacing and pore diameter variances are the same. Thus we may contrast these figures with the value of 0.045 for the pore diameter variance of 100Å Merck silica, as measured by NMR cryoporometry (see figure 96).

We see that the three Unilever silicas have similar variances of 0.195, 0.195, 0.198; that the three Merck silicas have the lowest variance, with a slightly wider spread of 0.166, 0.171, 0.178; and that the Sigma silica has the highest variance of 0.201. Thus we conclude that this suggests that the lattice spacing variance is larger than the pore diameter variance.

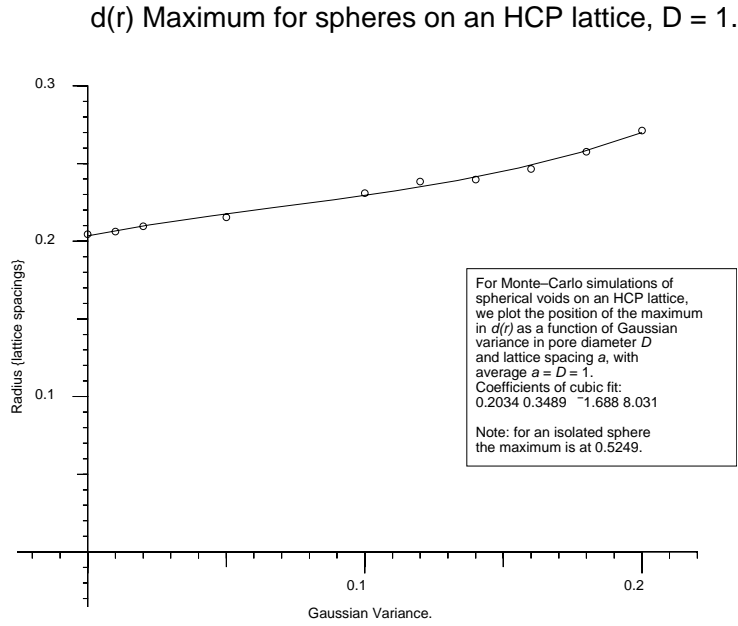


Figure 119:
 Position of maximum in $d(r)$, as a function of Gaussian variance, for spherical pores on an HCP lattice, as determined by Monte-Carlo integration.

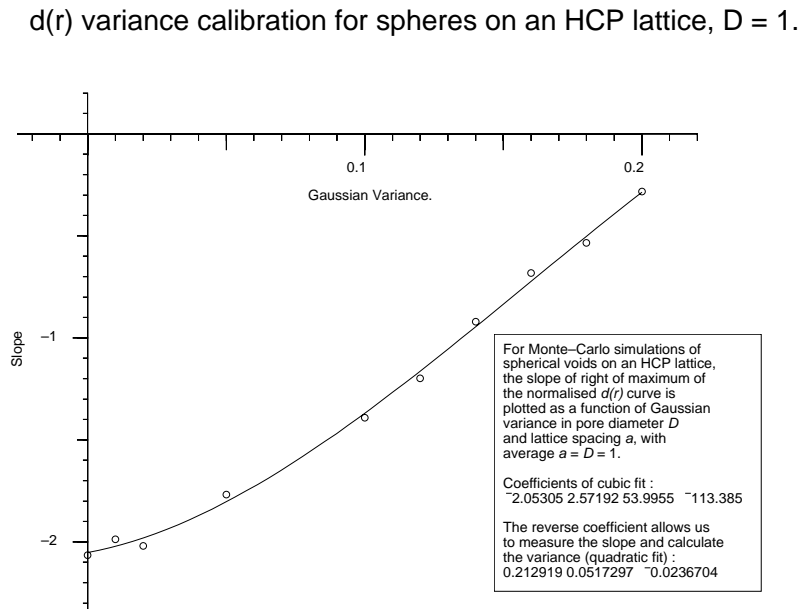


Figure 120:
 Relationship between high r slope of $d(r)$ peak and Gaussian variance of pore diameter D_s , for spherical pores on an HCP lattice, as determined by Monte-Carlo integration.

17.6 Neutron scattering pore diameter results.

From Monte-Carlo integration of our model porous structures we now know

$$d_{MaxHcp} \left(0.2 \leq \frac{D_v}{a} \leq 1.2, Var = 0 \right), \quad d_{MaxHcp} \left(\frac{D_v}{a} = 1, 0 \leq Var \leq 0.2 \right).$$

We particularly wish to know this function for random lattices for the range of $\frac{D_v}{a}$ and variance revealed by applying the above procedures to the real sol-gel silicas, i.e. for :

$$d_{MaxRan} \left(0.86 \leq \frac{D_v}{a} \leq 1.07, 0.16 \leq Var \leq 0.2 \right)$$

To do this one should evaluate d_{MaxMC} for HCP and Cubic lattices for this 2D set of parameters, and interpolate as a function of β as before, to obtain the function for a random lattice.

This has not yet been fully evaluated. However evaluating $d_{MaxHcp} \left(\frac{D_v}{a} = 0.86, Var = 0.2 \right)$ gives us sufficient additional information to generate an algebraic and linear polynomial approximation of the form

$$\begin{aligned} d_{MaxHcp} \left(\frac{D_v}{a}, Var \right) &= \mathcal{O}_{dMaxRan} \left(\frac{D_v}{a} \right) \times \left(1 + \left(\mathcal{O}_{VarDva} \left(\frac{D_v}{a} \right) \right) \times Var \right) \\ &= R_{Hcp} \times \eta \left(\frac{D_v}{a}, Var \right) \end{aligned}$$

If we now make the assumption that the η term will perform the same relative scaling correction in the random lattice case, we may write

$$d_{MaxRan} \left(\frac{D_v}{a}, Var \right) = R_{Ran} \times \eta \left(\frac{D_v}{a}, Var \right) = R_{cor}$$

We thus slightly modify our previous calculation to obtain table 21. If we plot the calculated pore diameters for the seven sol-gel silicas, against the nominal gas adsorption diameters we obtain figure 121.

We see there is a surprisingly close agreement at large pore diameters, with the scaling factors being within about 10%. However at small pore diameters we see that the neutron scattering scale effectively limits at about 60Å. Detailed examination shows that, while the exact scaling may well not have been established (see the above discussion), this limiting behaviour may be related to the raw neutron scattering data – if one examines figure 85 one sees that the scattering for the 25Å Sigma, 40Å Merck and C60 Unilever B sol-gel silicas are indeed far more similar than one would expect from their nominal pore diameters.

Silica	Nom. {Å}	d_{MaxNS} {Å}	Var.	f_g	D_v/a	R_{Ran} {a}	$\eta(D_v/a, Var)$	R_{cor} {a}	a Å	D_v Å
C500	453	147.7	0.195	0.261	1.056	0.267	1.372	0.366	403.7	426.4
C200	171.5	58.0	0.195	0.246	1.065	0.266	1.380	0.368	157.6	167.9
100Å	100	46.8	0.166	0.333	1.015	0.267	1.284	0.343	136.4	138.5
60Å	60	29.8	0.171	0.432	0.961	0.268	1.247	0.335	88.9	85.4
C60	46.3	25.8	0.198	0.432	0.961	0.268	1.286	0.345	74.7	71.7
40Å	40	25.4	0.178	0.460	0.945	0.269	1.244	0.334	76.0	71.8
25Å	25	24.7	0.201	0.593	0.860	0.270	1.192	0.322	76.7	66.0

Table 21: For 7 porous silicas we list the nominal (gas adsorption) pore diameter Nom , the radius d_{MaxNS} for the maximum in $d(r)$ as measured by neutron scattering, the variance Var as calculated from the right hand slope of the $d(r)$ curve, and, from bulk density, imbibation and NMR cryoporometry volumetric measurements, the grain filling factor f_g . From the latter, using simple analytic analysis of geometric models, we calculate for a random lattice D_v/a , the ratio of the pore void diameter to the lattice spacing. Using a polynomial fit to Monte-Carlo analysis of the geometric models, we use the value of D_v/a to calculate $d_{MaxRan}(D_v/a) = R_{Ran}$, the expected radius (as a fraction of the lattice spacing a) of the peak in $d(r)$ for a random lattice. We then calculate a correction to the position of this $d(r)$ peak, $\eta(D_v/a, Var)$, using 2D polynomial fits to Monte-Carlo analysis of the geometric models. We thus obtain the variance corrected value for $d_{MaxRan}(D_v/a) = R_{cor} = R_{Ran} \cdot \eta(D_v/a, Var)$. Dividing this into d_{MaxNS} gives us the measured lattice spacing a . Thus we may now use the ratio D_v/a to finally calculate the pore diameter D_v .

Thus either one is led to conclude that there is some process that preferentially modifies the scattering in the case of small pore silicas, that is not elucidated in the above analysis, or that it is the gas adsorption and NMR cryoporometric scales (which we have shewn to be co-linear when using water as the indicator liquid) that are in fact non-linear at small pore dimensions.

Although it seems improbable that the well established gas adsorption calibration should have such a gross error at small pores, this is indeed a possibility that must now be investigated. We note that gas adsorption however commonly uses the BJH method [Barret et al., 1951] based on the Kelvin equation to calculate pore size distributions from the desorption $P(v)$ curve, using a pore model of right cylinders, see chapter 1.3.1 [Gregg and Sing, 1967].

Other effects that may influence calibration at small pore diameters are molecular size effects and possible deviations from the bulk values for the thermodynamic constants. Larger pore zeolites and templated MCP silicas of known structure may play a useful calibration roll in further work at small pore dimensions.

In figure 122 we plot the NMR cryoporometrically measured pore diameters for the seven sol-gel silicas against pore diameters as measured by neutron scattering. The overall scaling is given by the gas adsorption calibration of the cryoporometric constant for the indicator liquid (water), and is, within the scatter, in good agreement with the neutron scattering results at large pore diameters.

However we now see (with the exception of the 100Å Merck silica) much tighter scatter from the NMR results than the gas adsorption ones. In particular we see that both NMR and neutron scattering show the pore diameters of the 40Å Merck and C60 Unilever B silicas to be very similar.

17.7 Summary.

In chapter 11 we consider geometric models of idealised porous structures, and analytically deduce relationships between their density, silica filling factor and the ratio of pore diameter to lattice spacing. In chapter 17 we use these relationships to obtain SANS calibration of pore size.

In chapters 11.5.2, 11.5.3 we show that just by measuring densities (chapter 11.4), by imbibing liquids into sol-gel media (chapter 11.5), and by determining NMR cryoporometric volumetric information (chapter 7.5.5) we may deduce the density of the (voidless) silica matrix as about 2.0 {g.ml⁻¹} (c.f. 2.1/2.2 for translucent/transparent silica), and show that we may construct model silicas that mimic the measured ones with the rules that the minimum wall thickness is 5Å, and that the diameter of the throats between the pores is about $\frac{1}{3} \times$ Pore Diameter. Thus there are about 10 throats into each pore, resulting in a surface areas of about 45% of the intact pore. We may also determine the grain packing fraction (wet and dry).

In chapter 16.2.1 we show that the measured $G(r)$ s for sol-gel silicas may be approximated by the calculated $G(r)$ for an isolated slab embedded in a uniform medium (figure 110), and that this fit is preferred to that for an isolated cylinder (figure 95).

However in chapter 16.1 we note that the $I(q)$ for sol-gel silicas is well fitted by the sum of a $sech\left(\frac{q}{Q_0}\right)$ and a small proportion of a Guinier-Porod random mixture of two phases. In chapter 16.2.3 we show that this agreement is carried over into the highly sensitive chordal analysis domain. In chapter 12.9 we show that $sech\left(\frac{q}{Q_0}\right)$ is consistent

Comparison of Gas Adsorption, Neutron Scattering calibrations.

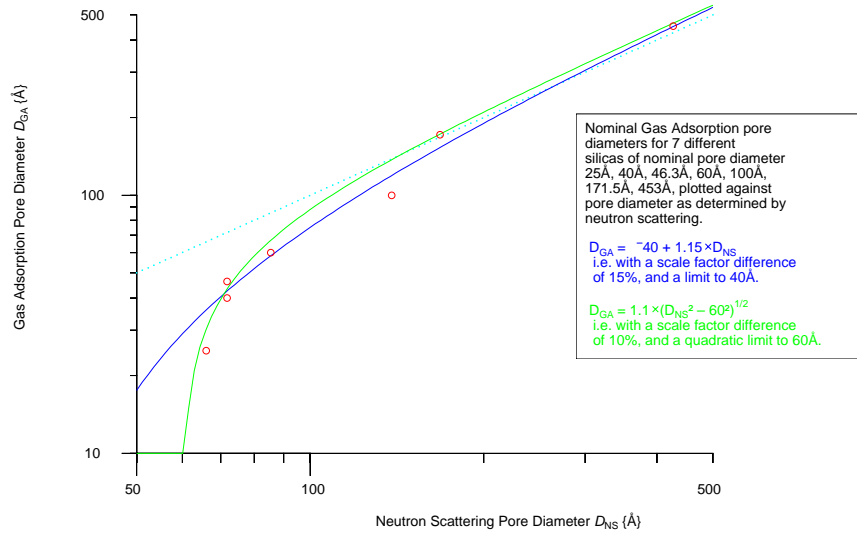


Figure 121:

Nominal gas adsorption pore diameter vs. that measured by neutron scattering.

Comparison of NMR Cryoporometry, Neutron Scattering calibrations.

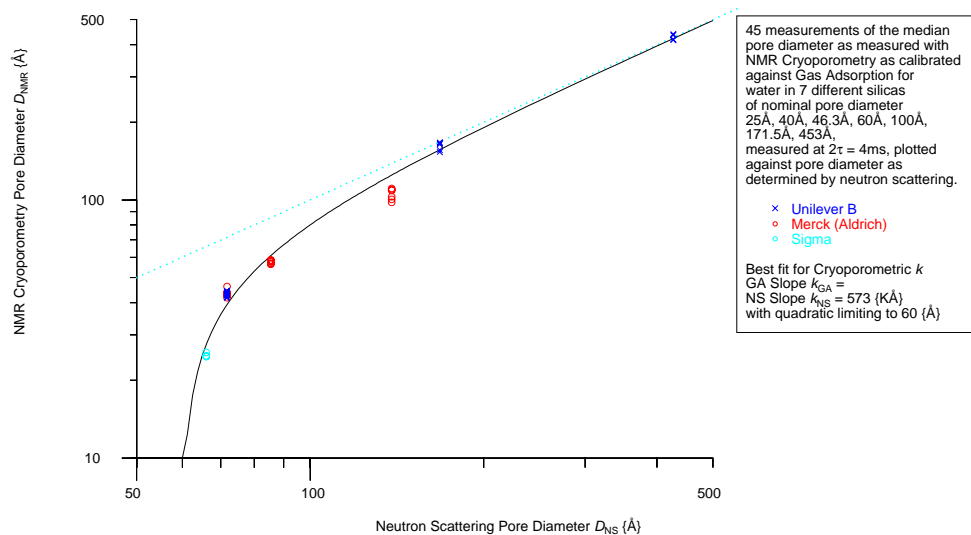


Figure 122:

NMR cryoporometric pore diameter vs. that measured by neutron scattering.

to the quadratic term with the Guinier representation; however we fail to find an isolated structure that gives us such a chordal representation.

In chapter 16 we show that using continuous media Monte-Carlo integration of $G(r)$ for models of porous media (chapter 15) the measured $G(r)$ for sol-gel silicas (chapters 13, 14) is well modelled by the $G(r)$ of structures of (intersecting) spherical voids.

In the $I(q)$ domain, the models reproduce the Guinier/Sech turn-over, with dimensions characteristic of the silica node between the pore voids and reproduce the q^{-4} /Guinier-Porod linear region characteristic of smooth surfaces. They also, most significantly, at least partly reproduce the feature seen in the measured scattering at low q . This is in spite of the models being constructed with pores of only a small range of characteristic size.

We find in chapter 16 that we require closely defined variance of pore size and lattice spacing for accurate modeling of the measured scattering from the sol-gel silicas. This is larger than that determined by NMR cryoporometry for the pore size alone (figures 62, 96) thus we conclude that lattice spacing variance is probably greater than pore diameter variance, in contradiction to our modelling assumption.

There is further modelling work needed, to more fully evaluate the behaviour of the maximum in $d = r^2 \cdot G(r)$, $d_{MaxRan} \left(\frac{D^*}{a}, Var \right)$. With particular reference to modelling MCM-41, further evaluation is needed of models of cylindrical voids on hexagonal lattices.

However there has been sufficient characterisation of the porous models to deduce the probable characteristics of random lattices of spherical voids, such that we may map the SANS measured d_{NaxNS} for sol-gel silicas to deduced pore-size with good precision. We find surprisingly good agreement with pore-diameters as calibrated by gas adsorption for large ($\sim 500\text{\AA}$) pore diameters, but a puzzling discrepancy for small ($\sim 50\text{\AA}$) pores (figures 121, 122).

We note that SANS gives in effect a direct linear scale measurement of structural dimension. Gas adsorption however uses the Kelvin equation to calculate pore size distributions from the desorption $P(v)$ curve, using a pore model of right cylinders. It is possible that the divergence between the two calibrations is related to this difference in model. However it is not clear how such a sharp (quadratic limiting) divergence could result.

Chapter 18

Conclusions.

This thesis has concerned itself with the study of porous materials, and the development of techniques for characterising them. Sol-gel silicas have been studied in the main, as offering commonly available samples with clearly defined porous properties.

This thesis has particularly concentrated on the parameter of median pore diameter, and the variance in this pore size. To this end, numerous advancements have been made to the technique of NMR cryoporometry, particularly with regard to adding spatial resolution, and this has been demonstrated as a most useful technique.

Density and imbibation experiments have been performed, and shown to give a surprising amount of information about the porous structure, when combined with analytic and Monte-Carlo studies of model porous systems.

Small Angle Neutron Scattering and neutron diffraction experiments have been performed, which, when combined with density and imbibation studies using the analytic and Monte-Carlo models, are shown to give a pore size calibration that is in unexpectedly good agreement with the gas adsorption calibrated pore sizes for the sol-gel silicas, at large pore diameters, but show a puzzling divergence at small pore diameters.

18.1 Developments of NMR Cryoporometry.

- Constructed the first full cool/warm cycle automated NMR cryoporometer, with continual pore size distribution graphing, based on a small solid-state spectrometer and permanent magnet, and a PC with IEEE based instruments (chapters 4, 5, appendix C).

- Introduced Boltzmann and NMR coil resistance corrections for pore volume, as a function of temperature (chapters 5, 7.3, 7.3.4).
- Shown how to obtain true volumetric pore size distributions, even in the presence of two different liquid relaxation times (chapters 7.3.5, 7.3.6, appendix E).
- Analysed the probe thermal characteristics analytically + with a 1st order numerical simulation – hence derived the cryoporometric resolution for the probe (chapter 5, appendices D, G).
- Shown that, using gas cooling, repeatable measurements are obtainable up to 2000Å pore diameter, within the above probe thermal characteristics (chapter 9).
- Shown that for a uniform resolution on a log scale, one needs to reduce the warming rate linearly with temperature as one approaches the bulk melting point (chapters 9.4, 9.5, appendix F).
- Obtained fractally related pore size distributions in naturally porous materials, up to 10µm, using the above technique. (chapter 10).
- Performed the first 1D, 2D and 3D resolved pore size distributions. Shown that one may obtain a full pore size distribution for any pixel in a 2D map of porosity (chapter 8).
- Calibrated the melting point depression constant for water and cyclohexane, with respect to a) gas adsorption b) neutron scattering (chapters 7, 17).
- Introduced NMR cryoporometry as a standard technique for regular industrial contract research.

18.2 Conclusions from density and imbibation experiments.

It is demonstrated that, with added NMR cryoporometry volumetric information, density and imbibation experiments provide information that can be analysed using simple geometric models representing the average properties of the sol-gel silicas (chapter 11). It is shown that for the sol-gel silicas studied, over a pore diameter range 25Å → 500Å, and a density ratio of 3:1, we may create models of porous structures that reflect the characteristics of measured ones for sol-gel silicas, with the triplet of rules : a) the

(voidless) silica density is close to $2.0 \text{ g}\cdot\text{ml}^{-1}$, b) the minimum pore wall thickness is 5\AA , c) the pore throat diameter is $1/3$ the pore diameter (chapter 11.5.3).

Measurements were made that are consistent with there being about the expected ten throats to each pore, resulting in the pore wall surface only being 50% of that of an intact pore (chapter 11.6).

18.3 Developments of SANS analysis of pore scattering.

- Measurement of scattering $I(q)$ from $q = 8\cdot 10^{-4}$ to $17.0 \text{ radians}\cdot\text{\AA}^{-1}$, for seven porous silicas (chapters 13, 16).
- Demonstration that water normalised diffraction data can provide information on incoherent scattering, allowing subtraction of this from water normalised coherent pore $P(q)$ scattering, to obtain pore scattering information over three decades in q and eight in scattering intensity (chapter 16.1).
- Demonstration that the data signal-to-noise is good enough to allow chordal analysis of the scattering forms (figure 111).
- Development of novel Monte-Carlo integration techniques for infinite arrays of pores excised from a continuous medium, offering a great improvement in computation efficiency (chapter 15).
- Calculation by analytic and above Monte-Carlo techniques of solid-solid density correlation function $G(r)$ for a number of simple bodies (chapter 15.6, appendices K, L).
- Creation of geometric intersecting and non-intersecting pore models, with variance of pore diameter and lattice spacing. Analysis by analytic and above Monte-Carlo integration techniques, giving excellent agreement with experimental scattering results (chapters 15, 16.2.4).
- Detailed calibration of sol-gel pore dimensions and variance, from measured scattering from sol-gel silicas, based on a geometric interpolation of the Monte-Carlo calculated scattering from pores on HCP and Cubic lattices, with variance of pore diameter and lattice spacing (chapter 17).

Appendix A

Equation of motion for a quantum spin in a magnetic field.

We wish to expand the derivation of the equation of motion for a quantum spin in a magnetic field. [Abragam, 1961, IIB], thus showing that this has the same form as the classical expression.

One has for the Hamiltonian of the interaction energy of an isolated spin \mathbf{I} with a magnetic field \mathbf{B}

$$\mathcal{H} = -\gamma\hbar(\mathbf{B}\cdot\mathbf{I})$$

where $\mathbf{J} = \hbar\mathbf{I}$ is the angular momentum operator.

Then for the equation of motion one has [Abragam, 1961, IIB, (11)] :

$$\frac{\hbar}{i} \frac{d\mathbf{I}}{dt} = [\mathcal{H}, \mathbf{I}] = -\gamma\hbar[\mathbf{B}\cdot\mathbf{I}, \mathbf{I}]$$

where we denote the commutator of two operators u, v by the Poisson brackets

$$[u, v] = uv - vu$$

hence we have for operators u, v, w

$$\begin{aligned} [(u + v), w] &= [u, w] + [v, w] \\ [uv, w] &= [u, w]v + u[v, w] \end{aligned}$$

for operator u , constant c

$$[c, u] = 0$$

for angular momentum $\hbar\mathbf{I}$ (note \hbar is external to \mathbf{I})

$$[I_i, I_j] = i\epsilon_{ijk}I_k$$

where the three dimensional Levi-Cevita symbol $\epsilon_{ijk} = 1$

Writing $\mathbf{B}\cdot\mathbf{I}$ in component form we get

$$\mathbf{B}\cdot\mathbf{I} = B_x I_x + B_y I_y + B_z I_z$$

and for \mathbf{I} we get

$$\mathbf{I} = I_x \mathbf{i} + I_y \mathbf{j} + I_z \mathbf{k}$$

Thus for the z component of $[\mathbf{B}\cdot\mathbf{I}, \mathbf{I}]$ we get

$$\begin{aligned} [\mathbf{B}\cdot\mathbf{I}, \mathbf{I}]_z &= [(B_x I_x + B_y I_y + B_z I_z), I_z] \\ &= [B_x I_x, I_z] + [B_y I_y, I_z] + [B_z I_z, I_z] \\ &= [B_x, I_z] I_x + B_x [I_x, I_z] \\ &+ [B_y, I_z] I_y + B_y [I_y, I_z] \\ &+ [B_z, I_z] I_z + B_z [I_z, I_z] \end{aligned}$$

The components of \mathbf{B} in the Poisson brackets are simple constants, so these terms go to zero; the last Poisson bracket commutes, so it also goes to zero. Thus we obtain :

$$\begin{aligned} \frac{\hbar}{i} \frac{dI_z}{dt} &= -\gamma \hbar (B_x [I_x, I_z] + B_y [I_y, I_z]) \\ &= -\gamma \hbar (B_x (-i\epsilon_{ijk} I_y) + B_y (i\epsilon_{ijk} I_x)) \\ &= \frac{-\gamma \hbar}{i} (B_x I_y - B_y I_x) \end{aligned}$$

Finally we may note that

$$\begin{aligned} \mathbf{B} \times \mathbf{I} &= \begin{vmatrix} B_x & I_x & \mathbf{i} \\ B_y & I_y & \mathbf{j} \\ B_z & I_z & \mathbf{k} \end{vmatrix} \\ &= (B_y I_z - B_z I_y) \mathbf{i} \\ &+ (B_z I_x - B_x I_z) \mathbf{j} \\ &+ (B_x I_y - B_y I_x) \mathbf{k} \end{aligned}$$

\therefore for the z component

$$(B_x I_y - B_y I_x) = (\mathbf{B} \times \mathbf{I})_z$$

Hence we obtain as expected [Abragam, 1961, IIB, (12)] :

$$\frac{\hbar}{i} \frac{dI_z}{dt} = \frac{-\gamma \hbar}{i} (\mathbf{B} \times \mathbf{I})_z$$

We have thus shown that the equation of motion has the same form as the classical expression.

Appendix B

The Dipolar Hamiltonian.

The dipolar Hamiltonian, in frequency units, is given by [Abragam, 1961, Ch. VIII G], [Harris, 1987, Ch. 4.1] :

$$h^{-1}\hat{\mathcal{H}}_{dd} = \frac{\mu_0}{4\pi}\gamma_1\gamma_2\frac{\hbar}{2\pi}r_{12}^{-3}\left(\mathbf{I}_1\cdot\mathbf{I}_2-3r_{12}^{-2}(\mathbf{I}_1\cdot\mathbf{r}_{12})(\mathbf{I}_2\cdot\mathbf{r}_{12})\right) \quad \{Hz\}$$

An inner (scalar, dot) product between vectors V_i, V_j may be written :

$$\begin{aligned} \langle V_i|V_j\rangle &= (V_{i1}V_{j1}+V_{i2}V_{j2}+V_{i3}V_{j3}) \\ &= |V_i||V_j| \cos \alpha_{ij} \end{aligned}$$

i.e. The result is a scalar whose magnitude depends on the magnitude of the vectors and on the included angle between the vectors α_{ij} . Hence for unit vectors $\hat{\mathbf{i}}, \hat{\mathbf{j}}, \hat{\mathbf{k}}$

$$\begin{aligned} \hat{\mathbf{i}}\cdot\hat{\mathbf{i}} &= \hat{\mathbf{j}}\cdot\hat{\mathbf{j}} = \hat{\mathbf{k}}\cdot\hat{\mathbf{k}} = 1 \\ \hat{\mathbf{i}}\cdot\hat{\mathbf{j}} &= \hat{\mathbf{j}}\cdot\hat{\mathbf{k}} = \hat{\mathbf{k}}\cdot\hat{\mathbf{i}} = 0 \end{aligned}$$

Thus for Cartesian components, we have :

$$\begin{aligned} \mathbf{I} &= \hat{\mathbf{i}}I_i + \hat{\mathbf{j}}I_j + \hat{\mathbf{k}}I_k \\ \mathbf{R} &= \hat{\mathbf{i}}R_i + \hat{\mathbf{j}}R_j + \hat{\mathbf{k}}R_k \\ \mathbf{I}\cdot\mathbf{R} &= I_iR_i + I_jR_j + I_kR_k \end{aligned}$$

Thus for the term $\mathbf{I}_1\cdot\mathbf{I}_2$ we get :

$$\mathbf{I}_1\cdot\mathbf{I}_2 = I_{1x}I_{2x} + I_{1y}I_{2y} + I_{1z}I_{2z}$$

If we now define a *Raising Operator* I_+ such that when it acts on a state $|\alpha, m\rangle$ we get $|\alpha, m+1\rangle$

and a *Lowering Operator* I_- such that when it acts on a state $|\alpha, m\rangle$ we get $|\alpha, m-1\rangle$

we find that $I_+ = I_x + i I_y$, $I_- = I_x - i I_y$

Thus

$$\begin{aligned} I_{1x} &= \frac{1}{2}(I_{1+} + I_{1-}), & I_{1y} &= \frac{-i}{2}(I_{1+} - I_{1-}) \\ I_{2x} &= \frac{1}{2}(I_{2+} + I_{2-}), & I_{2y} &= \frac{-i}{2}(I_{2+} - I_{2-}) \end{aligned}$$

Hence

$$\begin{aligned} \mathbf{I}_1 \cdot \mathbf{I}_2 &= \frac{1}{2}(I_{1+} + I_{1-})\frac{1}{2}(I_{2+} + I_{2-}) \\ &\quad + \frac{-i}{2}(I_{1+} - I_{1-})\frac{-i}{2}(I_{2+} - I_{2-}) + I_{1z}I_{2z} \\ &= \frac{1}{4}(I_{1+}I_{2+} + I_{1+}I_{2-} + I_{1-}I_{2+} + I_{1-}I_{2-}) \\ &\quad - \frac{1}{4}(I_{1+}I_{2+} - I_{1+}I_{2-} - I_{1-}I_{2+} + I_{1-}I_{2-}) \\ &\quad + I_{1z}I_{2z} \\ &= \frac{1}{2}(I_{1+}I_{2-} + I_{1-}I_{2+}) + I_{1z}I_{2z} \end{aligned}$$

For the other term we have :

$$\begin{aligned} (\mathbf{I}_1 \cdot \mathbf{r}_{12})(\mathbf{I}_2 \cdot \mathbf{r}_{12}) &= (I_{1x}r_x + I_{1y}r_y + I_{1z}r_z)(I_{2x}r_x + I_{2y}r_y + I_{2z}r_z) \\ &= \frac{1}{2}(I_{1+} + I_{1-})\frac{1}{2}(I_{2+} + I_{2-})r_x^2 \\ &\quad + \frac{-i}{2}(I_{1+} - I_{1-})\frac{-i}{2}(I_{2+} - I_{2-})r_y^2 \\ &\quad + I_{1z}I_{2z}r_z^2 \\ &\quad + \frac{1}{2}(I_{1+} + I_{1-})\frac{-i}{2}(I_{2+} - I_{2-})r_xr_y \\ &\quad + \frac{-i}{2}(I_{1+} - I_{1-})\frac{1}{2}(I_{2+} + I_{2-})r_xr_y \\ &\quad + (\frac{1}{2}(I_{1+} + I_{1-})I_{2z} + I_{1z}\frac{1}{2}(I_{2+} + I_{2-}))r_xr_z \\ &\quad + (\frac{-i}{2}(I_{1+} + I_{1-})I_{2z} + I_{1z}\frac{-i}{2}(I_{2+} - I_{2-}))r_yr_z \end{aligned}$$

Grouping in terms of Raising and Lowering operators :

$$\begin{aligned} \text{A: } & I_{1z}I_{2z}r_z^2 \\ \text{B: } & (I_{1+}I_{2-} + I_{1-}I_{2+})\frac{1}{4}(r_x^2 + r_y^2) \\ \text{C: } & (I_{1+}I_{2z} + I_{1z}I_{2+})\frac{1}{2}(r_xr_z - i r_yr_z) \\ \text{D: } & (I_{1-}I_{2z} + I_{1z}I_{2-})\frac{1}{2}(r_xr_z + i r_yr_z) \\ \text{E: } & (I_{1+}I_{2+})\frac{1}{4}(r_x^2 - 2ir_xr_y - r_y^2) \\ \text{F: } & (I_{1-}I_{2-})\frac{1}{4}(r_x^2 + 2ir_xr_y - r_y^2) \end{aligned}$$

Geometrically, converting the Cartesian components of \mathbf{r} to polar coordinates, we have

$$\begin{aligned}\mathbf{r}_x &= \hat{\mathbf{i}}r_x = \hat{\mathbf{i}}r \sin \theta \cos \phi \\ \mathbf{r}_y &= \hat{\mathbf{j}}r_y = \hat{\mathbf{j}}r \sin \theta \sin \phi \\ \mathbf{r}_z &= \hat{\mathbf{k}}r_z = \hat{\mathbf{k}}r \cos \theta\end{aligned}$$

Substituting, we get for $(\mathbf{I}_1 \cdot \mathbf{r}_{12})(\mathbf{I}_2 \cdot \mathbf{r}_{12})$

$$\begin{aligned}\text{A: } & I_{1z}I_{2z}r^2 \cos^2 \theta \\ \text{B: } & (I_{1+}I_{2-} + I_{1-}I_{2+})\frac{1}{4}r^2 \sin^2 \theta (\cos^2 \phi + \sin^2 \phi) \\ \text{C: } & (I_{1+}I_{2z} + I_{1z}I_{2+})\frac{1}{2}r^2 \sin \theta \cos \theta (\cos \phi - i \sin \phi) \\ \text{D: } & (I_{1-}I_{2z} + I_{1z}I_{2-})\frac{1}{2}r^2 \sin \theta \cos \theta (\cos \phi + i \sin \phi) \\ \text{E: } & (I_{1+}I_{2+})\frac{1}{4}r^2 \sin^2 \theta (\cos \phi - i \sin \phi)^2 \\ \text{F: } & (I_{1-}I_{2-})\frac{1}{4}r^2 \sin^2 \theta (\cos \phi + i \sin \phi)^2\end{aligned}$$

$$\text{but } e^{i\phi} = \cos \phi + i \sin \phi,$$

$$\text{hence by symmetry } e^{-i\phi} = \cos \phi - i \sin \phi$$

$$\text{and } 1 = (\cos^2 \phi + \sin^2 \phi)$$

Thus for $(\mathbf{I}_1 \cdot \mathbf{r}_{12})(\mathbf{I}_2 \cdot \mathbf{r}_{12})$

$$\begin{aligned}\text{A: } & I_{1z}I_{2z}r^2 \cos^2 \theta \\ \text{B: } & (I_{1+}I_{2-} + I_{1-}I_{2+})\frac{1}{4}r^2 \sin^2 \theta \\ \text{C: } & (I_{1+}I_{2z} + I_{1z}I_{2+})\frac{1}{2}r^2 \sin \theta \cos \theta e^{-i\phi} \\ \text{D: } & (I_{1-}I_{2z} + I_{1z}I_{2-})\frac{1}{2}r^2 \sin \theta \cos \theta e^{+i\phi} \\ \text{E: } & (I_{1+}I_{2+})\frac{1}{4}r^2 \sin^2 \theta e^{-2i\phi} \\ \text{F: } & (I_{1-}I_{2-})\frac{1}{4}r^2 \sin^2 \theta e^{+2i\phi}\end{aligned}$$

Writing for the dipolar Hamiltonian, in frequency units :

$$h^{-1}\widehat{\mathcal{H}}_{dd} = \frac{\mu_0}{4\pi}\gamma_1\gamma_2\frac{\hbar}{2\pi}r_{12}^{-3}(A + B + C + D + E + F) \quad \{Hz\}$$

Where :

for A we have :

$$\begin{aligned} & I_{1z}I_{2z}(1 - 3 r^{-2}r^2 \text{Cos}^2\theta) \\ = & I_{1z}I_{2z}(1 - 3 \text{Cos}^2\theta) \\ = & - I_{1z}I_{2z}(3 \text{Cos}^2\theta - 1) \end{aligned}$$

for B we have :

$$\begin{aligned} & (I_{1+}I_{2-} + I_{1-}I_{2+})(\frac{1}{2} - 3 r^{-2}\frac{1}{4}r^2 \text{Sin}^2\theta) \\ = & (I_{1+}I_{2-} + I_{1-}I_{2+})\frac{1}{4}(3 \text{Cos}^2\theta - 3 + 2) \\ = & (I_{1+}I_{2-} + I_{1-}I_{2+})\frac{1}{4}(3 \text{Cos}^2\theta - 1) \end{aligned}$$

We finally obtain, in terms of operators and second order spherical harmonics :

$$\begin{aligned} \text{A:} & - I_{1z}I_{2z}(3 \text{Cos}^2\theta - 1) \\ \text{B:} & (I_{1+}I_{2-} + I_{1-}I_{2+}) \frac{1}{4}(3 \text{Cos}^2\theta - 1) \\ \text{C:} & - (I_{1+}I_{2z} + I_{1z}I_{2+}) \frac{3}{2}\text{Sin} \theta \text{Cos} \theta e^{-i\phi} \\ \text{D:} & - (I_{1-}I_{2z} + I_{1z}I_{2-}) \frac{3}{2}\text{Sin} \theta \text{Cos} \theta e^{+i\phi} \\ \text{E:} & - (I_{1+}I_{2+}) \frac{3}{4}\text{Sin}^2\theta e^{-2i\phi} \\ \text{F:} & - (I_{1-}I_{2-}) \frac{3}{4}\text{Sin}^2\theta e^{+2i\phi} \end{aligned}$$

Thus we have derived the quoted expressions.

Appendix C

NMR CRYOPOROMETER.

Designer: J.B.W.Webber@ukc.ac.uk

This instrument is designed to measure pore sizes and pore size distributions by the technique of freezing a liquid in the pores, and measuring the melting temperature by Nuclear Magnetic Resonance. Since melting point is depressed for crystals of small size, the melting point gives a measurement of pore size.

With Cyclohexane as the liquid, pore sizes from less than 30Å to over 3000Å may be readily measured.

C.1 Over view.

This Cryoporometer is implemented on a standard PC compatible computer, using the graphical programming language LabVIEW™ for Windows™. This provides the software and interactive front panel to interface to an IEEE oscilloscope and digital volt meter, and a serially controlled temperature controller. The default NMR spectrometer is the standard UKC design, but others may be used with no modification, other than perhaps in the details of the temperature control. The spectrometer should normally be configured so that it is giving a $90^\circ_x - \tau - 180^\circ_y - \tau - \text{Echo}$ sequence, with the echo centralised on the oscilloscope screen.

This configuration provides the control to cool the sample down to a specified temperature, and then slowly warm up while taking measurements. Results may be displayed as measurements are taken. Finally the measured data may be plotted and saved.

C.2 Running the Cryoporometer.

After loading (see local installation and running instructions), one must set the instrument running – this is software, one does have to run it as normal (auto-run is possible).

For this one clicks on the **hollow arrow** in the top left corner.

However it should be noted that one should not just stop the instrument using the software-stop, as this may leave the instruments with their front panels locked out.

Instead, an **Off** switch is provided – top left on the front panel. Click on it using the mouse left button.

When the instrument is run, it throws up a window to allow the current Experimenter to be chosen, or a new one entered. This also creates the necessary directory for data storage.

C.3 Instrument Front Panel.

This is divided by function into three main areas.

On the left are controls and displays associated with doing a temperature run, and gathering new data.

In the centre are graphical displays of the melting point curve and the calculated pore size distribution, and at the bottom, the labelling of the data.

On the right are controls and displays associated with loading saving, and plotting the data, as well as a numeric listing of the data.

It is possible to alter the display (using the control at the top right), from the current data, to display the previous run, or data from file. This may be done even while measuring.

Controls and displays are colour coded, in that controls that may be directly altered are yellow, displays that may only be indirectly altered are blue.

C.3.1 Left of Display.

Next to the **Off** switch is an **Idle** switch, that terminates a temperature run and forces the temperature control to the Idle state; and a **Free** switch, that frees the IEEE instruments, and allows them to be controlled from their front panels. The later switch may be operated at any time data is not being captured. To start a new temperature run, switch to Idle and back again.

To the right of these three switches, are three LED tell-tales.

The top green one – **Activity** – just flashes to indicate that the instrument is still running – it changes state at every run cycle.

The middle blue one – **Cooling** – indicates that the machine is in the cool down state. Note, the instrument is designed to initially cool down below the lowest measurement temperature. (See below for more details on Temperature Control.)

The lower red one – **Measure** – indicates that Cryoporometric data is being captured. The large digital display below these – **Temperature** – gives the measured sample temperature. Temperature displays may be given either in Kelvin or Celcius, under control of a slide switch.

The next two digital controls – **Lower Temp** – **Upper Temp** – set the range of temperature over which Cryoporometric measurements are made. It should be noted the initial cool down will go below Lower Temp by a value currently set at 20°C – this is adjustable on the program diagram. This ensures that the NMR probe is all well cooled down. It should also be noted the actual measurement range may be up to about 1°C less than the values set, at each end of the range. [Note on digital controls : these may be incremented or decremented using the arrows; alternatively the mouse may be used to position the cursor on the numbers, and new numbers typed in. When finished, click on the front panel blue background, to enter the number.]

Below the temperature range controls one sets the pore filling liquid – **Liquid** – by default Cyclohexane. As well as incrementing and decrementing, or re-typing, one can also pop-up on the text with the left mouse button, and select from a list. [Technically this control is known as a Ring.] This control looks up the appropriate values for the Bulk Melting Point Temperature, the Slope or k-value, and the curvature compensating diameter D0, if any. If you wish to change any of these values, at the moment you have to select the look-up-table sub-program (labelled CRC) and edit the appropriate entries in the table. The **Melt Point**, **Slope** and **D0** are displayed here.

Next comes the **Temperature Control**.

On the left is displayed the measured **Splashpot Temperature** – i.e. the temperature as measured by the temperature controller thermocouple at the point where heating and cooling take place.

Below this is the **Target Temperature** – the temperature that the temperature controller is currently aiming at, and an approximation of which is written to the temperature control instrument via a serial link.

On the right of these is a LED display of the state of the temperature cycle. Initially in the **Idle** state, the temperature control will, if the switch at the top is not set to **Idle**, progress to **Cool**. The temperature will then be progressively ramped down ($5\text{ C}^\circ\cdot\text{min}^{-1}$), until a temperature 20C° below the **Lower Temp** is reached.

The state will then switch to **Dwell**, and this will be maintained for 15 min. After this the state switches to **Pre-warm**, when the controller aims to warm at $2\text{ C}^\circ\cdot\text{min}^{-1}$ until the **Lower Temp** is reached.

At this point the state switches to **Warm-up**, and the controller sets a temperature ramp at a rate set by the digital control **Rate** (in $\text{C}^\circ\cdot\text{min}^{-1}$). Suitable values range from $1\text{ C}^\circ\cdot\text{min}^{-1}$ for Cyclohexane in 40\AA silica, to $0.02\text{ C}^\circ\cdot\text{min}^{-1}$ for 1000\AA or larger silica. It maintains this rate of rise until the **Upper Temp** is reached, when the state switches to **Done**. At any point, the temperature rise or fall may be frozen, by switching the **RAMP** control to **HOLD**. When the temperature control instrument is being written to, the **Set LED** is lit (blue).

Below the temperature control are four controls defining which portions of the oscilloscope trace are used to measure the amplitude of the NMR echo – **Data Capture Windows %**.

The first two controls set the start and stop percentages within which the echo peak should occur (40%, 60% by default) – a cubic polynomial is driven through the data, this is then differentiated to get the slope, and the quadratic solved $= 0$, with the time value with the largest amplitude chosen as the peak. (A slightly different algorithm is used when there is insufficient amplitude to identify a peak at all.)

The second two controls set the window within which the baseline is measured (by simple averaging), and are usually 80%, 100% by default. The oscilloscope timebase should be adjusted so that T_2^* results in the echo being effectively zero in this window. Individual oscilloscope measurements are averaged together. How long the averaging takes place for is calculated from the set rate of temperature rise, and the set temperature range over which measurements are to be made. The calculation aims at about three hundred data points in the final melting point curve – the final number measured is dependent on how closely the actual temperature profile follows the target one.

C.3.2 Right of Display.

At the top right of the front panel is a Ring control – **Display** : popping up on this allows one to select what data is displayed : – the **Current** data set being or just been measured – the **Previous** data set, or – **File**, to display saved data. (The format is compatible with the origin BBC data format, as transferred by program.)

Below this is a numeric listing of the displayed data – **Temperature-Amplitude**. By default this shows the end of/just measured data, but this is alterable using the **Start**, **Index**, **End** buttons.

Here also is **N**, the number of displayed data points.

Below the numeric display is a row of buttons. The three left ones, **Load**, **Save**, **Plot**, do what they say, and are momentary action. **Auto** is auto save, and saves the data at the end of a measurement run (there must be at least 50 points, fewer are ignored). **AUTO** save is the default, and remains set until cancelled.

Load also forces file display, and throws up a file selector, so that any stored data can be viewed.

Save and **Auto** save use the file path as constructed below.

Plot throws up a window containing the two graphs. The axes can then be edited as desired (see below), after which **plot** is selected to send the graph to the printer. Which printer should be first chosen from the menu or the desktop default printer configuration. A blue LED lights during save or plot.

Below this is an editing window, where one can specify the **Save File Path** (by default d:\lab\porous), to where the individual experimenter's directories are located.

Then there is a window where one can select the **Experimenter**. Note, since the list is not defined at compile time (but is read from the list of Experimenter directories on disk) it can not be a pop-up Ring. One can increment or decrement to choose the Experimenter. To the right is a button **New**, which pops up a window, allowing the addition of new Experimenters (and directory creation).

The next window allows the selection of **Project** directory. To the right is again a button **New**, which pops up a window, allowing the addition of new Projects (and directories).

Below this are three windows that define the file name, a **File Name** window, a **Number** that is concatenated, and an **Increment** that is added to number at each auto save. Note if increment is Zero, then Number is not concatenated. The combined file name

must be 8 characters or less. Then, below two windows which give the date and time in ISO standard form, is a display containing the full path to which the data will be saved. The data is saved in raw format (i.e. Amplitude vs. EMF) into subdirectory 'raw'. This allows other format data, such as poresize, to be stored in other sub-directories, for the same project.

C.3.3 Centre of Display.

Below the instrument heading is the **Melting Point Curve** or **Echo Amplitude**, where the amplitude of the NMR signal from the echo is traced, as the liquid melts. One can pop-up on the graphs with the mouse button, to select auto scale (or not) for the X and Y axes. By default the Y-axis is autoscale, the X-axis is not. When not autoscale, each of the two end-of-axis scale readings are editable, when the intervening legend re-scales. (Click on background when the edit is complete.) Underneath this graph, to the right is **Current N**, the current number of points measured.

The lower graph is the calculated **Pore Diameter**, which can also be popped-up on. The parameters of the currently selected liquid are used in the calculation.

Underneath, to the right, is **Peak** – a cubic polynomial is fitted to the pore diameter peak, and as with the echo, differentiated and analytically solved to obtain a value for the peak pore diameter and amplitude.

Below this is the file **Name** of the graphs actually being displayed. This is also written as the first line of the file.

To the left, is a pop-up Ring, giving a choice of **Filter : Raw, Monotonic, Monotonic+Log.Smooth, Monotonic+Log.Smooth+5pt.Smooth**. **Monotonic** applies the constraint of monotonicity to the data – this is a very powerful noise reducing algorithm that does not blur the data. **Log.Smooth** applies a smoothing algorithm, with logarithmically varying resolution, to the data, to help remove measurement noise. In the centre is **Decade Resolution**, which allows one to adjust the number of resolvable peaks per decade for the logarithmic smoothing to suit the measurement.

Below this is a text box **Description**, in which one can describe the experiment.

Finally comes the full **Header** of the data being graphed, which is written as the second line of the file. After the file name comes the description, then the measuring liquid, then the date and time, and finally the Experimenter.

Appendix D

Determination of the cryoporometric resolution from the bulk liquid melting step.

We wish to determine the thermal characteristics of the cryoporometric sample in the NMR probe; in particular we wish to know the residual ΔT along the sample, at zero warming rate. When the liquid around the porous grains melts at the end of a cryoporometric run, there is a further trapezoidal step in the volume of melted liquid, at effectively the bulk melting point. We can obtain information about the residual ΔT from the way the slope of the bulk warming step changes with warming rate, as in the limit of no residual ΔT the slope would go to ∞ at zero warming rate. From this ΔT we may deduce the limits on the cryoporometric resolution of the system.

Using the data gathered for cryoporometric runs at warming rates of 0.2, 0.1, 0.05 $\text{C}^\circ \cdot \text{min}^{-1}$ using water in 200Å sol gel silica and warming rates of 0.05, 0.02, 0.01 $\text{C}^\circ \cdot \text{min}^{-1}$ using cyclohexane in 1930Å Trisopor[®] porous glass (see chapter 9), we may measure the parameters of the bulk melting step.

Apl routine *mpcstep* was written; given a project directory name, a data file mask and the name of a table of measured masses, this in turn reads in the melting point data (before application of the monotonic routine), displays the melting point data as a function of sample thermocouple temperature, and with user interaction normalises it in terms of melted mass of liquid per unit mass of dry porous solid and calculates a bulk melting point. The routine graphs this data and writes it to disk and then displays and saves the parameters. It then reads monotonic processed data to calculate a volume

normalised pore size distribution using the measured value of the bulk melting point; it graphs the distribution and writes it to disk.

When defining the bulk melting point step, the routine allows the user to mark with the cursor six points defining three regions where the data forms reasonably straight lines: the plateau corresponding to the melted pore liquid, the bulk melting step, and the plateau corresponding to all the liquid.

The routine then linear least squares fits the data bounded by the marked x values (returning the equations), plots the lines, and calculates the two intersections of adjacent sections. Given the equations of two straight lines :

$$y = c_1 + a_1 \cdot x$$

$$y = c_2 + a_2 \cdot x$$

then the lines intersect at

$$x = -\frac{c_1 - c_2}{a_1 - a_2}$$

$$y = c_2 + a_2 \cdot x$$

Thus, given a variable *Coefs* containing the coefficients of the equations of the lines, we may calculate the intersection x, y using the Apl expressions :

$$X \leftarrow - \div / -/[1] \text{ Coefs}$$

$$XY \leftarrow X, \text{ Coefs}[2;] \text{ genlin } X$$

These intersection $(T_l, M_l), (T_u, M_u)$ are marked on the graph (see figure 123), and used to calculate the parameters associated with the bulk liquid melting step.

Thus for the bulk step, we may write :

$$\Delta T_b = T_u - T_l$$

$$\Delta M_b = M_u - M_l$$

Thus the gradient G of the (trapezoidal) step is given by $G = \frac{\Delta M_b}{\Delta T_b}$.

A sample of liquid undergoing an isothermal phase transition will require a certain time Δt_m to melt, depending of the mass of liquid melting ΔM_b , and the size of the heat

Extracting the coefficients of the bulk melting point step.

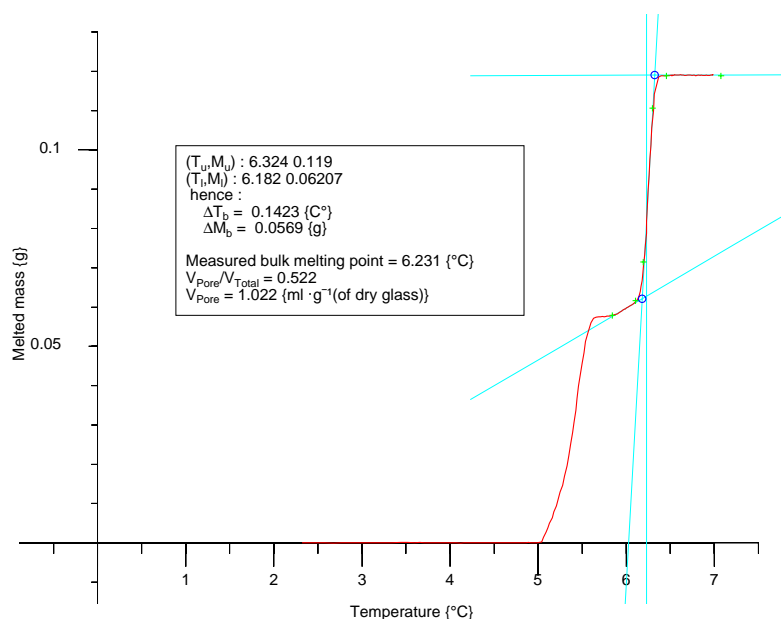


Figure 123: Calculation of the parameters associated with the bulk liquid melting step, for cyclohexane in 1930Å Trisopor at $0.01\text{C}^\circ\cdot\text{min}^{-1}$ warming rate.

flux into the sample W_s . Hence we have :

$$\Delta t_m = \frac{L_f \cdot \Delta M_b}{W_s}$$

where L_f = Latent Heat of Fusion of the solid to liquid transition.

Given that the probe is being warmed at a constant rate $\frac{dT}{dt}$, the thermocouple (that is insulated from the isothermal melting solid by the silica tube wall and a layer of porous silica and melted liquid) will measure a temperature rise ΔT_m while the liquid melts. Thus the measured melting step will be spread over a total temperature range $\Delta T_b = \Delta T_s + \Delta T_m$, where ΔT_s = the total temperature range along the sample due to thermal gradients (at zero heating rate).

Thus we have for the gradient G of the (trapezoidal) step :

$$\begin{aligned} G &= \frac{\Delta M_b}{\Delta T_b} \\ &= \frac{\Delta M_b}{\Delta T_s + \Delta T_m} \end{aligned}$$

If however we just consider ΔT_b directly, we have

$$\begin{aligned}\Delta T_b &= \Delta T_s + \Delta T_m \\ &= \Delta T_s + \Delta t_m \cdot \frac{\Delta T_m}{\Delta t_m} \\ &\approx \Delta T_s + \frac{L_f \cdot \Delta M_b}{W_s} \cdot \frac{dT}{dt}\end{aligned}$$

i.e. we see that provided the heat flux into the sample W_s is independent of the heating rate (it is not obvious that it should be), if we plot ΔT_b as a function of warming rate $\frac{dT}{dt}$, then we obtain a straight line with an intercept on the y axis that gives us ΔT_s , the temperature range along the sample due to thermal gradients, at zero heating rate. If the heat flux into the sample W_s was proportional to the heating rate, then the slope G of the melting curve would be independent of the heating rate, which is not what we see; if W_s was a function of the heating rate such that

$$W_s = W_{s0} \cdot \left(\frac{dT}{dt}\right)^p$$

where power $p < 1$, then we would have

$$\Delta T_b = \Delta T_s + \frac{L_f \cdot \Delta M_b}{W_{s0}} \cdot \left(\frac{dT}{dt}\right)^{1-p}$$

If we plot ΔT_b for water in 200Å sol gel silica at warming rates 0.2, 0.1, 0.05 C°·min⁻¹, and for cyclohexane in 1930Å Trisopor[®] porous glass, at warming rates 0.05, 0.02, 0.01 C°·min⁻¹, using power $p \approx 0.5(0.463)$ we obtain figure 124; we have a reasonably consistent fit, with a y intercept of 0.058C°.

Thus we conclude that the sample has a variation in temperature of about ± 30 mK at zero warming rate; for a sample with cyclohexane in 2000Å diameter pores, this corresponds to an instrument resolution function with a full width of about 130Å, and considerably less for smaller pore sizes – the corresponding value for 200Å is about 1.3Å. The values at finite warming rates are given for cyclohexane in table 22 and for water in table 23.

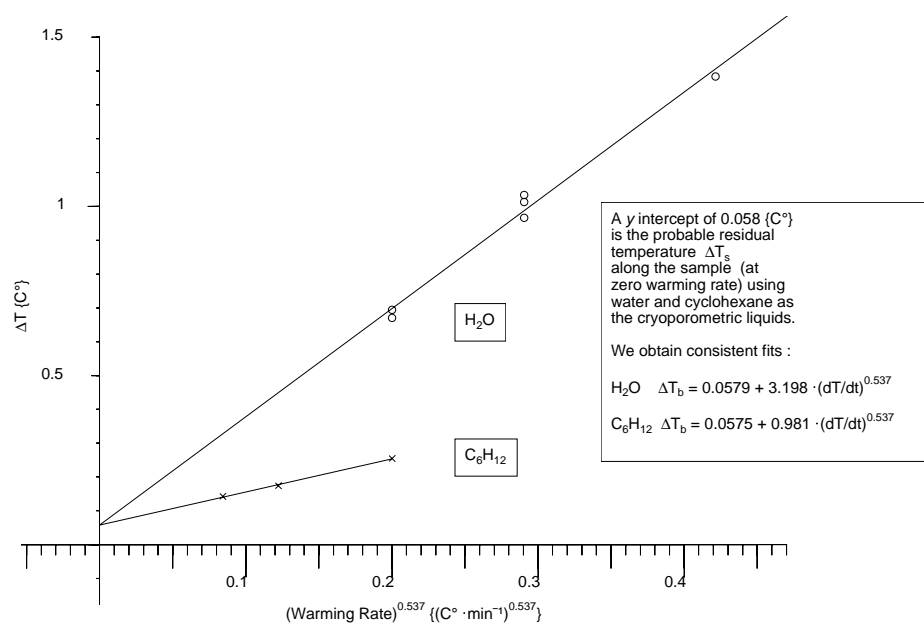
ΔT for cryoporometric bulk step vs. probe warming rate

Figure 124: Plot of ΔT_b for water in 200Å sol gel silica at warming rates 0.2, 0.1, 0.05 C°·min⁻¹, and for cyclohexane in 1930Å Trisopor porous glass, at warming rates 0.05, 0.02, 0.01 C°·min⁻¹.

Warming Rate {C°·min ⁻¹ }	ΔT_b {C°}	ΔM_b {g}	Resolution @ 2000Å {Å}
0.05	0.2548	0.0565	682
0.02	0.1744	0.0560	484
0.01	0.1423	0.0569	384
0	0.0575		126

Table 22:

Measured bulk step ΔT , ΔM values for various probe warming rates, and inferred effect on pore size resolution, when using cyclohexane as the cryporometric liquid.

Warming Rate {C°·min ⁻¹ }	ΔT_b {C°}	ΔM_b {g}	Resolution @ 200Å {Å}
0.2	1.384	0.06433	140
0.1	1.013	0.06153	98
0.1	1.033	0.06255	
0.1	0.9662	0.06377	
0.05	0.6705	0.09228	71
0.05	0.6944	0.06425	
0	0.0579		4.6

Table 23:

Measured bulk step ΔT , ΔM values for various probe warming rates, and inferred effect on pore size resolution, when using water as the cryporometric liquid.

Appendix E

T2 corrections for pore liquid signal to total liquid signal ratio.

We show that even if the pore liquid and bulk liquid have different relaxation times, we may describe a function of the ratio of the measured signal from the pore liquid to that from all the liquid with a single decay time, and hence obtain the true pore volume from a number of cryoporometric measurements at different τ values.

Consider, when the sample is a few degrees above the bulk melting point of the liquid, we obtain a signal from the total liquid V_{TL} . (In practice we assume this is slightly temperature dependent, and do a linear fit and extrapolate to find the value at the bulk melting point, see appendix D.)

Since we have measured the total mass of the liquid in the sample M_{TL} , and know the density ρ_L , we may calculate the effective sensitivity of the cryoporometer for this sample :

$$S = \rho_L \cdot \frac{V_{TL}}{M_{TL}} \quad \{V \cdot l^{-1}\}$$

Consider now the case during a cryoporometric run, when the liquid in the pores has all melted (giving a plateau), but that around the grains has not. If we knew the signal from just the liquid component in the pores V_{PL} at time 0 :

$$V_{PL}(0) = S \cdot v_P \quad \{V\}$$

then we could write for the pore volume :

$$v_P = \frac{1}{\rho_L} \cdot M_{TL} \cdot \frac{V_{PL}}{V_{TL}}(0) \quad \{l\}$$

(We have already compensated for Boltzmann and copper coil resistivity changes as a function of temperature, thus in case of any residual slope, measurement is by linear fitting of the plateaus and extrapolating to a common temperature – the bulk melting point.)

However at time $t = 0$ we also have the signal from the solid around the grains.

NMR is a sensitive technique for distinguishing between solid and liquid, as the coherent transverse nuclear spin magnetisation decays much more rapidly in a solid than in a mobile liquid. Measurement of the volume of liquid present is usually most conveniently done using a $90^\circ_x - \tau - 180^\circ_y - \tau$ -echo sequence [Abragam, 1961, Harris, 1987] where the time interval 2τ is set to be longer than the T_2 decay time in the solid but less than the T_2 decay time in the liquid [Strange et al., 1993]. For cyclohexane and water $\tau = 2\text{ms}$ to 20ms was mainly used.

However in pores the T_2 of the liquid will be reduced compared with the bulk value (see chapter 7.5.4) and we will measure echo amplitudes that are τ dependent.

If we have for the total signal from the liquid in the pores and the bulk liquid :

$$V_T(t) = V_{PL}(t) + V_{BL}(t) \quad \{V\}$$

where

$$V_{PL}(t) = V_{PL}(0) \cdot e^{-\frac{t}{\tau_P}} \quad \{V\}$$

and

$$V_{BL}(t) = V_{BL}(0) \cdot e^{-\frac{t}{\tau_B}} \quad \{V\},$$

then

$$\begin{aligned} \frac{V_{TL}}{V_{PL}}(t) &= \frac{V_{PL}(0) \cdot e^{-\frac{t}{\tau_P}} + V_{BL}(0) \cdot e^{-\frac{t}{\tau_B}}}{V_{PL}(0) \cdot e^{-\frac{t}{\tau_P}}} \\ &= 1 + \frac{V_{BL}(0)}{V_{PL}(0)} \cdot e^{-\left(\frac{1}{\tau_B} - \frac{1}{\tau_P}\right) \cdot t} \end{aligned}$$

hence

$$\begin{aligned} \frac{V_{TL}(t)-1}{V_{PL}} &= \frac{V_{BL}(0)}{V_{PL}} \cdot e^{-\left(\frac{1}{\tau_B} - \frac{1}{\tau_P}\right) \cdot t} \\ \therefore \frac{1}{\frac{V_{PL}}{V_{TL}(t)} - 1} &= \frac{V_{PL}(0)}{V_{BL}} \cdot e^{-\left(\frac{1}{\tau_P} - \frac{1}{\tau_B}\right) \cdot t} \\ &= \frac{V_{PL}(0)}{V_{BL}} \cdot e^{-\frac{t}{\tau}} \end{aligned}$$

We now have an expression in terms of the measured $\frac{V_{PL}}{V_{TL}}(t)$ with a single relaxation time $\tau = 1 / \left(\frac{1}{\tau_P} - \frac{1}{\tau_B} \right)$ with a y intercept of $\alpha = \frac{V_{PL}}{V_{BL}}(0)$.

We may thus write for the pore volume :

$$v_P = \frac{1}{\rho_L} \cdot \frac{M_{TL}}{1 + \frac{1}{\alpha}} \quad \{l\}$$

Appendix F

Warming rate for constant resolution.

F.1 Constant resolution on a linear scale.

If we ask the question, what warming rate profile do we require for a constant resolution in pore diameter, since we have from the simplified Gibbs-Thomson equation 2, for the melting point depression ΔT in pores of diameter x :

$$\Delta T = \frac{k}{x}$$

then we may write

$$\begin{aligned} \frac{dT}{dt} &= \frac{d}{dt}(k \cdot x^{-1}) \\ &= -k \cdot x^{-2} \cdot \frac{dx}{dt} \\ &= -\frac{1}{k} \cdot \Delta T^2 \cdot \frac{dx}{dt} \end{aligned}$$

Hence for a warming rate such that we scan pore diameters at a constant rate $\frac{dx}{dt}$, then the warming rate must reduce quadratically as we approach the bulk melting point, see figure 125, where for clarity an unrealistically fast warming rate, consisting of too few points in too short a time, is plotted for the range of pore diameters $100\text{\AA} \rightarrow 1000\text{\AA}$.

Heating rate for constant resolution.

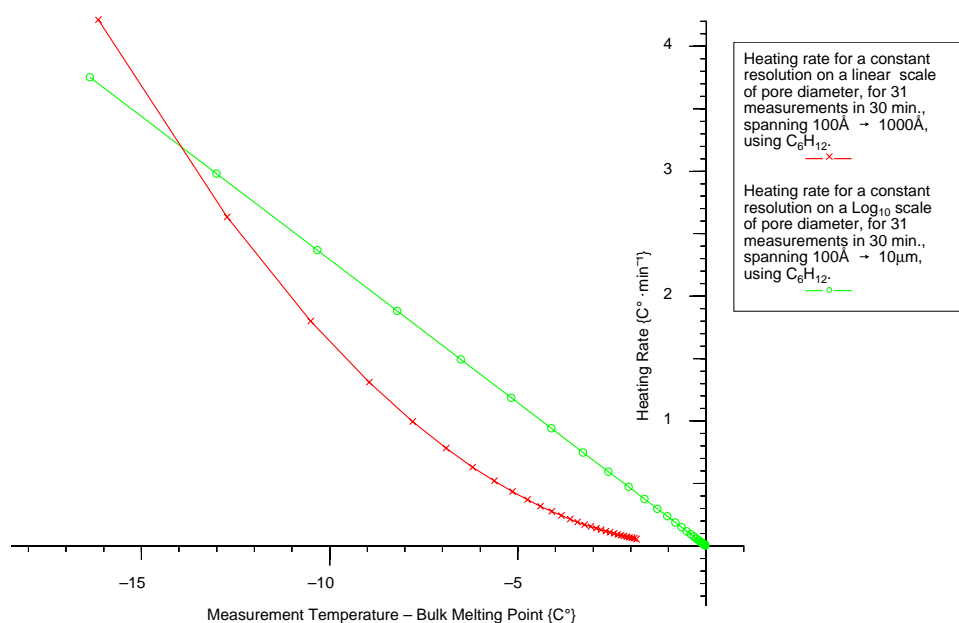


Figure 125:

Warming rate for constant resolution on linear and Log₁₀ pore diameter scales.

F.2 Constant resolution on a logarithmic scale.

Suppose, however, we ask the question what warming rate profile do we require for a constant resolution in logarithmic (base 10) pore diameter, such that we may write $x = 10^X$, then we have :

$$\begin{aligned}
 \Delta T &= \frac{k}{10^X} \\
 &= k \cdot 10^{-X} \\
 \therefore \frac{dT}{dt} &= \frac{d}{dt}(k \cdot 10^{-X}) \\
 &= -k \cdot \ln(10) \cdot 10^{-X} \cdot \frac{dX}{dt} \\
 &= -\ln(10) \cdot \Delta T \cdot \frac{dX}{dt}
 \end{aligned}$$

We see that we now have a warming rate that is proportional to $-\Delta T$, see figure 125, where we now plot for the range 100Å → 10μm. We see the largest temperature step is smaller than in the previous case, in spite of the much larger range.

F.2.1 Defining a warming profile.

In practice at low temperatures we do not wish to warm at the high rates implied by a linear change in warming rate, and set a (settable) upper limit on the warming rate. We arbitrarily choose, as an alterable default when using cyclohexane, to warm at a constant rate when the temperature is below 0°C (corresponding to about 280Å pore diameter), then decrease the warming rate linearly with temperature until we reach the temperature corresponding to measuring pores of diameter 10μm; this warming rate is maintained through the bulk melting point (BMP), then increased back to the maximum warming rate to measure the bulk step. The run is finally terminated at a (settable) upper temperature (default 8°C).

We may define this warming rate profile with the function :

$$WarmRate \leftarrow MaxWarmRate \cdot \left[\left(\frac{MaxWarmRate}{BMP} \cdot \frac{k}{10^5} \right) \cdot (SampleTemp > BMP) + \left| \frac{MaxWarmRate}{BMP} \cdot (SampleTemp - BMP) \right. \right]$$

The time required for a measurement run at constant warming rate is :

$$RunTime \leftarrow (UpperTemp - LowerTemp) \cdot \frac{1}{WarmRate}$$

This becomes for the above profile

$$RunTime \leftarrow \int_{LowerTemp}^{UpperTemp} \frac{1}{WarmRate} dT$$

which is given by :

$$RunTime \leftarrow ((UpperTemp - BMP) + BMP + \left(Ln(10) \cdot \left(5 - Log_{10} \frac{k}{BMP} \right) \cdot BMP \right) - LowerTemp) \cdot \frac{1}{MaxWarmRate}$$

Thus the averaging time for a reading at any one temperature is, since we wish to gather about 300 points per run, the run time divided by 300.

Appendix G

First order numerical simulation of bulk melting step behaviour.

The thermocouple that is attached to the sample tube in a scanning cryoporometer does not measure the actual temperature of the melting solid, since heat to melt the sample must flow past the measuring thermocouple.

We simulate numerically the behaviour of the bulk liquid melting curve, using a simple first order model, and predict a function for the displacement of measured bulk melting point as a function of warming rate that is in agreement with measured displacements.

In scanning cryoporometers the temperature is ramped at a rate that may be either constant or a function of time. Examining typical measured melting curves for constant warming rate (see figures 123, 128) we see that we have at least a second order process, due to distributed thermal masses and resistances.

We choose however, for simplicity, to use a first order model, consisting of a splashpot at temperature T_{sp} that is warmed at a constant rate $WarmingRate = \frac{dT_{sp}}{dt}$, connected by a single thermal resistance R to a sample at temperature T_s consisting of a single thermal mass M_{Th} composed of a glass tube of mass M_g , containing porous silica of mass M_s , and liquid of total mass M_l , of which mass M_m is undergoing a melting transition. We use appropriate specific heats c for each component, and latent heat of fusion L_f for the melting liquid so that prior to liquid melting we have

$$M_{Th} = J \cdot \sum_i c_i \cdot M_i$$

where J is $4.184 \text{ \{J}\cdot\text{Cal}^{-1}\}}$

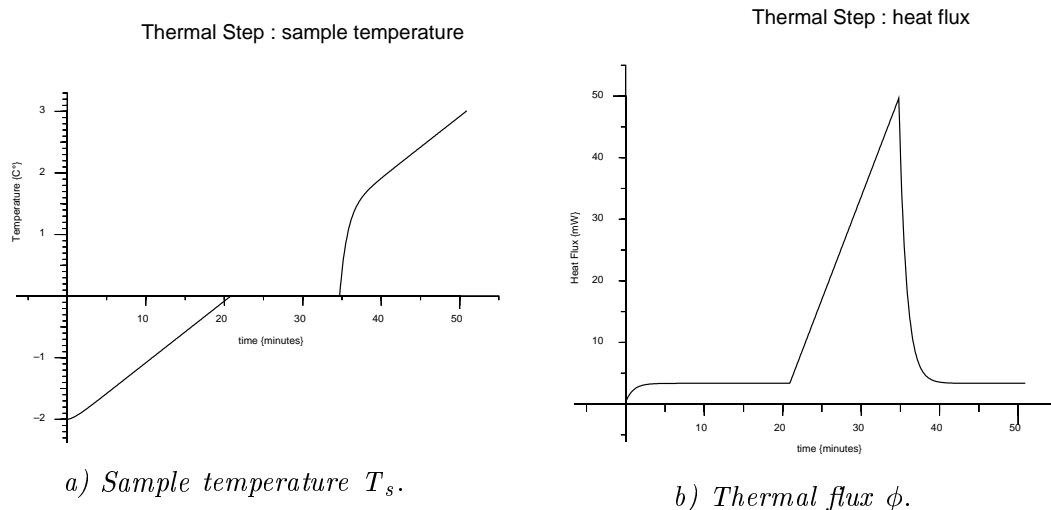


Figure 126: First order simulation of bulk melting step for water in 200Å Unilever silica sample warming at $0.1\text{C}^\circ\cdot\text{min}^{-1}$.

We thus assume that the flux of heat flowing into the sample is given by :

$$\phi(t) = \frac{T_{sp} - T_s}{R}$$

such that the heat added to the sample (from the start of the experiment at temperature T_L), to raise the temperature to T_s is given by :

$$Q(t) = \int_{T=T_L}^{T=T_s} \phi(t) dt$$

Further, since the experimental configuration has the sample thermocouple soldered to a copper foil around the sample tube, we assume that this heat flux passes through the thermal resistance R_m between the thermocouple and the melting solid/liquid, comprising the thermal resistance of the glass tube, that of the interfacial layers, and the thermal resistance of the porous silica. Thus we measure a temperature T_m that is $\phi \cdot R_m$ degrees above T_s .

If for simplicity we choose to consider liquid melting at the bulk melting point T_B (though the argument applies to any fractional mass of melting liquid), ramping the splashpot temperature from T_L to T_U through the bulk melting point T_B .

For $T_s(t) < T_B$

$$T_s(t) = T_L + \frac{Q(t)}{M_{Th}}$$

hence at the bulk melting point we have

$$Q_B = M_{Th} \cdot (T_B - T_L)$$

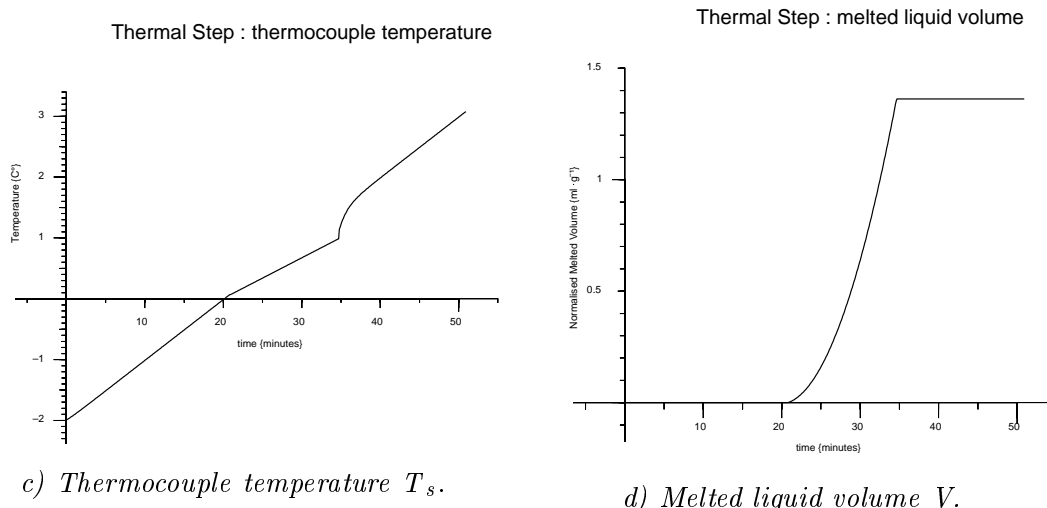


Figure 127: First order simulation of bulk melting step for water in 200Å Unilever silica sample warming at $0.1\text{C}^\circ\cdot\text{min}^{-1}$.

Thus we set all the system initially at T_L and then use the above expressions for ϕ , Q and T_s until $Q(t) = Q_B$

The sample temperature then remains constant while the bulk liquid melts; the splash-pot continues ramping however, and thus the total ΔT increases, and hence so does the flux of heat. Hence the measured temperature also increases.

Thus $T_s(t) = T_B$ and the silica mass normalised volume of melted liquid (density ρ) is given by :

$$V(t) = (Q(t) - M_{Th} \cdot (T_B - T_L)) \cdot \frac{M_m}{\rho \cdot J \cdot M_s \cdot M_m \cdot L_f}$$

until the total heat passed to the sample is

$$Q = M_{Th} \cdot (T_B - T_L) + J \cdot M_m \cdot L_f$$

and the liquid mass M_m has all melted. Thereafter any *additional* heat passed to the sample will act to raise the sample temperature as before.

We run this integral using masses and thermal values for a measured sample of 200Å pore diameter Unilever silica, at a warming rate of $0.1 \{\text{C}^\circ\cdot\text{min}^{-1}\}$; in figures 126, 127 we plot as a function of time the calculated values for :

- a) the sample temperature T_s ;
- b) the thermal flux ϕ ;
- c) the thermocouple temperature T_m ;
- d) the silica mass normalised volume of melted liquid V .

In figure 128 we plot deduced melting curves V vs. T_m for warming rates of 0.05, 0.1, 0.2 $\{\text{C}^\circ \cdot \text{min}^{-1}\}$, against the measured melting curves. Discrepancies due to the simplified first order model are clear, but the initial behaviour is modeled well.

First order simulation of bulk melting step.

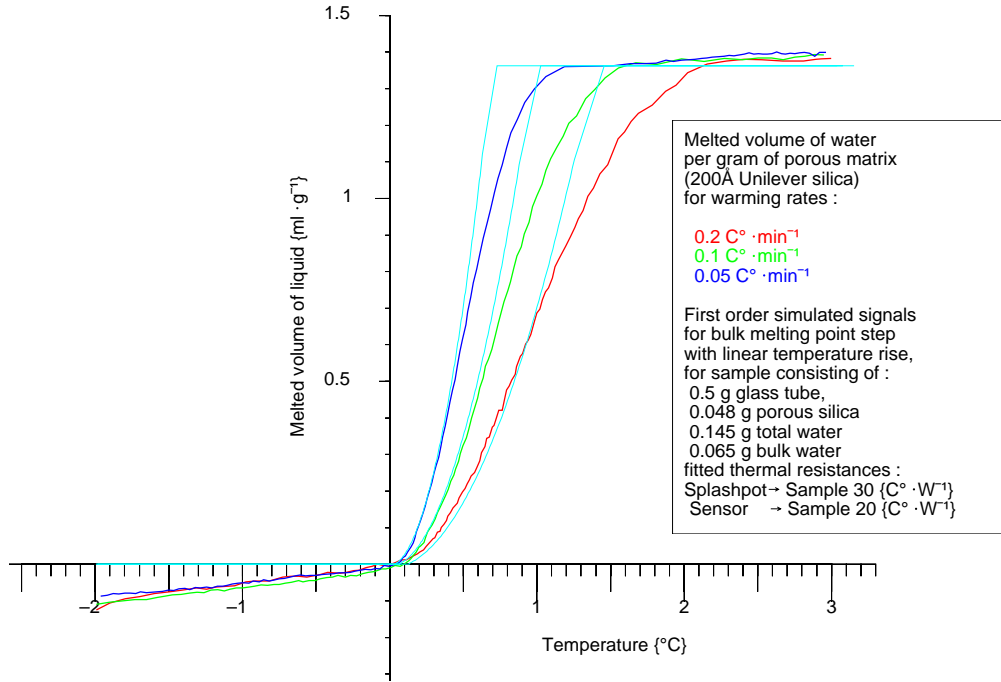


Figure 128: Bulk melting steps: measured and simulated.

We wish to predict the behaviour of the displacement of measured bulk melting point, as a function of warming rate. The above measured melting curves suggested that the displacement varied approximately as :

$$\text{WarmingRate}^{0.55} \text{ at } 1/3 \text{ amplitude of the bulk step.}$$

Calculations were performed for warming rates from 0.005 to 0.5 $\text{C}^\circ \cdot \text{min}^{-1}$, and were shown to result in displacements proportional to :

$$\text{WarmingRate}^{0.561} \text{ at } 1/3 \text{ amplitude of the bulk step, and}$$

$$\text{WarmingRate}^{0.544} \text{ at } 1/2 \text{ amplitude of the bulk step.}$$

Appendix H

Calculation of the maximum radius for a sphere enclosed in a tetragon of touching spheres of radius r .

We need to know the pore size between nanocrystals. Using a simple geometric argument we deduce that the maximum radius for a sphere enclosed in a regular tetragon of touching spheres of radius r is $\left(\frac{\sqrt{3}}{2}-1\right)\cdot r \approx 0.22474\cdot r$.

Consider four touching spheres of equal radius r arranged in a tetragon, at positions A, B, C, D (see figure 129).

We wish to know the maximum radius of sphere that can be enclosed in such a tetragon of spheres. i.e. we first need to know the location G of the centre of such a sphere.

First consider the triangle ABC at the base of the tetragon (see figure 130).

We drop normal from C onto AB at E ; by symmetry this must intersect the normals from A, B at F ; we wish to find F .

If we consider triangle CEB , we see that we have inter-column spacing $AB = a = 2\cdot r$, and that by Pythagoras the inter-row spacing $CE = b = \sqrt{3}\cdot r$.

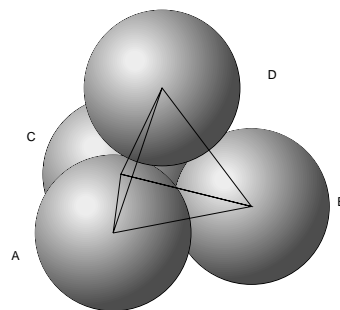


Figure 129: A regular tetragon of spheres.

We then have :

$$\begin{aligned}
 p + q &= \sqrt{3} \cdot r \\
 q^2 + r^2 &= p^2 \\
 &= (\sqrt{3} \cdot r - q)^2 \\
 \therefore q^2 &= 3 \cdot r^2 - 2 \cdot \sqrt{3} \cdot r \cdot q + q^2 - r^2 \\
 \therefore q &= \frac{1}{\sqrt{3}} \cdot r \\
 \therefore p &= \frac{2}{\sqrt{3}} \cdot r
 \end{aligned}$$

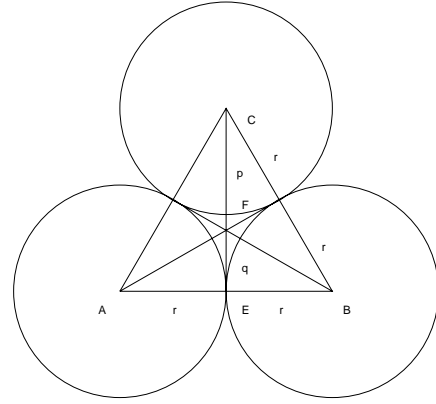


Figure 130:

Hence for A at $(-r, 0, 0)$, B at $(r, 0, 0)$, then C is at $(0, \sqrt{3} \cdot r, 0)$ and F is at $(0, \frac{1}{3} \cdot r, 0)$.

Triangle ABC : base of tetragon.

We note that by symmetry the line from the point G that we seek to F must be normal to the plane ABC , therefore we may draw figure 131.

We consider triangle ADF ; we have shewn that the distance $AF = p = \frac{2}{\sqrt{3}} \cdot r$, hence by Pythagoras the inter-layer spacing $FD = c = 2 \cdot \frac{\sqrt{2}}{3} \cdot r$.

We wish to determine the position of G ; i.e. we wish to position G so that triangle GAD is equilateral and thus $t = s$; we then have :

$$\begin{aligned}
 t &= s \\
 c &= s + h \\
 t^2 &= p^2 + h^2 \\
 \therefore p^2 + h^2 &= (c - h)^2 \\
 &= c^2 - 2 \cdot c \cdot h + h^2 \\
 \therefore h &= \frac{1}{2} \cdot \left(c - \frac{p^2}{c} \right) \\
 &= \frac{1}{\sqrt{6}} \cdot r \\
 \therefore s &= \frac{\sqrt{3}}{\sqrt{2}} \cdot r
 \end{aligned}$$

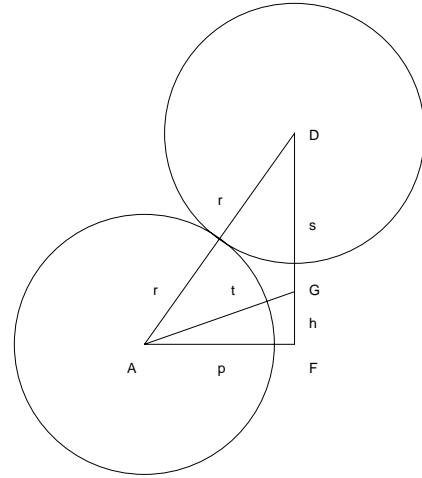


Figure 131: Side view of tetragon, with triangle ADF .

Hence G is at $(0, \frac{1}{\sqrt{3}} \cdot r, \frac{1}{\sqrt{6}} \cdot r)$, and it is at a distance $(\frac{\sqrt{3}}{\sqrt{2}} - 1) \cdot r \approx 0.22474 \cdot r$ from the enclosing spheres.

In chapter 17.3 we use the ratio $\frac{s}{r}$ as the parameter β for an HCP lattice.

Using *Apl* to check numerically that we have found the correct position :

We have for the tetragon *ABCD*:

$$+ \text{Tetragon} \leftarrow 4 \ 3 \ \rho \ -1 \ 0 \ 0 \ 1 \ 0 \ 0 \ 0, (3^* \div 2), 0 \ 0, (\div 3^* \div 2), 2 \times (2 \div 3)^* \div 2$$

$$\begin{array}{r} -1 \ 0 \quad 0 \\ 1 \ 0 \quad 0 \\ 0 \ 1.73205 \ 0 \\ 0 \ 0.57735 \ 1.63299 \end{array}$$

and for *G*:

$$+ G \leftarrow 0, (\div 3^* \div 2), (\div 6)^* \div 2$$

$$0 \ 0.57735 \ 0.408248$$

Thus we may calculate the vector lengths from *G* to each of *A, B, C, D*:

$$(+ / (\text{Tetragon} - [2] \ G)^* 2)^* \div 2$$

$$1.22474 \ 1.22474 \ 1.22474 \ 1.22474$$

We have thus confirmed that we have found the position we want, and the maximum radius of the sphere that just touches the other four is $\left(\left(\frac{3}{2} \right)^{\frac{1}{2}} - 1 \right) \cdot r \approx 0.22474 \cdot r$.

Appendix I

Volume of a cap of a sphere.

We require the volume of the cap of a sphere, as part of the calculation of the total void volume for intersecting spherical voids.

Consider a sphere, of radius R , centered on the origin O . We wish to know the volume of the sphere to the right of a plane parallel to the $x = 0$ plane, through $x = X$.

The sphere intersects the $z = 0$ plane, and traces out a circular locus, which we can represent in the first quadrant by $y^2 = R^2 - x^2$ (figure 132).

If we cut through the cap with two planes parallel to it's base, at x , $x + \delta x$, the enclosed slice will have a radius of

$$y = (R^2 - x^2)^{1/2}$$

and a volume of

$$\delta V = \pi y^2 \cdot \delta x$$

Hence the volume of the cap to the right of X is

$$\begin{aligned} V &= \int_X^R \pi y^2 dx \\ &= \pi \int_X^R (R^2 - x^2) dx \\ &= \pi \left[R^2 \cdot x - \frac{1}{3} x^3 \right]_X^R \\ &= \pi \left(\frac{2}{3} R^3 - R^2 \cdot X + \frac{1}{3} X^3 \right) \\ &= \frac{\pi}{3} \left(2 \cdot R^3 - 3 \cdot R^2 \cdot X + X^3 \right) \\ &= \frac{\pi}{3} (2 \cdot R + X) \cdot (R - X)^2 \end{aligned}$$

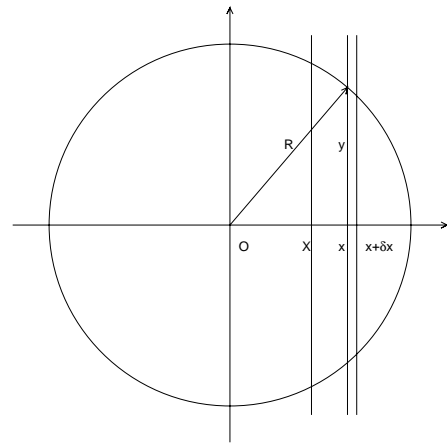


Figure 132: Geometry of slice δx , for the integration of the cap of a sphere.

Appendix J

Surface area of a cap of a sphere.

We require the surface area of the cap of a sphere, as part of the derivation of an analytic expression for the $G(R)$ of an infinite slab.

Consider a sphere, of radius R , centered on the origin O . We wish to know the surface area of the sphere to the right of a plane parallel to the $x = 0$ plane, through $x = X$. The sphere intersects the $z = 0$ plane, and traces out a circular locus, which we can represent in the first quadrant by $y^2 = R^2 - x^2$ (figure 133).

If we cut through the cap with two planes parallel to its base, at x , $x + \delta x$, the enclosed ribbon will have a radius of

$$y = (R^2 - x^2)^{1/2}$$

and a surface area of

$$\delta S = 2\pi y \cdot (\delta x^2 + \delta y^2)^{1/2}$$

We have

$$\begin{aligned} dy &= (1/2) \cdot (R^2 - x^2)^{-1/2} \cdot (-2 \cdot x) dx \\ &= \frac{-x}{(R^2 - x^2)^{1/2}} dx \\ \therefore dy^2 &= \frac{x^2}{R^2 - x^2} dx^2 \\ &= \frac{x^2}{y^2} dx^2 \end{aligned}$$

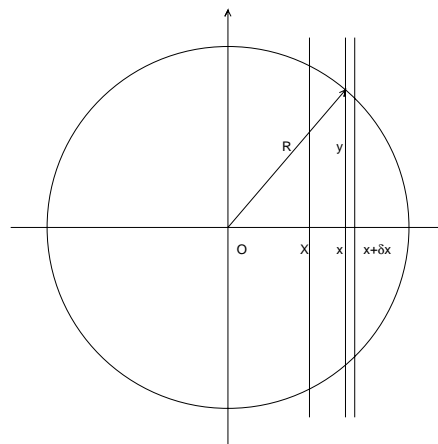


Figure 133: Geometry of slice δx , for the integration of the cap of a sphere.

Hence the surface area of the cap to the right of $X =$

$$\begin{aligned}
 S &= \int_X^R 2\pi y \cdot \left(\frac{dx^2 + dy^2}{dx^2}\right)^{1/2} dx \\
 &= 2\pi \int_X^R (R^2 - x^2)^{1/2} \cdot \left(1 + \frac{x^2}{R^2 - x^2}\right)^{1/2} dx \\
 &= 2\pi \int_X^R y \cdot \left(1 + \frac{x^2}{y^2}\right)^{1/2} dx
 \end{aligned}$$

Since we know that R , y and δS are real and positive, we may simplify this to :

$$\begin{aligned}
 S &= 2\pi \int_X^R R dx \\
 &= 2\pi R(R - X)
 \end{aligned}$$

In conclusion, we may note that if the sphere is located at $x = X_0$, the surface area of the cap, =

$$\begin{aligned}
 S &= 2\pi R(R - (X - X_0)) \\
 &= 2\pi R(R + X_0 - X)
 \end{aligned}$$

Appendix K

Analytic derivation of $G(\mathbf{r})$ for a uniform solid sphere.

We use analytically calculable $\gamma_0(r)$ for a sphere as a model system for scattering from pores, and as a check of our calibration when converting from q to r . The expected fall off in $g(r)$ due to a spherical test volume having a limited radius R is calculable analytically, and is just $\gamma_0(r)$ for a sphere. Thus we reproduce the standard derivation.

K.1 Effect on $g(\mathbf{r})$ of finite sample volume.

We place a test point at distance x from the centre of our sphere of radius R , and consider a spherical region around it of radius r ; we wish to know what proportion of the secondary test points on the surface at r fall within sphere radius R .

There are three cases for the function $F(r, R, x)$:

- 1) For all points $r < (R-x)$, all points on sphere surface of radius r will fall inside sphere radius R , $\therefore F(r, R, x) = 1$
- 2) For all points $r > (R+x)$, no points on sphere surface of radius r will fall inside sphere radius R , $\therefore F(r, R, x) = 0$
- 3) For all points $(R-x) < r < (R+x)$, a fraction of the surface of sphere of radius r will fall within sphere of radius R , and is given by [Steytler et al., 1983a] :

$$F(r, R, x) = 1/2 \cdot \left(1 - \frac{x^2 + r^2 - R^2}{2 \cdot x \cdot r} \right)$$

Integrating over all the values of x between $x=0$ and $x=R$, we get :

$$\gamma_0(r) = F(r, R) = 1 - \frac{3}{4} \cdot \left(\frac{r}{R}\right) + \frac{1}{16} \cdot \left(\frac{r}{R}\right)^3$$

Dividing the calculated $g(r)$ for a sphere of radius R by $F(r, R)$ will give a better approximation to $g(r)$ for an infinite volume, though of course we must truncate the representation at $r < 2 \times R$, for practical signal to noise limitations.

Note: this modification of the calculated $g(r)$ applies only to initial test calculations in this study. The main work was performed inside infinite lattices, using defined distributions of radial distances.

Appendix L

Calculation of $G(r)$ for an infinite slab.

Calculations of $G(r)$ for porous media show a rapid fall off at small radii from an initial value of unity. We can understand this behaviour if we approximate the geometry in and close to a pore wall as an infinite plane, with geometric effects due to wall curvature and pore lattice spacing only taking place at larger radii.

We wish to analytically calculate the form of $G(r)$ for an infinite slab, of thickness t and of unit density between $z = +T$, $z = -T$. We will in the process generate a semi-analytic description to aid our understanding (and act as a check), and compare these results with a Monte-Carlo calculation.

Consider a sphere of radius R , whose centre is at O , and lies within the slab, but distance Z from the $z = 0$ plane. We wish to know what fraction, ρ , of the surface of the sphere is embedded in the slab, as a function of R and of Z : i.e we wish to know $\rho(R,Z)$, for $0 \leq R < \infty$, $-T \leq Z \leq +T$.

With reference to figure 134, we can see that we have three main cases :

- 1) $R + |Z| \leq T$: $R \leq T - |Z|$: all embedded, $\rho = 1$
- 2) $R + |Z| \geq T$: $T - |Z| \leq R \leq T + |Z|$: a hemisphere imbedded.
 $R - |Z| \leq T$
- 3) $R - |Z| \geq T$: $R \geq T + |Z|$: sphere straddles slab.

In appendix J, we derive an expression for the surface area of the cap of a sphere; thus for case 3, when both hemispheres, (upper and lower), are only partly embedded in the slab, the surface area not in the slab =

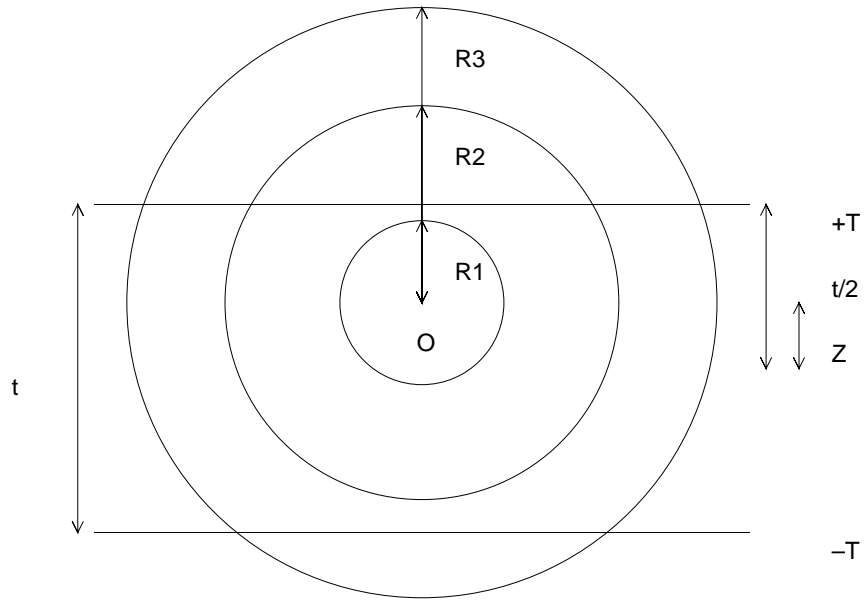


Figure 134: Intersection of a sphere with a plane slab.

$$S_u = 2\pi R(R + Z - T)$$

$$S_l = 2\pi R(R - Z - T)$$

Hence the fraction of the sphere embedded in the slab =

$$\begin{aligned} \rho &= \frac{4\pi R^2 - (S_u + S_l)}{4\pi R^2} \\ &= \frac{4\pi R^2 - 2\pi R \cdot (2R - 2T)}{4\pi R^2} \\ &= \frac{4\pi \cdot R \cdot T}{4\pi R^2} = \frac{T}{R} = \frac{t}{2 \cdot R} \end{aligned}$$

Thus we have the slightly surprising result that provided the sphere straddles the slab, the surface area inside the slab is independent of the Z position, and only depends on the ratio of the thickness of the slab to the radius R .

We can check this by generating 10^4 points on the surface of a sphere, using von Neuman's method [Powles, 1994], and causing the sphere to traverse a slab, while calculating the fraction of the points that fall within the slab (figure 135).

Sphere of radius 4 traversing a slab of width 2

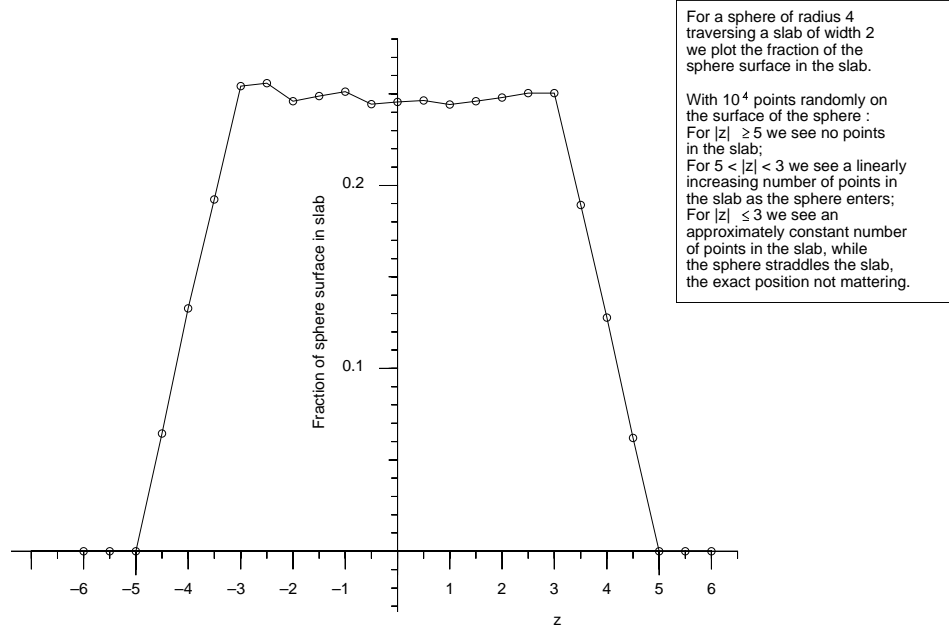


Figure 135: Confirmation that $G(r)$ is constant for a sphere straddling a slab.

Before treating the other cases in detail, we will note that at the point a hemisphere just touches the surface, the area of the hemisphere in the slab $= 2\pi R^2$, and is the same as the area when that hemisphere is fully embedded in the slab.

Thus we may write an expression for $\rho(R, Z)$ that covers all the above cases, (using the *floor* function \lfloor , that just returns the lower of its two arguments) :

$$\begin{aligned} \rho(R, Z) &= \frac{4\pi R^2 - ((2\pi R^2) \lfloor (S_u) + (2\pi R^2) \lfloor (S_l))}{4\pi R^2} \\ &= \frac{4\pi R^2 - ((2\pi R^2) \lfloor (2\pi R \cdot (R + Z - T)) + (2\pi R^2) \lfloor (2\pi R \cdot (R - Z - T)))}{4\pi R^2} \\ &= \frac{1}{2} \cdot \left(1 \lfloor \frac{T - Z}{R} + 1 \lfloor \frac{T + Z}{R} \right) \end{aligned}$$

This defines a surface in two dimensions; we may plot it as an aid to understanding the regions we have to consider to derive a fully analytic expression for $G(R)$ (figure 136). To calculate the solid-solid radial density distribution, we need to calculate the average value of the above function for all possible sphere centres within the slab (this is effectively the correlation of $\rho(R, 0)$ with the top-hat density profile of the slab) :

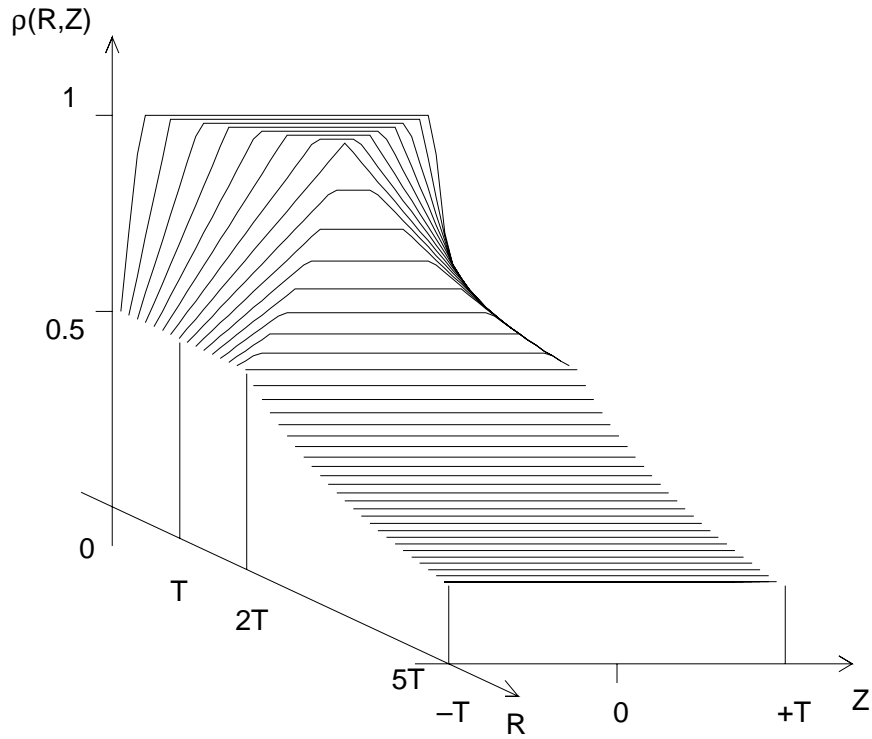


Figure 136: Integration surface for $\rho(R,Z)$ for $G(r)$ for a slab.

$$\begin{aligned}
 G(R) &= \frac{\int_{-T}^{+T} \rho(R, Z) dZ}{\int_{-T}^{+T} dZ} \\
 &= \frac{1}{2T} \int_{-T}^{+T} \rho(R, Z) dZ \\
 &= \frac{1}{4T} \int_{-T}^{+T} \left[1 - \frac{T-Z}{R} + 1 - \frac{T+Z}{R} \right] dZ
 \end{aligned}$$

We may readily evaluate this integral numerically; this is plotted in figure 137.

However we wish for an analytic expression for $G(R)$.

Returning to case 3), we have $R \geq T + |Z|$, where $|Z|$ has a maximum value of T .

Therefore,

For $R \geq 2T = t$:

$$G(R) = \frac{\int_{-T}^{+T} \frac{T}{R} dZ}{\int_{-T}^{+T} dZ} = \frac{T}{R} = \frac{t}{2R}$$

which is seen to be in agreement with the the numerical integration in figure 137.

For $R \leq T = t/2$,

we see with reference to figure 136 that the integral for $G(R)$ is a combination of case 1) and the two parts of case 2).

We have for case 1) : $R \leq T - |Z|$, i.e. $|Z| \leq T - R$,

$\therefore -(T - R) \leq Z \leq T - R$, while $\rho(R, Z) = 1$.

We have for case 2) :

$R \leq T + |Z|$, i.e. $|Z| \geq R - T$,

$\therefore -T \leq Z \leq -(T - R)$, while $\rho(R, Z) = \frac{R+T+Z}{2R}$

and

$T - R \leq Z \leq +T$, while $\rho(R, Z) = \frac{R+T-Z}{2R}$.

$$\begin{aligned} \therefore G(R) &= \frac{1}{2T} \cdot \left(\int_{Z=-T}^{Z=-(T-R)} \frac{R+T+Z}{2R} dZ + \int_{Z=-(T-R)}^{Z=T-R} 1 dZ + \int_{Z=T-R}^{Z=+T} \frac{R+T-Z}{2R} dZ \right) \\ &= \frac{1}{2T} \cdot \left(\frac{1}{2R} \cdot \left[R \cdot Z + T \cdot Z + \frac{1}{2} \cdot Z^2 \right]_{-T}^{-T+R} + [Z]_{-T+R}^{T-R} + \frac{1}{2R} \cdot \left[R \cdot Z + T \cdot Z - \frac{1}{2} \cdot Z^2 \right]_{T-R}^T \right) \\ &= \frac{1}{2T} \cdot \left(\frac{3}{4} \cdot R + 2 \cdot (T - R) + \frac{3}{4} \cdot R \right) \\ &= 1 - \frac{1}{4} \cdot \frac{R}{T} = 1 - \frac{1}{2} \cdot \frac{R}{t} \end{aligned}$$

For $T \leq R \leq 2T = t$,

we see that the integral for $G(R)$ is a combination of case 3) and the two parts of case 2).

We have for case 3) : $R \geq T + |Z|$, i.e. $|Z| \leq R - T$,

$\therefore -(R - T) \leq Z \leq R - T$, while $\rho(R, Z) = T/R$,

and again for case 2) :

$R \leq T + |Z|$, i.e. $|Z| \geq R - T$,

however, since $R > T$ and $|Z| \leq 1$, the limits interchange : $-T \leq Z \leq -(R - T)$, while

$\rho(R, Z) = \frac{R+T+Z}{2R}$,

and

$R - T \leq Z \leq +T$, while $\rho(R, Z) = \frac{R+T-Z}{2R}$.

$$\begin{aligned}
\therefore G(R) &= \frac{1}{2T} \cdot \left(\int_{Z=-T}^{Z=-(R-T)} \frac{R+T+Z}{2R} dZ + \int_{Z=-(R-T)}^{Z=R-T} \frac{T}{R} dZ + \int_{Z=R-T}^{Z=+T} \frac{R+T-Z}{2R} dZ \right) \\
&= \frac{1}{2T} \cdot \left(\frac{1}{2R} \cdot \left[R \cdot Z + T \cdot Z + \frac{1}{2} \cdot Z^2 \right]_{-T}^{-R+T} + \frac{T}{R} \cdot [Z]_{-R+T}^{R-T} + \frac{1}{2R} \cdot \left[R \cdot Z + T \cdot Z - \frac{1}{2} \cdot Z^2 \right]_{R-T}^T \right) \\
&= \frac{1}{2T} \cdot \left(\left(-\frac{1}{4} \cdot R + \frac{T^2}{R} \right) + 2 \cdot \left(T - \frac{T^2}{R} \right) + \left(-\frac{1}{4} \cdot R + \frac{T^2}{R} \right) \right) \\
&= 1 - \frac{1}{4} \cdot \frac{R}{T} = 1 - \frac{1}{2} \cdot \frac{R}{t}
\end{aligned}$$

Thus in summary, for $r \leq 2T = t$, we obtain a linear profile for $G(r)$, with a slope of $-\frac{1}{2t}$. This can be seen to be consistent with the numerical integration in figure 137.

Such a triangular function is characteristic of the correlation function of two top-hat functions; it is slightly surprising to obtain it for a sphere and a slab.

For $r \geq 2T = t$, we obtain an inverse linear profile for $G(r) = \frac{t}{2r}$, as approximately might be expected for a sphere of surface area $\propto R^2$ intersecting a slab with a cross-section $\propto R$.

Finally we perform a Monte-Carlo integration (chapter 15) for 10^9 radial evaluations, and plot this as points on figure 137, which shows good agreement with the other two methods.

Calculated G(R) for an infinite plane slab

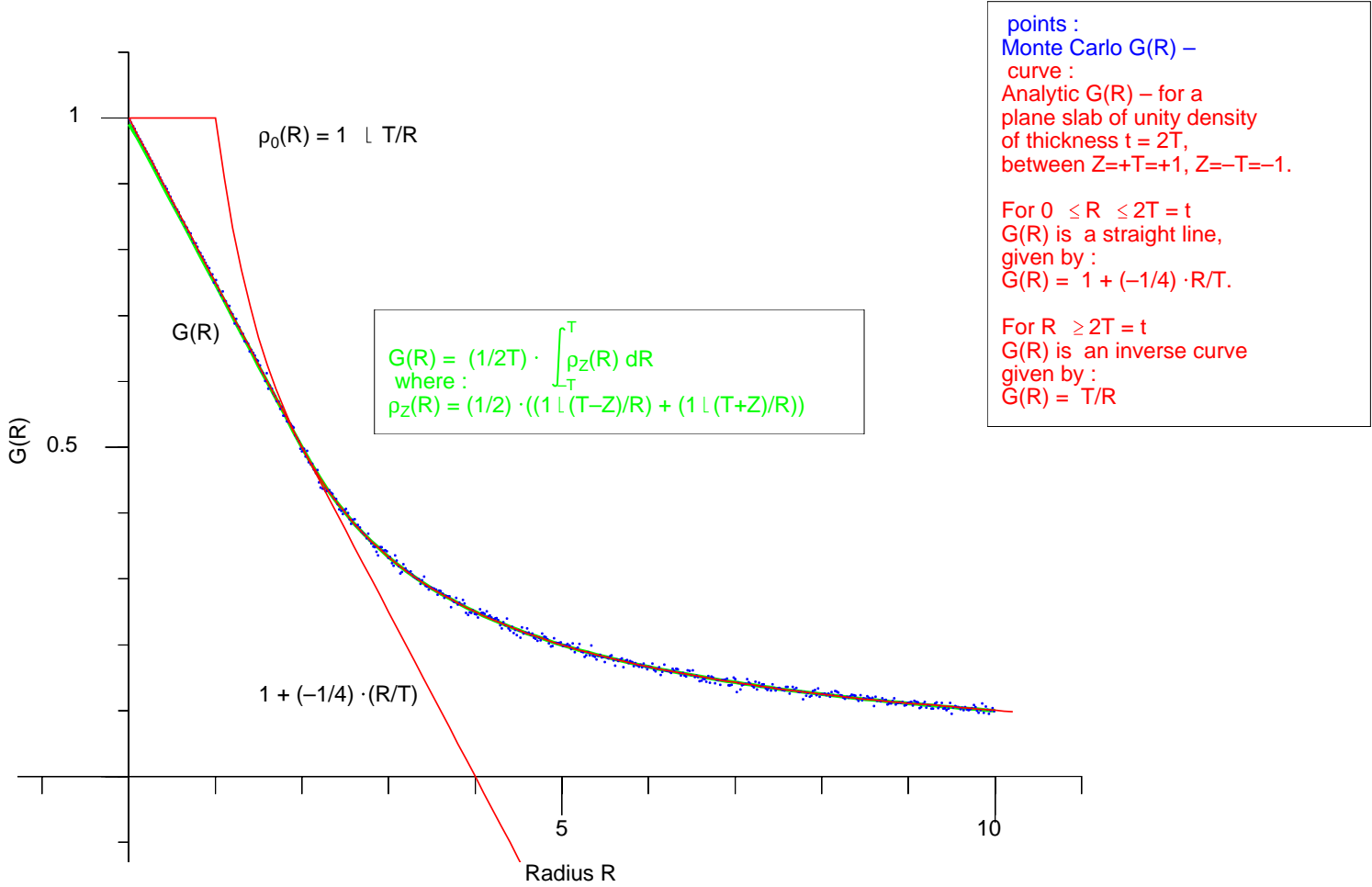


Figure 137: G(r) for an infinite plane slab, calculated by numerical integration, Monte-Carlo integration, and analytic integration.

Appendix M

I(q) to G(r) transformations for standard forms.

We calculate $G(r)$ analytically (using the algebraic language *Maple*) for the standard neutron scattering $I(q)$ functions : Guinier (Gaussian), Porod (q^{-4}), Ornstein-Zernike (Lorentzian), Guinier-Porod (Lorentzian²), and for the porous media form of *sech*.

M.1 q domain to r domain transformation.

In section 12.2 we have the relationship for the solid-solid density correlation function

$\gamma(r)$:

$$\gamma(r) = \rho_{\infty} \cdot (G(r) - 1) = -i \cdot \frac{1}{4\pi^2 \cdot r} \cdot \int_{-\infty}^{\infty} q \cdot I(q) \cdot e^{i \cdot q \cdot r} dq$$

Thus we may use the algebraic language *Maple* to readily obtain the following expressions for $\gamma(r)$. We plot $I(q)$ and $\gamma(r)$ in figure 138.

M.1.1 Guinier : I(q) Gaussian.

For a Gaussian of the form :

$$I(q) = e^{-\frac{q^2}{2\sigma^2}}$$

we obtain the Gaussian

$$\gamma(r) = \frac{1}{2\pi\sqrt{(2\pi)}} \cdot \sigma^3 \cdot e^{-\frac{\sigma^2 \cdot r^2}{2}}$$

If we write the Guinier equation in the form :

$$I(q) = e^{-\frac{q^2}{Q_0^2}}$$

we obtain the Gaussian

$$\gamma(r) = \frac{1}{8\pi\sqrt{\pi}} \cdot Q_0^3 \cdot e^{-\left(\frac{Q_0 \cdot r}{2}\right)^2}$$

M.1.2 Ornstein-Zernike : I(q) Lorentzian.

If we write the Ornstein-Zernike expression in the form :

$$I(q) = \frac{1}{1 + \frac{q^2}{Q_0^2}}$$

where the correlation length = $\xi = \frac{1}{Q_0}$, we obtain the symmetric bi-exponential \times inverse r function :

$$\gamma(r) = \frac{Q_0^2}{4\pi \cdot r} \cdot \left(\mathcal{H}(r) \cdot e^{-Q_0 \cdot r} - \mathcal{H}(-r) \cdot e^{Q_0 \cdot r} \right)$$

where $\mathcal{H}(x)$ is the Heaviside function, such that

$$\begin{aligned} x < 0 : \quad \mathcal{H}(x) &= 0 \\ x = 0 : \quad \mathcal{H}(x) &\text{ is undefined} \\ x > 0 : \quad \mathcal{H}(x) &= 1 \end{aligned}$$

M.1.3 Guinier-Porod : I(q) Lorentzian squared.

If we write the Guinier-Porod expression in the form :

$$I(q) = \left(\frac{1}{1 + \frac{q^2}{Q_0^2}} \right)^2$$

we obtain the symmetric bi-exponential function :

$$\gamma(r) = \frac{Q_0^3}{8\pi} \cdot \left(\mathcal{H}(r) \cdot e^{-Q_0 \cdot r} - \mathcal{H}(-r) \cdot e^{Q_0 \cdot r} \right)$$

M.1.4 Porod : $I(q)$ inverse quartic q .

If we write the Porod expression in the form :

$$I(q) = \left(\frac{q}{Q_0}\right)^{-4}$$

we obtain the symmetric linear function :

$$\gamma(r) = -\frac{Q_0^4 \cdot r}{8\pi} \cdot (\mathcal{H}(r) - \mathcal{H}(-r))$$

Since this function is always non-positive it is only physical as a modifier of some other function with a finite $\gamma(r)$.

M.1.5 Porous media : $I(q)$ sech.

Up to the point where there is a q^{-4} departure, the $I(q)$ for porous media is well described by an $I(q)$ with the form :

$$I(q) = \operatorname{sech}\left(\frac{q}{Q_0}\right) = \frac{2}{e^{-\frac{q}{Q_0}} + e^{\frac{q}{Q_0}}}$$

It is possible to show that the Fourier transform of sech is another sech [Powles, 1972-1999, discussions], [Evans, 1972-1999, discussions], appendix R. We may then configure *Maple* so that it knows this relationship, see appendix R.

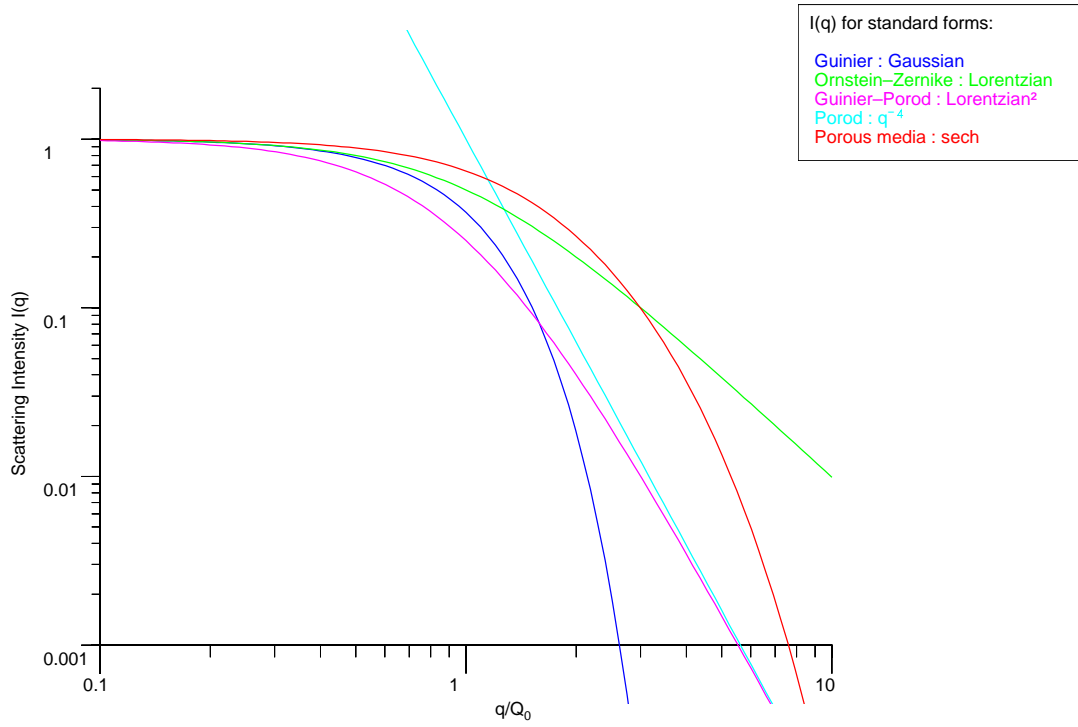
We then obtain the symmetric function :

$$\begin{aligned} \gamma(r) &= \frac{Q_0^2}{8 \cdot r} \cdot \sinh\left(\frac{\pi Q_0 \cdot r}{2}\right) \cdot \left(\operatorname{sech}\left(\frac{\pi Q_0 \cdot r}{2}\right)\right)^2 \\ &\approx \frac{\pi Q_0^3}{16} \cdot \left(1 - \frac{1}{3} \cdot \theta^2 + \frac{1}{8} \cdot \theta^4 - \frac{31}{560} \cdot \theta^6 + \dots\right) \cdot \operatorname{sech}(\theta) \end{aligned}$$

where $\theta = \frac{\pi Q_0 \cdot r}{2}$.

i.e. $\gamma(r)$ is thus sech like, particularly at small θ .

$I(q)$ for standard scattering functions.



$\gamma(r)$ for standard scattering functions.

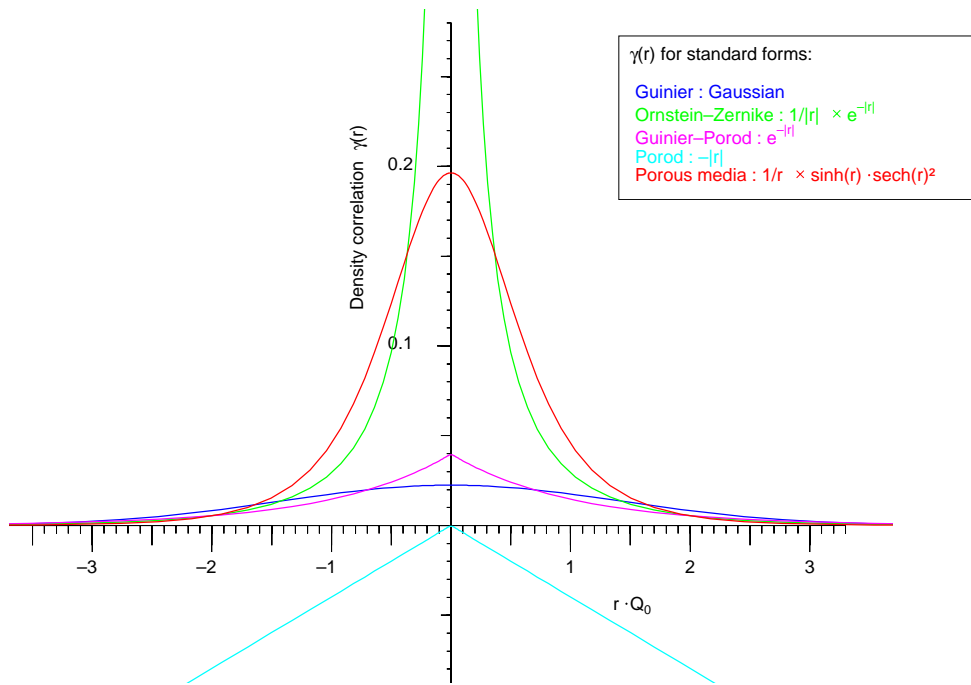


Figure 138: $I(q)$, $\gamma(r)$ for various standard forms.

Appendix N

Angular fall-off in measured intensity due to a flat detector.

Neutrons scattered at a large angle onto a flat detector will be spread over a larger detector area than those scattered through a smaller angle. We calculate this geometric fall off in intensity, and compare it with the measured fall-off. The agreement is quite reasonable, but in practice we find we need to measure the fall-off at each detector position using a water sample.

With reference to figure 139 we place a scattering sample at O , distance D from a flat detector. Neutrons scattered at angle θ_s will impinge on the detector at A , a radial distance x , where :

$$x = D \cdot \tan(\theta_s)$$

Thus we may immediately conclude that a infinitesimal width of scattering $d\theta_s$ will be spread over

$$\begin{aligned} dx &= D \cdot d \tan(\theta_s) ds \\ &= D \cdot (1 + \tan^2(\theta_s)) ds \end{aligned}$$

We may confirm this geometrically, by considering neutrons scattered at angle $\theta_s + \Delta\theta_s$, which will impinge on the detector at B , a radial distance $x + \Delta x$. If we drop perpendicular AP onto OB , we see that it has length $R \cdot \sin(\Delta\theta_s)$. Hence

$$\Delta x = \frac{R \cdot \sin(\Delta\theta_s)}{\cos(\theta_s + \Delta\theta_s)}$$

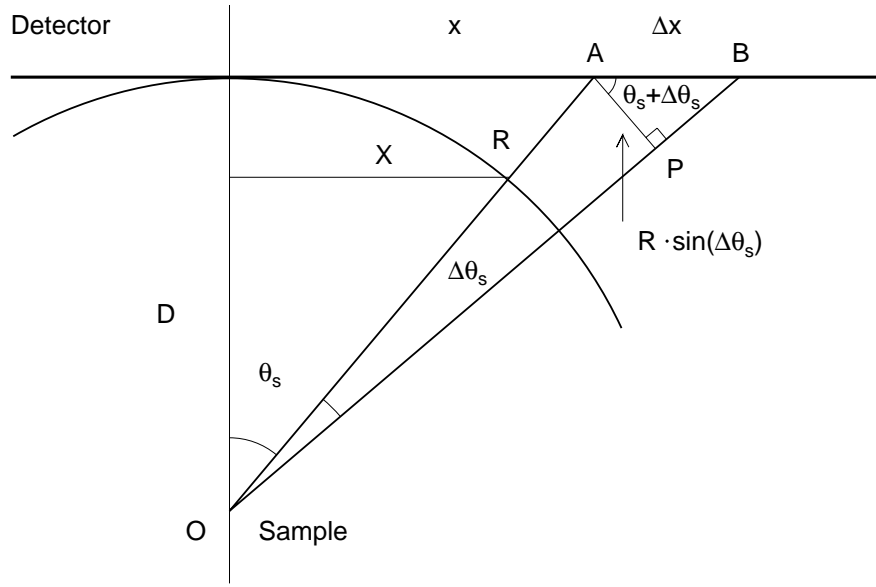


Figure 139: Angled scattering onto a flat detector.

$$\begin{aligned}
 &= \frac{D \cdot \sin(\Delta\theta_s)}{\cos(\theta_s) \cdot \cos(\theta_s + \Delta\theta_s)} \\
 \therefore dx &\approx \frac{D}{\cos^2(\theta_s)} d\theta_s
 \end{aligned}$$

Simple application of Pythagoras shows these two answers to be the same.

However we have a second effect to consider, in that AB will trace out an annulus of radius $x + \frac{\Delta x}{2}$, such that the area on the plane detector is

$$\begin{aligned}
 \Delta A_p &= \frac{\pi}{2} \cdot \left(D \cdot \tan(\theta_s) + \frac{\Delta x}{2} \right) \cdot \Delta x \\
 \therefore dA_p &\approx \frac{\pi}{2} \cdot D \cdot \tan(\theta_s) \cdot \frac{D}{\cos^2(\theta_s)} d\theta_s
 \end{aligned}$$

However if we consider the projected area on a sphere of radius D, we see that this will trace out an annulus of radius $X + \frac{\Delta X}{2}$, of area

$$\begin{aligned}
 \Delta A_s &= \frac{\pi}{2} \cdot (D \cdot \sin(\theta_s) + D \cdot \sin(\theta_s + \Delta\theta_s)) \cdot D \cdot \Delta\theta_s \\
 &= \frac{\pi}{2} \cdot D^2 \cdot \left(\sin(\theta_s) + \frac{1}{2} \cdot \cos(\theta_s) \cdot \Delta\theta_s \right) \cdot \Delta\theta_s \\
 \therefore dA_s &\approx \frac{\pi}{2} \cdot D^2 \cdot \sin(\theta_s) d\theta_s
 \end{aligned}$$

The larger $\frac{\Delta A}{\Delta\theta_s}$ the more pixels the scattering is spread over, and hence the lower the

measured intensity in any particular pixel. Thus we conclude that the measured intensity for a uniform scattering will fall-off as

$$\begin{aligned}\frac{dA_s}{dA_p}(\theta_s) &= \frac{\sin(\theta_s) \cdot \cos^2(\theta_s)}{\tan(\theta_s)} \\ &= \cos^3(\theta_s)\end{aligned}$$

We compare this with the measured fall-off for water with the detector at 1.43m (offset 350mm) in figure 141. The agreement is quite reasonable at all angles, but is not exact. In practice a symmetric quartic polynomial $\wp^4(\theta) = \alpha + \beta \cdot \theta^2 + \gamma \cdot \theta^4$ was used to approximate the fall-off behaviour of water and the geometric fall-off calculated with allowance for the angled attenuation due to a thick sample (see appendix O). We then write

$$Geom(\theta_s) = \frac{\wp^4(\theta_s)}{Atten(\theta_s)}$$

Appendix O

Attenuation due to angled scattering in a thick sample.

Neutrons scattered at an angle in a thick sample will have a longer path length in the sample, and will suffer increased attenuation. We calculate this using a simple single-scattering/attenuation model.

For neutrons in an adsorbing or scattering medium, the direct path beam will be attenuated; for a $1/e^{\text{th}}$ attenuation path length = P_e we have :

$$I(x) = I_0 \cdot e^{-\frac{x}{P_e}}$$

For distilled water in a 1mm thick Helma cell we have for $\lambda = 12\text{\AA}$ neutrons

$$\frac{I(x = 1\{\text{mm}\})}{I(0)} = 0.414$$

$$\therefore P_e = -\frac{1\{\text{mm}\}}{\ln 0.414} = 1.133 \{\text{mm}\}$$

For a flat slab sample of thickness t , we consider those (attenuated) neutrons that travel a distance x and then suffer a scattering through angle $\theta_s = 2 \cdot \theta_{\text{Bragg}}$. We treat the effects of all further scatterings from this ensemble as though they were an attenuation due to the remaining path length l_r .

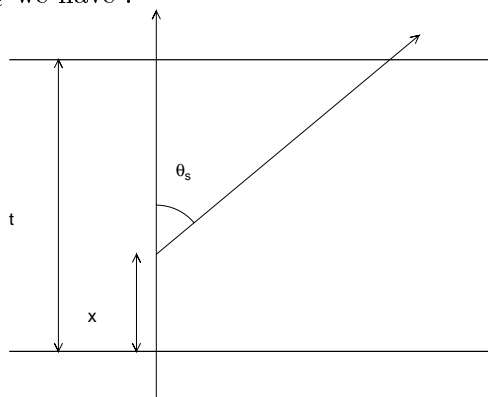


Figure 140: Angled scattering through a thick sample.

Thus the total path length in the medium is given by (see figure 140)

$$l(x, \theta_s) = x + \frac{t-x}{\cos(\theta_s)}$$

$$\therefore I(x, \theta_s) = I_0 \cdot e^{-\frac{1}{P} \cdot \left(x + \frac{t-x}{\cos(\theta_s)}\right)}$$

Hence, averaging over all x we obtain :

$$\begin{aligned} \therefore \text{average } Ln \left(\frac{I(\theta_s)}{I_0} \right) &= \frac{-\frac{1}{P_e} \cdot \int_{x=0}^{x=t} \left(x + \frac{t-x}{\cos(\theta_s)}\right) dx}{\int_{x=0}^{x=t} 1 dx} \\ &= -\frac{1}{t \cdot P_e} \cdot \int_{x=0}^{x=t} \left(\frac{t}{\cos(\theta_s)} + x \cdot \left(1 - \frac{1}{\cos(\theta_s)}\right) \right) dx \\ &= -\frac{1}{t \cdot P_e} \cdot \left[\frac{t \cdot x}{\cos(\theta_s)} + \frac{1}{2} \cdot x^2 \cdot \left(1 - \frac{1}{\cos(\theta_s)}\right) \right]_0^t \\ &= -\frac{1}{t \cdot P_e} \cdot \left(\frac{t^2}{\cos(\theta_s)} + \frac{1}{2} \cdot t^2 \cdot \left(1 - \frac{1}{\cos(\theta_s)}\right) \right) \\ &= -\frac{t}{2 \cdot P_e} \cdot \left(1 + \frac{1}{\cos(\theta_s)}\right) \end{aligned}$$

Thus for a sample of thickness t and for

EC_{T,S} : Empty Cell (Transmission, Scattering)

S_{T,S} : Sample (Transmission, Scattering)

we obtain for the $1/e^{th}$ path length

$$P_e = -\frac{t}{Ln \left(\frac{S_T}{EC_T} \right)}$$

and a normalised angular fall off in S_S due to angled path length variation in the thick sample :

$$Atten(\theta_s) = \frac{EC_T}{S_T} \cdot e^{-\frac{t}{2 \cdot P_e} \cdot \left(1 + \frac{1}{\cos(\theta_s)}\right)}$$

Although not exact this is a reasonable first approximation, given that even for water the maximum loss of intensity on D22 is not large (see figure 141).

Water : $\text{Geom}(\theta_s)$ and $\text{Atten}(\theta_s)$.

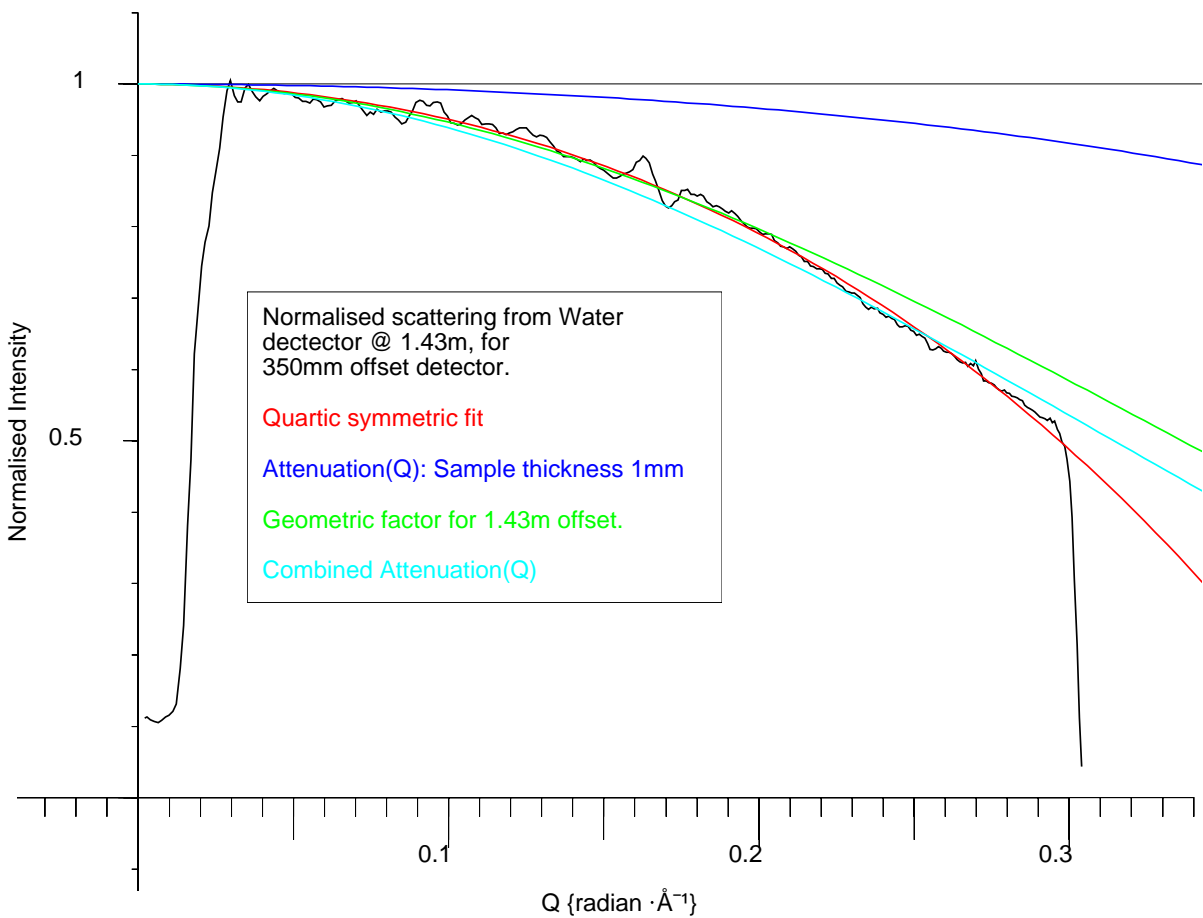


Figure 141: D22 (1.43m offset detector) measured fall-off in nominally flat water scattering from 1mm thick water sample, plotted with symmetric quartic fit and calculated geometric fall-off $\text{Geom}(\theta_s)$ and angled attenuation $\text{Atten}(\theta_s)$.

Appendix P

Fourier transformation of measured $I(q)$ results to $G(r)$, of calculated $G(r)$ to $I(q)$.

P.1 $I(q)$ to $G(r)$.

Generating suitable data for transformation.

We see in chapter 12 that we may use a Fourier transform to convert $qI(q)$ data to $r\gamma(r)$ data. We wish to use a Fast Fourier Transform for efficiency reasons, and this needs equally spaced data for $0 \leq q \leq Q_{max}$, whereas the data from the area detector at different detector distances is not equally spaced; further, data near $q = 0$ is missing. First we note that for the measured scattering from the sol-gel silicas the low q data is well fitted by a Guinier (Gaussian) approximation (see chapter 12). Such fits were made, and the low q data that could not be measured around the beam-stop at 18m re-created.

At high q the hydrogen subtracted data for the scattering from the pores drops with an approximately q^4 falloff at high q (see figures 99, 100, 101). The linear part of these log-log data sets were straight line fitted, and extrapolated to an arbitrary q_{max} of $1\{\text{radian}\cdot\text{\AA}^{-1}\}$, to obtain good resolution in the spatial domain.

Since the expected scattering from pores at large q falls monotonically, we neglect the atomic scattering to obtain a form that is effectively $P(q)$ for the pores.

The scattering data was then fitted in the log-log domain by a five part quartic piecewise polynomial. i.e. five polynomials $\wp^4_{1..5}(q)$ each constrained to be continuous at

the four break-points in amplitude, gradient and curvature. This is, incidentally, an extremely compact representation of the scattering data.

I(q) to G(r) transformation routine.

Using these analytic descriptions of the measured data, uniformly spaced data was generated for Fast Fourier Transforming, using a 32k point complex 64bit FFT. A routine *sq2gr* was written in *Apl* to take $I(q)$ data, multiply by q , create anti-symmetric data, Fast Fourier transform using a well tested algorithm, take the resulting imaginary data, (throwing away the data for $r \leq 0$), scale the spatial axis by 2π (since the FFT was scaled to convert time to frequency, see chapter 12), and divide by r , returning $\gamma(r)$ data measured in $\{\text{\AA}\}$.

This routine was written in *Apl*, translated to *C* [Budd, 1988, Sirlin, 1988..1999], screen plotting of the intermediate and final results added, and compiled to run under Linux on a 200MHz PC. It was tested by generating $I(q)$ data for a sphere, and transforming it to $\gamma(r)$. This transformed data was co-linear with the analytic data for $\gamma_0(r)$ of a sphere (with the exception of the missing point at zero radius).

Finally, for our silica data we use the values measured in chapter 11.5 for ρ_s (density of the voidless silica lattice) and ρ_g (density of the silica grain = $\rho_s \times f_g$) to re-scale the $\gamma(r)$ data to density units $\rho_g \times G(r)$, such that at $r = 0$ the density was the (voidless) silica density ρ_s , and at $r = \infty$ the density was the grain density $\rho_g = f_g \times \rho_s$.

We plot the resulting $G(r)$ s for the seven sol-gel silicas in figures 113, 114.

P.2 G(r) to I(q).

G(r) to I(q) transformation routine.

A matching $G(r)$ to $I(q)$ transformation was written to transform Monte-Carlo calculated $G(r)$ data to $I(q)$.

Since the Monte-Carlo calculations give us data in the form $f_s \cdot G(r)$, which tends at large r to an average value f_s , we first need to convert this to $\gamma(r)$, with an average value of 0. Thus this routine accepts 2+1/8 k data pairs, averages the last 1/4 k to find f_s , subtracts this, throws the last 1/8 k away, zero extends to 8k, multiplies by r , forms the anti-symmetric data, performs a 16k point complex 64bit FFT, takes the imaginary data, throws data for $q \leq 0$ away and divides by q to obtain $I(q)$. See figures 106, 107, 108, 109 where the Monte-Carlo calculated scattering is compared with the measured scattering for seven sol-gel silicas.

Appendix Q

Appendices for Monte-Carlo integration of $G(r)$.

*To enable verification of the Monte-Carlo integration of $G(r)$ for model structures,
we list the main subroutines called.*

Q.1 Generating random unit vectors in 3D, using von Neuman's method.

We wish to generate N random unit vectors in 3D [Powles, 1994], as part of the modified Monte-Carlo integration of $G(r)$:

Generate just over $2N$ random points in a cube of side 2, centered on 0; reject those points outside the unit sphere; then re-normalise the remainder (usually just over half) to the surface of the sphere; trim to N .

This may be expressed as :

```
Vec ← runitvec N;S;L2;L;Sel
    ϱ
    ϱ produces N random unit vectors
    ϱ using von Neuman's method :
    ϱ
S ← -1 + 2 × 1E-6 × -1 + ? ((2+⌈2.1×N⌋),3) ρ 1000001
L2 ← +/ S*2
Sel ← 1 ≥ L2
L2 ← Sel/L2
S ← Sel/[1]S
L ← L2*0.5
Vec ← (N,2) ρ S ÷ [1] L
```

Q.2 Generate a Gaussian distribution, using the Central Limit Theorem.

The Central Limit Theorem states that if we convolve together sufficient distributions of any form, the result will tend towards a Gaussian distribution [Powles, 1994].

This routine convolves together 12 uniform distributions; in principle any large number would do, but 12 has the advantage that this gives directly a variance of 1, since the variance of a uniform distribution is $\frac{1}{12}$. This method is inaccurate in the wings: it can not generate values outside ± 6 .

Generating 10000 points in such a distribution, with Mean = 1, Variance = 0.005, and binning into 101 bins in the range 0..2, we get the Gaussian distribution in figure 143.

This may be expressed as :

```
Distribution ← SizeShape gauss MeanVar
  ϱ
  ϱ generate a Gaussian distribution :
  ϱ samples from a univariate normal distribution
  ϱ (sizeshape) gauss (mean,variance)
  ϱ
Distribution ← MeanVar[1] + (MeanVar[2]*÷2) × -6 + 1E-6 × -12 +
  +/ ? (SizeShape,12) ϱ 1000001
```

Q.3 Generate non-uniform distributions by remapping a uniform distribution.

In a probability distribution, the probability of x being less than X_L is given by [Abramowitz and Stegun, 1954, Evans, 1972-1999] :

$$Pr(x \leq X_L) = \frac{1}{C_n} \cdot \int_{-\infty}^{X_L} f(x) dx = R$$

Where C_n is a normalisation constant.

We then need to revert this, to obtain x as a function of R ; i.e. to get a mapping function that can be applied to a uniform distribution R_u , to give us our required non-uniform distribution.

Q.3.1 Generate a distribution $\propto x$ by remapping a uniform distribution.

When calculating $S(Q)$ from $G(r)$ we wish to obtain $r \cdot G(r)$; thus it is useful to be able to selectively increase the density of radial evaluations at large r – i.e we wish to generate a probability distribution that is (at least partly) weighed to have a density $\propto r, r^2$.

For a simple distribution $\propto x$ we have for limits of $0, L$:

$$\frac{\int_0^L x dx}{\int_0^L x dx} = \frac{x^2}{L^2} = R_u$$

Thus we may obtain the non-uniform distribution by remapping a uniform distribution R_u by :

$$x = L \cdot \sqrt{R_u}$$

Generating 600 points in such a distribution, and 300 points in a uniform distribution and binning into 10 bins in the range 0.5, we get the distribution in figure 142, This contains the first two parts of a function to generate $G(r)$ data with weighting suitable for viewing both as $G(r)$ and $r \cdot G(r)$.

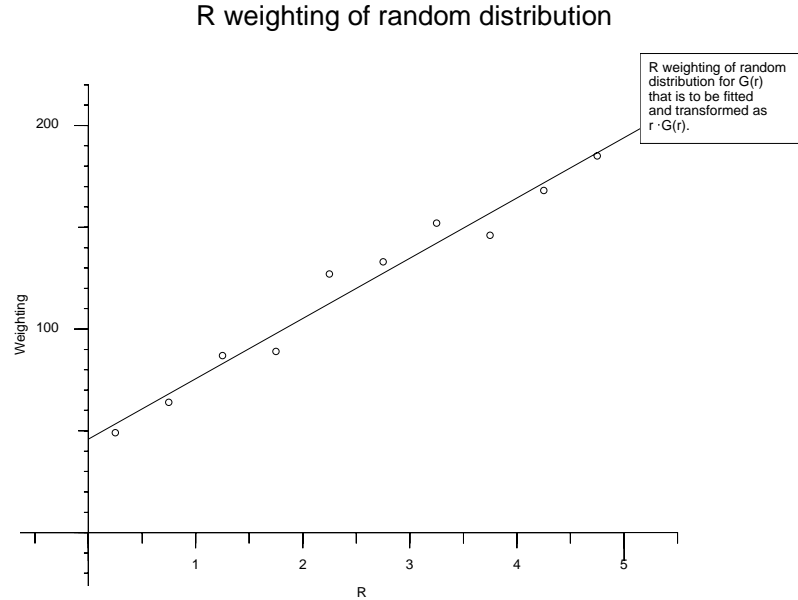


Figure 142: Distribution $\propto x +$ Uniform Distribution.

Q.3.2 Generate a Sech distribution by remapping a uniform distribution.

For $\text{sech}(x)$ we have [Abramowitz and Stegun, 1954, Evans, 1972-1999, Maple, 1999] :

$$\frac{\int \text{sech}\left(\frac{x-X_d}{X_0}\right) dx}{\int_{-\infty}^{+\infty} \text{sech}\left(\frac{x-X_d}{X_0}\right) dx} = \frac{X_0}{X_0 \cdot \pi} \tan^{-1}\left(\sinh\left(\frac{x-X_d}{X_0}\right)\right) = R_u$$

Thus we may obtain a Sech distribution by remapping a uniform distribution R_u by :

$$x = X_d + X_0 \cdot \sinh^{-1}(\tan(\pi \cdot R_u))$$

Generating 10000 points in such a distribution, with $X_d = 1$, $X_0 = 0.05$, and binning into 101 bins in the range 0..2, we get the *sech* distribution in figure 143.

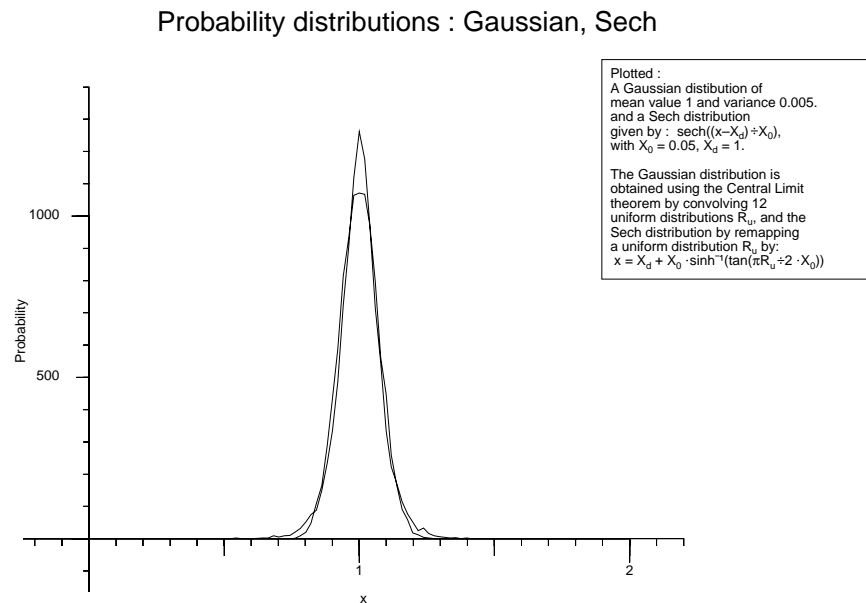


Figure 143: Gaussian and Sech Distributions.

This may be expressed as :

```
Distribution ← SizeShape prsech MeanVarRange;Xd;X0;Xr
ρ
Xd ← MeanVarRange[1]
X0 ← MeanVarRange[2]
Xr ← MeanVarRange[3 4]
Distribution ← Xd + X0 × -5○ 3○ ○ (-0.5×+/Xr)+
(-1+? SizeShape ρ 1000001) ÷ 1000000 ÷ - -/Xr
```

Appendix R

Fourier transform of Sech is Sech.

We measure scattering from sol-gel silicas that is well fitted by Sech functions. Thus we need an analytic Fourier transform of Sech.

It is not generally appreciated outside UKC Physics that in the same way the Fourier transform of a Gaussian is another Gaussian, so the Fourier transform of Sech is another Sech. We use the algebraic language Maple to demonstrate this relationship. We then show how Maple can be instructed to use this relationship in further Fourier transformations.

It is possible to prove that the Fourier transform of *Sech* is another *Sech*, either by equating series [Powles, 1972-1999, discussions] or by a contour integration technique [Evans, 1972-1999, discussions].

Here we just use the algebraic language *Maple* to indicate the relationship, and then show how *Maple* can be induced to use this relationship in further transformations, such as the $I(q)$ to $\gamma(r)$ transformation.

R.1 Demonstration of relationship : Sech \leftrightarrow Ft(Sech).

Maple worksheet ft_sech_proof.mws :

'Proof' of Fourier transform of sech \leftrightarrow sech - Maple version

J.B.W.Webber@ukc.ac.uk 99_10_7

```
> assume(n>0,n,integer);
```

```
> f(x) := sech(a*x);
```

```
f(x) := sech(a x)
```

```
> f(x) := convert(f(x),exp);
```

$$f(x) := 2 \frac{1}{e^{ax} + \frac{1}{e^{ax}}}$$

> f(x) := simplify(f(x));

$$f(x) := 2 \frac{e^{-ax}}{1 + e^{-2ax}}$$

we have for the Taylor expansion of $1/(1+p)$:

> T(p) := 1/(1+p);

$$T(p) := \frac{1}{1+p}$$

> series(%,p);

$$1 - p + p^2 - p^3 + p^4 - p^5 + O(p^6)$$

Thus the n th term is :

> fn(x) := 2*exp(-a*x)*(-1)^n*exp(-2*a*n*x);

$$fn(x) := 2 e^{-ax} (-1)^n e^{-2anx}$$

such that the sum of the series is $\operatorname{sech}(ax)$:

> sum(fn(x),n=0..infinity);

$$2 \frac{e^{-ax} e^{2ax}}{e^{2ax} + 1}$$

> simplify(%);

$$2 \frac{e^{ax}}{e^{2ax} + 1}$$

We want the Fourier transform :

$$F(k) = \int_{-\infty}^{\infty} f(x) * \exp(ikx), x=-\infty..infinity)$$

we note that $f(x)$ is symmetric, therefore

$$F(k) = 2 * \int_0^{\infty} f(x) * \cos(kx), x=0..infinity)$$

$$= 2 * \int_0^{\infty} (\sum_{n=0}^{\infty} fn(x)) * \cos(kx), x=0..infinity)$$

$$= 2 * \sum_{n=0}^{\infty} (\int_0^{\infty} fn(x) * \cos(kx), x=0..infinity), n=0..infinity)$$

at this point we need to define a as positive :

> assume(a>0,a,real);

> Fn(k) := 2 * int(fn(x)*cos(k*x),x=0..infinity);

$$\begin{aligned} \text{Fn}(k) &:= 4(-1)^{n^{\sim}} \sqrt{a^{\sim 2} + 4 a^{\sim 2} n^{\sim} + 4 a^{\sim 2} n^{\sim 2} + k^2} / \left(\sqrt{\%1} \left(\frac{a^{\sim 2}}{\%1} + 4 \frac{a^{\sim 2} n^{\sim}}{\%1} + 4 \frac{a^{\sim 2} n^{\sim 2}}{\%1} \right. \right. \\ &+ \frac{k^2}{\%1} + \frac{k^2 a^{\sim 2}}{(a^{\sim} + 2 a^{\sim} n^{\sim})^2 \%1} + 4 \frac{k^2 a^{\sim 2} n^{\sim}}{(a^{\sim} + 2 a^{\sim} n^{\sim})^2 \%1} + 4 \frac{k^2 a^{\sim 2} n^{\sim 2}}{(a^{\sim} + 2 a^{\sim} n^{\sim})^2 \%1} \\ &\left. \left. + \frac{k^4}{(a^{\sim} + 2 a^{\sim} n^{\sim})^2 \%1} \right) \right) \\ \%1 &:= 1 + \frac{k^2}{(a^{\sim} + 2 a^{\sim} n^{\sim})^2} \\ &> \text{Fn}(k) := \text{simplify}(\text{Fn}(k)); \end{aligned}$$

$$\text{Fn}(k) := 4 \frac{(-1)^{n^{\sim}} a^{\sim} (1 + 2 n^{\sim})}{a^{\sim 2} + 4 a^{\sim 2} n^{\sim} + 4 a^{\sim 2} n^{\sim 2} + k^2}$$

Thus we now have the Fourier transform of a sech expressed as an infinite sum of Lorentzians, with the nth term of the form :

$$\begin{aligned} &> \text{t}(n) := 4 * (-1)^n / (a * ((2 * n + 1)) * (1 + (k / (a * (2 * n + 1)))^2)); \\ \text{t}(n) &:= 4 \frac{(-1)^n}{a (2 n + 1) \left(1 + \frac{k^2}{a^2 (2 n + 1)^2} \right)} \end{aligned}$$

At this point Maple has difficulties caused by the presence of the constant a (probably because I have not told it something it needs to know) and it generates hypergeometric expressions.

If we write $K = k/a$, we have :

$$\begin{aligned} &> \text{Fn}(K) := 4 * (-1)^n * (1 + 2 * n) / (a * (1 + 4 * n + 4 * n^2 + K^2)); \\ \text{Fn}(K) &:= 4 \frac{(-1)^{n^{\sim}} (1 + 2 n^{\sim})}{a^{\sim} (1 + 4 n^{\sim} + 4 n^{\sim 2} + K^2)} \\ &> \text{F}(K) := \text{sum}(\text{Fn}(K), n=0..infinity); \\ \text{F}(K) &:= \frac{(1 + I K) (-1 + I K) \pi}{a^{\sim} (1 + K^2) \sin\left(\frac{1}{2} \pi (3 + I K)\right)} \\ &> \text{F}(K) := \text{expand}(\text{F}(K)); \\ \text{F}(K) &:= \frac{\pi}{a^{\sim} (1 + K^2) \cosh\left(\frac{1}{2} \pi K\right)} + \frac{\pi K^2}{a^{\sim} (1 + K^2) \cosh\left(\frac{1}{2} \pi K\right)} \\ &> \text{F}(K) := \text{simplify}(\text{F}(K)); \\ \text{F}(K) &:= \frac{\pi}{\cosh\left(\frac{1}{2} \pi K\right) a^{\sim}} \\ &> \text{a} := 'a'; \end{aligned}$$

$$a := a$$

Hence we have obtained $F(k)$, the Fourier transform of $f(x) = \text{sech}(a * x)$:

> f(x);

$$2 \frac{e^{-ax}}{1 + e^{-2ax}}$$

> F(k) := (Pi/a)*sech((Pi*k)/(2*a));

$$F(k) := \frac{\pi \operatorname{sech}\left(\frac{1}{2} \frac{\pi k}{a}\right)}{a}$$

We may now add this to the definition of known Fourier transforms using :

> with (inttrans);

[addtable, fourier, fouriercos, fouriersin, hankel, hilbert, invfourier, invhilbert,
invlaplace, invmellin, laplace, mellin, savetable]

> addtable(fourier, 1/(exp(a*t)+exp(-a*t)), (Pi/(2*a))*sech(Pi*w/(2*a)), t

> ,w,{a},a::Range(0,infinity));

> savetable(fourier, 'ftsech_defn.m');

This saves the definitions in a file; in a later session we may say :

> with (inttrans);

[addtable, fourier, fouriercos, fouriersin, hankel, hilbert, invfourier, invhilbert,
invlaplace, invmellin, laplace, mellin, savetable]

> read('ftsech_defn.m');

> assume(Q0>0);

> fourier(sech(q/Q0),q,r);

$$\operatorname{fourier}\left(\operatorname{sech}\left(\frac{q}{Q0}\right), q, r\right)$$

> simplify(%);

$$\frac{Q0 \pi}{\cosh\left(\frac{1}{2} \pi r Q0\right)}$$

and for the neutron scattering $I(q) \leftrightarrow G(r) - 1$ transform we have :

> Gs(r) := I*(1/rho)*(1/r)* fourier(q*sech(q/Q0),q,r);

$$Gs(r) := - \frac{\frac{\partial}{\partial r} \operatorname{fourier}\left(\operatorname{sech}\left(\frac{q}{Q0}\right), q, r\right)}{\rho r}$$

> simplify(%);

$$\frac{1}{2} \frac{Q0^{-2} \pi^2 \sinh\left(\frac{1}{2} \pi r Q0\right)}{\rho r \cosh\left(\frac{1}{2} \pi r Q0\right)^2}$$

Bibliography

- A. Abragam. *Principles of Nuclear Magnetism*. Clarendon Press, Oxford, 1961.
- M. Abramowitz and I.A. Stegun. *Handbook of Mathematical Functions*. Dover Publications, Inc., New York, London, dover edition, 1954.
- R.S. Aikens and W.J. Kerwin. Single amplifier, minimal RC , Butterworth, Thomson, and Chebyshev filters to sixth order. *Proc. Int. Filter Symp.*, pages 81–82, 1972.
- S.G. Allen, P.C.L. Stephenson, and J.H. Strange. Morphology of porous media studied by nuclear magnetic resonance. *J. Chem. Phys.*, 106(18):7802–7809, 1997.
- S.G. Allen, P.C.L. Stephenson, and J.H. Strange. Internal surfaces of porous media studied by nuclear magnetic resonance. *J. Chem. Phys.*, 108(19):8195–8198, 1998.
- T.A. Allen. *Particle Size Measurement*. Chapman and Hall Ltd., London, 2nd edition, 1975.
- S.M. Alnaimi. *The Characterisation of Porous Media by NMR*. Phd, Physics, University of Kent at Canterbury, UK., 1994.
- S.M. Alnaimi, J.H. Strange, and E.G. Smith. The characterisation of porous solids by NMR. *Magnetic Resonance Imaging*, 12(2):257–259, 1994.
- J.M. Baker, J.C. Dore, and P. Behrens. Nucleation of ice in confined geometry. *Journal of Physical Chemistry B*, 101(32):6226–6229, 1997.
- M. Barnsley. *Fractals everywhere*. Academic Press, Inc., London, 1988.
- E.P. Barret, L.G. Joyner, and P.P. Halenda. The determination of pore volume and area distributions in porous substances. i. computations from nitrogen isotherms. *J. Am. Chem. Soc.*, 73:373–380, 1951.

- F. Bloch. Nuclear induction. *Phys. Rev.*, 70(7,8):460–474, 1946.
- Boas.M.L. *Mathematical Methods in the Physical Sciences*. John Wiley & Sons,Inc, New York, 1966.
- H.F. Booth and J.H. Strange. Organic nanocrystals: an NMR study of cyclohexane in porous silica. *Mol. Phys*, 93(2):263–269, 1998.
- D.W. Breck. *Zeolite molecular sieves. Structure, chemistry and use*. John Wiley & Sons, London, 1974.
- C.J. Brinker and G.W. Scherer. *Sol-gel science. The Physics and Chemistry of Sol-Gel Processing*. Academic Press, Inc, London, 1990.
- K.R. Brownstein and C.E. Tarr. Spin-lattice relaxation in a system governed by diffusion. *J.Magn.Resn.*, 26:17–24, 1977.
- K.R. Brownstein and C.E. Tarr. Importance of classical diffusion in NMR studies of water in biological cells. *Phys. Rev. A.*, 19:2446–2453, 1979.
- M. Brun, A. Lallemand, J-F. Quinson, and C. Eyraud. A new method for the simultaneous determination of the size and the shape of pores: The thermoporometry. *Thermochimica Acta*, 21:59–88, 1977.
- S. Brunauer, P.H. Emmett, and E. Teller. Adsorption of gases in multimolecular layers. *J. Am. Chem. Soc.*, 60:309–319, 1938.
- T. Budd. *An APL Compiler*. Springer Verlag, New York, Berlin, 1988.
- P.T. Callaghan. *Principles of Nuclear Magnetic Resonance Microscopy*. Oxford Science Publications, Clarendon Press., Oxford, 1993.
- A.S. Clarke and J.D. Wiley. Numerical simulation of the dense random packing of a binary mixture of hard spheres: Amorphous metals. *Phys. Rev. B*, 35(14):7350...7356, 1987.
- S.L. Codd. *3DFT NMR Imaging of Solid-Like Materials*. Phd, Physics, University of Kent at Canterbury, UK., 1996.
- J.M. Cowley. *Diffraction Physics*. North-Holland, Amsterdam, 1975.

- L De Broglie. *L. De Broglie and L. Brillouin, Selected Papers on Wave Mechanics*. Blackie, London, 1929.
- R. Defay, I. Prigogine, A. Bellemans, and D.H. Everett. *Surface tension and adsorption*. Longmans, Green & Co Ltd, London, english edition, 1951, 1966.
- C. DePanfilis and K.J. Packer. Characterisation of porous media by NMR imaging and flow-diffraction. *European Physical Journal - Applied Physics*, 8(1):77–86, 1999.
- F. d’Orazio, S. Bhattacharja, W.P. Halperin, K. Eguchi, and T. Mizusaki. Molecular-diffusion and NMR relaxation of water in unsaturated porous silica glass. *Phys. Rev. B.*, 42:9810–9818, 1990.
- J.C. Dore, F. Coveney, and M-C. Bellissent-Funel. The structure and nucleation properties of liquids in confined geometry, 1991. Paper presented at Recent Developments in the Physics of Fluids, Int. Symposium, Oxford, UK.
- J.C.. Dore, M. Dunn, T. Hasebe, and J.H Strange. Orientationally disordered crystals in porous silica - cyclohexane. *Colloids and Surfaces*, 36(2):199–207, 1989.
- F.A.L. Dullien. *Porous Media. Fluid Transport and Pore Structure*. Academic Press, London, 1979.
- M. Dunn, J.C.. Dore, and P. Chieux. Structural studies of ice formation in porous silicas by neutron-diffraction. *Journal of Crystal Growth*, 92(1-2):233–238, 1988.
- A. Dyer. *An Introduction to Zeolite Molecular Zieves*. John Wiley & Sons, Chichester, 1988.
- W.A.B. Evans, 1972-1999. Discussions.
- H. Farman, F.M.. Coveney, and J.C. Dore. Structural features of the liquid plastic crystal phase-transition for cyclohexane in bulk and confined geometry. *Physica B*, 180(PtB):857–860, 1992.
- T.C. Farrar and E.D. Becker. *Pulse and Fourier Transform NMR, Introduction to Theory and Methods*. Academic Press Inc, New York, London, 1971.
- L.A. Feigin and D.I. Svergun. *Structure Analysis by Small-Angle X-Ray and Neutron Scattering*. Plenum Press, New York, 1987.

- J.L. Finney. Random packings and the structure of simple liquids. *Proc. Roy. Soc. London, Ser A*, 319:479, 1970.
- M. Francon. *Diffraction: Coherence in Optics*. Pergamon Press, Oxford, 1st edition, 1966. Babinet Proof.
- D.P. Gallegos, K. Munn, D.M. Smith, and D.L. Stermer. A NMR technique for the analysis of pore structure: Application to materials with well-defined pore structure. *Journal of Colloid and Interfacial Science*, 119(1):127–140, 1986.
- M.A. Gardner, A.N. North, J.C. Dore, C.S.M. Delecea, and D. Cazorlaamoros. Characterization of pore-size in activated carbons by small-angle x-ray-scattering. *Studies in Surface Science and Catalysis*, 87:273–281, 1994.
- J.W. Gibbs. On the equilibrium of heterogeneous substances. *Transactions of the Connecticut Academy*, III:108–248, 343–524, 1875, 1878.
- J.W. Gibbs. *The scientific papers of J. Willard Gibbs*, volume 1: Thermodynamics. Dover Publications, Inc., Constable and Co., New York, London, new dover edition, 1906 reprinted 1961.
- J.W. Gibbs. *Collected Works*. Longmans, Green and Co., New York, 1928.
- T.A.P. Green. Three dimensional visualization in NMR imaging,. Msc, Physics, University of Kent at Canterbury, UK., 1994.
- S.J. Gregg and K.S.W. Sing. *Adsorption, Surface Area and Porosity*. Academic Press, London, 2nd edition, 1967.
- A. Guinier. La diffraction des rayons x aux tres petits angles: applications a l'etude de phenomenes ultra microscopiques. *Annales de Physique*, 12(11th series):161–237, 1939.
- Hague.B. *An Introduction to Vector Analysis for Physicists and Engineers*. Methuen & Co. Ltd., London, 5th edition, 1965.
- W.P. Halperin, S. Bhattacharja, and F. d'Orazio. Relaxation and dynamic properties of water in partly filled porous media using NMR techniques. *Mag. Res. Imag*, 9(5): 733–737, 1991.

- J.M. Hammersley and D.C. Handscomb. *Monte Carlo Methods*. Methuen & Co. Ltd, London, 1964.
- E.W. Hansen, M. Stocker, and R. Schmidt. Low-temperature phase transition of water confined in mesopores probed by NMR. influence on pore size distribution. *J. Chem. Phys.*, 100(6):2195–2200, 1996.
- R.K. Harris. *Nuclear Magnetic Resonance Spectroscopy. A Physico chemical view*. Longman Scientific & Technical, London, 1987.
- C.E. Hayes, J.F. Scheneck, O.M. Mueller, and M. Eash. An efficient, highly homogeneous radiofrequency coil for whole-body NMR imaging at 1.5T. *J. Mag. Reson.*, 63:622–628, 1985.
- D.I. Hoult and R.E. Richards. Critical factors in the design of sensitive high resolution nuclear magnetic resonance spectrometers. *Proc. Roy. Soc.*, A344:311–340, 1975.
- L.P. Huelsman, editor. *Active RC Filters. Theory and Application*. Dowden, Hutchinson & Ross, Inc., John Wiley & Sons, Inc., Stroudsburg, Pennsylvania, 1976.
- A.J. Hurd, D.W. Schaefer, and J.E. Martin. Surface and mass fractals in vapor-phase aggregates. *Phys. Rev. A*, 35(5):2361–2364, 1987.
- K. Ishikiriyama and M. Todoki. Pore size distribution (psd) measurements of silica gels by means of differential scanning calorimetry ii. thermoporosimetry. *Journal of Colloid and Interface Science*, 171:103–111, 1995.
- K. Ishikiriyama, M. Todoki, and K. Motomura. Pore size distribution (psd) measurements of silica gels by means of differential scanning calorimetry i. optimisation for determination of psd. *Journal of Colloid and Interface Science*, 171:92–102, 1995.
- K.E. Iverson. *A Programming Language*. Wiley, New York, 1962.
- C.L. Jackson and G.B. McKenna. The melting behavior of organic materials confined in porous solids. *J. Chem. Phys.*, 93(12):9002–9011, 1990.
- C. Jallut, J. Lenoir, C. Bardot, and C Eyraud. Thermoporometry. modelling and simulation of a mesoporous solid. *Journal of Membrane Science*, 68:271–282, 1992.

- J.-Y. Jehng, D.T. Sprague, and W.P. Halperin. Pore structure of hydrating cement paste by magnetic resonance relaxation analysis and freezing. *Mag. Res. Imag.*, 14(7/8):785–791, 1996.
- W.S. Jodrey and E.M. Tory. Computer simulation of close random packing of equal spheres. *Phys. Rev. A*, 32(4):2347...2351, 1985.
- L.W. Johnson and R.D. Riess. *Numerical Analysis*. Addison-Wesley Publishing Company, Inc, New York, 2nd edition, 1982.
- G.W.C. Kaye and T.H. Laby. *Tables of Physical and Chemical Constants and some Mathematical Functions*. Longmans, Green and Co., London, 13th edition, 1966.
- R. Kimmich, S. Stapf, A.I. Maklakov, V.D. Skirda, and E.V. Khozina. Self-diffusion in fluids in porous glass: Confinement by pores and liquid adsorption layers. *Magnetic Resonance Imaging*, 14(7-8):793–797, 1996a.
- R. Kimmich, S. Stapf, A.I. Maklakov, V.D. Skirda, and E.V. Khozina. Self-diffusion in fluids in porous glass: Confinement by pores and liquid adsorption layers. *Magnetic Resonance Imaging*, 14(7-8):841–846, 1996b.
- D.J. Kroon. *Philips Technical Library*, chapter Laboratory Magnets, pages 186–189. Philips, Eindhoven, 1968.
- L.D. Landau and E.M. Lifshitz. *Quantum Mechanics, non-relativistic theory*. Pergamon Press, Oxford, 2nd edition, 1965.
- I. Langmuir. The adsorption of gases on plane surfaces of glass, mica and platinum. *J. Am. Chem. Soc.*, 40:1361–1403, 1918.
- J-C Li and D.K. Ross. Dynamical scaling for spinodal decomposition - a small-angle neutron scattering study of porous vycor glass with fractal properties. *J. Phys. Condens. Matter.*, 6:351–362, 1994.
- A. Macnair. *A Targetted System for High Resolution in Vivo Broad-Line MRI*. Phd, Physics, University of Kent at Canterbury, UK., 1995.
- B.B. Mandelbrot. *The fractal geometry of nature*. W.H.Freeman and Co., New York, 1983.

- Maple, 1999. Maple Programming Language V5.
- F.M.A. Margaca, I.M. Miranda Salvaado, and J Teixeira. SANS of ZrO₂.SiO₂ gels. *Journal of Non-Crystalline Solids*, 209:143–148, 1997.
- F.M.A. Margaca, I.M. Miranda Salvado, and J. Teixeira. Small angle neutron scattering study of silica gels: influence of ph. *Journal of Non-Crystalline Solids*, 258(1-3):70–77, 1999.
- J.E. Martin, D.W. Schaefer, and Hurd A.J. Fractal geometry of vapor-phase aggregates. *Phys. Rev. A*, 33(5):3540–3543, 1986.
- Mason.G. A model of the pore space in a random packing of equal spheres. *Journal of Colloid and Interface Science.*, 35(2):279...287, 1971.
- H.S.W. Massey and H. Kestelman. *Ancillary Mathematics*. Isaac Pitman & Sons Ltd., London, 2nd edition, 1964.
- W.M. Meier and D.H. Olson. *Atlas of zeolite structure types*. Butterworths, London, 2nd edition, 1987.
- A. Mitzithras, F.M. Coveney, and J.H. Strange. Nmr-studies of the diffusion of cyclohexane in porous silica. *Journal of Molecular Liquids*, 54(4):273–281, 1992.
- G. Mountjoy, 1999. Discussions.
- K.L. Murray, N.A. Seaton, and M.A. Day. Use of mercury intrusion data, combined with nitrogen adsorption measurements, as a probe of pore network connectivity. *Langmuir*, 15(23):8155–8160, 1999.
- R.J Newport, B.D. Rainford, and R. Cywinsky, editors. *Neutron Scattering at a Pulsed Source*. IOP Publishing Ltd., Adam Hilger, Bristol, 1988.
- M.O. Norris and J.H. Strange. A nuclear magnetic resonance sample temperature controller using liquid nitrogen injection. *J.Phys. E*, 2(2):1106–1108, 1969.
- D. Pines-Rojanski, D. Huppert, and D. Avnir. Pore-size effects on the fractal distribution of adsorbed acceptor molecules as revealed by electronic energy transfer on silica surfaces. *Chem. Phys. Lett.*, 139(1), 1987.
- C.M. Planck. *Theory of Heat*, volume 3,4. Macmillan Co., London, 1929.

- G Porod. Die rontgenkleinwinkelstreuung von dichtgepackten kolloiden systemen. *Kolloid. Z.*, 124(2):83–114, 1951.
- J.G. Powles, 1972-1999. Discussions.
- J.G. Powles, 1994. Lectures.
- H.J. Rahman. *M.R.I. Studies of Polymeric Systems*. Phd, Physics, University of Kent at Canterbury, UK., 1991.
- J.D.F. Ramsay. Surface and pore structure characterisation by neutron scattering techniques. *Advances in colloid and interface science*, 77:13–37, 1998.
- J.D.F. Ramsay and B.O. Booth. Determination of structure in oxide sols and gels from neutron scattering and nitrogen adsorption measurements. *Journal of the Chemical Society - Faraday Transactions I*, 79(Pt1):173–184, 1983.
- F. Reif. *Fundamentals of Statistical and Thermal Physics*. McGraw-Hill Kogakusha, Ltd., Tokyo, London, international student edition, 1965.
- M.D. Rintoul and S. Torquato. Computer simulations of dense-hard-sphere systems. *J. Chem. Phys.*, 105(20):9258...9265, 1996.
- H.L. Ritter and L.C. Drake. Pore-size distribution in porous materials: Pressure porosimetry and determination of complete macropore-size distributions. *Ind. Eng. Chem.*, 17:782–786, 1945.
- P.W. Schmidt. Small-angle scattering studies of disordered, porous and fractal systems. *J. Appl. Cryst.*, 24:414–435, 1991.
- G.D. Scott and D.M. Kilgour. The density of random close packing of spheres. *J. Phys. D*, 2:863, 1969.
- P.A. Sermon, Y. Wang, and M.S.W. Vong. Fractal analysis of sol-gel derived silica by adsorption. *Journal of Colloid and Interface Science*, 168:327–332, 1994.
- S. Sirlin, 1988..1999. maintainer, Apl to C compiler, Nasa.
- C.G. Sonwane and S.K. Bhatia. Structural characterization of MCM-41 over a wide range of length scales. *Langmuir*, 15(8):2809–2816, 1999.

- H.E. Stanley and N. Ostrowsky, editors. *On growth and form. Fractal and non fractal patterns in Physics*. Martinus nijhoff, Dordrecht, The Netherlands, 1986.
- S. Stapf, R. Kimmich, and R.O. Seitter. Field-cycling NMR relaxometry of liquids confined in porous glass: Evidence for levy-walks. *Magnetic Resonance Imaging*, 14(7-8):841–846, 1996.
- D.C. Steytler and J.C. Dore. Neutron-diffraction studies of water in porous silica .ii. temperature-variation in the super-cooled regime. *Molecular Physics*, 56(5):1001–1015, 1985.
- D.C. Steytler, Dore J.C., and Wright C.J. Neutron diffraction studies of water in meso- and micro- pores. *Molecular Physics*, 48(5):1031–1051, 1983a.
- D.C. Steytler, Dore J.C., and Wright C.J. Neutron-diffraction study of cubic ice nucleation in a porous silica network. *Journal of Physical Chemistry*, 87(14):2458–2459, 1983b.
- J.H. Strange. Cryoporometry: A new NMR method for characterising porous media. *Nondestr. Test. Eval.*, 11:261–271, 1994.
- J.H. Strange and M.R. Halse. *Imaging Techniques for Solids and Quasi-solids. Encyclopaedia of NMR*. Wiley, 1996.
- J.H. Strange, M. Rahman, and E.G. Smith. Characterisation of porous solids by NMR. *Phys. Rev. Let.*, 71(21):3589–3591, 1993.
- J.H. Strange and J.B. Webber. Characterization of porous solids by NMR. In *12th Specialized Colloque Ampere, Corfu.*, Athens, 1995.
- J.H. Strange and J.B.W. Webber. Multidimensionally resolved pore size distributions. *Appl. Magn. Reson.*, 12(2-3):231–245, 1997a.
- J.H. Strange and J.B.W. Webber. Spatially resolved pore size distributions by NMR. *Meas. Sci. Technol.*, 8(1-7):555–561, 1997b.
- J.H. Strange, J.B.W. Webber, and S.D. Schmidt. Pore-size distributions mapping. *Magn. Reson. Imag.*, 14(7/8):803–805, 1996.

- J. Teixeira, J.M. Zanotti, M.C. Bellissent-Funel, and S.H. Chen. Water in confined geometries. *Physica B*, 234:370–374, 1997.
- M. Teubner and R. Strey. Origin of the scattering peak in microemulsions. *J. Chem. Phys.*, 87(5):3195–3200, 1987.
- J. Thomson. Theoretical considerations on the effect of pressure in lowering the freezing point of water. *Trans. Roy. Soc. Edinburgh*, xvi(5):575–580, 1849.
- J. Thomson. On crystallization and liquefaction, as influenced by stresses tending to change form in the crystals. *Proc. Roy. Soc.*, xi:473–481, 1862.
- J.J. Thomson. *Application of dynamics to Physics and Chemistry*. Macmillan & Co, London, 1888.
- W. Thomson. On the equilibrium of vapour at a curved surface of liquid. *Phil. Mag., series 4*, 42(282):488–452, 1871.
- R.R. Valiullin, V.D. Skirda, S. Stapf, and R. Kimmich. Molecular exchange processes in partially filled porous glass as seen with NMR diffusometry. *Physical Review E*, 55(3):2664–2671, 1997.